RICE UNIVERSITY

Dissolution, processing and fluid structure of graphene and carbon nanotube in superacids: The route toward high performance multifunctional materials.

by

Natnael Behabtu

A Thesis Submitted
in Partial Fulfillment of the
Requirements for the Degree
Doctor of Philosophy

Approved, Thesis Committee:

Matteo Pasquali, Chair
Professor of Chemical and Biomolecular Engineering

Sibani Lisa Biswal
Assistant Professor in Chemical and Biomolecular Engineering

Clarence A. Miller
Louis Calder Professor Emeritus in Chemical and Biomolecular Engineering

Edwin Thomas
William and Stephanie Sick Dean of The George R. Brown School of Engineering

Wade Adams
Director of the Smalley Institute for Nanoscale Science and Technology

Houston, Texas
January, 2012

Dissolution, processing and fluid structure of graphene and carbon nanotube in superacids: The route toward high performance multifunctional materials.

by

Natnael Behabtu

Carbon allotropes have taken central stage of nanotechnology in the last two decades. Today, fullerenes, carbon nanotubes (CNTs), and graphene are essential building blocks for nanotechnology. Their superlative electrical, thermal and mechanical properties make them desirable for a number of technological applications ranging from lightweight strong materials to electrical wires and support for catalysts. However, transferring the exceptional single molecule properties into macroscopic objects has presented major challenges.

This thesis demonstrates that carbon nanotubes and graphite dissolve in superacids and these solution can processed into macroscopic objects. Chapter 2 reviews neat CNT fiber literature. Specifically, the two main processing methods —solid–state and solution spinning — are discussed. CNT aspect ratio and fibers structure are identified as the main variables affecting fiber properties. Chapter 3 shows that graphite can be exfoliated into single-layer graphene by spontaneous dissolution in chlorosulfonic acid. The dissolution is general and can be applied to various forms of graphite, including graphene nanoribbons. Dilute solutions of graphene can be used to form transparent conductive films. At high concentration, graphene and graphene nanoribbons in chlorosulfonic acid forms a liquid crystal and can be spun directly into continuous fibers. Chapter 4 describes a solution–based method to form a thin CNT network. This network is an ideal specimen support for electron microscopy. Imaging nanoparticles with atomic resolution and sample preparation from reactive fluids demonstrate the unique feature of solution–based CNT support compared to state–of–the–art TEM supports . Chapter 5 describes CNT liquid crystalline phase.

Specifically, CNT nematic droplets shape and merging dynamics are analyzed. Despite nanotube liquid crystals having been reported in various CNT systems, a number of anomalies such as low order parameter and spaghetti–like, nematic droplets are reported. However, CNTs in chlorosulfonic acid show elongated, bipolar droplets typical of other rod–like molecules. Moreover, their large aspect ratio allows capturing the transition from homogeneous to bipolar transition expected from scaling arguments.The equilibrium shape and merging dynamics demonstrate the liquid nature of CNT liquid crystals. Chapter 6 describes the CNT/chlorosulfonic acid fiber spinning. The influence of starting material, spinning dope concentration, spin draw ratio and coagulation on fiber properties is discussed. The linear scaling of fiber strength with CNT aspect ratio is demonstrated experimentally, once the best properties from different batches are compared. Moreover, Successful multi–hole spinning demonstrates the intrinsic scalability of wet spinning to meet the typical production output of industrial–scale spinning. Chapter 7 compares acid–spun CNT fibers to other CNTs fibers as well as existing engineered materials. Acid–spun CNT fibers combine the typical specific strength of high–strength carbon fibers to the thermal and electrical conductivity of metals. These properties are obtained because of a highly aligned, dense structure. The combined strength and electrical conductivity allow acid-spun fibers to be used as structural as well as conducting wire while the combined electrical and thermal properties allow for exceptional field emission properties.

In conclusion, we demonstrate that multifunctional properties of carbon nanotubes that have fuelled much of the research in the past 20 years, can be attained on a macroscopic level via rational design of fluid–phase processing.

Contents

Illustrations

Tables

Chapter 1

Introduction

Closed-cage carbon allotropes were postulated and discovered in the second half of the 20th century [Smalley, 1997, Monthioux and Kuznetsov, 2006]. Carbon allotropes have grown to include fullerenes, carbon nanotubes (CNTs) and graphene [Kroto et al., 1985, Novoselov et al., 2004, Iijima, 1991, Bethune et al., 1993, Kratschmer et al., 1990]. The excitement around these molecules stem from their properties. From one side, the carbon–carbon bond allows thermal, chemical and mechanical stability rarely met by other elements. On the other side, the variety of 3D structures (spheres, cylinders with various radii, single layer 2D macromolecules) creates a wide range of electronic structures. Their perfect structure allows ballistic electron and phonon transport [Hone et al., 1999a, Choi et al., 2000, Novoselov et al., 2004], associated with mechanical properties [Treacy et al., 1996, Sanchez-Portal et al., 1999] unmet in the macroscopic word. The potential scientific and technological implications of such versatile and robust molecules were clear since the early stage of their discovery and they have been an essential building block in creating what we now call "nanotechnology".

Materials based on carbon allotropes can be the building block of lighter and stronger materials for fuel efficient and safer cars and airplanes, efficient wires that transport the energy produced from remote renewable sources and computer transistors that are reduced to single layer molecules with optimal transport of both heat and electrons. Thus, the new carbon allotropes may represent for the 21^{st} century

what polymers were in the 20^{th} century. Yet, engineering applications have been lagging behind, because they require processing. In fact, for carbon allotropes to have similar impact, high–throughput processing techniques such as wet spinning, roll coating, and pressure molding need to be adapted to handle CNTs, fullerene, and graphene. The ease of these processing techniques is what allowed polymers to be such dominant and ubiquitous materials of the 20^{th} century. A major advantage of polymers over CNTs and graphene is their ability to form processable fluid phases (polymer melts or solutions). Carbon nanotubes and graphite do not melt and they were considered insoluble, with spontaneous dissolution proved only recently [Davis et al., 2009, Behabtu et al., 2010].

Successful processing begins with understanding and control of dissolution, coupled with scientific understanding of fluid structure and structural evolution. In applications such as fibers and films, the goal is to retain the electronic and mechanical properties of individual CNTs and graphene in the final product. Ideally, the final product would consist of a solid, ordered material made solely of CNTs, graphene, or a hybrid structure. The present thesis addresses some of the challenges related to the dissolution and processing of CNTs and graphite. Chapter 2 describes the different processing approaches employed to produce CNT fibers, highlighting advantages and drawbacks of the different processing techniques. Chapter 3 describes graphite dissolution in superacids and the different fluid structures attained as a function of concentration. In chapter 4 processing techniques for manufacturing TEM specimen support using graphene and CNTs are covered. Chapter 5 deals with CNT liquid crystals; more specifically, CNT nematic droplets are analysed. Chapter 6 revolves around the multitude of parameters influencing fiber spinning and, more specifically, CNT/superacid wet spinning. We will highlight the parameters that show

the strongest correlation to fibers strength and conductivity. Chapter 7 describes the structure and properties of fibers obtained form CNT/superacid solution spinning.

Chapter 2

CNT Fiber spinning: A Review

The discovery*, and development of new materials often catalyzes technological breakthroughs, particularly when a qualitative leap in electrical, thermal or mechanical properties occurs. The field of fiber applications is poised for such a breakthrough. In the past fifty years, fibers composed of rod–like polymers have had a strong impact on aerospace, military, and industrial applications requiring lightweight, mechanically strong materials [Adams et al., 1989]. Carbon nanotubes (CNTs) have a rod–like geometry and high molecular stiffness [Duggal and Pasquali, 2006, Yakobson et al., 2000, Treacy et al., 1996], similar to rod–like polymers, and they possess a unique combination of excellent mechanical, thermal and electrical properties. Single Walled Carbon Nanotubes (SWNTs) and Multi Walled Carbon Nanotubes (MWNTs), being a roll-up of graphene sheet, share with graphene the exceptional mechanical properties (modulus and tensile strength) [Yamamoto et al., 2008]. Experiments indicate an average modulus of 1 TPa [Krishnan et al., 1998, Treacy et al., 1996] and tensile strength of 13-100 GPa for SWNTs [Yu et al., 2000a, Peng et al., 2008]; these values are nearly independent of diameter. Electrical conductivity and current carrying capacity of metallic SWNTs exceed those of copper, and their thermal conductivity is higher than diamond [Tans et al., 1997, Baughman, 2000, Hone et al., 1999a]. Fibers composed of such CNTs have the

*This chapter is an updated version of a published review article (See reference [Behabtu et al., 2008])

potential to form high strength, lightweight, thermally and electrically conducting elements [Baughman, 2000]. However, a number of hurdles must be overcome in order to realize this potential, including the difficulty of processing CNTs into macroscopic articles that retain a relevant fraction of the properties of the constituent CNTs.

The method of CNT synthesis controls the type (MWNT vs. SWNT), length (sub-micron to millimeter), chirality, and processability, which in turn determines the properties of the final CNT–based macroscopic products. Here, we briefly describe the various means of synthesizing CNTs and review the various approaches used for neat fiber production.

2.1 Synthesis of Nanotubes

Research on CNT synthesis and CNT fibers are interdependent, with fibers and other applications driving new discoveries in CNT catalysis and growth. Many of the key advances in CNT synthesis led immediately to new results in fiber production. Below we review various synthesis techniques that can produce either shorter CNTs (including arc–discharge, laser oven, HiPco, fluidized bed CVD) or longer CNTs (substrate growth CVD, catalytic gas flow CVD).

Programmatic research in CNTs began with Ijima's observation of MWNTs produced in an arc–discharge fullerene reactor [Iijima, 1991]. Gram–level production was attained rapidly [Ebbesen and Ajayan, 1992]. SWNTs were discovered soon after by means of metal catalysts in the arc–discharge system [Bethune et al., 1993]. The properties of individual SWNTs are even more promising than those of MWNTs, particularly in regard to electrical and optical properties.

Milligram–level quantities of SWNTs were produced by adapting laser ablation, a technique used to produce fullerenes [Kroto et al., 1985], to attain a high yield (>70%) of feedstock into defect–free SWNTs (∼1.4 nm diameter) [Guo et al., 1995, Thess et al., 1996]. A laser beam evaporates a graphite sample containing 1% nickel and cobalt catalyst particles; in the resulting vapor, the metal aggregates into carbon-saturated catalyst nanoparticles, which sprout the growth of SWNTs. Without the catalyst particles SWNTs cannot be produced [Arepalli, 2004]. A gas-phase chemical vapor deposition (CVD) process, termed HiPCO (high-pressure CO), was developed [Nikolaev et al., 1999, Nikolaev, 2004]; this process was the first high throughput production of high quality SWNTs, and much of the early fiber spinning efforts were based on this material [Vigolo et al., 2000, Ericson et al., 2004].

These alternative CVD processes involve the formation of CNTs on preformed metal nanoparticles that catalyze the decomposition of a gaseous carbon compounds and subsequent growth of either SWNTs or MWNTs [Dai et al., 1999]. Different carbon precursors can be used, including methane, CO, alcohols, and acetylene. These alternative CVD processes are attractive because the reaction temperatures can be ∼400 K lower than the arc discharge and laser ablation techniques. Several different CVD approaches have been used, including fluidized bed [See and Harris, 2007], substrate-growth [Fan et al., 1999, Zhang et al., 2004, Li et al., 2006a], and "catalytic gas flow CVD" [Li et al., 2004, Koziol et al., 2007, Lashmore et al., 2006]. Fluidized bed CVD, along with laser oven, arc discharge, and HiPco produce short SWNTs in the 0.05 - 3 μm range while substrate growth and catalytic gas flow CVD can produce much longer CNTs. The use of fluidized bed CVD is cost-effective

and results in high CNT production rates [See and Harris, 2007]. One particularly intriguing fluidized bed CVD process is the CoMoCat technique. This process combines the scalability of fluidized bed reactors to high diameter selectivity [Resasco et al., 2002]. Thus, it is attractive when fibers with specific SWNT diameter are desired.

CNTs that are orders of magnitude longer (100 μm - cm) can be produced as vertical arrays by depositing catalyst nanoparticles on a substrate and exposing them to carbon feedstock gas [Fan et al., 1999, Li et al., 2006a]. Both MWNTs and SWNTs can be produced; SWNT formation is favored by using smaller catalyst particles and lower carbon feed rates at the particle surface. Scaling the deposition of catalyst on the substrate seems possible [Nishino et al., 2007], although it is still too early to estimate relative complexity and costs. Another method for growing very long CNTs is catalytic gas flow CVD [Koziol et al., 2007]. This method can grow millimeter–long CNTs (a mixture of MWNTs and SWNTs) with a variety of carbon sources. Depending on the carbon source, it is possible to control the composition of MWNTs and SWNTs [Li et al., 2004]. Recent theoretical insights [Ding et al., 2009] are leading to new experiments where SWNT chirality is shifting from semiconductors to "armchair" SWNTs [Ding et al., 2009].

Control of length, chirality (particularly for electrical applications), and minimization of defects are the most pressing challenges in the field of CNT synthesis. Along with the scalability of the synthesis process, these challenges are critical for materials applications of CNTs, including the production of neat CNT fibers [Joselevich et al., 2008].

2.2 Formation of CNT Fibers

There are two main methods for production of fibers: liquid and solid–state spinning. Natural fibers like wool and cotton are formed by solid–state spinning (assembling discrete fibers into a yarn), while most synthetic fibers are created from a concentrated, viscous liquid. This liquid is a melt or solution of the starting material, which is aligned by flow processing, and converted into a fiber through cooling or solvent removal.

Both liquid and solid–state spinning have been adapted for CNT–based fibers. The development of liquid-state process has been particularly challenging due to difficulties in processing CNTs in the liquid state. CNTs do not melt due to their high stiffness and high molecular weight, and they are not soluble in organic or aqueous solvents. CNTs tend to form bundles rather than dissolving because of strong van der Waals forces between their side walls. This is problematic because the CNTs cannot be controlled and aligned in solution unless they are dispersed at the molecular (single–CNT) level. A number of techniques have been adopted to overcome this problem. CNTs have been functionalized with side groups that make them soluble in common solvents [Liang et al., 2004]. However, such covalent functionalization destroys their electronic properties and limits the ultimate ordering and packing of the CNTs in the fiber; it is therefore not a viable option for multifunctional fibers. CNT dispersions can be stabilized in surfactant solution and super-acids; both of these fluid phases have been used to spin CNT–based fibers. A completely different approach is solid–state spinning, which circumvents the dissolution problem by drawing a fiber from a vertically–grown array of CNTs or drawing directly from an aerogel in the furnace. In the following sections, both solution and solid–state spinning will be analyzed.

2.2.1 Surfactant–Based Solution Spinning

Dispersion

Surfactants are used to stabilize CNT dispersions because of their ability to form micellar structures around individual CNTs. These CNT/micelle structures are kinetically stable because the surrounding surfactant molecules prevent CNTs from bundling together again [Vigolo et al., 2000, Poulin et al., 2002].

CNTs are dispersed in an aqueous solution containing a surfactant such as sodium dodecyl sulfate (SDS); the solution is then sonicated to break up CNT bundles and allow the surfactant micelles to encase the CNTs [O'Connell et al., 2002]. The surfactant concentration is critical for the formation of a good dispersion. If too low, stabilization is inadequate; conversely, if too high, the osmotic pressure of the excess micelles causes depletion–induced aggregation. In the case of HiPco SWNTs stabilized by SDS in water, optically homogeneous solutions can be formed with 0.35% wt of SWNTs and 1% wt SDS; however, the exact phase boundaries are a function of SWNT diameter and length. This process has been extended to DWNTs and MWNTs [Miaudet et al., 2005, Razal et al., 2007], and other surfactants such as tetratri-methylamonium-bromide (TMB) and lithium dodecylsulfate (LDS) have also been used [Kozlov et al., 2005, Poulin et al., 2002].

A different approach to CNT solution spinning involves the use of ethylene glycol with the aid of ultrasonic dispersion [Zhang et al., 2008c]. MWNTs with outer diameters of 50± 25 nm and lengths of 100±80 μm formed a nematic phase at ∼1%, which was spun into diethyl ether to form a solid fiber [Zhang et al., 2008c]. This fiber

had weak tensile strength (150-200 MPa) but good modulus (70-140 GPa). The high modulus values reflect the good alignment (order parameter of 0.85) coming from liquid crystalline phase processing while the low tensile strength values are a consequence of low aspect ratio (2000) molecules. The conductivity along the MWCNT fiber axis at room temperature was between 12500 $\mu\Omega$ cm(8 kS m^{-1}) and 3330 $\mu\Omega$ (30 kS m^{-1}). Heating at 2000 °C did not improve the fiber properties [Zhang et al., 2008c].

Processing

Vigolo *et al.* were first to produce fibers with high SWNT content (above 60% wt) [Vigolo et al., 2000, 2002]. In this process, a surfactant-stabilized SWNT solution is coagulated in a poly-vinyl alcohol (PVA)/water bath; PVA displaces the surfactant and induces flocculation of the SWNTs into an intermediate gel–like fiber structure, termed a "proto–fiber". This proto–fiber simultaneously undergoes solvent loss, solidification, stretching, and CNT alignment to form a final solid fiber structure. Some PVA is retained in the solid fiber (up to 40%) and can be removed by post-processing.

The coagulant must flow faster than the proto–fiber in order to promote alignment (Fig.2.1b). Vigolo *et al* accomplished this by rotating the coagulant container (Fig. 2.1). The method was made continuous and faster by injecting the SWNT dispersion into a cylinder with the coagulant flowing in the same direction [Dalton et al., 2003, Munoz et al., 2004, Mercader et al., 2010].

Coagulation baths other than PVA/water were utilized in order to produce polymer–free fibers [Kozlov et al., 2005]. The coagulants were low–viscosity polymer-

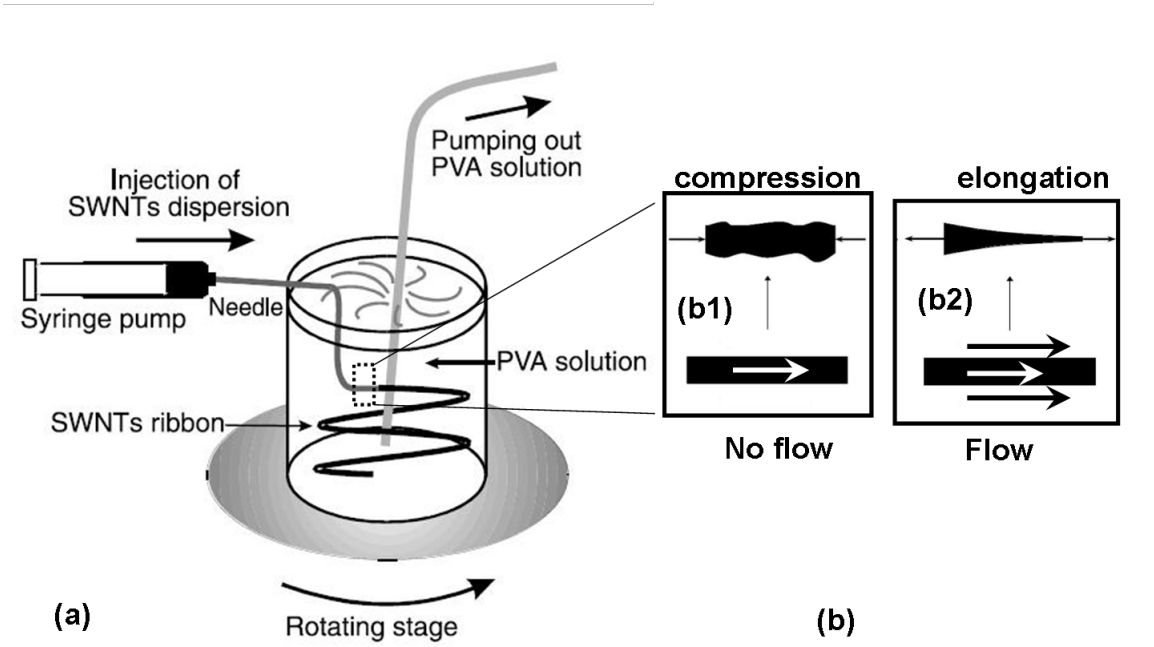

Figure 2.1 : Schematic of the rotating bath (a) used for coagulating surfactant-dispersed SWNTs into a fiber. When the coagulation bath is not flowed (b1), a net compressive force acts on the proto–fiber, compromising alignment. When the coagulant flows along with the extruded fiber (b2), a net stretching (elongational) force results and increases alignment. Fig 2.1(a) is reproduced from [Vigolo et al., 2000]

free acids or bases that promote the flocculation of the initial CNT dispersion. Near–instantaneous flocculation occurs with coagulants with pH<1 or pH>13. The as-spun fiber retains much of the coagulant (90% liquid content), which can lead to a hollow fiber morphology depending on how the liquid is further removed (such hollow morphologies are promising for some specialized applications, but they show poor mechanical properties). Fibers spun using these polymer-free coagulants have weak mechanical properties (tensile strength, modulus, and toughness) compared to PVA-coagulated fibers [Kozlov et al., 2005]. Ethanol/glycerol (volume ratio 1:1) or ethanol/glycol mixtures (1:3) can also be used as coagulants for surfactant-stabilized solution spinning [Steinmetz et al., 2005]. The resulting fibers are flexible when wet but become brittle upon drying. Coagulants other than PVA have the advantage of creating polymer-free, electrically conducting fibers; however, the weak mechanical properties limit PVA free coagulants as alternative coagulants.

The PVA coagulation bath technique has also been used for non-surfactant dispersions of SWNTs. Barisci *et al* dispersed a higher concentration (1wt%) of SWNTs in an aqueous DNA solution [Barisci et al., 2004]. The DNA stabilizes the SWNTs by wrapping around the CNT surface and increasing inter–CNT repulsion. The resulting fiber properties are inferior to the more recent SDS–based SWNT/PVA fibers. Neri *et al* coagulated a basic dispersion (10 pH) of oxidized MWNTs in an acidic (2 pH) PVA (5% wt)/water dispersion [Neri et al., 2006]. Compared with the SDS–based fibers, the resulting fibers had similar toughness, better resistivity but lower tensile strength and modulus.

2.2.2 Post–Processing

Different post-processing treatments have been developed in order to increase SWNT content in the final fiber and to improve mechanical and electrical properties. For example, the fiber can be stretched by swelling it in a PVA solvent and drying it under load [Vigolo et al., 2002]. The fiber does not dissolve in pure PVA solvent, showing that the CNT–PVA interaction is strong. This technique improves both the Young's modulus (up to 40 GPa) and the tensile strength (up to 230 MPa) of the fiber.

High drawing (5 times the initial length) can also improve fiber properties as shown by Munoz *et al* [Munoz et al., 2004]. This is possible because necking behavior, typical of thermoplastic polymer fibers, does not occur. These fibers have high toughness —high tensile strength combined with large failure elongation— and showed the highest energy-to-break (over 600 J/g) ever measured at that time. However, the energy absorbed at low strain was comparatively low; these tough SWNT/PVA fibers absorb an energy of 10 J/g for a strain up to 10% (for comparison, polyaramide fibers absorb an energy of 35 J/g within 3% strain). To improve the low-strain energy absorption, the as-spun fibers are dried and drawn at 850% while heated at 180 °C, higher than the glass transition of PVA, to induce PVA crystallization. The post-processed fiber has a lower strain-to-failure and toughness but absorbs more energy at low strain. The tensile strength increases up to 1.4-1.8 GPa but the maximum strain to failure decreases [Miaudet et al., 2005].

The load transfer between CNT and PVA in a PVA/CNT fiber is extremely effective. In fact, the mechanical tensile strength of this fiber is an order of magnitude higher than the fibers coagulated without PVA. However, these fibers do not

substantially improve the modulus and tensile strength of pure PVA–made fibers, although they have excellent toughness. Moreover, the presence of the polymer between CNTs compromises the fibers' electrical properties. The electrical properties can be improved by stretching the as-spun fiber ($2{\cdot}10^8$ $\mu\Omega{\cdot}$cm) or by eliminating the polymer by annealing the fiber in hydrogen at 1000 °C (50000 $\mu\Omega{\cdot}$cm)[Badaire et al., 2004]. However, the elimination of PVA is likely to affect the mechanical properties.

2.2.3 Spinning from Acid Solutions

Dispersion

Superacids are the only known solvents for cabon nanomolecules, including CNTs and graphene [Ramesh et al., 2004, Rai et al., 2006, Davis et al., 2009, Behabtu et al., 2010, Parra-Vasquez et al., 2010, Rai et al., 2007]. Strong acids like fuming sulfuric acid are inexpensive solvents that are easily handled industrially [Cremlyn, 2002]; they have been used in the commercial production of high-performance synthetic fibers composed of rod–like polymers [Choe and Kim, 1981]. SWNTs behave as rigid rods when dissolved in superacids [Davis et al., 2004]. SWNTs dissolve spontaneously because they are protonated; the ensuing electrostatic repulsion counteracts the attractive van der Waals interactions. The protonation is fully reversible [Ramesh et al., 2004, Engtrakul et al., 2005, Davis et al., 2009, Parra-Vasquez et al., 2010]. Depending on the concentration, three distinct regimes are observed. At low concentrations SWNTs are randomly oriented (isotropic) in the acid. At intermediate concentrations, a biphasic equilibrium between coexisting isotropic and liquid crystalline phases is observed; higher concentrations result in a fully liquid crystalline solution (Fig. 2.2) [Davis et al., 2004]. For rigid–rod

molecules, the specific phase boundaries are a function of different parameters such as rod aspect ratio [Onsager, 1949, Flory, 1956], polydispersity [Flory and Frost, 1978, Odijk and Lekkerkerker, 1985], and solvent quality [Flory, 1956]. All these parameters (aspect ratio, polydispersity, solvent quality and concentration) need to be considered to quantitatively capture the CNTs phase diagram [Davis et al., 2009, Green et al., 2009b].

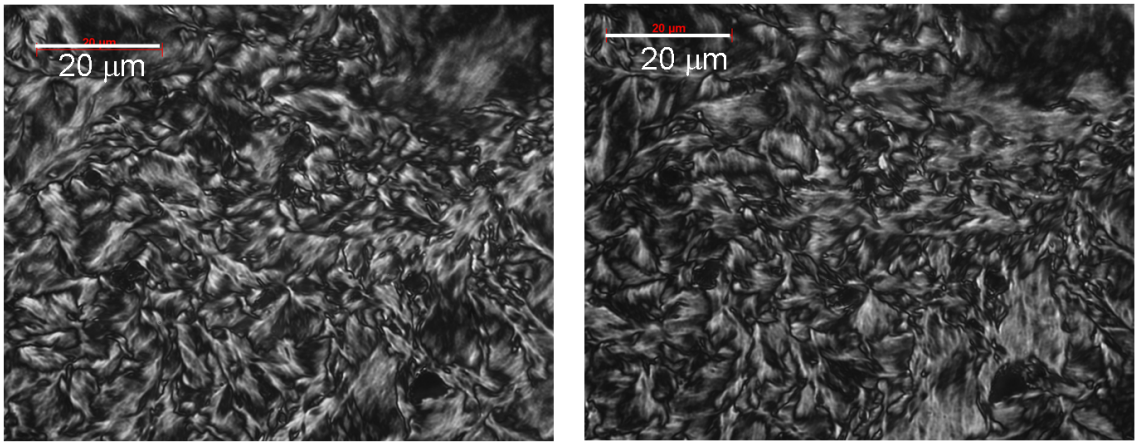

Figure 2.2 : Microscopy images under cross polars of SWNT (8% wt) dissolved in sulfuric acid. Left and right images are rotated by 0° and 45°, respectively. The birefringent texture is typical of liquid crystalline solutions.

Acid solvents have the unique ability to form liquid crystalline dopes with high concentration of CNTs; in sulfuric acid, fibers are spun at 8% wt SWNT concentration, over one order of magnitude higher than what can be achieved by using surfactants. Chlorosulfonic acid yields even higher liquid crystalline concentrations, and allows formation of liquid crystalline phases from a number of CNTs sources [Davis et al., 2009, Parra-Vasquez et al., 2010].

Processing

Of the possible coagulants for fuming sulfuric acid/SWNT dopes, the use of water or dilute sulfuric acid solutions results in optimal fibers. The density of fibers coagulated in water is 1.11 $\pm$ 0.07 g/cm^3 (about 77% of a perfectly packed crystal); coagulation in ether yields a low-density (0.87$\pm$ 0.08 g/cm^3) dogbone-shaped fiber [Ericson et al., 2004]. The microstructure of the fiber shows large bundles, termed "super-ropes", between 200-600 nm in diameter, and each super-rope is characterized by smaller ropes/bundles with diameters of $\sim$ 20 nm. These bundles are an order of magnitude larger than bundles observed in the raw material. Thus, the acid process creates a substantial change in the morphology of the initial SWNT powder, although the role of coagulation in the formation of these super-ropes is still poorly understood [Hua, 2007]. Although chlorosulfonic acid is the most flexible of CNT solvents, fiber spinning from such a solvent is more challenging since this solvent is highly reactive with water as well as a number of common organic solvents [Davis et al., 2009].

A key parameter for improving SWNT alignment, and thus fiber properties is the extrusion orifice diameter. This affects both shear rate and coagulation dynamics (see also Eq. 6.2 and 6.8), with small orifices giving higher shear rate (thus, better alignment) and smaller fibers with optimal coagulation. In fact, as the extrusion spinneret diameter is decreased from 500 to 125 μm, both room temperature thermal (from 5 to 17 W/mK) and electrical resistivity (from 6400 to 2500 $\mu\Omega$ cm) improve because of the increased alignment (X-ray FWHM decrease from 63° to 45°) [Zhou et al., 2004b]. The as–spun fiber has a low

resistivity due to acid doping but also has a low modulus. Annealing the fiber in an inert gas at 850 °C improves the modulus but simultaneously increases fiber resistivity by an order of magnitude by removing the acid [Zhou et al., 2004a]. Spinneret aspect ratios (spinneret length over its diameter) used for SWNT/super acid fiber spinning are usually high (> 50), and there is not a clear correlation between fiber alignment and spinneret aspect ratio in the range of 50-200 [Ericson, 2003]. Because of the spontaneous ordering in the liquid crystalline phase, these fibers have high alignment without the need for post-treatments [Ericson et al., 2004].

The acid–spun fiber modulus and electrical properties (see Table 2.4) are among the best values ever reported for CNT–based fibers. However, the tensile strength is low compared to both water/PVA coagulated fibers and solid–state drawn CNT–fibers (see Table 2.3. However, this process has not been used for MWNTs or long ($> 10\mu$m) CNTs. Chapter 7 shows new progress in acid–spun fibers.

2.2.4 Post–Processing

Not much work has beeb done on acid–spun post–processing. Acid–spun fibers have high packing fraction, thus, polymer infiltration, a technique widely used for solid–state fibers (see next section), has not been tried. High temperature annealing, a technique often used for rigid–rod polymeric fibers [Adams et al., 1989, Kwolek et al., 1977], has not yielded significant thermal conductivity and mechanical strength improvement while it significantly degrades electrical properties (resistivity increases by an order of magnitude) [Zhou et al., 2004b].

2.2.5 Solid–State Spinning

Naturally–occurring fibers include cotton and wool; these materials consist of discrete fibrils (diameter 15 μm, length 3 cm) that can be assembled into a continuous fiber, termed a yarn, by solid–state spinning [Morton and Hearle, 1962]. Yarn properties improve with increasing fibril length and decreasing fiber diameter [Zhang et al., 2004]. CNTs have been used in an analogous fashion to produce yarns in a process where individual CNTs or bundles of CNTs act as the constituent fibrils in the yarn.

Yarns of CNTs were first observed as discrete fibers formed by CNTs made by gas phase CVD, with 10-20 cm length and ∼5 to ∼20 μm diameter [Cao et al., 2002] These strands had promising electrical resistivity (5 $\mu\Omega$ m) and tensile strength (0.8 GPa), although not as good as those of individual CNTs. Using the same CVD reaction, Li *et al* were able to spin the CNT aerogel formed in the reaction zone directly into a continuous fiber [Li et al., 2004].

A different technique was used by Jiang *et al.* [2002]; it involves fiber spinning from a vertically–grown CNT array and has been used by a number of different research groups [Zhang et al., 2004, 2007a, 2006, 2008b]. Other studies used solid–state spinning of cotton–like raw material to produce yarns as well [Ci et al., 2007, Zheng et al., 2007].

Synthesis Requirements

Not all raw CNT materials can be converted into a yarn. For example, Zhang *et al* emphasize the bundling within the vertically grown CNTs and the disordered regions

on the top and bottom of the forests; these disordered regions help to preserve fiber integrity by interlocking the CNTs [Zhang et al., 2004]. Conversely, studies by Zheng *et al* [2006] and Li *et al* [2006] found that highly aligned CNTs that are free of amorphous carbon are critical for successful solid–state spinning. However, later work showed that cotton–like, disordered aggregates of CNTs can be spun into fibers [Ci et al., 2007, Zheng et al., 2007]. These results challenge the notion of pre-alignment as a key element for solid–state spinning. The debate is still open with some recent studies supporting the idea of CNT alignment as the key requirement for carpet spinning [Zhang et al., 2010a], while others [Kuznetsov et al., 2011] were highlighting small bundles interconnecting the large–diameter MWNT bundles as key for CNT forest spinnability.

For both vertically grown CNT and gas-phase CVD solid–state spinning, the carbon source is a critical factor [Li et al., 2004, Jia et al., 2011]. For gas phase CVD spinning, CNTs formed from carbon sources that contain oxygen (i.e., acetone, diethyl-ether) have been successfully spun, while CNTs formed from aromatic hydrocarbons have not. This is likely due to the increased amorphous carbon associated with aromatic carbon sources. For vertically grown CNT fibers, fibers grown with ethylene (C_2H_4) as carbon source gave better mechanical properties than fibers grown with acetelene (C_2H_2) [Jia et al., 2011]. The main difference between these two carbon sources is the diameter and number of walls of the produced CNTs, with ethylene giving smaller diameters with fewer walls.

On the synthesis level, other key properties for successful drawing are CNT type (diameter and number of walls) and length. The type and dimension of the

catalyst nano-particles and carbon source are typically used to control the numbers of walls, while reaction time controls their length [Zhang et al., 2007b, Li et al., 2006a, Jia et al., 2011]. Motta *et al.* [2007] argue that large diameter SWNTs and DWNTs (>5 nm for SWNTs) are particularly desirable because they flatten (buckle radially) into flat sheets, increasing the contact between CNT surfaces and improving load transfer at the molecular scale [Motta et al., 2007]. Longer CNTs have larger surfaces for load transfer, and lower fiber defect density (Fig. 2.3). However, for vertically–grown arrays, the growth of longer CNTs comes at the price of increased amorphous carbon, which limits the maximum spinnable length. In the gas-phase CVD reaction, a reduced catalyst flow rate results in fibers with improved mechanical properties [Motta et al., 2005]. This may be due to increased content of SWNT, or it may be due to longer CNTs [Carver et al., 2005].

Figure 2.3 : This schematic depicts two fibers composed of CNTs of different length (Top - shorter CNTs; bottom - longer CNTs). The density of end points (indicated by a $\star$) between CNTs decreases with growing CNT length. The end point of a CNT is a defect because the intermolecular interactions between CNTs at the end points are much weaker than chemical bonds within the single molecule. Decreasing the density of end points should yield fibers with higher tensile strength.

Processing

Increases in inter–bundle contacts and density improve fiber mechanical properties. A number of different processing and post-processing techniques have been used to achieve this goal, including high speed drawing, twisting and surface tension-driven densification.

In gas-phase CVD fiber spinning, the CNT–aerogel take–up velocity (winding rate) is a critical parameter: Higher winding rates lead to improved alignment and higher density. The maximum achievable winding rate is limited by aerogel breakage.

Twisting is useful because it increases the load transfer between fibers (Fig. 2.4); it is essential when there are no significant transverse forces to bind the fiber assembly together. Zhang *et al* [2004] obtained continuous yarns from relatively (relative to solid–state spun fibers) short MWNTs (∼100 μm) when twisting is applied. The twisted yarn diameter has to be smaller than the length of the constituent CNTs in order for twisting to be effective [Zhang et al., 2004]. Thinner fibers contain a higher fraction of CNTs with an optimal twist angle. When CNT length is increased, even untwisted yarns are strong enough to be handled and tested [Zhang et al., 2007a].

2.2.6 Post–Processing

Surface tension-driven densification is a widely used technique to increase fiber density. When fibers spun from vertically–grown arrays are pulled through droplets of ethanol, the yarn thickness shrinks to 20-30 μm fibers and increases the starting carpet density (0.05 g/ml) to 1 g/ml [Zhang et al., 2006]. In gas-phase CVD

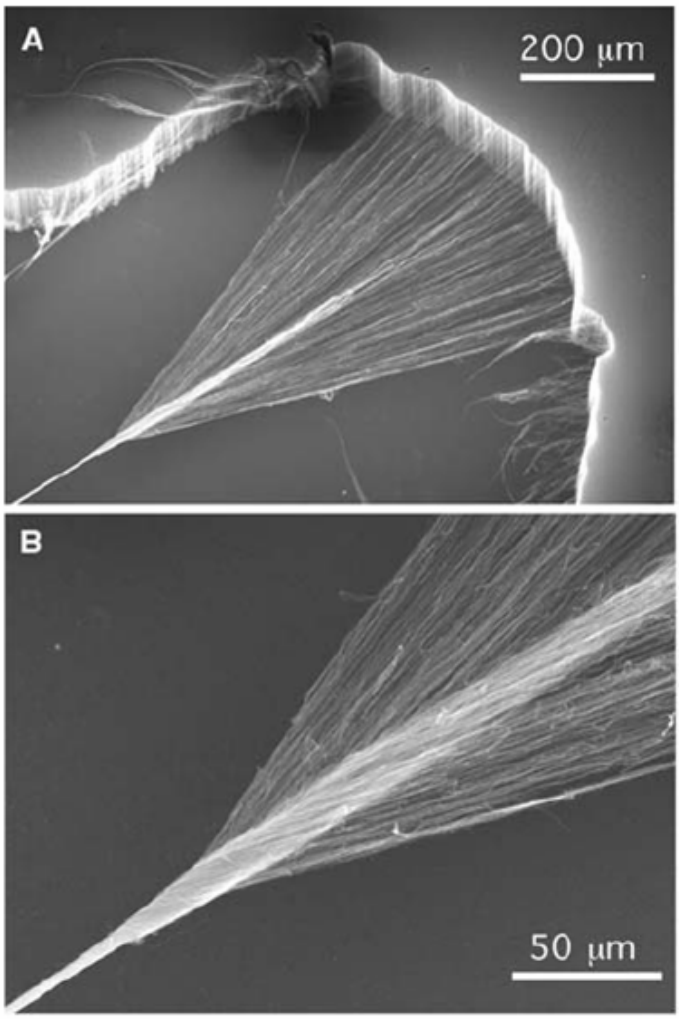

Figure 2.4 : SEM images of a CNT yarn twisted during solid–state spinning. Reproduced from [Zhang et al., 2004]

reactions, acetone vapor densification increases yarn density by two orders of magnitude [Koziol et al., 2007, Zhong et al., 2010]. Ci *et al* [2007] noted that the starting, cotton–like material must be wet in order to draw a continuous fiber because the wet material is denser and has stronger inter–CNT interactions.

Solid–state drawn fibers are usually flexible. Zhang *et al* [2006] attribute this property to fibers small diameter and weak inter–tube bonding, which results in smaller bending stresses. Flexible fibers reported so far are usually characterized by low fiber modulus [Zhang et al., 2004, 2006]. However, thermal annealing can reduce this flexibility and increase fiber modulus [Zhang et al., 2006]; thus, thermal annealing of flexible fibers can be used to lock the geometry of a given shape [Zhang et al., 2006]. This can be rationalized by the tendency of CNTs to create covalent bonds at high temperature (1500 °C) by "welding" each other [Kim et al., 2004, Fantini et al., 2006].

Another useful post-processing technique is infiltration by a polymer solution such as PVA, which can double fiber strength [Zhang et al., 2004]. Polymer infiltration is indeed a technique often used to improve fiber properties [Ma et al., 2009, Jia et al., 2011, Naraghi et al., 2010, Cheng et al., 2009, Liu et al., 2010a, Ryu et al., 2011]. Unlike coagulation in water/PVA, this technique does not dramatically compromise fiber electrical properties because PVA fills up voids and improves inter–CNT load transfer without compromising inter–CNT connectivity. This technique is particularly effective for porous fibers, including most solid–state drawn fibers. However, if polymer coating is needed because of unoptimal load transfer between CNT molecules, ultimate failure of such a composite material will be caused by the polymer intrinsic strength limitation and not to the CNTs one. Thus, the

tensile strength of the fibers will be only a small fraction of the strength of CNT bundles [Naraghi et al., 2010].

The mechanical and electrical properties of solid–state drawn fibers are limited because of the porous morphology. Typical fiber morphology involves three levels of organization. The constitutive macromolecules are CNTs, the next level involves CNT bundles with typical diameters of 20-60 nm (smaller than the "super-ropes" obtained for the super acid process). This bundles connect into a network with a preferred orientation along the fiber axis. The density of these fibers is only 30-50% of the perfect CNT packing density even after densification. High porosity is a manifestation of low bundle overlap. In fact, even when considering specific properties (fiber properties normalized by density), solid–state fibers show tensile strengths that are below expectation for the length of their constitutive molecules (See Fig. 2.7(b)).

2.3 Fiber Properties

CNTs' unique combination of mechanical, thermal, and electrical properties makes CNT–based fibers perfect candidates for multi–functional materials. In the following section, we review the theoretical limits for the properties of a macroscopic assembly and compare with actual experimental values.

2.3.1 Mechanical Properties

Although the tensile strength of individual CNTs is very high, the properties of a macroscopic CNT assembly are dictated by their structure. Fiber structure is determined by supra-molecular elements such as bundles, alignment of the molecules along fiber axis, the amount of undispersed particles and their size, radial and

axial inhomogeneity,and density. Thus fiber strength and its optimization has to be tackled keeping in mind a multidimensional variable space. Even in the ideal case of single CNTs perfectly aligned into a single bundle, the failure of this assembly can occur by the slippage of the constitutive CNTs at a stress lower than the failure stress of the single molecule [Yakobson et al., 2000]. Staudinger was the first to recognize the influence of length (or molecular weight) on the tensile strength of a perfect polymeric crystal; CNTs are not an exception [Staudinger, 1932]. This understanding has deeply shaped the research of high strength polymeric fibers where high molecular weight and/or strong intramolecular interactions augmented by perfect packing and alignment are the sought-after features [Wang et al., 2011].

Three main forces maintain bundle integrity: intrinsic CNT strength, capillary forces (energy required to form free surface), and inter–CNT friction [Yakobson et al., 2000]. Depending on the aspect ratio, three regions can be distinguished (Fig. 2.5). At low aspect ratio, capillary forces dominate and the failure strength is independent of the aspect ratio. At intermediate aspect ratios, the failure strength depends on inter–CNT friction (which correspond to van der Waals force per unit length for pristine surfaces) and is linearly proportional to the length; at high aspect ratio, the fiber tensile strength is equal to that of the individual CNTs.

A plot of measured tensile strength of neat CNT fibers versus CNT aspect ratio confirms that tensile strength increases with aspect ratio (Fig. 2.6), indicating that among the multitude of variables influencing CNT–fiber tensile strength, aspect ratio stands out. Yakobson *et al* estimate a SWNT length of 10 μm (1 nm diameter) is necessary for a perfectly packed fiber to attain the potential failure strength of the

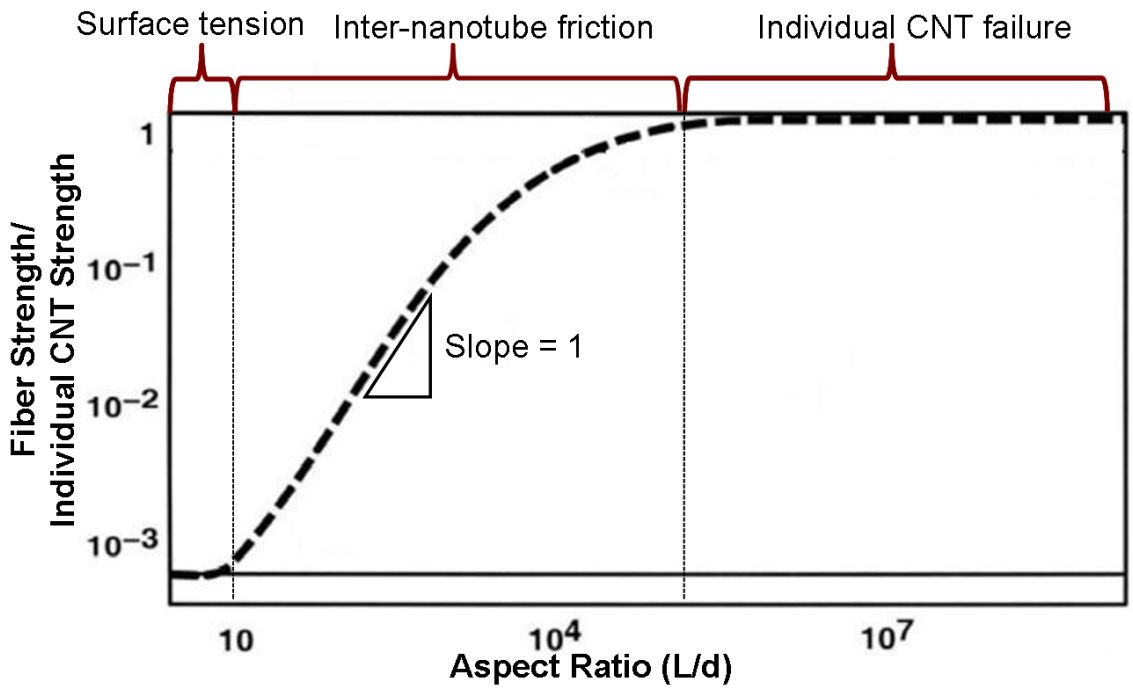

Figure 2.5 : Tensile strength of a perfectly aligned bundle of CNTs as a function of aspect ratio. Three regions can be distinguished. The first is dominated by capillary forces and is independent of aspect ratio. The intermediate region is dominated by inter–CNT friction, and tensile strength is linearly proportional to CNT aspect ratio (slope of one in a log–log plot). In the final region (at higher aspect ratios), bundle tensile strength coincides with the strength of a single CNT. Reproduced from [Yakobson et al., 2000]

individual SWNT. So far, even fibers produced from millimeter long CNTs [Koziol et al., 2007, Zhang et al., 2007a] show a tensile strength that is nearly two orders of magnitude lower than the breaking stress on a single CNT; this is due most likely to poor alignment and packing of the CNTs in the constitutive bundle, and/or low inter–bundle connectivity.

The theoretical linear relationship between strength and aspect ratio should generally hold for experimental fibers with imperfect morphology (This is readily seen in the three fibers from Zhang *et al.* [2007a] [Zhang et al., 2007b] in Fig. 2.6). Fiber properties that belong to a left shifted line indicate improved fiber morphology since the same fiber strength can be obtained by shorter molecules. This shift is readily achieved in solid state fibers by twisting and polymer infiltration (Fig. 2.6). Thus, the strength of these fibers is limited by morphological imperfections (alignment, porosity, undispersed particles etc.) rather than by the length of the constitutive molecules [Davies et al., 2009, Naraghi et al., 2010]. If the morphology of acid-spun fibers (alignment and packing) is obtained with longer constitutive CNTs, this can lead to fibers with better tensile strength.

Koziol *et al* [2007] emphasize the effect of fiber "weak points" on fiber tensile strength measurements. Tensile strength is low if these weak points occur within the gauge length, while testing the portion of fibers without weak points can assess the true potential of the material. In gas-phase CVD fiber spinning, tensile strength can increase by almost an order of magnitude when the gauge length is decreased from 20 mm to 1 mm [Koziol et al., 2007].

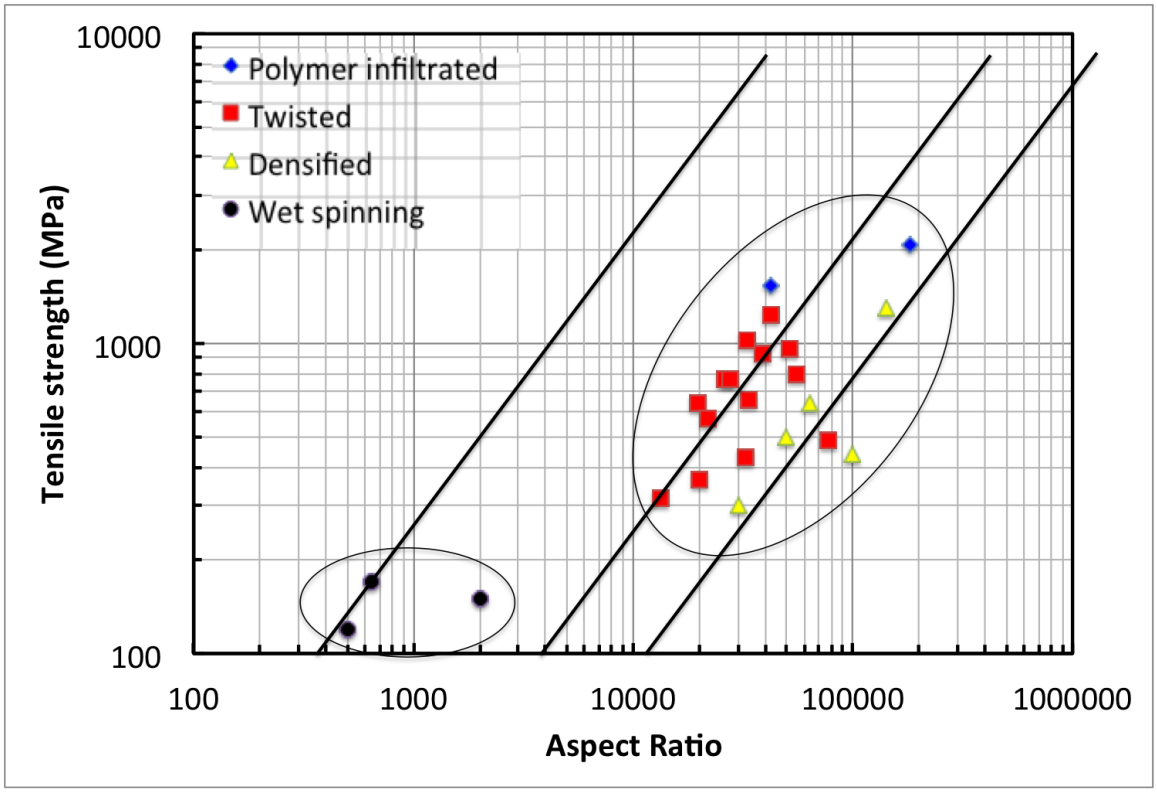

Figure 2.6 : Tensile strength of different CNT fibers as a function of the aspect ratio. Two areas can be identified: a low strength region that corresponds to wet-spun fibers and a high strength region corresponding to solid–state spun fibers. A slope of one has been drawn through each data point to indicate how the tensile strength of these fibers will scale with CNT length. This allows the morphology of the fibers to be compared independently of the aspect ratio of the constituent CNTs. The graph is color coded with red dots indicating twisted fibers, blue dots standing for polymer infiltrated fibers, yellow dots for solvent densified fibers, and black dots referring to wet–spun fibers. Reference and data can be found in Table 2.2

Another important variable, unique to CNTs when compared to polymeric fibers, is the number of walls of a constitutive molecule. The weak stress transfer between CNT walls makes the external wall the one that hold most of the load transferred by the adjacent molecules. Single molecules mechanical test have confirmed this idea with MWNT's failure occurring because of the failure of the external wall in a "sword–in–sheath" fashion [Yu et al., 2000b]. This is particularly undesired when specific (density normalized properties) instead of absolute mechanical properties are important since the internal walls add weight that is not supporting any load. Vilatela *et al.* proposed the following functional form for the specific strength of a perfectly aligned CNT bundle [Vilatela et al., 2011]:

$$\sigma' = \frac{1}{6}\omega_1\omega_2\tau_f L \tag{2.1}$$

$$\sigma' \sim \frac{L}{N} \tag{2.2}$$

where σ' is the specific strength (tensile strength divided by fiber density), ω_1 is the load bearing fraction layers (in the case of individual CNTs, it is approximately $1/N$, where N is the number of graphene layers in the tube), ω_2 is the fraction of cylindrical surface involved in the stress transfer process, τ_f is the shear strength between two graphene layers and L is the length of constitutive molecules. Since ω_2 and τ_f should not depend on the type of CNT, the specific tensile strength should be linearly dependent on $\frac{L}{N}$. A plot of specific strength vs. $\frac{L}{N}$ (Fig. 2.7(a)) can indeed reduce some of the scatter in the specific strength vs. aspect ratio data (Fig. 2.7(b)), indicating that the number of walls plays a significant role in specific strength. Thus, for the same aspect ratio and fiber morphology, SWNT fibers are expected to yield higher specific properties compared to MWNT fibers.

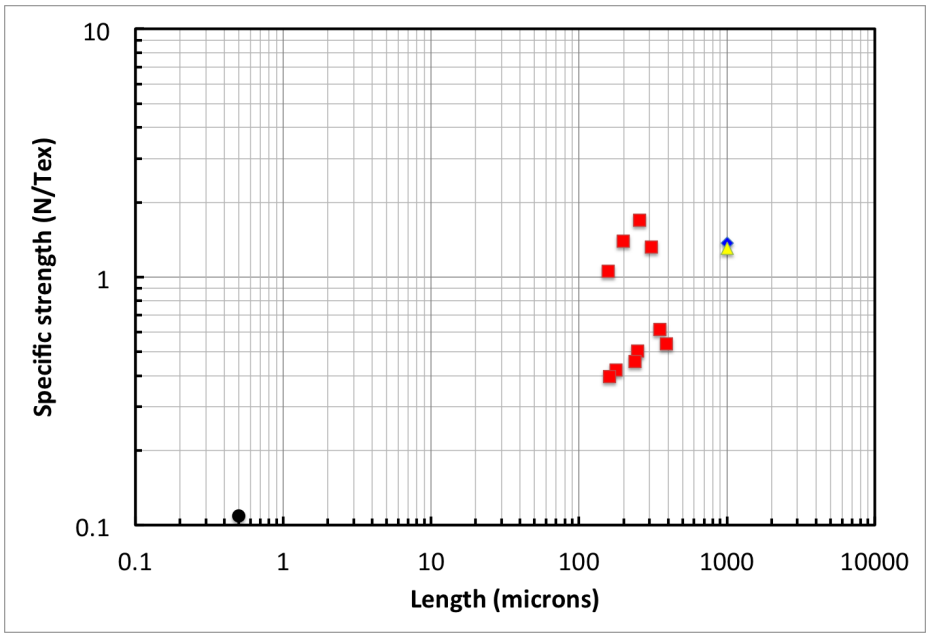

(a)

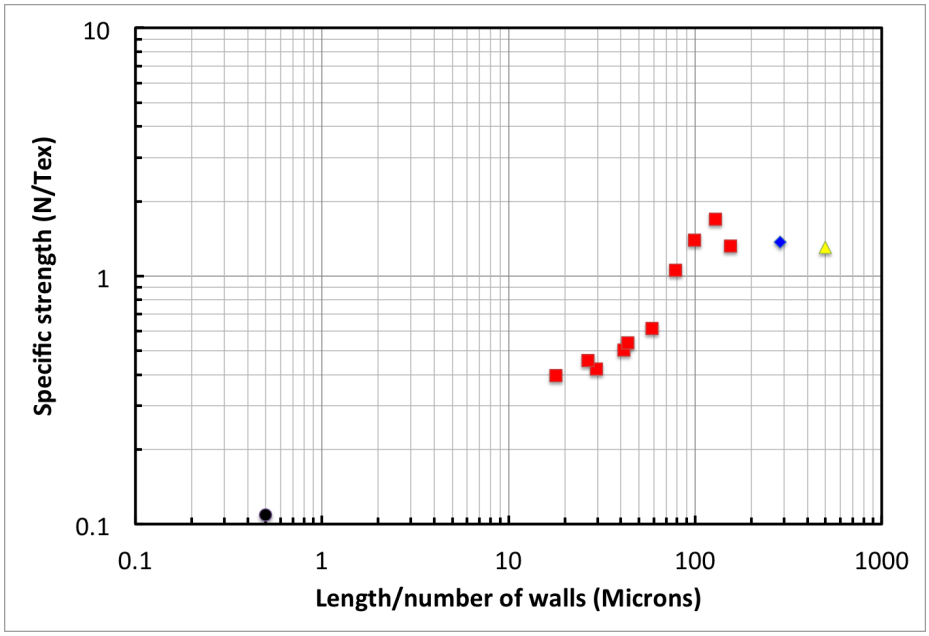

(b)

Figure 2.7 : Figure 2.7(a) shows the dependence of specific tensile strength on CNT aspect ratio. Some of the scatter within the plot can be reduced (Fig. 2.7(b)) if the data are plotted as a function of CNT length normalized by CNT number of walls. The graph is color coded with red dots indicating twisted fibers, blue dots indicating polymer infiltrated fibers, yellow dots standing for solvent densified fibers, and black dots representing wet–spun fibers. Reference and data can be found in Table 2.3

CNT–based fiber moduli reported thus far are 1 to 2 orders of magnitude below the theoretical limit. Fiber modulus is not strongly correlated to CNT aspect ratio [Behabtu et al., 2008]. This is in strong contrast with rod–like polymer fibers, where commercial fiber moduli have actually matched the theoretical crystal modulus [Chae and Kumar, 2006]. An exception to this is the modulus reported by Zhang *et al.* [Zhang et al., 2007a] (263 GPa); however, the specific modulus (Modulus/density) of this fiber is higher than what is theoretically achievable.[†] This inconsistency remains unexplained. Similarly to polymeric fibers, CNT fibers show a strong dependence of modulus with tensile strength. In fact, higher strength is often associated with higher modulus, and lower elongation to break [Cheng et al., 2009, Koziol et al., 2007, Jia et al., 2011]. Such a trend indicates that alignment, a critical parameter to gain high modulus, is also critical to tensile strength since it improves load trasfer between adjacent molecules and/or bundles [Cheng et al., 2009].

SWNT–PVA composite fibers have exhibited the highest toughness attained so far, although the low–strain energy absorption is comparatively low. Some of the solid–state drawn CNT fibers show very high toughness as well (maximum 975 J/g, average 309 J/g) [Zhang et al., 2007a]. These high values of toughness are related to the non–brittle behavior of these fibers. In fact, these fibers do not fracture at the highest stress; instead, they yield gradually until they finally break.

[†]Zhang *et al.* [2007b] the measured fiber density is 0.195 g/cm^3, hence the specific modulus becomes 1348 GPa/SG, when dividing the single molecule modulus (1 TPa) by the single molecule density 0.78 (reported by the authors in the supplementary info), the specific modulus becomes 1282 GPa/SG

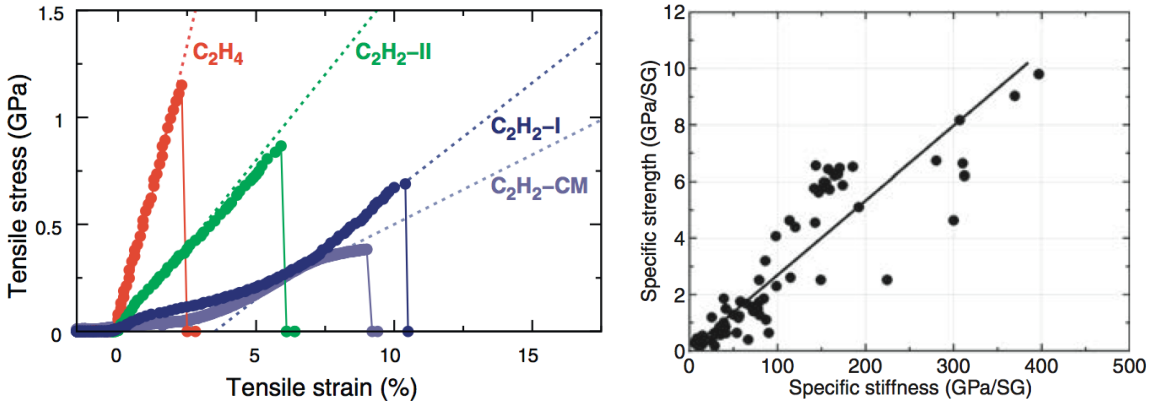

(a) (b)

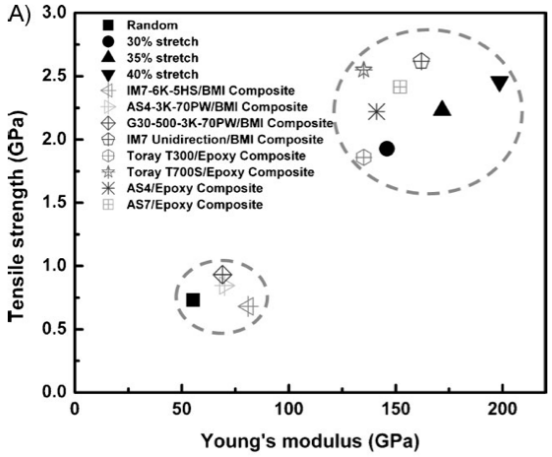

(c)

Figure 2.8 : Figure 2.8(a) shows stress-strain curve for CNT fibers spun from vertically grown CNTs indicating how high modulus is correlated to high strength and low elongation to break (Figure reproduced from [Jia et al., 2011]. Figure 2.8(b) and 2.8(c) show that linear strength-modulus correlation is also found on aerogel spun fibers (Figures reproduced from [Koziol et al., 2007] and [Cheng et al., 2009]).

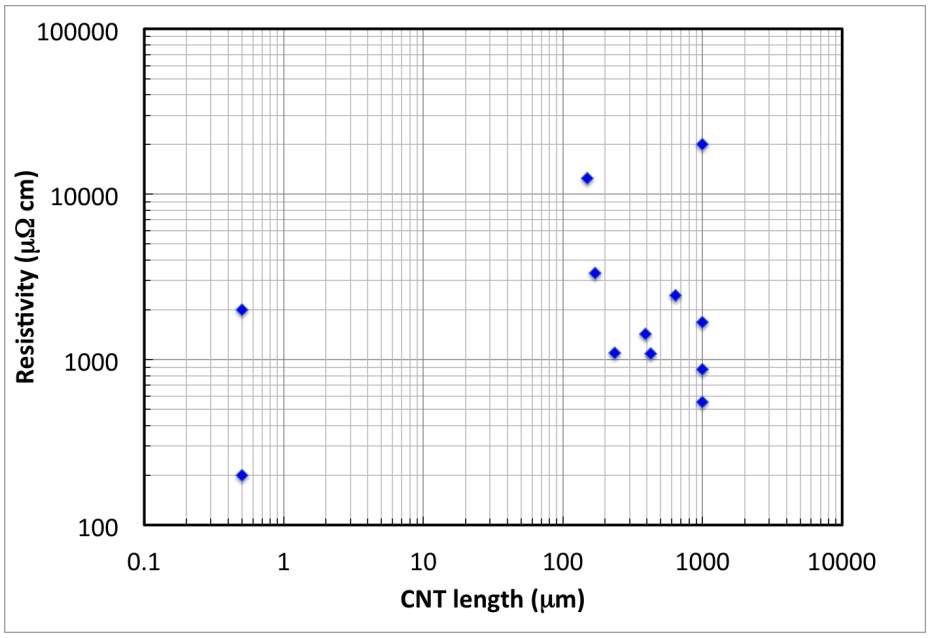

(a)

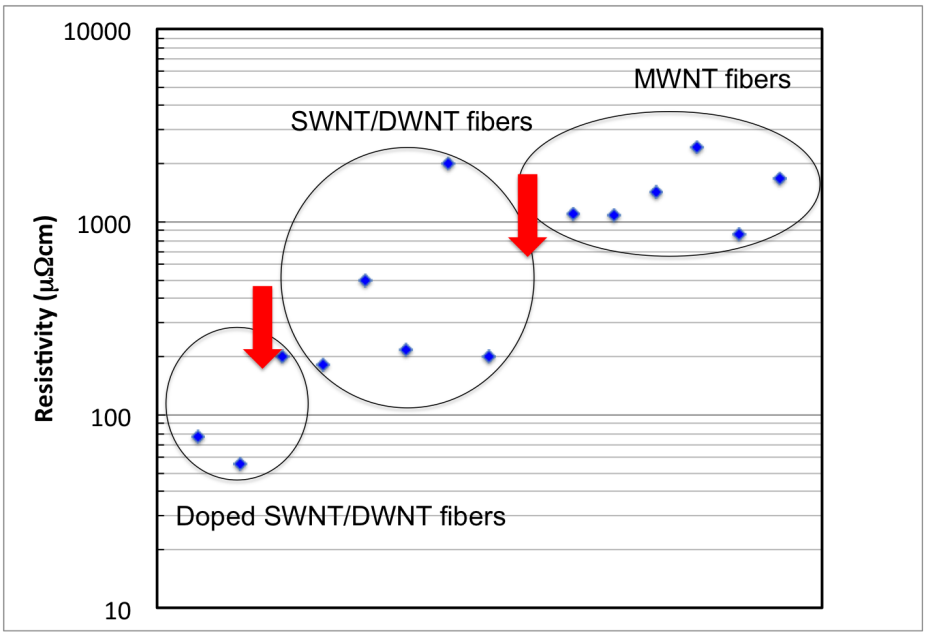

(b)

Figure 2.9 : Electrical resistivity of different CNT fibers as a function of the CNT aspect ratio. Figure 2.9(a) shows that there is not a clear correlation between CNT aspect ratio and electrical resistivity. Figure 2.9(b) shows how CNT type and fiber doping have stronger effect on electrical resistivity. References and data can be found in Table 2.4. Note that figure 2.9(b) does not have an x axis.

2.3.2 Electrical Conductivity

Individual SWNTs can be metallic or semiconducting (with a band gap $E_g \approx 0.7\text{eV}/d_t$ (nm), with d_t SWNT diameter) based on their chirality [Biercuk et al., 2008]. Both semiconducting and metallic tubes show large ($\sim \mu m$) room temperature electron mean free paths [Durkop et al., 2004, Tans et al., 1997]. Conduction in a ballistic regime has a finite conductance of $4e^2/h$ where e and h are the elementary charge and Planck constant. Thus, a quantum wire possesses a finite resistance of 6.5 kΩ, irrespective of its size and diameter [Biercuk et al., 2008]. If we assume a tube length of 1 μm and a diameter of 1 nm, single molecule resistivity would be 1 $\mu\Omega\cdot$cm, lower than the room temperature conductivity of copper (1.72 $\mu\Omega\cdot$cm at 300 K [Matula, 1979]). In ballistic conduction, single molecule resistivity increases linearly with length; this behaviour, however, is expected to become sub-linear as diffusive regime sets in and for long enough length, the resistivity is no longer a function of wire length. Nevertheless, resistivity of single CNTs is remarkably low. However, lattice defects such as vacancies, substitutions, pentagon-heptagon (also called stone-wall) defects, and chirality mismatches within a CNT can decrease the conductivity [Biercuk et al., 2008]. Also, despite metallic SWNTs are better conductors than the semiconducting ones, there are currently no production nor separation methods that can yield bulk quantities (mg or higher) of metallic CNTs. Doping is an effective way to improve conduction of mixed (metallic and semiconducting) samples [Lee et al., 1997, Grigorian et al., 1998, Zhou et al., 2004b]. In fact, various dopants (potassium, iodine and acids are commonly used as dopant) can increase electrical conductivity by an order of magnitude. This may be attributed to the improved conductivity of semiconducting CNTs, although doping can also improve on junction resistance of two adjacent CNTs. Temperature dependent conductivity is a good tool for more insight about the

conduction mechanism. In fact, electrical resistivity of CNT assembly can be fitted by the following functional form [Fischer et al., 1997]:

$$\rho = A + B/T + CT \tag{2.3}$$

where A, B and C are fitting constants. Thus a critical Temperature exists (T^*) where the electrical resistivity is minimum. The crossover phenomenon is a general feature of electrical conduction in CNTs assembly. Various values can be measured for T^* for different samples, with smaller values indicating lower defects and/or disorder. Thus, T^* is a good indicator of the morphology of CNT assemblies [Fischer et al., 1997].

Other reasons for decreased electrical conductivity of a macroscopic assembly are related to CNT length and alignment. The resistance is the sum of intrinsic CNT resistance and inter–CNT contact resistance. Contact resistance can be lowered by using longer nanotubes and/or increasing CNT overlap through better alignment. CNT fiber electrical conductivity versus constitutive molecules length does not show any clear trend (Fig. 2.9). In fact, acid-spun fibers show very low resistivity (200 $\mu\Omega$·cm [Ericson et al., 2004]) when acid doped (as spun and washed fibers with residual acid), and they maintain relatively low resistivity upon annealing (2620 $\mu\Omega$·cm). Even after annealing, the resistivity of acid-spun fibers is lower than most of the solid state drawn fibers [Zhang et al., 2004]. Such good electrical conductivity may stem from several different causes. *In primis*, in acid–spun fibers, the CNTs coalesce into more regular ropes than in solid state drawn fibers. *In secundis*, HiPco SWNTs used for acid spinning have fewer defects than array-grown ultra long MWNTs. For solid–state drawn fibers, resistivity decreases as the aspect ratio

increases [Li et al., 2007]; nevertheless, the resistivity difference between acid-spun and solid–state drawn fibers shows the importance of good coalescence as a means to improve properties. In current fiber production methods, CNT type and fiber doping control resistivity more than aspect ratio does. In fact, the clearest trend of CNT fiber resistivity is traced when the values are grouped by CNT type and doping (Fig 2.9(b)). SWNT and DWNTs–based fibers have electrical resistivity an order of magnitude lower than MWNTs. Doping can further decrease resistivity by an order of magnitude.

2.3.3 Thermal Conductivity

Similarly to electrical and mechanical properties, CNT fiber thermal conductivity is affected by both fiber structure and the intrinsic single–molecule thermal conductivity, where the single molecule property represents the limiting value. Some of the excitement for CNTs as thermal conductors stem from large phonon mean free ($\sim \mu m$) path at room temperature [Yu et al., 2005] and the large thermal conductivity values measured for individual molecules [Brown et al., 2005]. However, experimental thermal conductivity values for individual SWNTs and MWNTs span two orders of magnitude (290 - 25000 $W/m \cdot K$ [Choi et al., 2006, Brown et al., 2005, Kim et al., 2001, Choi et al., 2005, Pop et al., 2006, 2005]. This discrepancy emphasizes the experimental challenge related to single molecule properties measurements, and the multitude of variables that affect thermal conductivity [Savin et al., 2009]. For example, measurements on CNTs deposited on a substrate will yield results that are different than the ones obtained from freely suspended CNTs [Savin et al., 2009]. CNT length [Wang et al., 2007], defects density [Yamamoto et al., 2008], and diameter will also affect the

measured conductivity [Hone, 2001]. For instance, in the ballistic transport regime, thermal conductivity scales linearly with CNT length. As the CNT length is increased and becomes longer that the phonon mean free path, thermal transport will become diffusive. For long enough CNTs, the thermal conductivity will be independent of length [Yamamoto et al., 2008, Wang et al., 2007]. This behaviour is similar to what we have already encountered for electron transport. The dependence of thermal conductivity on temperature is also an important reference behaviour to understand if bulk conductivity is approaching single molecule behaviour. At low temperature, thermal conduction is quantized, similar to electron conduction, and it increases linearly with temperature [Hone, 2001]. At high temperature, three-phonon Umklapp scattering inverts the temperature dependence and the thermal conductivity decays as $1/T$ [Pop et al., 2005]. A maximum in thermal conductivity may not be observed if defect scattering dominates thermal transport [Hone, 2001], similar to what is observed for crystalline versus amorphous graphite. Large diameter MWNTs follow 2D system (graphene) conduction with low temperature thermal conductivity growing as T^2.

The experimental work on bulk CNT thermal conductivity is not as extensive as mechanical and electrical properties. The few available data on nanotube films and fibers show that thermal conductivity is a fraction of the single molecule value (Tab 2.1). This suggests, as seen for fiber tensile strength and electrical conductivity, that fiber structure is the true limiting factor of thermal conductivity. CNT fiber thermal conductivity is low even when compared to K-1100 (1100 W/m·K [Minus and Kumar, 2005]), a commercial carbon fiber that shows the highest thermal conductivity of engineered materials. Unfortunately, lack of extensive experimental data on fiber thermal conductivity does not allow trends to be drawn. Further

advances in thermal and electrical conductivity should track together because the two are affected by related physical mechanisms [Lavin et al., 1993].

2.3.4 Future Directions

The properties of fibers of CNTs are still far below those of their constituent elements. Further improvements will result from increased control in CNT production and better fiber processing and/or post processing. For example, effective coalescence has been demonstrated in solution spinning, and post-processing has improved the tensile strength of the first CNT–based fibers by an order of magnitude. However, solution-spinning methods have not yet been used to successfully process long CNTs, in contrast to solid–state spinning. For these solid–state drawn fibers, the mechanical properties have been improved by an order of magnitude through the use of longer CNTs as well as post-processing techniques, such as twisting, and liquid or vapor condensation. However, even millimeter long CNTs have not yet matched what is theoretically achievable due the poor coalescence observed in solid–state spinning.

These same fiber qualities are also required for improved thermal and electrical properties, although CNT type and quality seem to be more critical for electrical conductivity. Few data are available to draw any conclusion regarding thermal conductivity. CNT type and fiber morphology and alignment are critical factors for thermal and electrical properties, whereas CNT aspect ratio is critical for mechanical properties. A challenge specific to electronic applications is the production and/or separation of specific SWNT chiralities. Current SWNT synthesis methods produce a mixture of either metallic or semiconducting SWNTs, but unfortunately no separation

CNT type	Comments	Thermal Conductivity (W/mK)	Reference
Arc discharge SWNT (random mat).	Value correcting for the volume filling fraction of the sample	35	[Hone et al., 1999b]
SWNT	Magnetically aligned mats	200	[Hone et al., 2000]
SWNTs fibers	Acid–Spun	20	[Ericson et al., 2004]
MWNT	Spun from vertical arrays, twisted yarns	26	[Aliev et al., 2007]
MWNTs fibers	Spun from vertical arrays, twisted	60	[Jakubinek et al., 2012]

Table 2.1 : Overview of bulk CNT thermal conductivity.

technique has yet demonstrated the ability to effectively separate bulk quantities.

2.4 Conclusions

In the last decade, a number of different techniques for CNT–based fiber assembly have emerged. Specifically, there are two main processes by which CNTs fibers can be assembled. The first is solution spinning, where the CNTs are dispersed in surfactant or solubilized in acid and then coagulated into a fiber. The second is solid–state spinning, where fibers are drawn from a vertically–grown array of CNTs or directly collected from the aerogel formed in the reaction furnace. Solution spinning is readily scalable but has not yet shown the ability to process long CNTs. Solid state spinning has exhibited the best mechanical properties for CNT fibers to date. However, the process scalability and fiber morphology are problematic.

Future developments in CNT–based fibers will stem from two areas: improvements in the starting material (i.e., longer, defect–free, type-specific CNTs), or improvements in the processing and post-processing of the fibers. Given the wide range of achievements in CNT synthesis and fiber processing of the past decade, the prospect of high–performance CNT–based fibers is quite promising, particularly as researchers continue to apply the effective techniques of rigid–rod polymer processing to SWNT fibers.

Aspect ratio	Strength (MPa)	Comments	References
182000	2088	Polymer infiltrated	[Cheng et al., 2009]
43000	1540	PVA infiltrated	[Jia et al., 2011]
26000	770	Twisted	”
33000	1020	”	”
43000	1240	”	”
5200	970	”	”
20000	640	”	”
28000	760	”	”
39000	930	”	”
22000	580	”	”
33000	660	”	”
55000	800	”	”
78000	490	”	”
13000	320	Twist	[Fang et al., 2010]
20000	360	”	”
33000	430	”	”
100000	440	Solvent densified	[Zhang et al., 2008b]
143000	1300	Solvent densified	[Koziol et al., 2007]
30000	300		[Zhang et al., 2007b]
50000	500		”
64200	640		”
2000	150	Wet–spun	[Zhang et al., 2008c]
650	170	”	”
500	120	Superacid–spun	[Ericson et al., 2004]

Table 2.2 : Data used for Figure 2.6

CNT length (L) μm	Number of walls (n)	L/n	Specific strength mN/Tex	References
1000	3.5	285.7	1370	[Cheng et al., 2009]
160	2	78.5	1050	[Jia et al., 2011]
200	”	99	1390	”
260	”	128	1700	”
310	”	154.5	1320	”
180	6	29.7	420	”
250	”	41.7	500	”
350	”	58.5	610	”
160	9	17.9	400	[Fang et al., 2010]
240	”	26.7	445	”
390	”	43.4	540	”
1000	2	500	1300	[Koziol et al., 2007]
0.5	1	0.5	110	[Ericson et al., 2004]

Table 2.3 : Data used for Figure 2.7

CNT Type	Electrical Resistivity $\mu\Omega$ cm	Comments	Length μm	References
SWNT	77	$KAuBr_4$ doped	-	[Alvarenga et al., 2010]
SWNT	500	undoped	-	”
DWNT	56	Iodine doped average	-	[Zhao et al., 2011]
DWNT	220	undoped average	-	”
SWNT	200	acid doped	0.5	[Ericson et al., 2004]
SWNT	2000	annealed	0.5	”
DWNT	560	misaligned	1000	[Cheng et al., 2009]
DWNT	180	aligned	”	”
DWNT	200		-	[Zhong et al., 2010]
MWNT	20000	twist	1000	[Zhang et al., 2008b]
MWNT	1100		235	[Liu et al., 2010b]
MWNT	1090	PVA infiltrated	425	[Liu et al., 2010a]
MWNT	1430		391	[Fang et al., 2010]
MWNT	2440		642	[Zhang et al., 2007b]
MWNT	870	Au coated	1000	[Li et al., 2007]
MWNT	1680		1000	”

Table 2.4 : Data used for Figure 2.9

Chapter 3

Graphite Dissolution in Superacids and Formation of Liquid Crystals

3.1 Introduction

Graphene* combines unique electronic properties and surprising quantum effects with outstanding thermal and mechanical properties [Segal, 2009, Novoselov et al., 2004, Lee et al., 2008, Balandin et al., 2008]. Many potential applications, including electronics and nanocomposites, require the graphene to be dispersed and processed in a fluid phase [Stankovich et al., 2006].

Many promising macroscopic applications of graphene require the development of new routes for effective graphite exfoliation and processing [Segal, 2009, Ruoff, 2008]. Micromechanical cleavage [Novoselov et al., 2005], the first reported method to isolate graphene from graphite, has extremely low yield and cannot be used in bulk applications. Large amounts of graphene sheets can be obtained by oxidizing graphite layers through various processes to yield water soluble graphene oxide [Hummers and Offeman, 1958, Stankovich et al., 2007]. Further chemical reduction and derivatization yield functionalized graphene that is soluble in common organic solvents [Stankovich et al., 2006]. Although functional groups aid dissolution, they also compromise many of graphenes desirable electrical and thermal properties [Schwamb et al., 2009]. Re-

*This chapter was published as a research article (see reference [Behabtu et al., 2010])

duction of graphite oxide only partially restores these properties [Becerril et al., 2008]. Liquid phase dispersion in organic solvents — e.g., N-methyl pyrrolidone (NMP) — can be attained without chemical modification by sonication [Hernandez et al., 2008] or by potassium intercalation without sonication [Valles et al., 2008]. Graphene has also been dispersed in water by sonication and stabilization via surfactants [Lotya et al., 2009]. However, liquid phase dispersions yield low concentrations (0.01 mg/mL [Hernandez et al., 2008], 0.15 mg/mL [Valles et al., 2008]), and sonication limits the attainable size of graphene flakes. Superacids have been successfully used to dissolve single–walled carbon nanotubes (SWNTs) and show great promise for the bulk processing of SWNT-based materials [Davis et al., 2009]. Chlorosulfonic acid, the most promising SWNT solvent, was first produced in 1854 [Williamson, 1854] and today is a commodity chemical with a production of more than 300,000 tons/year. It is used chiefly as a sulfonating chemical in detergent and dye production [Cremlyn, 2002]. Although the intercalation of graphite by strong acids, including chlorosulfonic acid, has been studied for decades [Melin et al., 1977], there are no reports indicating that graphite is soluble in strong acids. Graphene solubility in superacids is also interesting from a fundamental point of view. Carbon allotropes' solubility in super acids is strongly dependent on their curvature [Rai et al., 2007, Duque et al., 2010]. In fact, fullerenes, the graphitic molecule with the highest curvature, dissolve in acids as weak as 70% sulfuric acid [Rai et al., 2007] while (SWNTs) with average diameter of 1.4 nm and higher are not soluble in acids as strong as 120% sulfuric acid. Since graphene represent an extrema in curvature, the solvent that dissolves graphene will also dissolve molecules with intermediate curvature.

3.2 Dissolution in Superacids: Effect of Starting Graphite, Centrifugation and Sonication

We study the behaviour of pristine graphite in chlorosulfonic acid. Three different sources of graphite were used: Graphoil (commercial graphitic material used in seals), microcrystalline graphite, and highly ordered pyrolytic graphite (HOPG). Figure 3.1 shows that the acid disperses graphene from various graphite sources at high concentrations without sonication; these isotropic solutions are ten to one hundred times more concentrated than those previously attained by sonicating graphite in organic solvents or in water in the presence of surfactants.

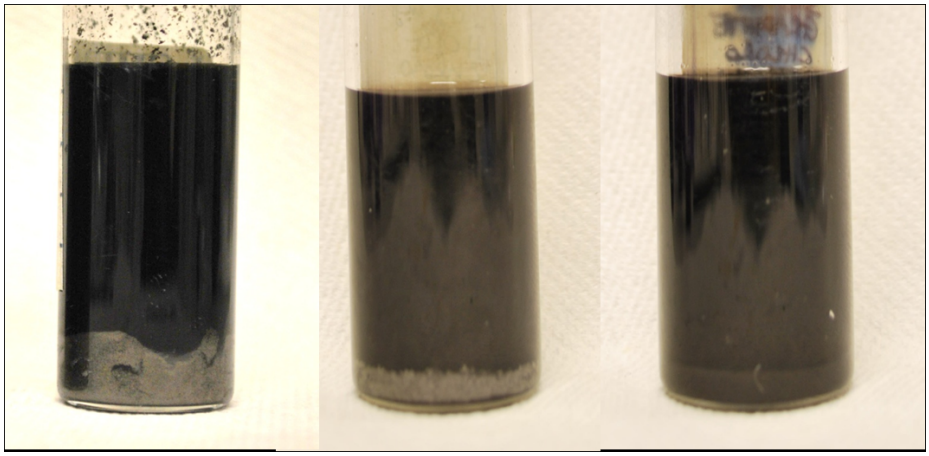

Figure 3.1 : Comparison of chlorosulfonic acid dispersion of graphite (25 mg/mL initial concentration) obtained from different sources. From left to right is graphoil, HOPG and microscystalline graphite, respectively. A dark upper portion (top) is obtained for all the different sources after 12 h of centrifugation (5000 rpm), with a gray-colored lower portion (bottom). A clear interface between the top and bottom phase is visible in the three vials. The soluble portion was removed and isolated for the solubility determinations.

The concentration of the dispersed phase was determined by centrifuging the initial dispersion, extracting the top (isotropic) phase, and measuring its absorbance

by UV–vis–nIR spectra (Fig. 3.2). The UV–vis–nIR spectrum is featureless as a function of wavenumber, in agreement with previous reports [Hernandez et al., 2008].

The phase separation that occurs during centrifugation is not an equilibrium one; instead, a fraction of the original material goes into solution while the remainder is insoluble (Fig. 3.3(a)). When varying the initial graphite concentration, the concentration of the centrifuged top phase increases (Fig. 3.3(a)). Thus, there is just a fraction of the initial material that is soluble in acid, similar to what is observed for surfactant dispersions and NMP [Hernandez et al., 2008, Lotya et al., 2009].

We also investigated the effects of sonication and high shear mixing, as shown in Figure 3.3(b). The isotropic concentration increases remarkably (more than double) after only 10 minutes of sonication. It has already been reported that even mild sonication, such as bath sonication, has an important effect on graphene size [Kosynkin et al., 2009], thus, as graphene flakes are broken upon sonication, they become Brownian molecules that go into the isotropic phase. When the same solution is mixed using high shear mixing, the isotropic concentration does not increase considerably. Thus, sonication is not simply a better mixing process than stir bar mixing.

3.3 Dissolution Mechanism

Acid strength affects dispersion quality. We control acid strength by mixing chlorosulfonic acid and concentrated (98%) sulphuric acid in varying proportions [Rai et al., 2006]; hereafter, mixed solvents are denoted by the concentration of chlorosulfonic acid. Figure 3.4(a) shows that graphite solubility decreases markedly as the acidity is lowered to 80% chlorosulfonic acid; solubility drops further as the acidity is lowered. For comparison, we disperse the same material in NMP, an organic solvent previously reported for pristine graphene dissolution [Hernandez et al., 2008, Valles et al., 2008].

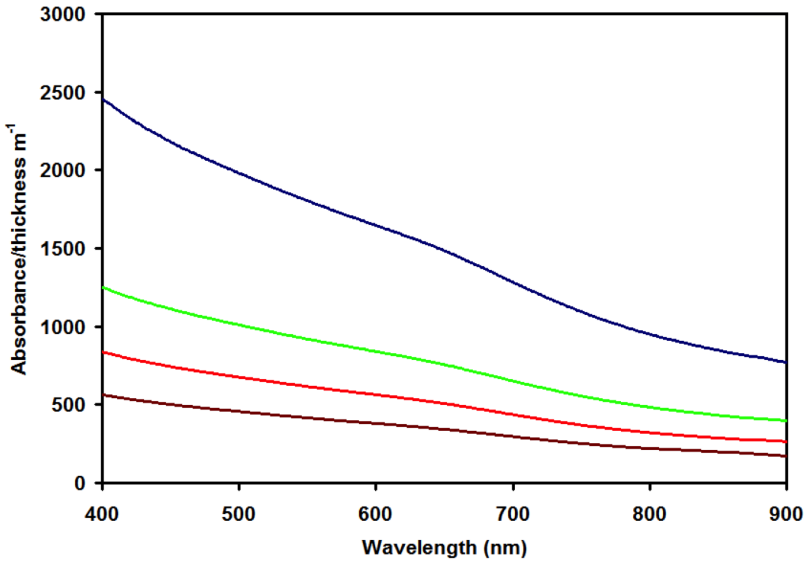

(a)

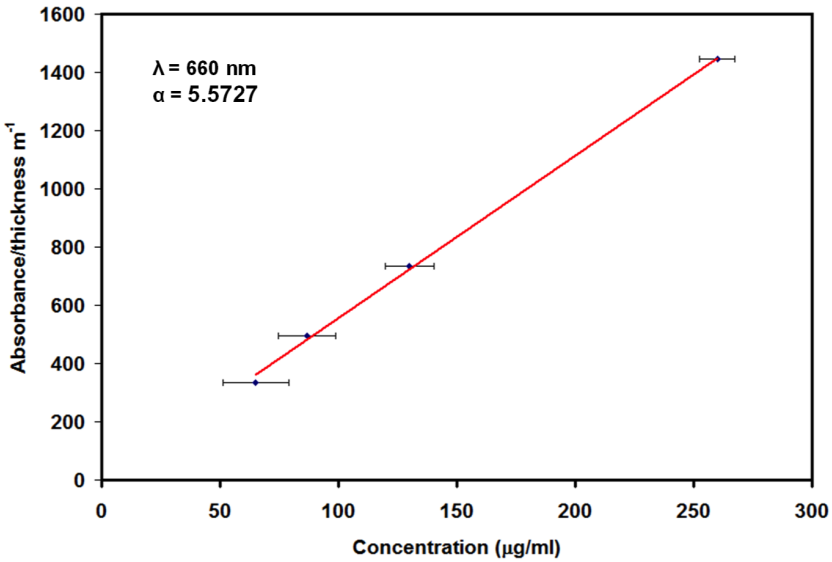

(b)

Figure 3.2 : UV–vis absorption spectra from the top phase from the vials after centrifugation. The dispersions were obtained from the microcrystalline graphite dispersion. The four different spectra represent different concentration (the top phase and three different dilutions). (b) Optical absorbance divided by the cell length as a function of different concentrations. The solution follows the Lambert-Beer law with an absorption coefficient of 5.6 mL $g^{-1}m^{-1}$ at 660 nm. The error bar is a combination of instrument resolution for the UV–vis absorption, volume and mass measurement. The main contribution to the error bar is the determination of graphene mass in the isotropic solution.

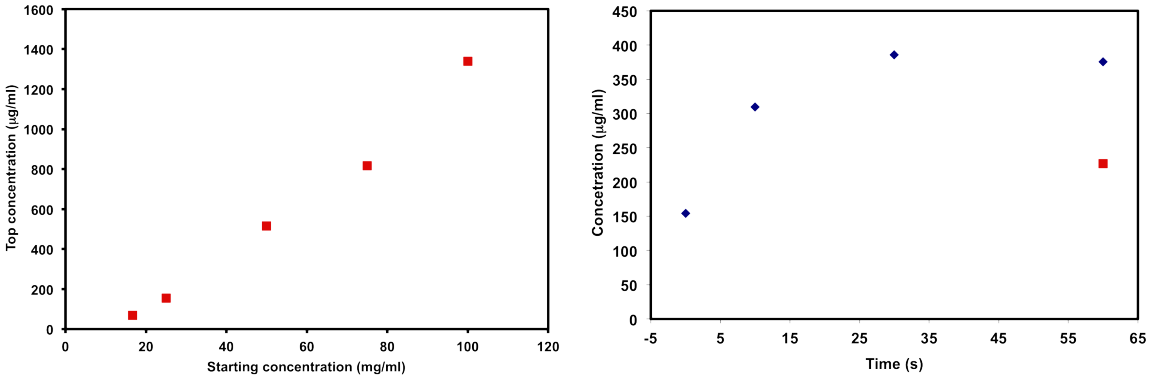

(a) (b)

(c)

Figure 3.3 : 3.3(a): Effect of the initial dispersion concentration on the isotropic concentration. Figure 3.3(c) visualizes the significant change of the top phase concentration as a function of initial concentration. From left to right the initial concentration is varied from 0.5, 1, 3 and 6 mg/ml, respectively. Note how the initial two vials show almost a transparent top. 3.3(b): Effect of sonication time (blue dots) and high shear mixing (red dot) on the isotropic concentration in chlorosulfonic acid. All the initial dispersions were made at 25 mg/mL. Sonication was carried out for 10, 30 and 60 min in a bath sonicator (Cole-Parmer, Ultrasonic model 08849-000), while high shear mixing was conducted with IKA- S 25N (10G dispersing element) at 11000 rpm for 60 min. For both graphs, microcystalline graphite was used as starting material. The concentrations were calculated by measuring the UV–vis–nIR absorption and using the extinction coefficient previously calculated. The solution were first mixed for 3 days with standard stir bars and sonicated or high shear mixed. Then, they were centrifuged for 12 hours at 5000 rpm.

Without sonication, the level of dispersion in NMP is negligible.

We next investigate the mechanism of graphene dissolution in superacids. Prior work with superacid/SWCNT solutions showed that dispersion is due to protonation of the SWNT sidewalls, which causes electrostatic repulsion and debundling. The degree of protonation (positive charge per carbon atom) in graphitic materials is measured through the acid-induced shift (dG) in the location of the G peak in the Raman spectra [Rai et al., 2006, Ramesh et al., 2004, Sumanasekera et al., 1999]. Figure 3.4(b) reports dG for the various acid mixtures; the Raman shift dG drops with decreasing acidity, mirroring the decrease in solubility. Figure 3.6(a) shows the Raman spectra of a sample of graphite powder before and after acid dissolution, quenching in water, and drying. The spectrum is essentially unchanged (in particular, the D–band, characteristic of sp3 carbon content, remains low), hence acid dissolution does not introduce defects in the starting material. This indicates no damage or functionalization by the acid, the same behaviour as seen in SWNTs [Davis et al., 2009]. X–ray photoelectron spectroscopy (XPS) further supports this conclusion (Fig.3.5).

Compared to SWNTs, graphene is less soluble in the same acid; SWNTs are soluble in weaker superacids, such as 102% sulfuric acid.

We further characterize the top and bottom phases to better understand the dispersion mechanism. Raman spectroscopy (Fig. 3.6(b)) shows a higher D–peak in the top than in the bottom phase; this D–peak grows with longer centrifugation time. However, XPS does not reveal any oxygen or sulfur in the quenched top phase (Fig. 3.5). The most plausible explanation of this difference is graphene flake size. Even when a molecule is thermodynamically stable in solution, gravitational sedimentation can cause phase separation between solvent and solute. Sedimentation becomes important as the size of the molecule becomes larger. The bottom phase is

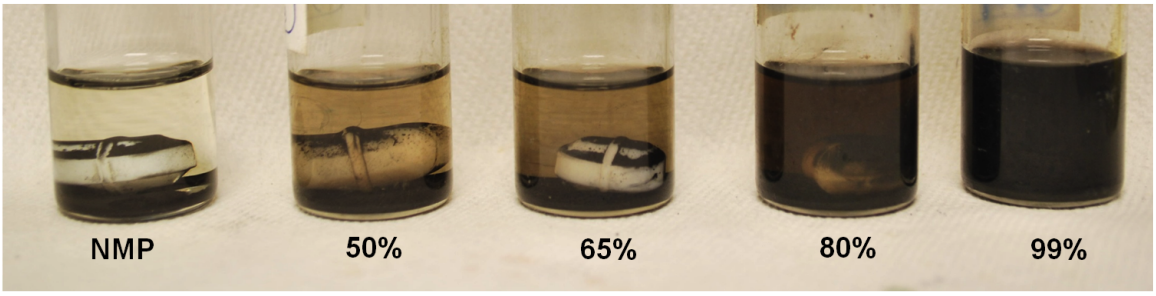

(a)

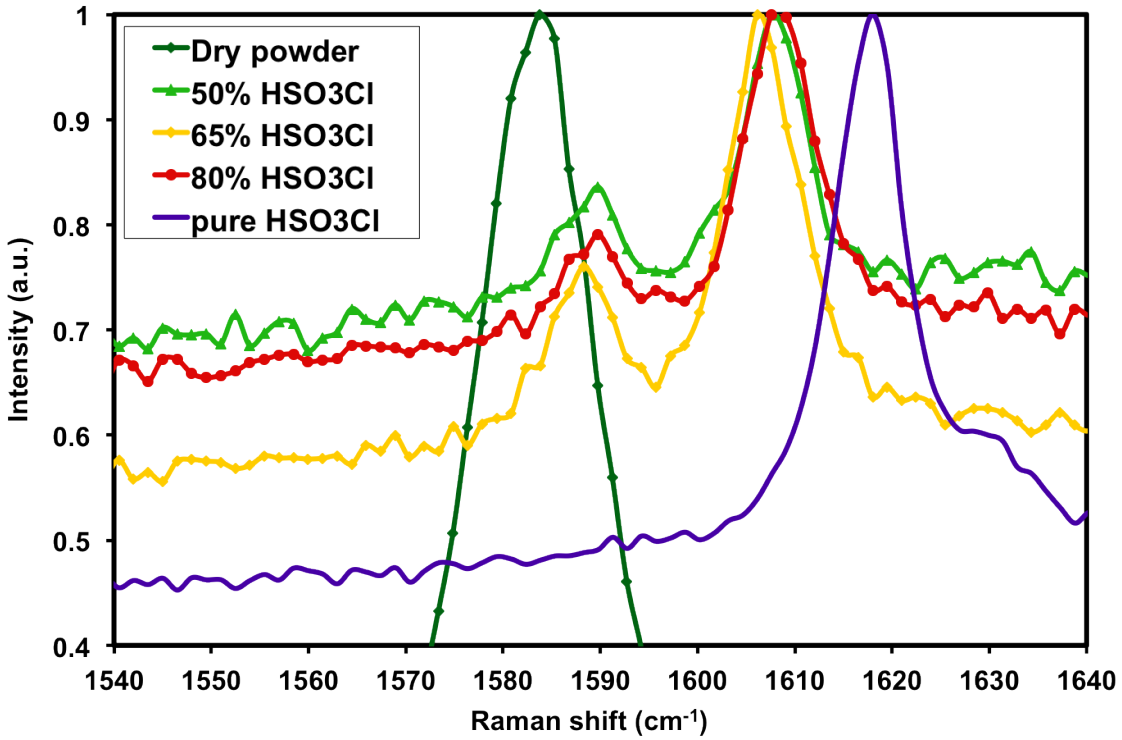

(b)

Figure 3.4 : Image 3.4(a) shows a qualitative comparison between graphite dissolution into different solvents showing graphite in vials with a Teflon–coated stir bar to promote dissolution. Starting from left, graphite is dissolved in NMP, 50%, 65%, 80% vol. chlorosulfonic acid (HSO_3Cl) in sulfuric acid (H_2SO_4) and pure chlorosulfonic acid. The dispersions were prepared at 10 mg/mL. The acid dispersions were then centrifuged at 5000 rpm for 12 hours while the NMP dispersion was centrifuged for 3 hours. The amount of centrifugation time is different in the two cases since the settling time is linearly dependent on density differential between particles and solvent. Thus, the centrifugation time is scaled by this density difference. Graph 3.4(b) shows a comparison of acid-induced shifts in the liquid–phase Raman G-peak for graphite dispersed in the same mixtures of chlorosulfonic acid in sulfuric acid. The G–peak shift is a quantitative measure of the degree of protonation.

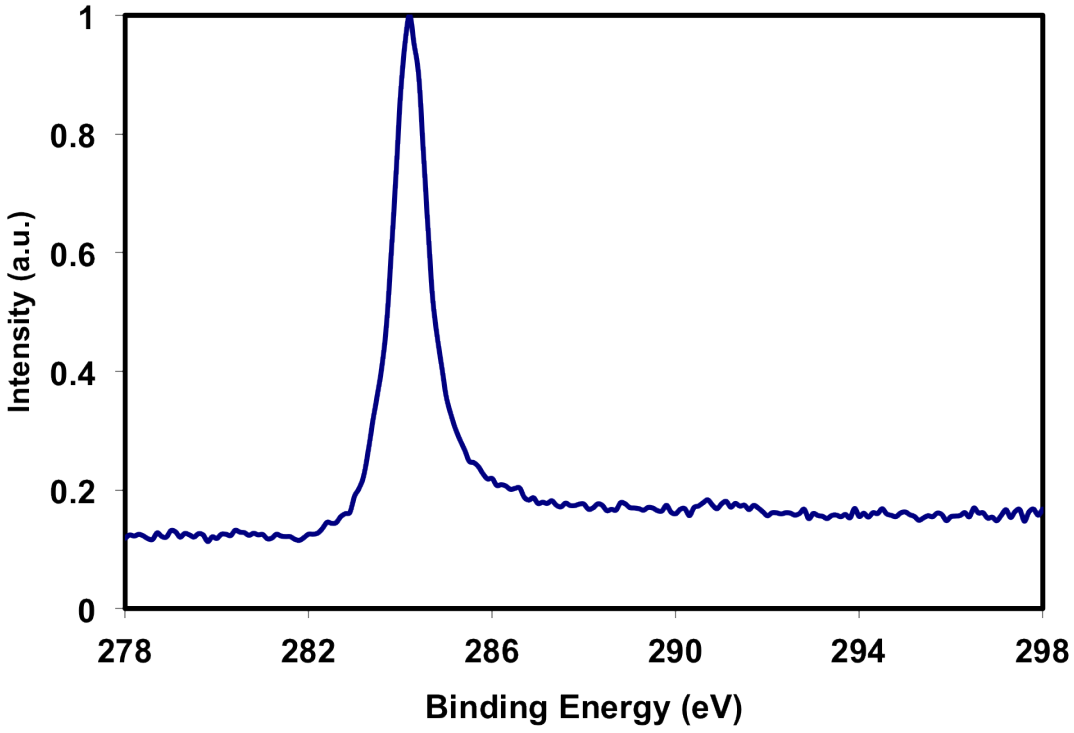

Figure 3.5 : 1s core-level XPS spectrum from the dry material obtained upon quenching HOPG from chlorosulfonic acid dispersion. The powder was dryed under vacuum over night at 100 C. The data was acquired by Jay Lomeda, Dr. Tour Group, Rice University, Houston, TX

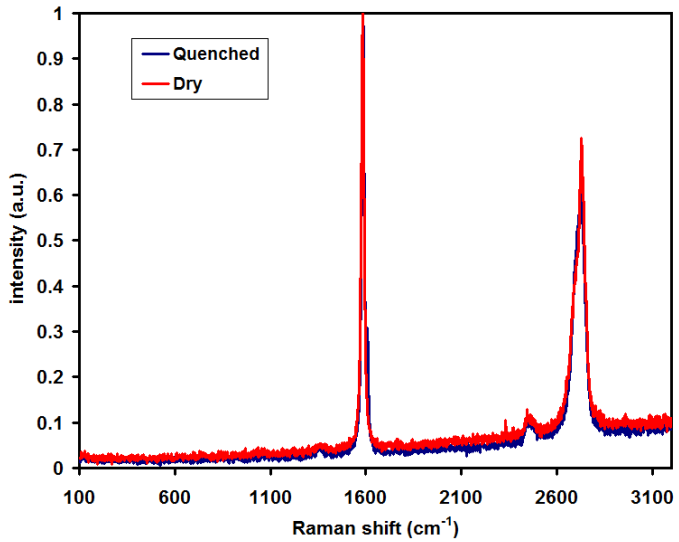

(a)

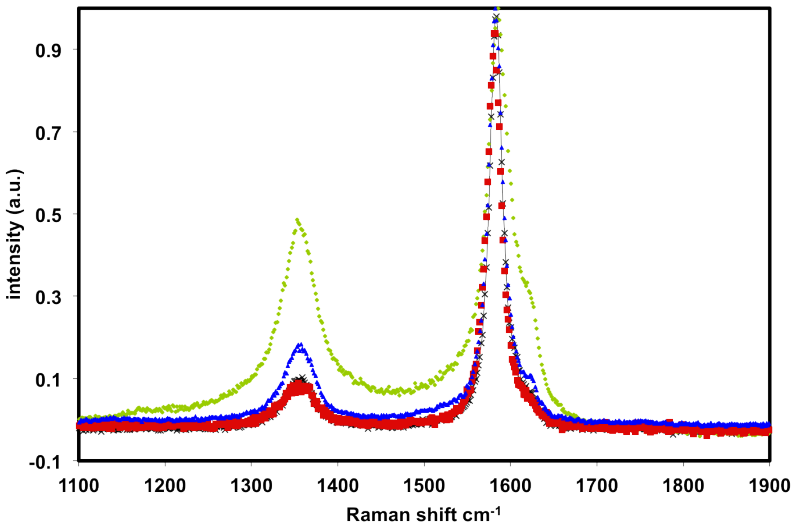

(b)

Figure 3.6 : Figure 3.6(a) shows the solid-state Raman spectra of the initial graphite dry powder and the graphite quenched from the acid dispersion. The two spectra are virtually identical, indicating that protonation is reversible. Figure 3.6(b) shows the influence of centrifugation time on Raman spectra. The red curve refers to the initial powder, the black to the quenched bottom phase, the blue to the quenched top phase after 30 min centrifugation at 5000 rpm and the green after 12 h of centrifugation at 5000 rpm. Each curve is obtained by averaging the Raman spectra of 5 different spots. Note how the bottom phase Raman is almost indistinguishable from the original powder. The graphite source was microcrystalline graphite. Raman spectra were taken with 514 nm excitation wavelengths and long working-distances on a 50x lens.

then composed of sedimenting non–Brownian graphene/graphite flakes. Thus, the amount of material that remains dispersed in the top isotropic phase is governed by the balance between Brownian diffusive forces and gravitational forces. Interestingly, the intensity of the D peak increases as a function of centrifugation time (Fig. 3.6(b)). This can also be interpreted in terms of flake size. In fact, the amount of graphene edge per flake (which determines the D peak intensity of pristine graphene [Gupta et al., 2009]) increases as the flake size decreases, while the D peak of the bottom phase remains unchanged compared to the initial powder. Therefore, we conclude that the graphite flakes in the top phase are smaller — i.e., they have a larger perimeter-to-surface ratio.

We further investigated the difference between the dissolved top phase and the sedimented bottom one by measuring the Raman G′ peak. This peak allows differentiation between different graphite stacking [Cancado et al., 2008]. Specifically, the typical Bernal stack of graphite is characterized by two Lorentzians centered at ≈2690 (G'_{3DA}) and 2730 (G'_{3DB}) while the amount of random (turbostatic) stacking is characterized by a Lorentzian peak centered 2710 (G'_{2D}).The relative intensity of these peaks identifies the degree of order of various phases. We measure a significant increase of G'_{2D} peak for samples prepared by quenching the top phase compared to the bottom and initial powder. (Fig. 3.7). Thus, the quenched top phase attains the turbostratic stacking typical of disordered graphite, indicating that the molecules in solution were largely exfoliated. Also, lack of Bernal stacking indicates that number of graphene layers within a given flake are fewer than 10 [Ferrari et al., 2006].

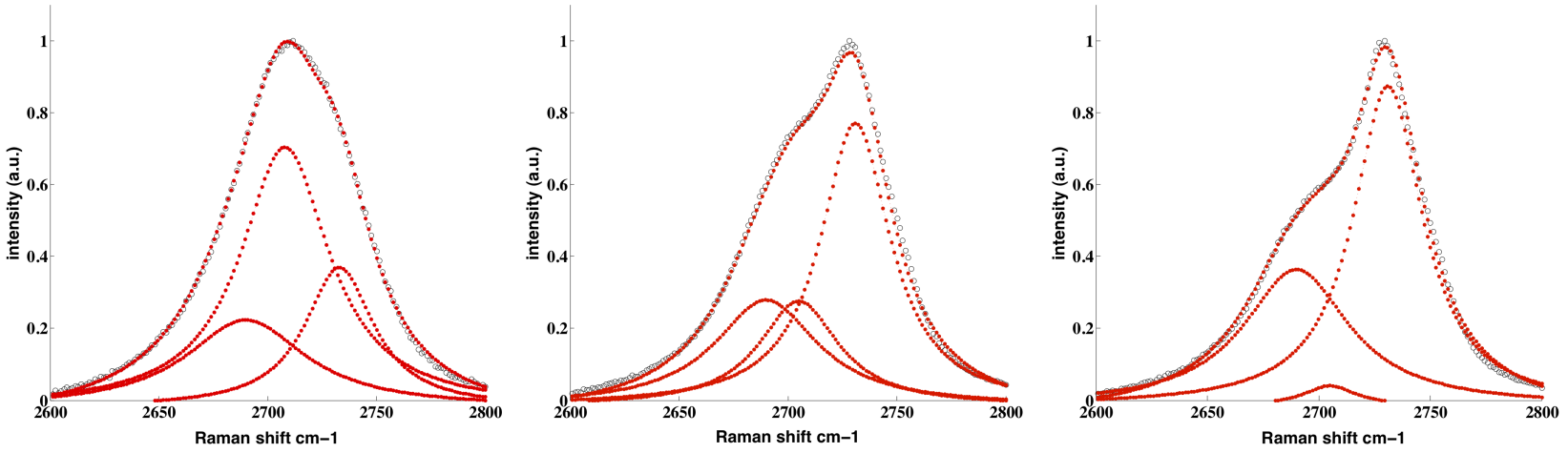

(a) (b) (c)

Figure 3.7 : G′ band Raman spectra performed using the excitation laser wavelength of 514.5 nm. The spectra were obtained using graphoil as a starting material. The top and bottom phase spectra were obtained on solid samples by quenching the acid-dispersed material. The experimental curves were fitted with three Lorentzians centered at 2690 (G'_{3DA}), 2710 (G'_{2D}) and 2730 (G'_{3DA}) respectively. The G′ peak of top phase is mostly composed by the G'_{2D} peak, while the undispersed bottom phase is mostly composed by G'_{3DA} and G'_{3DB} peaks, although it has a higher G'_{2D} peak compared to the initial graphite powder.

3.4 Evidence of Single Layer Exfoliation, Molecular Conformation and Formation of Liquid Crystals

Conclusive proof of single–layer exfoliation requires transmission electron microscopy (TEM) or atomic force microscopy (AFM). However, the properties of chlorosulfonic acid pose challenges to the preparation of TEM samples (because holey carbon grids are damaged by the acid) and AFM substrates (because the low volatility, high surface tension, and hygroscopicity of acid cause substantial re-aggregation). We solved this problem by capturing graphene flakes on custom–made SWNT grids (see also Chapter 4) that were then transferred onto a standard grid for TEM or silica substrate for AFM. High–resolution TEM (HR-TEM) was then used to image graphene layers. Figures 3.8(a) and 3.8(b) show low and high magnification images of a single–layered graphene flake, while figure 3.8(c) shows a HR-TEM image of a few-layered graphite flake. The SWNT network is clearly visible through the flake. Electron diffraction (Fig. 3.8(d)) shows the typical [Meyer et al., 2007] Bragg reflections intensity ratio of single layer graphene (Fig. 3.8(e)).

Monolayer graphene is characterized by a weak dependence of its diffraction intensity as a function of sample tilting angle with respect to the incident beam [Meyer et al., 2007]. On the contrary, multi-layer graphene has a diffraction intensity that changes dramatically with tilt angle. Figures 3.9(a) and 3.9(b) show the diffraction intensity of the inner and outer spots versus tilt angle for a monolayer flake. As the sample holder is tilted from 0 to 30 degrees there is just a weak variation of the intensity profile, as expected for monolayer graphene. We decided to use a range of 30 degree for the tilting angle because for multilayer graphite, the period of a full variation of intensity is roughly 30 degree [Meyer et al., 2007].This is further confirmation

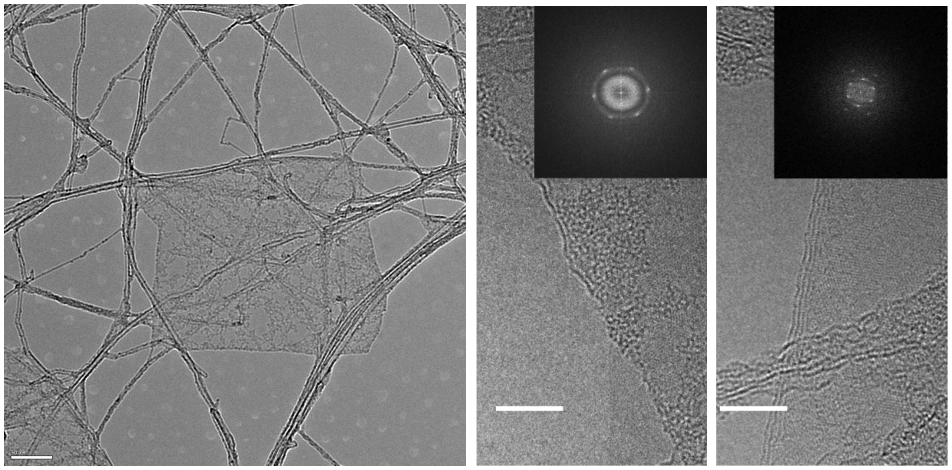

(a) (b) (c)

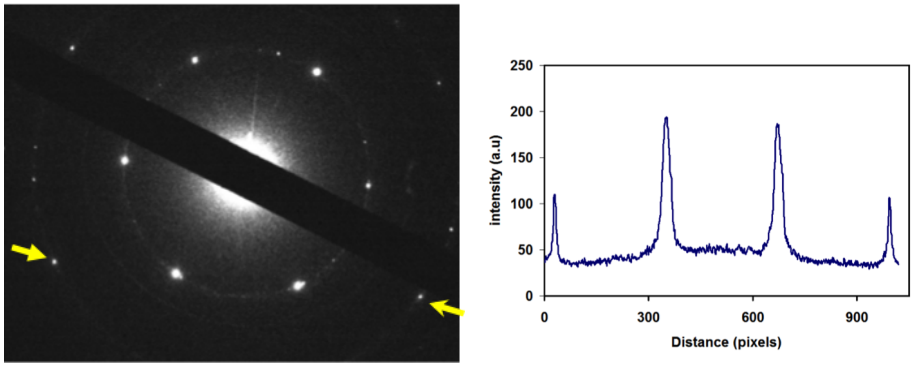

(d) (e)

Figure 3.8 : Evidence for single–layer dissolution. 3.8(a)) Low magnification TEM image showing a small flake graphene. Note how the CNT network beneath the graphene flake is clearly visible (scale bar 50 nm). 3.8(b)) HR-TEM of a single layer edge with fast Fourier transform (FFT) insert (scale bar 5 nm). 3.8(c)) HR-TEM of a few layer edge with its FFT (scale bar 5 nm). Adsorbates of unknown origin are clearly visible at high magnification, similar to flakes obtained by micromechanical cleavage. 3.8(e)) Electron diffraction showing the typical intensity profile along the line delimited by the two yellow arrows(3.8(d)).Figures 3.8(b) and 3.8(c) were acquired by Yaron Kauffmann at Technion, Israel Institute of Technology, using FEI Titan 80-300 S/TEM operated at 300 kV.

of the presence of graphene and of our ability to identify it visually.

Once a single layer is identified by means of electron diffraction, statistics on the number of layers can be conducted by a simple intensity analysis. In fact, electron and light absorption are quantized [Nair et al., 2008] (Fig. 3.10). The highest intensity correspond to vacuum and each discrete decrease in intensity corresponds to one layer.

High–resolution TEM and electron diffraction were used to analyze over 30 flakes and quantify the degree of exfoliation. 70% of the dispersed graphene flakes were single layer. A combination of SEM and STEM was used to assess size distribution. We found that the average size depends on the graphite source. Microcrystalline graphite and graphoil have an average flake size of 300 nm and 900 nm respectively (Fig. 3.11).

The persistence length ($L_p = K/k_bT$) is a measure of the rigidity of a submicroscopic object where K is the bending stiffness, k_b the Boltzmann factor and T the absolute temperature. When$L_p >> L$ (where L is the object leading dimension), the object does not deform appreciably under the action of thermal forces; when $L_p << L$, the opposite is true. In graphene nanoribbons, the bending stiffness can be expressed as $K = (\pi/12)Yh^3d$, where Y is the Young's modulus, h the ribbon thickness, and d the ribbon width [Bets and Yakobson, 2009]. Atomistic simulations from Bets and Yakobson showed that narrow nanoribbons ($\sim$1 nm in width) act as flexible at high temperature ($\sim$700 K) with persistence length L_p $\sim$100 nm, shorter than their length [Bets and Yakobson, 2009]. However, when the width is increased to $\sim$100-200 nm (the typical width of the nanoribbons used in our experiments [Kosynkin et al., 2009]) L_p increases to $\sim$10 μm; thus, nanoribbons used in our experiments are not expected to deform under thermal forces. The previous analysis does not consider intramolecular self attraction or repulsion that would alter the graphene conformation

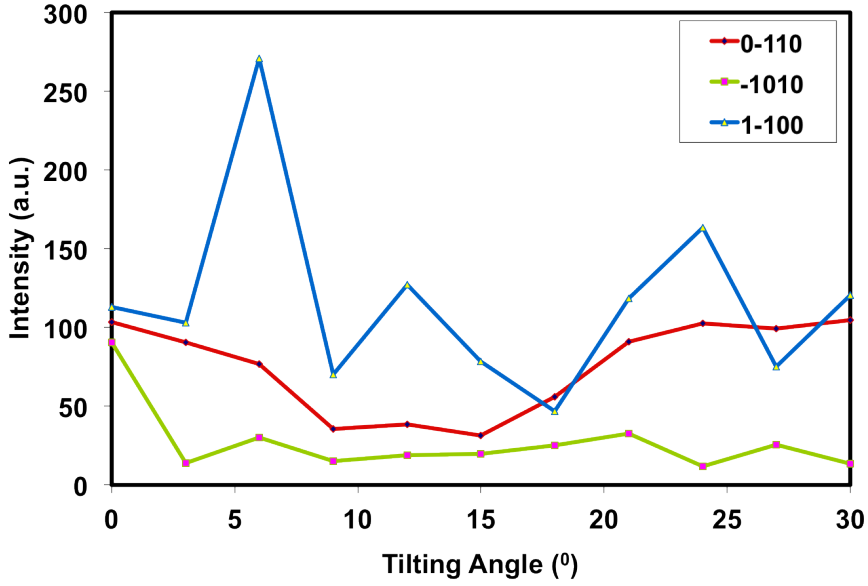

(a)

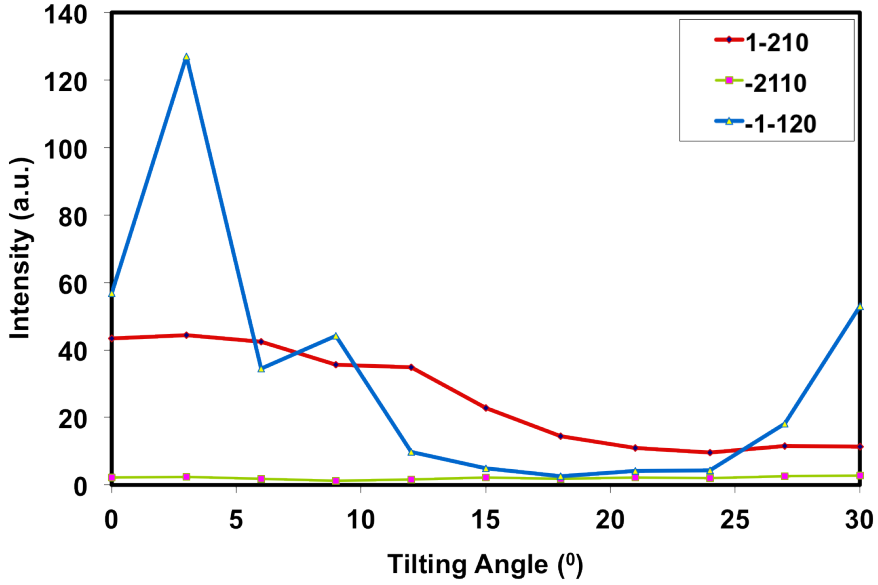

(b)

Figure 3.9 : Selected area diffraction of a monolayer graphene flake for a wide range of tilt angles. (3.9(a)) Intensities of inner spots. (3.9(b)) Intensities of outer spots.Selected area diffraction was acquired by Yaron Kauffmann at Technion, Israel Institute of Technology, using FEI Titan 80-300 S/TEM operated at 300 kV

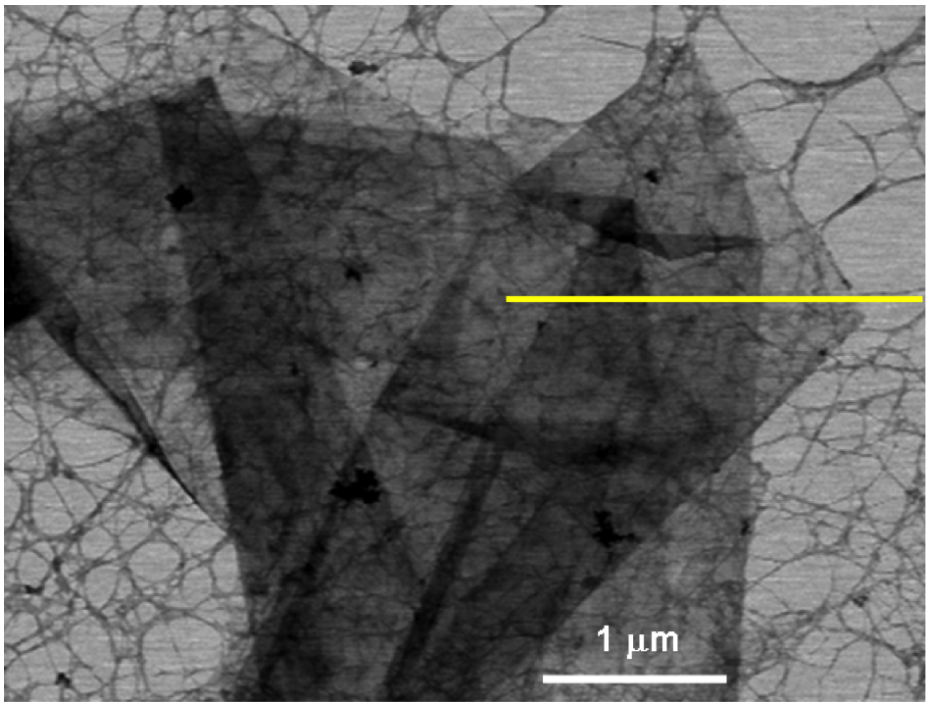

(a)

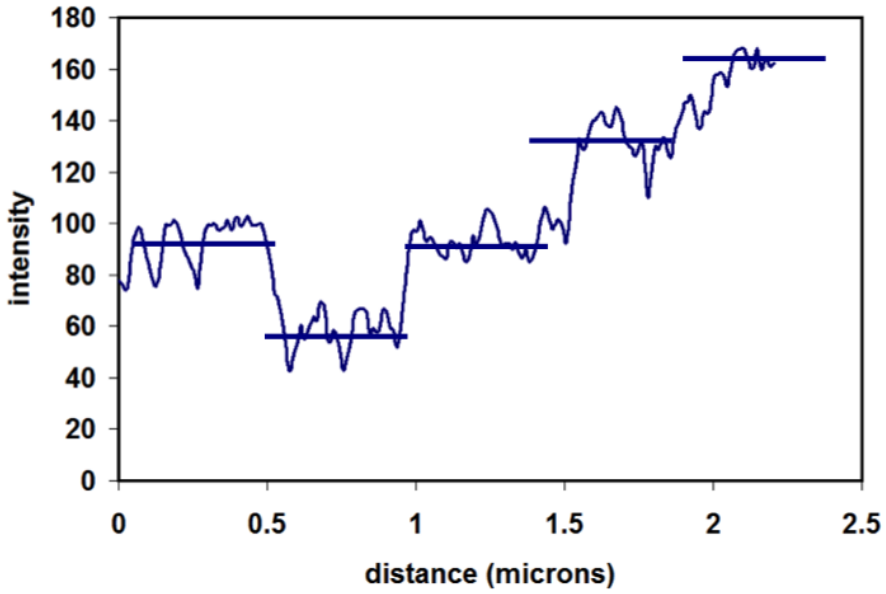

(b)

Figure 3.10 : 3.10(a)) Folds of an HOPG flake showing quantized electron absorption. 3.10(b)) Intensity profile taken from the picture along the yellow line from left to right. As the flake folds increasing the number of layers the intensity decreases by a discrete values. The image was acquired in STEM mode at 30 kV using Hitachi S-5500.

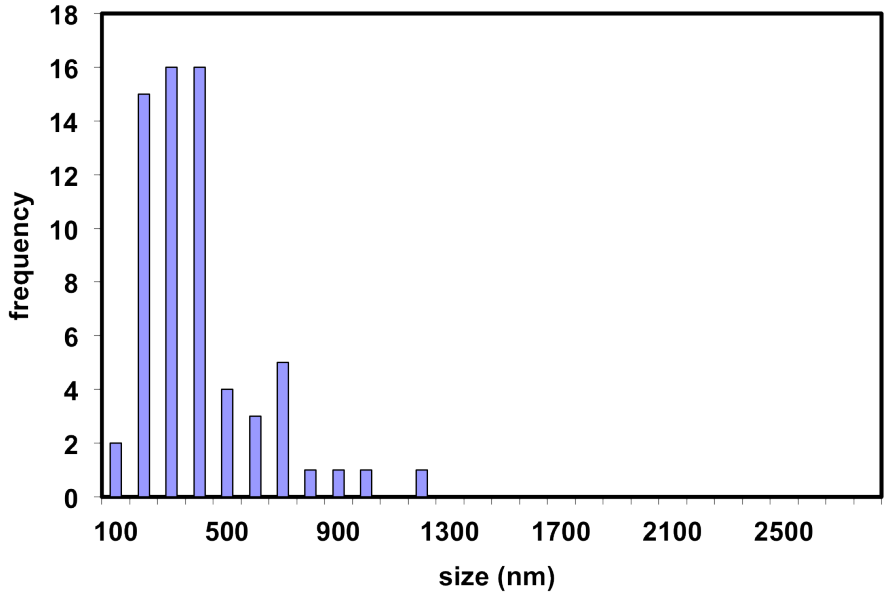

(a)

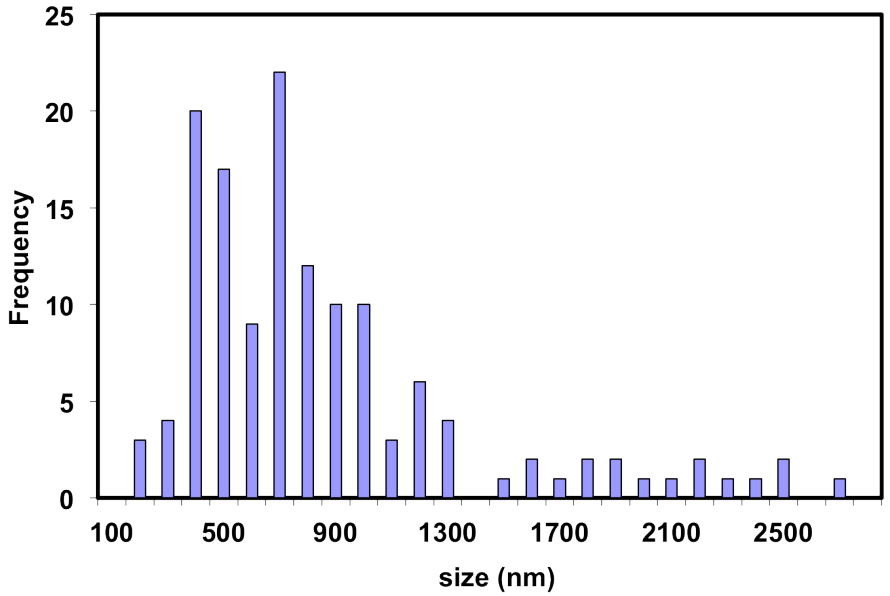

(b)

Figure 3.11 : Typical size distribution of the graphene flakes. The distribution was evaluated based on more than 60 flakes for each graphite source. The size was evaluated by measuring the largest end to end distance of the irregularly shaped flakes. Figure 3.11(a) and 3.11(b) correspond to microcrystalline graphite and graphoil, respectively.

in solution. Since graphene dissolution mechanism in chlorosulfonic acid is protonation, this should induce self repulsion and decrease the likelihood of folding. Indeed, the vast majority of the graphene flakes examined with SEM and STEM (Fig. 3.12) show a fully extended molecular conformation. In comparison, GO in acetone was visualized using the same sample preparation technique. Acetone acts as a poor solvent for GO and promotes folding and compact structure [Spector et al., 1994]. Most of the visualized GO sheets had folded conformation (Fig. 3.13).

This suggests that STEM and HR-TEM provide a reasonable representation of graphene conformation in solution. However, sample preparation, more specifically the flow regime and drying process during sample preparation could alter molecular conformation. Thus, we imaged graphene flakes under cryo–TEM and confirmed that the flakes are indeed extended (Fig. 3.14).

Rigid anisotropic molecules undergo an isotropic-liquid crystalline transition as their concentration is raised [Onsager, 1949]. van der Kooij *et al.* [2000] experimentally observed this transition with clay particles and used Onsager-like theories to determine the phase diagram [Bates and Frenkel, 1999, van der Kooij et al., 2000, van der Kooij and Lekkerkerker, 2000]. The transition concentration scales inversely with the aspect ratio (diameter/thickness). As in rigid rods [Wensink and Vroege, 2003, Green et al., 2009b], polydispersity broadens the biphasic region, and both the maximum isotropic concentration of the platelets and the ability to form liquid crystals depends on solvent quality [van der Beek and Lekkerkerker, 2004]

We tested these concepts in the graphene/superacid systems. The top phase was extracted and quenched by a non solvent after centrifugation. The powder was then re-dissolved at 20 mg/mL and centrifuged to induce phase separation. The top phase is structureless and has a concentration of 1.8 mg/mL. With cross polarizer, the

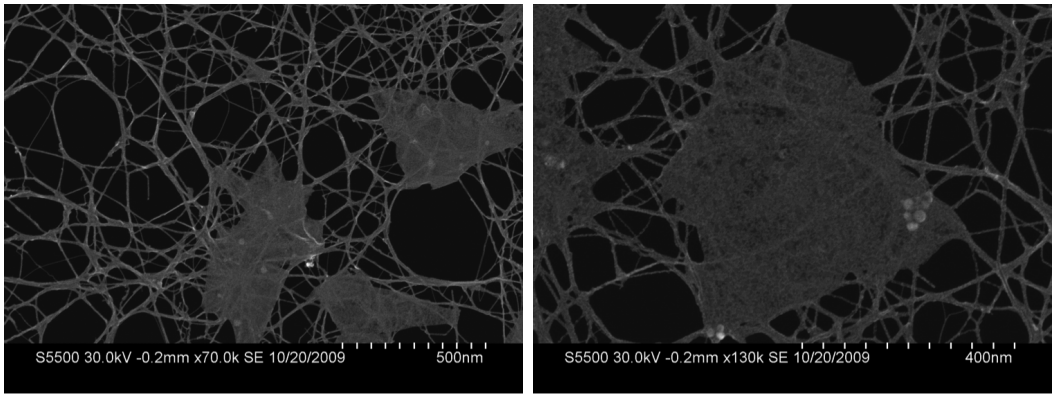

(a) (b)

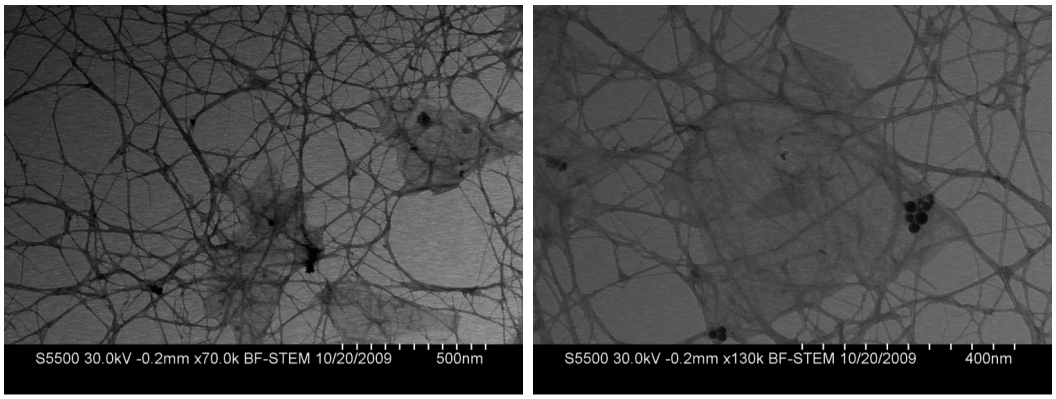

(c) (d)

Figure 3.12 : Representative images of graphene flakes from Chlorosulfonic acid solution. (3.12(a)) and (3.12(b)) are SEM images while (3.12(c)) and (3.12(d)) are the same flakes imaged in STEM mode. Note how the nanotube network beneath the graphene flake is visible also in the SEM mode.The images were acquired using Hitachi S-5500.

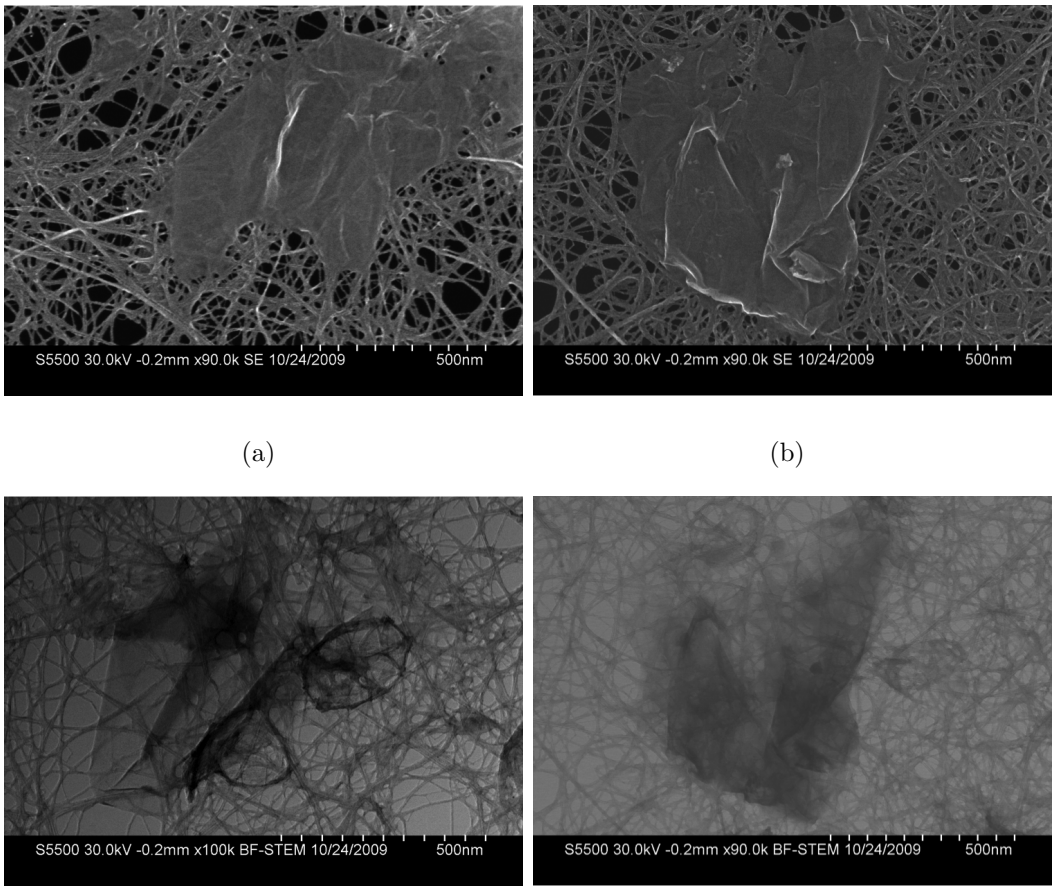

Figure 3.13 : Representative images of graphene oxide flakes from acetone solution. (3.13(a)) and (3.13(b)) are SEM images while (3.13(c)) and (3.13(d)) are the same flakes imaged in STEM mode.The images were acquired using Hitachi S-5500.

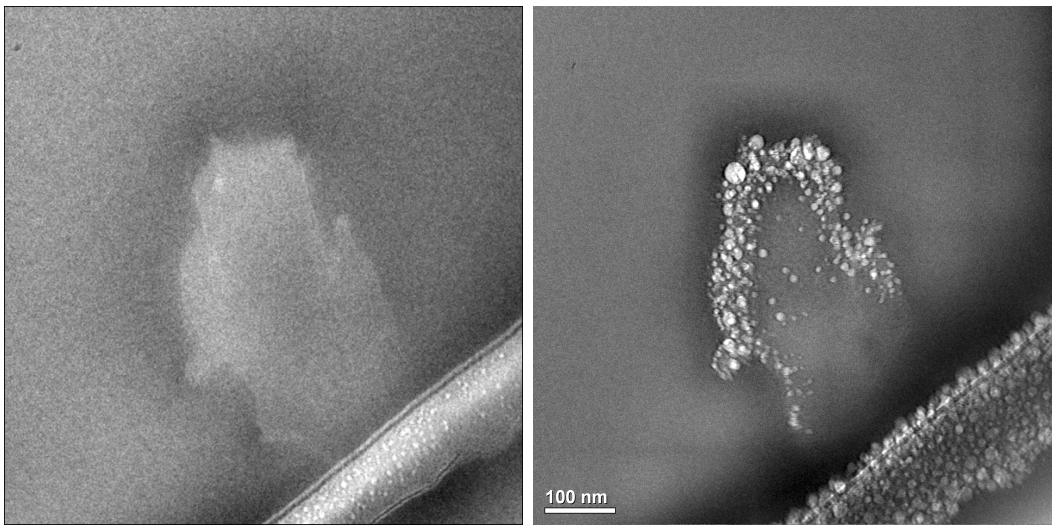

(a) (b)

Figure 3.14 : Graphene as a rigid platelet. Image (3.14(a)) and (3.14(b)) display cryogenic-temperature transmission electron microscopy (cryo–TEM) images of graphene flakes dispersed in chlorosulfonic acid. A graphene flake (3.14(a)) is shown nearby the TEM lacey carbon edge at very low imaging conditions (<10 electrons/Å^2). After some irradiation from the electron beam of 50-80 electrons/Å^2, (3.14(b)) the contrast between the graphene and acid is heightened nearby the graphene edges as acid is preferentially etched at these sites. No dark lines (which indicates folding points) are observed. Images were acquired by Judith Schmidt and Ellina Kesselman (Yeshayahu Talmon group) at Technion, Israel Institute of Technology, using a FEI T12 transmission electron microscope operated at 120 kV, using an Oxford CT3500 cooling holder, operated at about -180 ^{0}C.

bottom phase shows birefringence typical of a liquid crystal (Fig. 3.15(a) – 3.15(c)). Therefore, unlike the starting material, dispersion of an entirely-soluble graphene source yields isotropic/liquid–crystalline phase separation as expected in a solution of rigid platelets. Various liquid–crystalline phases (nematic, chiral, columnar) have been reported for disc-like platelets (called discotics); the nematic phase is the most probable case for polydisperse, unfunctionalized systems such as ours. The liquid–crystalline Schlieren texture in 3.15(b) and 3.15(c) is very similar to typical discotic nematic samples [Chandrasekhar, 1992]. This liquid–crystalline phase is promising for processing of neat graphitic macroscopic articles such as fibers and films, particularly in light of recent improvements in graphene size control and bulk manufacturing, such as the production of controlled-size graphene nanoribbons (GNRs) [Kosynkin et al., 2009, Campos-Delgado et al., 2008]. We measured the solubility of both oxidized and reduced GNRs in chlorosulfonic acid as 3.4 mg/mL. No undispersed material was observed; instead, the entire sample is soluble and it forms liquid crystals at high concentration. (Fig. 3.15(d) – 3.15(f)). Again, the fact that the reduced GNRs are entirely soluble with no precipitate indicates that chlorosulfonic acid disperses graphene at the single–layer level.

3.5 Thin Film Fabrication

High–concentration isotropic solutions are attractive both for nanocomposites and for functionalization of graphene. We use isotropic dispersions to make thin films by filtration, including transparent and conducting films. Thin films were made via vacuum filtration on a PTFE substrate filters (Millipore Omnipore membrane, 13 mm, 0.2 μm), and the deposited mass was calculated by weighing the mass of the filter before and after filtration. Two types of graphite sources were used: Graphoil and

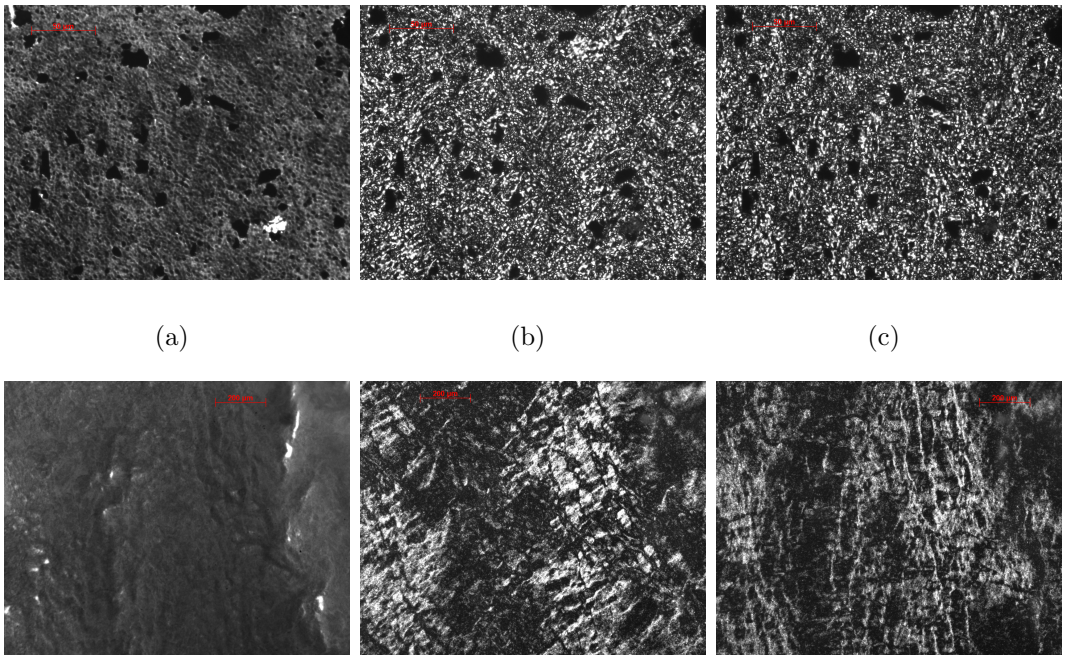

(a) (b) (c)

(d) (e) (f)

Figure 3.15 : Evidence for graphene liquid crystalline phase. (3.15(a)-3.15(c)) Light micrographs of high concentration (∼2 wt%) graphene dispersion in chlorosulfonic acid (50 μm scale bar). (3.15(a)) Transmitted light. (3.15(b)) Transmitted polarized light with analyzer and polarizer crossed at 90 degree. (3.15(c)) Crossed analyzer and polarizer rotated by 45 degree with respect to image 3.15(b). (3.15(d)-3.15(f)) Light micrographs of high concentration (∼2 wt%) oxidized nanoribbons dispersion in chlorosulfonic acid (200 μm scale bar). (3.15(d)) Transmitted light. (3.15(e)) Transmitted polarized light with analyzer and polarizer crossed at 90°. (3.15(f)) Crossed analyzer and polarizer rotated by 45° with respect to image 3.15(e).

Sigma graphite. The resistance of the film was measured using a four–point probe. Sheet resistivity was calculated as $\rho = (V/I)\pi t/ln(2)$, where ρ is sheet resistivity, V is voltage, I is current, and t is the film thickness. The thickness was calculated by dividing the known mass by graphite density (assumed to be 2.1g/cm^3) multiplied by the filter area, assuming uniform coverage. The resistivity values for the two films are 9.1 $\mu\Omega$ m for Graphoil, and 633.6 $\mu\Omega$ m for Sigma graphite. These values differ by two orders of magnitude. SEM images of the films are shown in Fig. 3.16. A measurable difference between these different graphite sources is their size (Fig. 3.11). Attempts to produce transparent films from microcrystalline graphite by filtering on alumina substrate failed because it was not possible to make a free-standing film upon dissolution of the alumina substrate. These thin films break into small pieces when detached from the substrate. However, it was possible to make such a film from HOPG dispersions as well as graphoil dispersions.

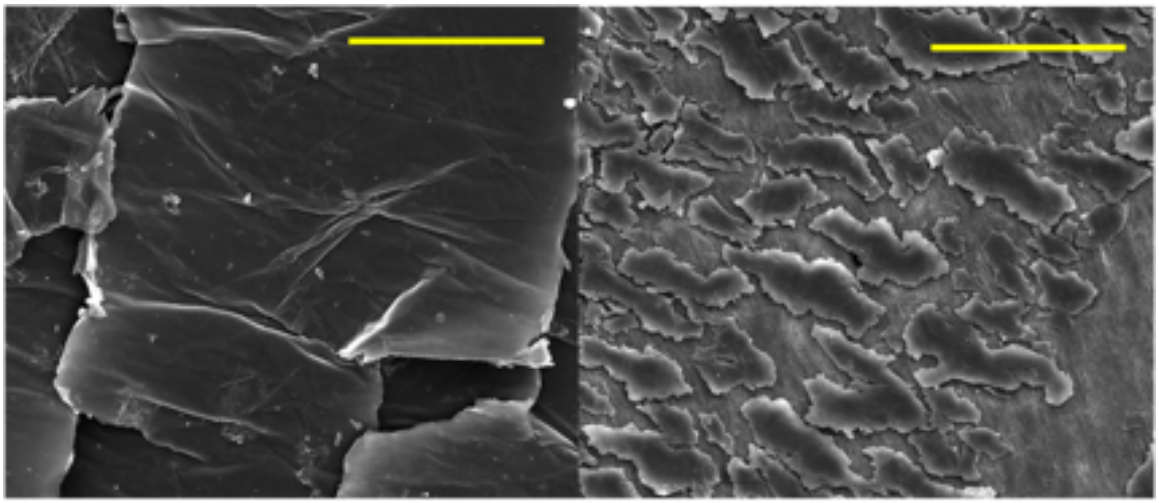

Figure 3.16 : SEM results showing the typical morphology of films made by vacuum filtration on Teflon with 100 μm scale bars. Left: Graphoil source. Right: Sigma graphite.

We also measured a sheet resistance of 1000 $\Omega/\square$ on an 80% transparent film

(Fig. 3.17) made from a 10 ppm Graphoil dispersion. Sheet resistance of thin films was measured using an Alessi four–point probe fitted with custom–made film attachment with Platinum leads. Measurements were taken in ambient conditions by securing and pressing the graphene thin films on glass substrate against the Platinum leads.

Figure 3.17 : 80% transparent (at 550 nm) film made by vacuum filtration of a 10 ppm isotropic Graphoil dispersion in chlorosulfonic acid. The measured sheet resistance was 1000 Ω/□.

We compare these values against others in the literature. Lotya et al. [2009] report 62% transmittance and 22,000 Ω/□ for a surfactant-stabilized dispersion of graphene after annealing. Hernandez *et al.*[2008] report a sheet resistance of 7100 Ω/□ with 42% transmittance (after annealing). It is noteworthy that these films were not transferred to a clear substrate; instead, the transparency was measured relative to an alumina substrate. Also, these values are for films that have been annealed whereas the values obtained here have not been annealed. Pre-annealing numbers for Hernandez et al. are 7,200,000 Ω/□ and 61% transmittance. Other, slightly better properties (100-1000 Ω/□ at 80% transmittance) have been observed

for films produced from graphene oxide films, which were then reduced via hydrazine to graphene and annealed at 1100 ^{o}C [Becerril et al., 2008]. However, annealing is not compatible with most practical substrates, and could hinder possible applications.

3.6 Experimental Details

We analysed and characterized three different sources of graphite in this study: (i) graphoil (expanded graphite; EGS Enterprises), (ii) microcrystalline graphite (Sigma Aldrich, batch no. 08017EH), and (iii) highly ordered pyrolytic graphite (HOPG) (SPI Supplies, lot no. 1091028). Chlorosulphonic acid (Sigma Aldrich, 99%, batch no. 16096EJ) and sulphuric acid (Fisher Chemical, certified ACS plus, lot no. 083290) were used as solvents.

Raman spectroscopy was performed on a Renishaw Raman microscope using a 514 nm He2Ne laser. Raman spectra of solid samples were taken by depositing the graphite on a glass slide with the aid of double tape. To measure the solid-state Raman spectra of the top and bottom phase of a centrifuged sample, the sample was quenched by the addition of excess water. (Note that extreme care has to be taken during this operation due to the highly exothermic reaction of chlorosulphonic acid with water; dropwise addition of water into the acid is advised. The researcher also needs the appropriate protective equipment.) Once the graphite precipitated, the mixture was filtered to yield a solid sample. To measure the Raman shift in the fluid, samples were prepared in a glovebox (dew point -50 °C, to avoid contact with moisture), deposited on glass slides, covered with cover slips and sealed with wax or tape to prevent moisture ingress during the measurement outside the glovebox. The same procedure was followed for the preparation of microscopy slides. TEM and HRTEM imaging and electron diffraction were performed using a JEOL 2010 operated at 100

kV and a FEI Titan 80-300 S/TEM operated at 300 kV with a point-to-point resolution below 1 Å. The cryo–TEM techniques followed those of Davis and colleagues [Davis et al., 2009] . The standard cryo–TEM procedure [Talmon, 1996] was modified to account for unique difficulties associated with working with superacids. Soluble graphene was acquired by dispersing 250 mg graphoil in 10 ml chlorosulphonic acid, centrifuging at 5,000 r.p.m. for 12 h, removing the top phase through a glass syringe, and quenching the top phase by slowly adding it to excess water. The quenching process produces solid graphene that could be entirely redispersed in chlorosulphonic acid with no insoluble portion. Using this source, soluble graphene was dispersed in chlorosulphonic acid at concentrations of 0.042 mg ml^{-1} (50 ppm by mass). Dispersions were prepared and mixed for 1 day in a glovebox (dew point -50 °C) in a nitrogen gas atmosphere to prevent contact with water and consequent evolution of gaseous hydrochloric acid. Samples (2 ml) of either dispersion were transferred into a vial and placed in the vitrification apparatus with a glass filter paper and glass pipette. The entire set-up was placed in a glove bag and purged with ultra–pure nitrogen (99.9995%) for 30 min. A drop of the graphene dispersion was then placed on 200 copper mesh, lacey carbon grid (Ted Pella). The glass filter paper (not reactive with chlorosulphonic acid) was then used to blot the sample, leaving a thin film of liquid. The grid was then quickly vitrified by dipping into liquid nitrogen (77 K) and was placed in a cryo-specimen holder for transfer into the TEM. Cryo–TEM imaging was carried out on an FEI T12 transmission electron microscope operated at 120 kV, using an Oxford CT3500 cooling holder, operated at about -180 °C. XPS was performed on a PHI Quantera SXM scanning X–ray microprobe with a pass energy of 26.00 eV, 45° takeoff angle and a beam size of 100 μm. Polarized light microscopy was performed on a Zeiss Axioplan microscope in transmission mode. The samples were

sensitive to humidity and had to be sufficiently thin for light to be transmitted. Slide preparation was critical for preventing water contamination and for ensuring consistent sample thickness. Excessively thick samples appeared homogeneously dark simply due to the near–complete blockage of light. Glass slides and cover slips for microscopy were cleaned with diethyl ether and dried (100 °C, -25 mmHg, relative to atmospheric) overnight under vacuum and covered with aluminium foil. Slides were prepared in the glovebox, and the cover slips were sealed with aluminium tape. High–concentration samples were thinned by slowly hand–pressing on the cover slip to create a sufficiently thin region through which light was partially transmitted. AFM images were obtained with a Digital Instruments Nanoscope IIIa, operating in tapping mode, using silicon tips n-doped with 110 Ω cm phosphorus (Veeco, MPP-11100-140) at a scan rate of 0.5 Hz and a resolution of 512 512. AFM samples were prepared by transferring free–floating thin films on a silicon substrate.

3.7 Conclusions

We have shown that chlorosulfonic acid exfoliates graphite into isotropic graphene dispersions at concentrations one order of magnitude higher than any other known solvent or dispersant. The acid protonates the graphene to induce repulsion between layers; the mechanism is similar to acid protonation of SWNTs and does not damage or functionalize the material. A minimum degree of protonation is required for dissolution at high concentrations. Moreover, chlorosulfonic acid disperses new forms of graphene such as graphene nanoribbons. High–concentration dispersions of fully soluble material yield liquid–crystalline phases. The highly concentrated isotropic and liquid crystalline phases are promising for functionalization, and for scalable manufacturing of nanocomposites, films, coatings, and high performance fibers. In particular,

we envision graphene liquid crystals as a replacement for traditional discotic pitch–based liquid crystals used as precursors for carbon fibers, films, and weaves.

Chapter 4

CNT Films as TEM Grids

4.1 Introduction

Transmission Electron Microscopy (TEM) is an essential tool that renders details and hence understanding of structures at length scales below the wavelength of light, such as crystal defects, chemical structures [Muller et al., 2008], micelles [Talmon, 2007] and proteins [Ludtke et al., 2004]. Thus, TEM is an essential and routine tool in research fields spanning materials science, nanotechnology, and biology. However, quality of the micrograph and related analysis, e.g., electron diffraction and elemental mapping, is only as good as the sample. Ideally, the sample comprises the specimen alone. Usually, a support film must hold the specimen. Thus, advances in specimen supports are critical to improving TEM imaging.

Sample supports must be almost invisible to the electron beam. Because atoms with higher atomic number and thick areas appear darker when visualized using bright field microscopy [Brandon and Kaplan, 2008] sample supports are usually thin and consist of low atomic number materials. Supports must also be electrically conductive to avoid charging effects. Controllable pore size and high surface area, together with chemical, thermal and mechanical stability are also highly desirable. Carbon is the lightest element with sufficient structural integrity, stability, and conductivity to serve as a TEM support. Typically, a thin film of amorphous carbon on a metal grid is

used to support the specimen*.

Because of their conductivity and thinness, CNT and gra-phene TEM supports are the most promising current alternatives to conventional TEM grids. Graphitic carbon is also stable under electron radiation, with noticeable damage occurring at high voltage (100 kV and higher) under extensive exposure (30 minutes and higher)[Smith and Luzzi, 2001]. Super–aligned carbon nanotube (CNT) forests and graphene flakes grown by Chemical Vapor Deposition (CVD) have shown superior performance as TEM specimen support [Nottbohm et al., 2008, Zhang et al., 2008a]. However, so far fabrication is complicated because CNTs must be grown by CVD in an array configuration that can be spun into a membrane, and graphene must be grown into extremely large flakes and transferred onto a metal grid. Thin films of solution processed graphene oxide have also been used as TEM supports, but have limited applicability because of their easy dissolution in solvents and poor electrical conductivity and thermal stability [Wilson et al., 2009, Paredes et al., 2008, McAllister et al., 2007].

4.2 Thin Film Fabrication

Here we present a simple and highly reproducible technique for fabricating electron microscopy imaging supports from readily available commercial CNTs. The resulting ultra-thin supports are mechanically stable and perform as well as TEM support made from aligned CNT membranes [Zhang et al., 2008a].

The raw CNT powder was dissolved in chlorosulfonic acid at low concentration (5-50 ppm) as reported previously [Behabtu et al., 2010, Davis et al., 2009]. Chlorosulfonic acid was used because it is the only solvent that dissolves carbon nanomaterials as individuals without damaging them [Behabtu et al., 2010, Davis et al.,

*http://www.tedpella.com/supflm_html/suptfilm.htm

2009, Parra-Vasquez et al., 2010, Ramesh et al., 2004]. Ultra–thin films were formed through simple vacuum filtration through commercial 20 nm pore size alumina membranes, followed by washing with a quenching solvent (chloroform) to remove residual acid trapped in the film. The films readily detached from alumina membrane filter upon immersion in water. They floated on the water surface and were transferred easily to standard TEM grids (Fig. 4.1).

The CNT films fully cover the metal grid (Fig. 4.2(a) and 4.2(b)). We visualized 49 adjacent holes (7X7) and found no interruption on the CNT network. Also, we have reproduced CNT-based TEM grid multiple (∼100) times with different operators. Thus this sample preparation is both repeatable and reproducible and has now become our standard methodology to analyze superacid dispersion. Film thickness and porosity was controlled by the mass deposited per unit area (Fig. 4.3).

Robust and transferable thin films were reliably formed using various CNT starting materials including HiPCO SWNT [J. et al., 2001], laser oven SWNT [Landi and Raffaelle, 2007], CVD grown Single-Walled Carbon Nanotube (SWNT) and Multi–Walled Carbon Nanotube (MWNTs) carpets [Pint et al., 2009]. We have noted that CVD grown MWNTs CNTs yield clean (from residual catalyst particles) high surface area TEM support compared to HiPco SWNTs (Fig. 4.4).

Thus, the choice of the starting material is essential for optimal imaging performance. Laser oven SWNTs[Landi and Raffaelle, 2007] and MWNTs thin films used as TEM specimen support displayed high transparency and conductivity: respectively, they showed sheet resistance of 295 Ω/□ and 4000 Ω/□ at 92% transparency (∼10^6 10^5 S/m). These values are one to two orders of magnitude higher than amorphous carbon electrical conductivity [Mominuzzaman et al., 1999]. Improved conductivity is beneficial in dissipating to dissipate sample electron charging.

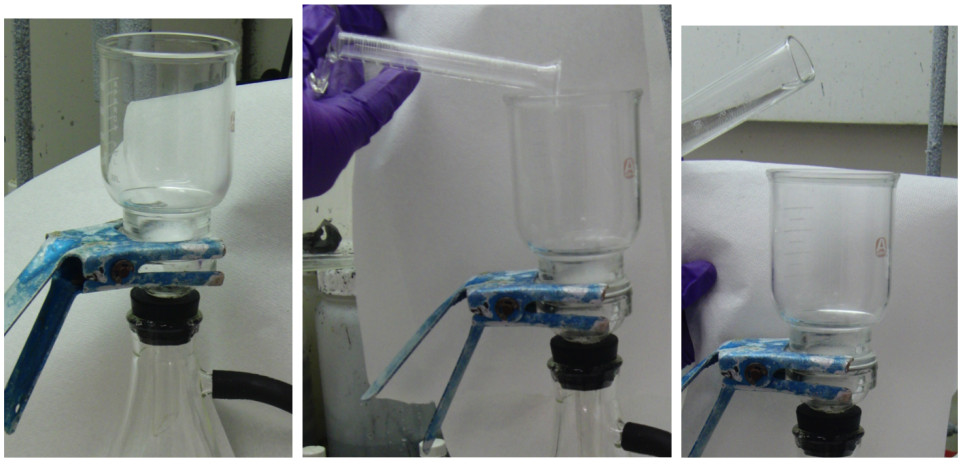

(a) (b) (c)

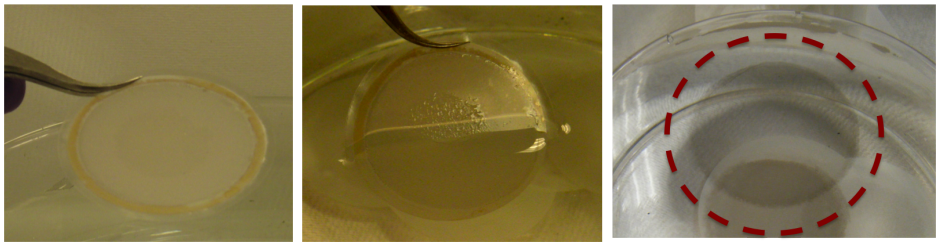

(d) (e) (f)

(g) (h)

Figure 4.1 : The following set of pictures describes the various steps involved during thin film fabrications from superacid. A simple filtration setup (4.1(a)) is used with house vacuum with alumina filters (Anodisc 47 0.02 um pore size, Whatman). The acid/CNT mixture is then filtered (4.1(b)). Once the filtration is complete (few tens of seconds for 5 ml of solution), chloroform is filtered to remove residual solvent from the filter. Chloroform or dichloromethane are usually used during this step because they mix with chlorosulfonic acid with no reaction and negligible heat of mixing (4.1(c)). The produced thin film (4.1(d)) is than immersed in a large beaker with water. By slowly immersing the alumina filter in water (4.1(e)) the CNT thin film detaches itself from the membrane while the membrane falls at the bottom of the beaker. A free standing thin film (circled in red to distinguish it from the membrane) is thus formed (4.1(f)) and can be lifted into a TEM grid and/or glass substrate for further characterization (4.1(g), 4.1(h)).

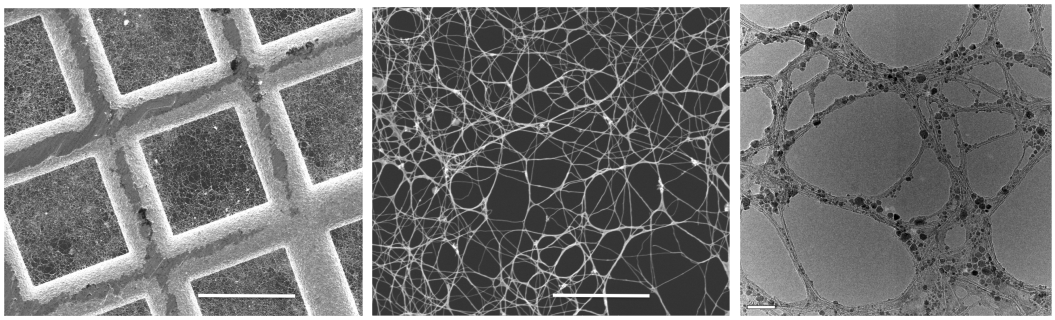

(a) (b) (c)

Figure 4.2 : Structure of CNT thin films for TEM support. SEM images showing the coverage of the CNT thin film on copper grid (figure 4.2(a) and 4.2(b)). The thin film spans across the entire grid cover each square. Figure 4.2(c) shows FeCu oxide supported by the CNT network. Scale bars are 40 μm, 4 m and 50 nm, respectively.

SWNT ultra thin films have also been fabricated from surfactant and organic solvent/SWNT dispersions [Dan et al., 2009, Scardaci et al., 2010] using sonication, which reduce tube length [Lucas et al., 2009]. We formed ultra thin films (transparency >90%) by sonicating CNTs in water and surfactant and organic solvents and subsequent filtering. These films could not be transferred onto grids because they broke at the air–water interface during the process. We conclude that sonication shortens the CNTs and damages the mechanical stability of the films; therefore, individualized, high–aspect ratio CNTs are required for film robustness.

4.3 Thin Film Imaging Performance

We tested the imaging performance of our CNT supports by imaging graphene flakes as well as FeCu and FeCo oxide na-noparticles (synthesized by co-condensation of metal acety-lacetonate precursor) [Crouse and Barron, 2008]. Both samples are particularly challenging to visualize; nanoparticles require very thin supports of thickness

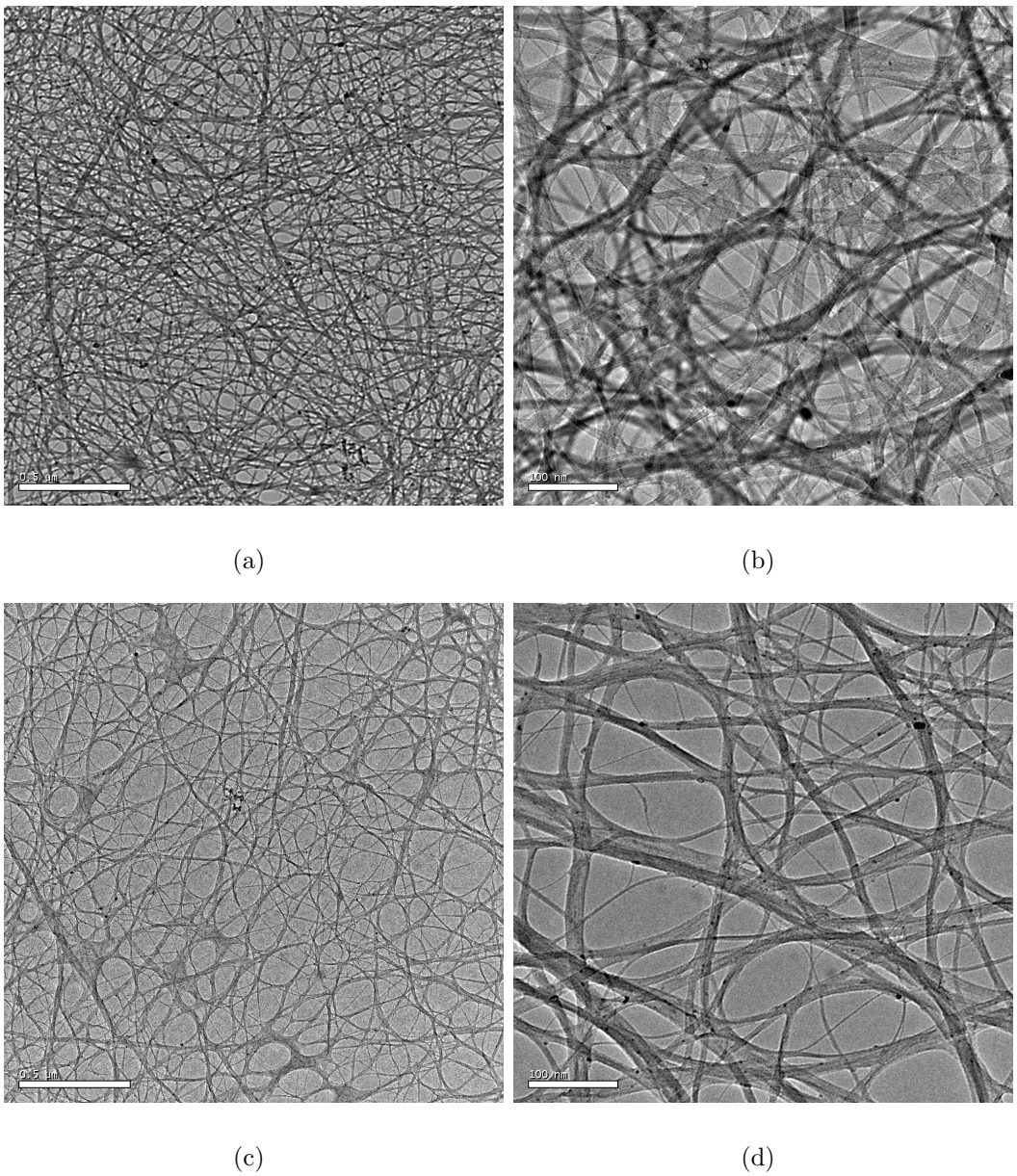

(a) (b)

(c) (d)

Figure 4.3 : SWNT TEM grid fabricated using purified HiPco SWNT. (4.3(a)) and (4.3(b)) are low and high magnification images of a thin film produced by filtering 5 ml of 5 ppm wt% SWNT/chlorosulfonic acid solution on an anodisc filter (20 nm pore size, 47 mm diameter) (which yields an area coverage of 0.025 μg/mm^2). (4.3(c)) and (4.3(d)) are low and high magnification of a thin film obtained by filtering half the concentration of the initial solution. To have comparable filtration time, we have kept the amount of filter fluid constant. The produced thin films are large enough to be suspended on a transparent substrate and be characterized for transparency and sheet resistance. The scale bars are 500 and 100 nm for figure (4.3(a)) and (4.3(b)) respectively. Figure (4.3(c)) and (4.3(d)) were taken at the same magnification as 4.3(a) and 4.3(b) respectively. The images were acquired using JEOL 2010, operated at 100 kV.

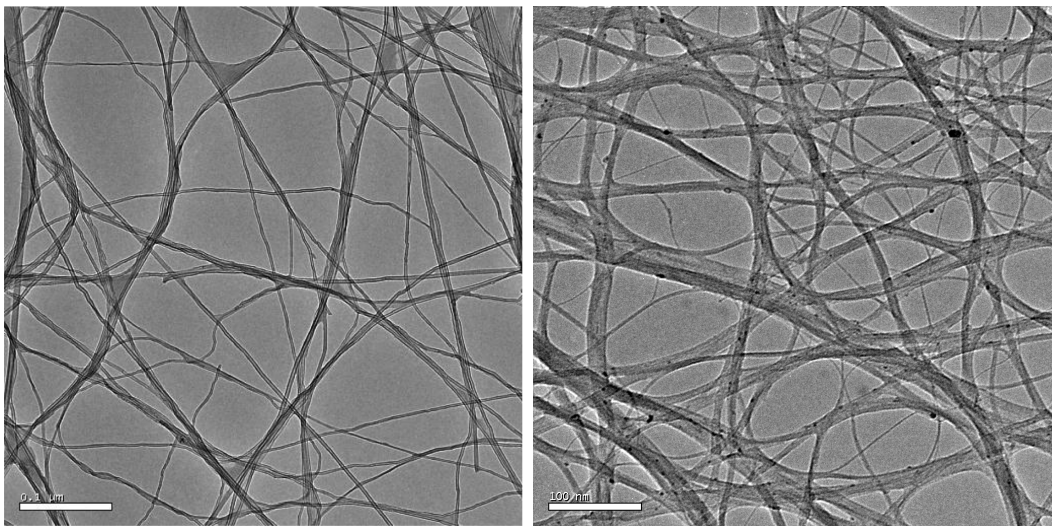

(a) (b)

Figure 4.4 : MWNTs TEM support (figure 4.4(a)) versus HiPco SWNT TEM support (Figure 4.4(b)). Note that SWNT thin films are characterized by few dark spots while MWNTs support are cleaner. This is a consequence of residual catalyst after in HiPco SWNT left after the purification process, while CVD grown MWNTs carpet have lower catalyst content (thus they have better performance as TEM support). Also, HiPco SWNTs create a network of 10–50 nm bundles (lowering the effective surface network surface) while MWNTs carpets create a network of un-bundles CNTs)

comparable to their diameter for optimal atomic resolution. Graphene flakes are even more challenging because carbon has a low atomic number (the same as the support thin film when using amorphous carbon support) and sub–nanometer thickness. The CNT network has high surface area (see also Fig. 4.2(c)) and provides sites where nanoparticles adhere to but do not overlap with CNTs, offering ideal conditions to gain maximum contrast. We compared the performance of CNT support to state of the art lacy carbon grid support[†] under identical TEM operating conditions (same instrument, voltage, exposure time and electron density) (Fig. 4.5).

Ultra thin lacy carbon (Fig. 4.5 a-c) yields noisier images compared to CNT films (Fig. 4.5 d-f) (see also Fig. 4.6). We quantified background noise of two different supports by the ratio of the intensity standard devia-tion to the average intensity. We measured 0.1 and 0.5 for CNT and lacy carbon support respectively, indicating that lacy carbon background noise is higher than CNT supports. In fact, the lattice fringes are clearly distinguishable in the magnified image on CNT support (Fig. 4.5 f), whereas the signal-to-noise ratio is markedly poorer in the image acquired on lacy carbon support (Fig. 4.5 e). Even metal oxide nanoparticles overlapping with the CNT support yield clearer images than those on amorphous carbon (not shown here). This is not surprising because the thinnest amorphous carbon exceeds 3 nm (ten or more layers of carbon), whereas few layer CNTs (2 to 4 walls) have lower effective thickness. Imaging graphene flakes dissolved in super acid was particularly challenging. Such imaging is essential for sample–size characterization as well as the number of layers composing each flakes [Behabtu et al., 2010] . The lacy carbon support is destroyed and the acid corrodes the copper grid during standard sample preparation (dip coating or drop drying) (Fig. 4.7).

[†]http://www.tedpella.com/supflm_html/suptfilm.htm

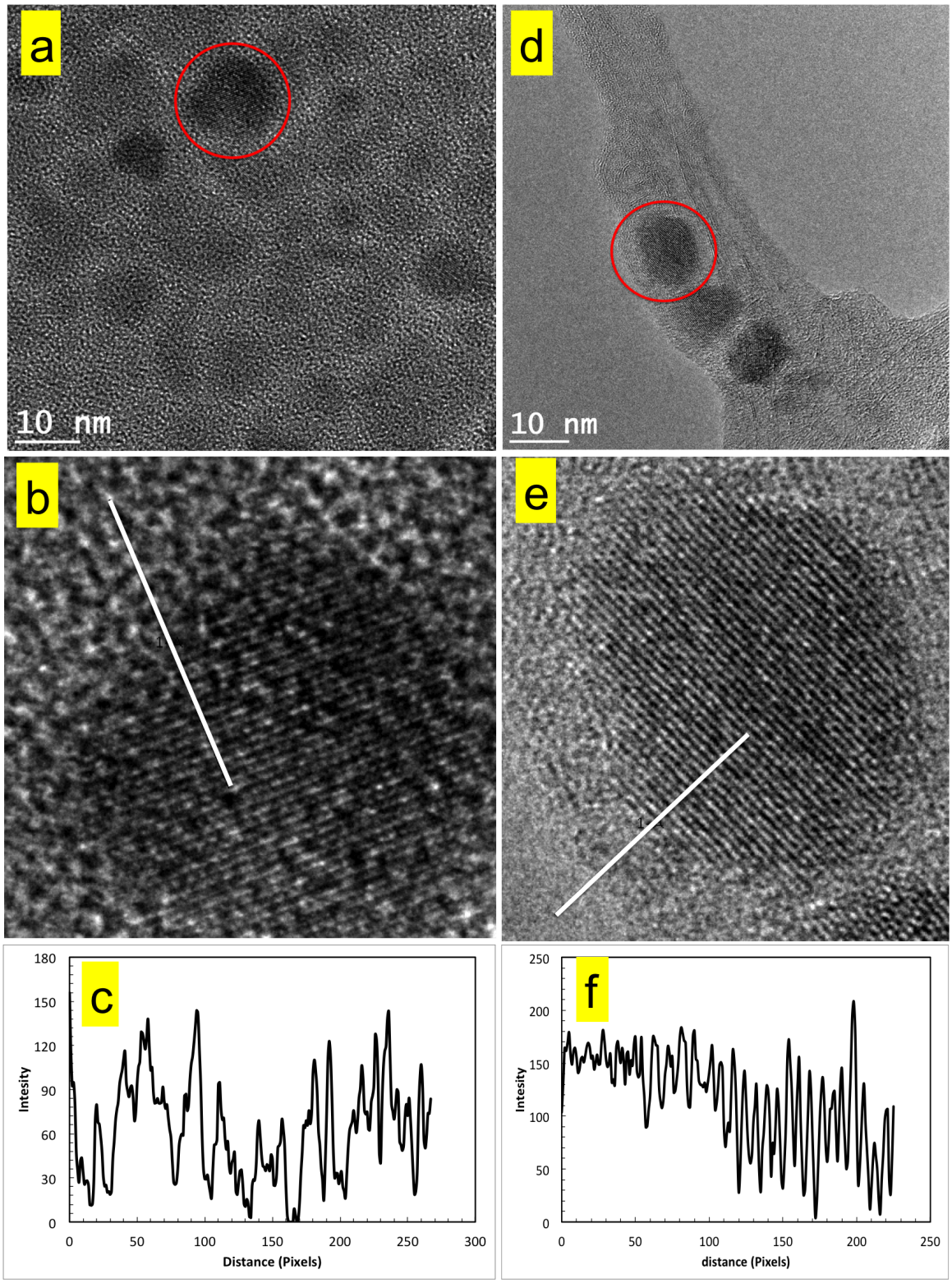

Figure 4.5 : TEM images of FeCu oxide nanoparticles comparing imaging from ultrathin carbon (a-b) support and CNTs support (d-e). Figure C and F show the intensity profile along the white line of figure b and e. All the images were acquired using the JEOL 2100 FETEM operated at 200 kV. The images were acquired with current density of 40 pA/cm2 and one second exposure time.

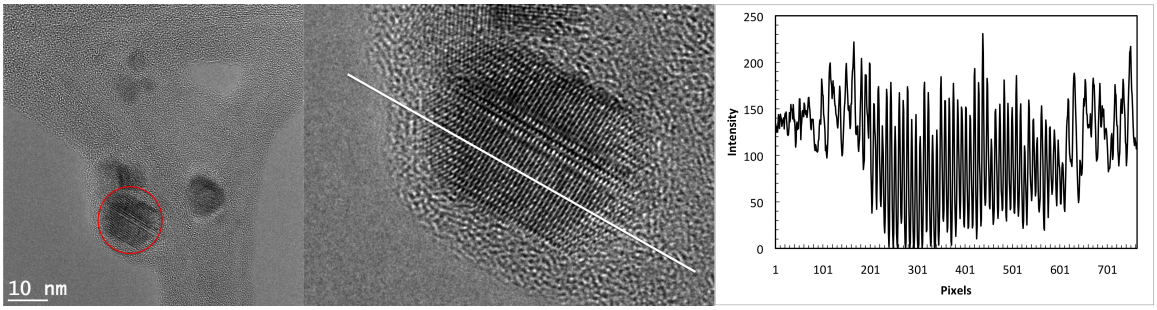

(a)

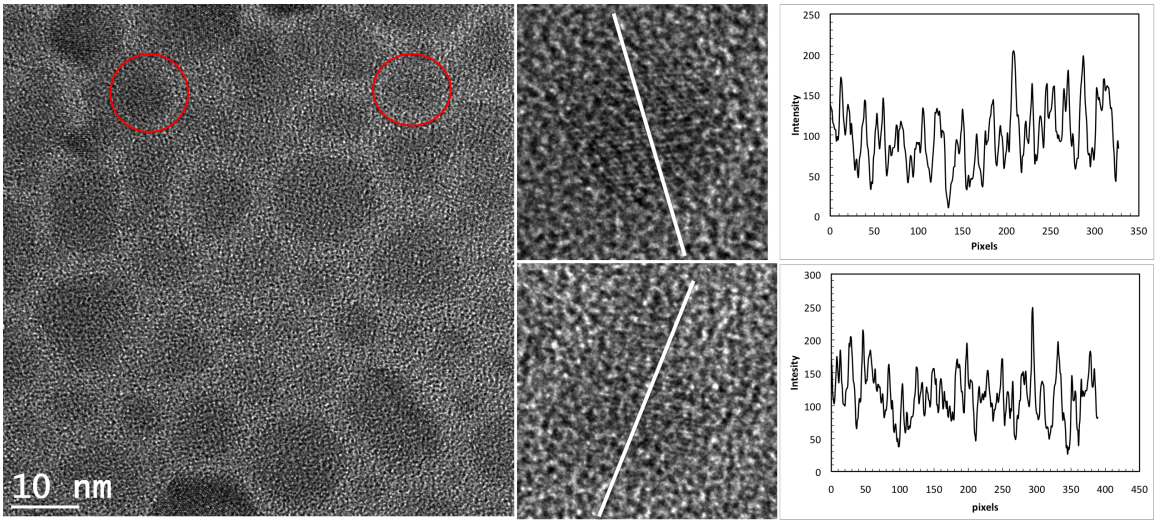

(b)

Figure 4.6 : FeCu nanoparticles on CNT thin films vs. lacy carbon substrate. Figure 4.6(a) shows FeCu nanoparticles on CNT substrate. The intensity profile is plotted along the white line showing a high contrast of the specimen image with respect to the background. Figure 4.6(b) shows FeCu nanoparticles on lacy carbon. This image was acquired under the same condition as figure 4.6(a) and figure 4.5. The intensity profiles are plotted along the white lines showing a low contrast of the specimen image with respect to the background.

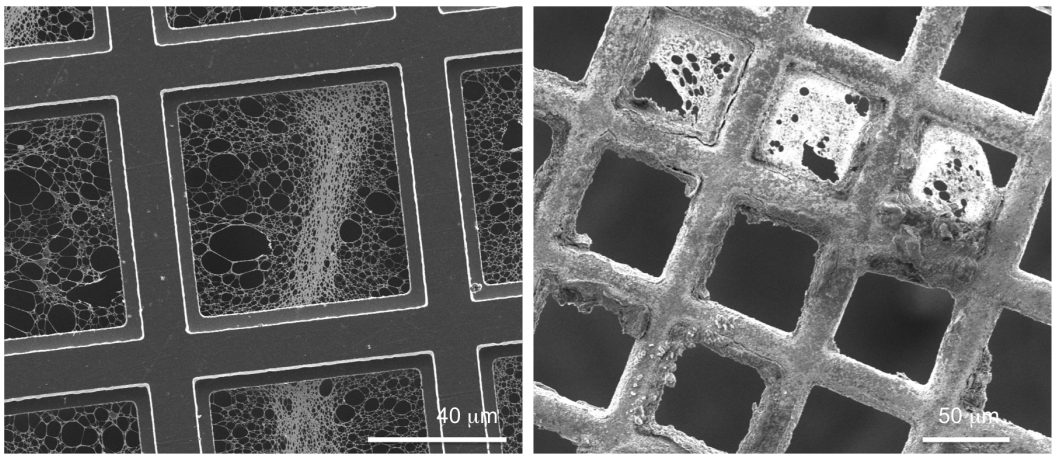

(a) (b)

Figure 4.7 : Figure 4.7(a) is a pristine TEM grid with lacy carbon support. When a drop of chlorosulfonic acid is filtered through and quenched by chloroform, the grid is completely compromised, making imaging impossible (Fig. 4.7(b)).

Moreover, drop drying can cause graphene flakes reaggregation prior to sample fixation on the supporting substrate (similar artifacts can occur during the drop drying of nanoparticle suspensions). We avoided aggregation by forming the CNT support and depositing the graphene flakes by vacuum filtering sequentially the CNT and the graphene solutions prior to fixation with chloroform and flotation of the film, thereby avoiding drying–induced aggregation and preventing exposure of the TEM copper grid to acids. Sample preparation by sequential filtration of the CNT support and suspended specimen can be useful also when the specimen suspension liquid has high boiling point, particularly if heating can compromise the specimen.

Figure 4.8 shows low and high magnification TEM image of graphene flakes. Because of low mass thickness contrast, graphene flakes are hard to identify. This task becomes easier on CNT substrates since large portions of the flake are freely suspended with no substrate beneath (Fig. 4.8(a)). High–resolution images are also

easily attained and the number of flakes can be readily identified if there are folded areas (Fig. 4.8(b)). CNT substrates are also beneficial to SEM imaging. In fact, this supports reduces the interaction volume from which secondary electron are generated. SEM images have better contrast compared to TEM (Fig. 4.8(c) and 4.8(d)). Thus, SEM can be used to measure directly graphene flake size (Fig. 4.8(e)). Although we were able to form unsupported (by CNTs) graphene thin films by filtering directly the graphene solution onto the alumina filter, only films with transparency below 80%, (∼9 layers of graphene [Nair et al., 2008], 3 nm thickness) had sufficient mechanical stability to survive the water–based transfer process–thinner films ruptured. Thinner, yet robust films may be obtainable by using larger flakes [Behabtu et al., 2010].

The CNT supports are stable at 400 °C in an atmosphere of equimolar Ar/H2 (Fig. 4.9 a). We examine the effect of heat treatment on the size of FeCo oxide nanoparticles. The initial distribution of particles below 10 nm coarsened to yield larger particles, including some elongated ones. Particle mobility and Ostwald ripening [Amama et al., 2009, Borjesson and Bolton, 2011] are the main mechanisms for particle coarsening. Although similar effects are observed with lacy carbon support (Fig. 4.9 b), the extent of coarsening is more pronounced on CNT grids. The observed variations may be due to different substrate crystallinity, as previously observed on graphite vs. amorphous carbon [Egelhoff and Tibbetts, 1979] as well as CNT dimensionality. In fact, CNT grids are a network of one–dimensional, crystalline paths in contrast to two–dimensional amorphous carbon. Although a detailed analysis of nanoparticle coarsening phenomenon is beyond the scope of this article, the observed coarsening highlights the potential of the CNT supports to study diffusion dynamics and sintering at temperatures below the Tammann temperature [Moulijn et al., 2001] under various gaseous environments [Thomas and Walker, 1964].

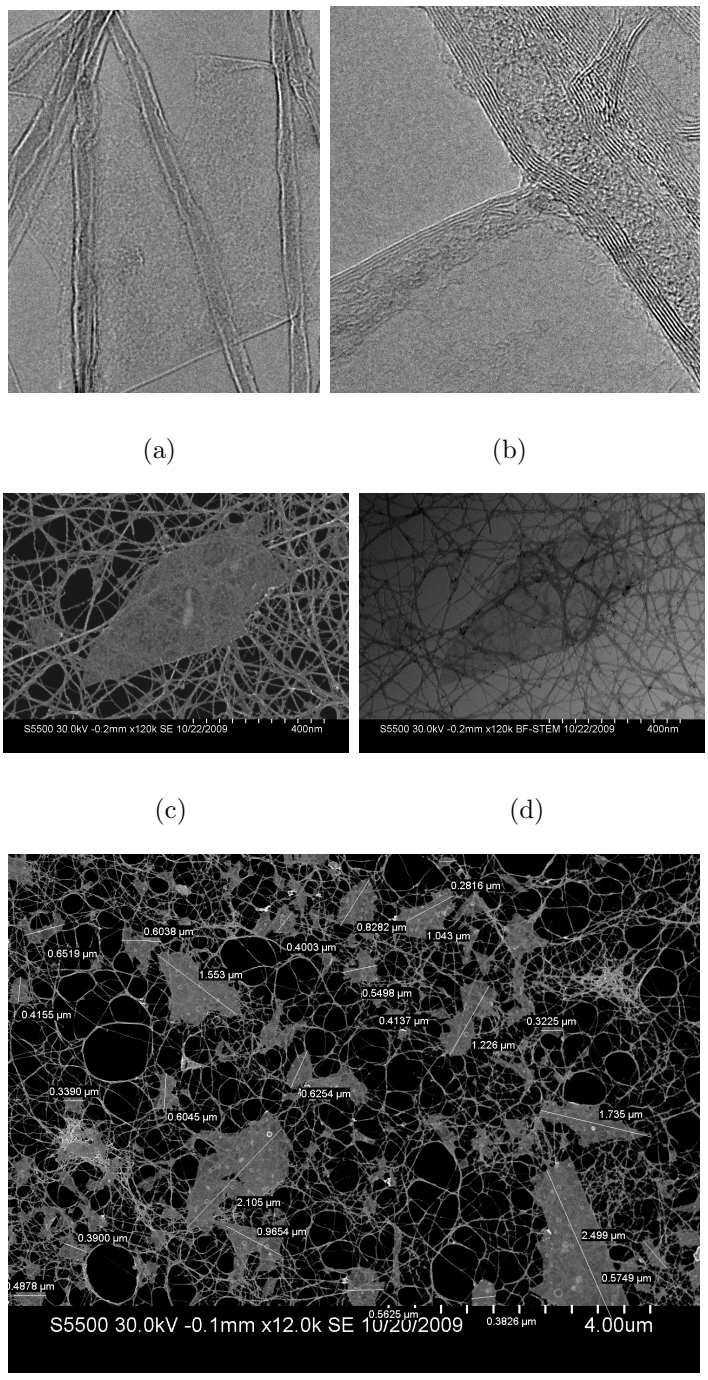

(a) (b)

(c) (d)

(e)

Figure 4.8 : (4.8(a)) low magnification image of a graphene flake suspended on a MWNTs thin films. (4.8(b)) High magnification of the fold (top left of the low magnification image). Images were acquired using the JEOL 2100 FETEM operated at 200 kV. 4.8(c)-4.8(d) are images of the same flake visualized using secondary electron and scanning transmission electron microscopy modes, respectively (Hitachi S-5500 operated at 30 KV). Note how the flake is clearly visible using secondary electrons. 4.8(e)) Low magnification view of a larger area of graphene flakes. The image was used to assess the later size distribution of the graphene flakes.

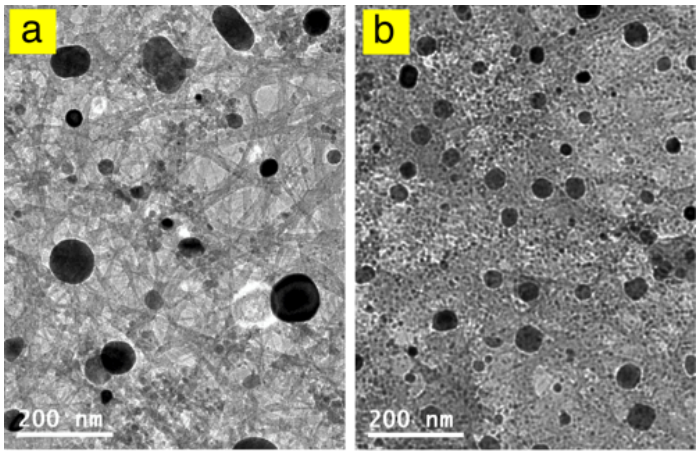

Figure 4.9 : TEM images of FeCo oxide nanoparticles after exposure to Hydrogen and Argon at 400 C. CNT thin film substrate (a) yield greater coarsening as compared to standard amorphous carbon susbtrate (b).

These coarsening phenomena are relevant to a diverse field of research ranging from studying catalyst for CNT growth [Amama et al., 2009] and amplification [Orbaek et al., 2011, Smalley et al., 2006, Crouse et al., 2008] fuel cells and batteries [Reddy et al., 2010] and Hydrogen production from biofuels [Seelam et al., 2010]. With our sample preparation technique, the graphitic material relevant to the specific application can be directly manufactured as the supporting grid, avoiding the need to transfer on to a TEM support. This allows, for example, visualization of relevant dynamics or recursive investigations to determine long term, or cumulative effects.

4.4 Conclusions

In conclusion, we have demonstrated a facile route to fabricate a new class of supports for TEM analysis using CNT solution processing. Pristine CNTs yield a mechanically stable, electrically conducting support with superior performance in high resolution imaging when compared to state of the art lacy carbon grid. CNT chemical inertness

allows sample preparation from reactive solvents as well as high boiling point fluids. The thermal stability and structure of the CNT grids also allows studying the coarsening dynamics of supported nanoparticles under various thermal and environmental conditions.

Chapter 5

Carbon Nanotube Liquid Crystals: Nematic Droplets and Coarsening Dynamics

5.1 Introduction

Understanding the liquid crystalline phase represents an essential step in the rational design of carbon nanotube (CNT) fluid–phase processing. Fiber spinning dopes, as well as film making fluids, are fully or partially liquid crystalline. On a fundamental basis, CNTs are new model–molecules to explore various aspects of rigid–rod theories [Green et al., 2009b, Fakhri et al., 2010, Puech et al., 2010]. Biological model systems such as Tobacco Mosaic Virus (TMV), bacteriophage *fd* and actin filaments are often used to study the behavior of rigid–rod systems [Dogic and Fraden, 2006]. CNTs offer additional advantages because of their intrinsic fluorescence [O'Connell et al., 2002], tunable stiffness [Fakhri et al., 2009], chemical, thermal and mechanical stability [Baughman, 2000] unmet in biological specimens. Moreover, these molecules can be synthesized with aspect ratios that are orders of magnitude higher than biological specimens.

A number of studies have reported CNT nematic phases [Song and Windle, 2005, 2008, Puech et al., 2010, Davis et al., 2004, 2009, Badaire et al., 2005]. Often CNT liquid crystalline behavior is described as novel, unique, or unusual. Sometimes the uniqueness is attributed to their large persistence length [Song and Windle, 2008] and aspect ratios, or polydispersity, other times to attractive forces [Davis, 2011,

Murali et al., 2010]. Unexpectedly, a low order parameter is also measured. This is surprising since CNTs' large aspect ratios should yield high order. The low order of the liquid phase persists also in the final solid structure [Zamora-Ledezma et al., 2008, Dan et al., 2011].

CNTs' liquid crystallinity is often only probed through their anisotropic optical properties (birefringence). However, birefringence probes the crystalline nature of liquid crystals. Thus, while necessary, birifrengence is not a sufficient condition to prove liquid crystallinity. Showing the liquid–like nature of liquid crystals is particularly important when the liquid crystals consist of large, anisotropic molecules. In fact, large size could hinder mobility and enhance the interaction per unit length, increasing the total interaction between two molecules. Thus, percolating networks and gels can be the dominating structures instead of liquids [Vigolo et al., 2005, Solomon and Spicer, 2010].

In light of the previous considerations, this chapter aims at addressing two main issues:

1. Do CNT liquid crystals show expected (as opposed to novel) structures that arise from free energy minimization?

2. Are CNT liquid crystals "liquid"? Can their dynamics be rationalized within an existing theoretical framework?

We will address these issues by considering the equilibrium shape of nematic droplets and their coarsening dynamics.

5.2 Background on Liquid Crystals and Nematic Droplets

5.2.1 Frank Elasticity and Surface Tension

A nematic phase is an ordered liquid with long range directional order of anisotropic molecules. Molecules are free to flow and the position of their centers of mass are randomly distributed as in a liquid. A dimensionless unit vector describes the direction of alignment. This vector is called the nematic director, and it is indicated by **n** where **n** and -**n** are equivalent. In an unbounded fluid and in absence of kinetic considerations, molecules try to order themselves in such a way that the director is uniform over the whole fluid. However, such uniform arrangement may conflict with conditions at boundaries or may be frustrated by slow dynamics after nonequilibrium processes, e.g., mixing. Hence, spatial variations of the director field can arise, and these are called distortions. Distortions of the director field generate an elastic response and increase the free energy of the system. The elastic free energy of a liquid crystalline phase is [Frank, 1958, Nehring and Saupe, 1971]:

$$F_E = \int_v d^3r \left[\frac{1}{2}K_1(\nabla \cdot \mathbf{n})^2 + \frac{1}{2}K_2(\mathbf{n} \cdot \nabla \times \mathbf{n})^2 \right. \tag{5.1}$$

$$\left. + \frac{1}{2}K_3[\mathbf{n} \times (\nabla \times \mathbf{n})]^2 - K_{24}\nabla \cdot [\mathbf{n}\nabla \cdot \mathbf{n} + \mathbf{n} \times (\nabla \times \mathbf{n})] \right]$$

where the integration is over volume V and the elastic constants K_1, K_2, and K_3, refer to the splay, twist, and bend deformation modes of a bulk nematic. K_{24} refers to saddle-splay deformation mode. The volume integral of this term is usually ignored in studies of bulk nematics because it can be transformed into a surface integral [Prinsen and van der Schoot, 2003]. A topological defect is a configuration of the order param-

eter that cannot be transformed continuously into a uniform state; both bulk (3D) point defects and surface (2D) singular points, called boojums* can be encountered.

Defects can be classified through their topological charge N. The topological charge of a point defect in 3 (Eq. 5.2) and 2 (Eq. 5.3) dimensions are [Lavrentovich, 1998]:

$$N^{(3D)} = \frac{1}{4\pi}\oint\left[\frac{\partial\theta}{\partial u}\frac{\partial\varphi}{\partial\nu} - \frac{\partial\theta}{\partial\nu}\frac{\partial\varphi}{\partial u}\right] sin\theta du d\nu \tag{5.2}$$

$$N^{(2D)} = \frac{1}{2\pi}\oint\left[n_1\frac{dn_2}{dl} - n_2\frac{dn_1}{dl}\right] dl \tag{5.3}$$

where the vector field is parameterized as $\mathbf{n}(u,\nu)$= (sin θ cos φ; sin θ sin φ; cos θ), with both the polar (θ) and the azimuthal (φ) angles being functions of the coordinates u and ν specified on a sphere surrounding the defect. l is the natural parameter defined along the loop enclosing a two dimensional point defect and n_1 and n_2 are the 2D components of the two dimensional vector $\mathbf{n}$.

The *Poincaré* and *Gauss theorems* regulated the total charge that a vector field have in a closed surface and in a given volume [Lavrentovich, 1998]. The conservation of the total topological charge is an important concept in understanding dynamics of liquid crystalline phase. This implies that a given charge cannot be generated without concurrently generating a charge of the opposite sign, so that the total topological

*Mermin called the singularity point *boojum*, inspired by Lewis Carroll′s The Hunting of the Snark. In the poem, anyone encountering the imaginary creature *boojum*, softly and suddenly vanished away. Similarly, point defects vanish from bulk phases into surface boojums [Lavrentovich, 1998].

charge of the system is conserved. Also, topological charges with opposite signs (and same magnitude) can annihilate.

Another important quantity to define when dealing with nematic droplets is the total interfacial free energy. The following functional form describes the total surface free energy [Prinsen and van der Schoot, 2003, Rapini and Papoular, 1969]:

$$F_S = \tau \int_A d^2\mathbf{r}[1 + \omega(\mathbf{q} \cdot \mathbf{n})^2] \tag{5.4}$$

where $\mathbf{q}$ is the surface normal to the position $\mathbf{r}$, τ is the interfacial tension and ω is a dimensionless anchoring strength. Surface free energy is minimized when $\mathbf{q}$ is orthogonal to $\mathbf{n}$ (tangential anchoring condition). The dimensional anchoring strength ω influences the specific alignment of the constitutive molecules along the surface. When ω is large, there is a large free energy penalty to violating tangential anchoring conditions.

5.2.2 Shape of Nematic Droplets: Theoretical Considerations

The shape of nematic droplets stems from the interplay of surface tension τ, Frank elasticity K, and anchoring strength ω. Spherical shapes minimize the surface of a given volume and hence minimize surface tension; however, spherical shapes also require large distortion of the nematic director, increasing droplet free energy.

Thus, when elasticity is significant, the equilibrium shape is elongated into a spindle-shaped droplet, commonly referred to as tactoid. Prinsen *et al.* have theoretically investigated the underlying scaling laws and relevant dimensionless numbers that stem from the interplay of elasticity, surface anchoring, and surface tension [Prinsen and van der Schoot, 2003, 2004a,b]. Specifically, two types of tactoids can be

encountered: bipolar, with tangential anchoring and distorted nematic director, and homogeneous, with no director distortion but oblique anchoring (Fig. 5.1).

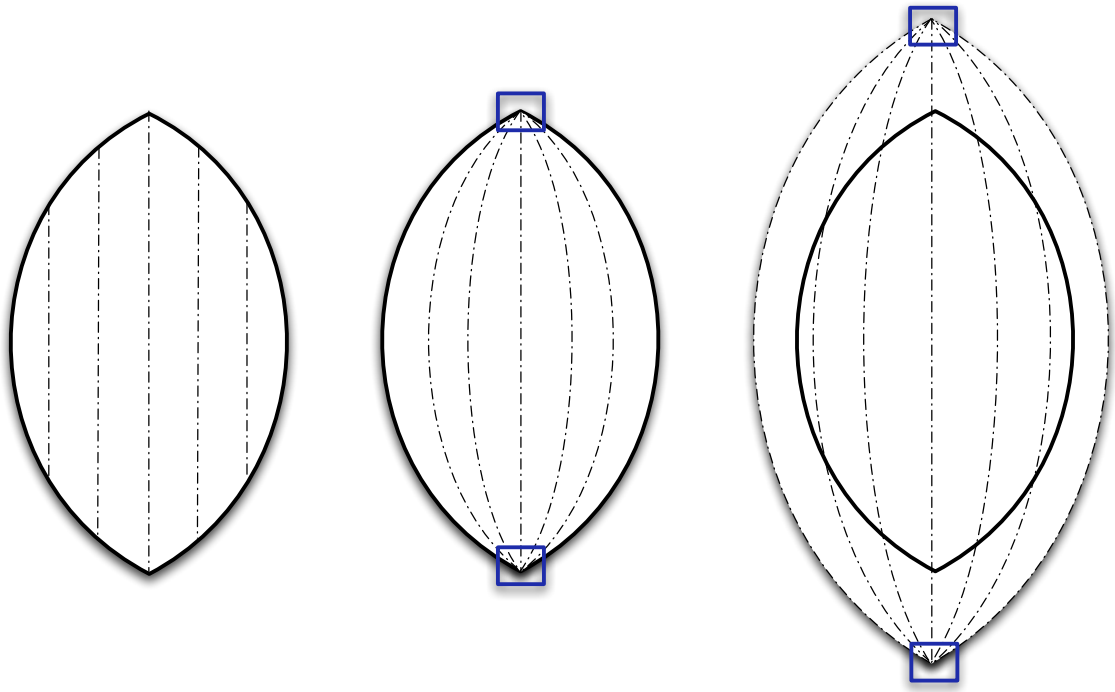

Figure 5.1 : Schematic showing homogeneous, bipolar, and quasi bipolar nematic droplet. Quasi bipolar droplets are characterized by virtual boojums that are detached from the droplet surface. Blue squares indicate real and virtual boojms. The dash-dotted lines indicate the nematic director field while the solid line indicates droplet interface.

Two potential mechanisms can be identified for the transition from homogeneous to bipolar tactoids. The first one is a sharp transition from tangential anchoring to a homogeneous director field [Prinsen and van der Schoot, 2003]. The second is a continuous director–field transformation, with virtual boojums (Fig. 5.1) that continuously change their relative distance to infinity [Prinsen and van der Schoot, 2004a]. In the first case, homogeneous droplets are expected to have size-independent aspect ratios, and the aspect ratio to be a function of a dimensionless anchoring

strength (Eq. 5.5):

$$\frac{R}{r} \approx \kappa^{3/5} \tag{5.5}$$

$$\frac{R}{r} \approx \omega^{1/2}, \tag{5.6}$$

where R and r are tactoid long and short axis lengths, R/r is droplet aspect ratio, while κ is a dimensionless elasticity parameter defined as:

$$\kappa = \frac{K}{\tau V_d^{1/3}}, \tag{5.7}$$

where K is an average Frank elasticity and V_d is the droplet volume.

For continuous transformation from homogeneous to bipolar tactoids, the limiting homogeneous aspect ratio is expected to be $R/r = 2\sqrt{\omega}$, while in the bipolar regime the aspect ratio has a complex dependence on the dimensionless elasticity [Prinsen and van der Schoot, 2004a]. The crossover between homogeneous and bipolar droplets can be estimated as follows [Prinsen and van der Schoot, 2003, 2004a]:

$$V_d \approx \left(\frac{K}{\tau}\right)^3 \left(\frac{1}{\omega}\right)^{\alpha}. \tag{5.8}$$

For large dimensionless anchoring strength and virtual boojums α=5/2 [Prinsen and van der Schoot, 2004a]. When virtual boojums are not considered, α=18/5 [Prinsen and van der Schoot, 2003]. Thus, a combination of large Frank elasticity, low surface tension, and low anchoring strength is required to generate large homogeneous, observable droplets. The ratio of elasticity to surface tension (K/τ) is also known as extrapolation length and is proportional to the critical droplet size at the homogeneous to bipolar transition [Verhoeff et al., 2011, de Gennes, 1974]. Using rigid–rod

theories based on Onsager formalism, elasticity and surface tension can be estimated as [Straley, 1973, van der Schoot, 1999, Koch and Harlen, 1999]:

$$K_i = \beta_i \rho^2 L^4 D k T \tag{5.9}$$

$$\tau \sim kT/(DL) \tag{5.10}$$

where K_i is the Frank elastic constant and index $i = 1, 2, 3$ corresponds to splay, twist, and bend distortions, respectively. ρ is the number concentration of the liquid crystalline phase, L and D are length and diameter of the constitutive rod, k is the Boltzmann constant and T is the temperature of the system. The dimensionless pre-factors β_i are 0.065, 0.022 and 0.44 for splay, twist and bend distortions, respectively [Straley, 1973]. The density $\rho = \phi_N / \mathrm{V}_{rod}$ of nematic droplets formed in a biphasic region can be estimated from Onsager theory (ϕ_N= 4.49 D/L) [Onsager, 1949], with V_{rod} the volume of a rod and ϕ_N the volume fraction at the biphasic to nematic transition. Thus, the extrapolation length for rigid rod molecules is:

$$\frac{K}{\tau} \sim L \tag{5.11}$$

Considering the inverse proportionality (Eq. 5.8) of crossover size with surface anchoring ω (where $\omega \gg 1$ for elongated nematic droplet [Prinsen and van der Schoot, 2004a]), the transition from a bipolar to a homogeneous tactoid is expected at length scales smaller than the rod length. Thus, a homogeneous to bipolar transition should not be expected based on macroscopic approximation. However, the macroscopic approximation might break down for small drops where the drop size is comparable to rod length. In fact, computer simulations indicate that homogeneous to bipolar transition should still hold [Trukhina et al., 2009] and the transition should occur

when the droplets size becomes comparable to the constitutive rod length. Thus, for the transition to be observable under a light microscope (micron scale resolution) the constitutive molecules should have length of few microns of longer.

5.2.3 Shape of Nematic Droplets: Experimental Observations

Experimental observation of tactoids dates back to early 20th century [Zocher, 1925, Bernal and Fankuchen, 1941a,b]; they have been observed in a number of experimental systems since then [Dogic, 2003, Oakes et al., 2007, Verhoeff et al., 2011, Kaznacheev et al., 2002]. However, the experimental observations do not show the expected bipolar to homogeneous transition (Fig. 5.2). The only system that shows homogeneous droplets of rod–like systems are surfactant stabilized SWNT droplets [Puech et al., 2010]. Yet, even this system fails to show the expected transition to bipolar droplets for the range of sizes considered. Thus, there is a need for an experimental system able to experimentally probe this transition. As highlighted in the previous subsection, such a system has to be characterized by molecules that are several microns in length.

5.2.4 Nematic Droplets: Merging Dynamics

The structural stability of macroscopic droplets is kinetic, and not thermodynamic, where the true thermodynamic minimum is achieved by full coalescence of all droplets in one phase. The driving force for two droplets to merge is minimization of surface energy. However, liquid crystalline droplets need to balance additional contributions coming from elastic energy and topological defects. Conservation of topological charges is a requirement unique to nematic droplets compared to isotropic droplets, and dominates the stability and dynamics of nematic liquid crystals [Lavrentovich,

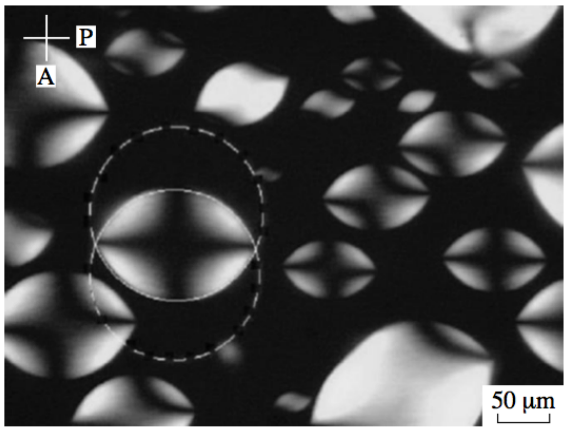

(a)

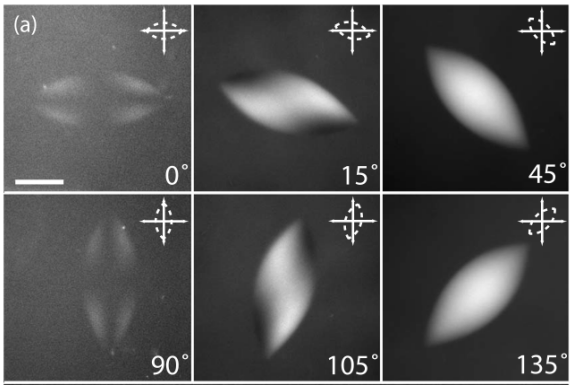

(b)

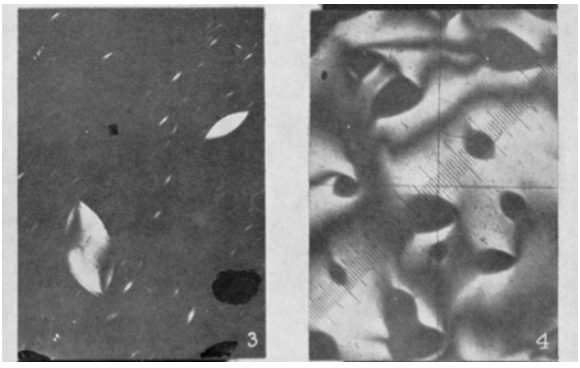

(c)

Figure 5.2 : Overview of tactoids optical texture from the literature. Figure 5.2(a) shows vanadium pentoxide (V2O5) nematic droplets (figure reproduced from [Kaznacheev et al., 2002]). Figure 5.2(b) shows nematic droplets from actin filaments. Figure scale bar is 25 μm (figure reproduced from [Oakes et al., 2007]. Figure 5.2(c) shows TMV droplets. On the left negative tactoids (isotropic droplets in a continuum of liquid crystal) can be seen (Figure reproduced from [Bernal and Fankuchen, 1941a]).

1998, Poulin and Weitz, 1998, Lubensky et al., 1998].

For example, when two nematic droplets with normal anchoring boundaries with topological charge N=1 merge, a defect with point charge N=-1 must be created to obtain a final droplet with N=1 charge [Terentjev, 1995]. For bipolar tactoids merging (Fig. 5.3), the total topological charge for the two droplets has to decrease from four to two (Fig. 5.3(a)). This, in turn, requires nucleation of two negative boojums (Fig 5.3(b)) to annihilate the extra positive boojum.

Defect nucleation represents a formidable energy barrier ($\delta \sim KR$) hindering further coarsening of nematic droplets. As a consequence, small droplets coalesce until a critical value $R^* \sim K/\tau\omega$ [Tixier et al., 2006].Thus, nematic droplets with topological charges should display a narrow monomodal distribution [Tixier et al., 2006].

5.2.5 Nematic Droplet: Capillary Break-up

The mechanism responsible for droplet size reduction is capillary break-up (see also Fig. 5.19). For isotropic materials, a cylindrical fluid filament is unstable to capillary-driven shape perturbations that break the filament into spherical drops. The fluid break-up is known as the Plateau–Rayleigh instability. In the case of nematic fluid, the classical theory needs to be modified to capture gradient elasticity and anchoring energy. The dominant breaking mechanism depends on the dimensionless number $p = 2a\tau/K$ [Rey, 2007], where a is the fluid filament radius. For $p > 1$, elastic deformation dominates and the critical wavelength λ_c and growth rate of the fastest growing mode α_{max} are as follows [Cheong and Rey, 2004]:

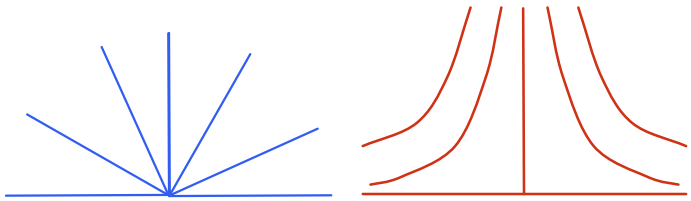

(a) (b)

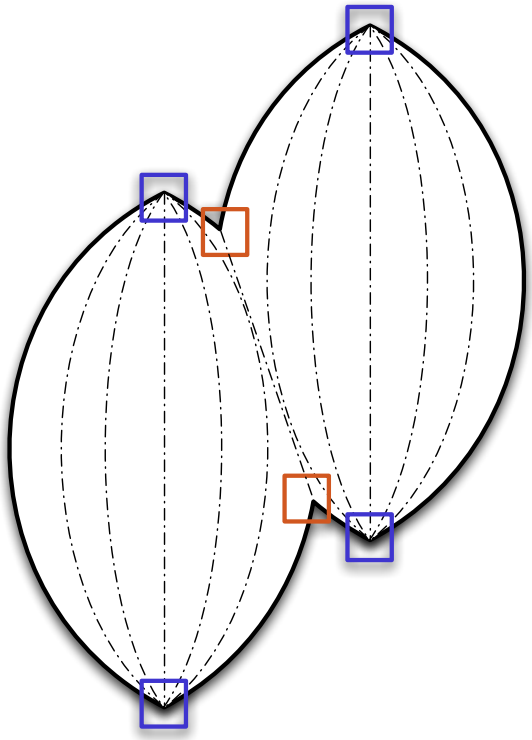

(c)

Figure 5.3 : Positive (Fig. 5.3(a)) and negative (Fig. 5.3(b)) boojums showing nematic director orientation. A schematic (Fig. 5.3(c)) of defect structure during merging of two droplets . The blue squares indicate positive boojums and the red square indicate the newly created negative boojums.

$$\lambda_c = 2\pi a\left(1+2\frac{K}{a\tau}\right)^{1/2} \tag{5.12}$$

$$\alpha_{max} = \frac{1}{2\sqrt{\rho_f a^3/\tau}}\left(\frac{1}{2(2\frac{K}{a\tau}+1)}\right)^{1/2}, \tag{5.13}$$

where ρ_f is the fluid filament mass density. For p<1, anchoring energy dominates and gradient elasticity does not play a role. Note that this is a breaking regime that will eventually occur during a breaking event. The critical growth rate in this case is [Rey, 1997] :

$$\alpha_{max} = \frac{1}{\sqrt{\frac{8a^3(1+2\omega)\rho}{\tau}}+\frac{a\eta}{\tau}}, \tag{5.14}$$

where η is an average viscosity. Under the limit of Onsager theory, the viscosity of a liquid crystalline fluid scales with the cube of rod aspect ratio [Lee and Meyer, 1986]. Thus, when the constitutive molecules have large aspect ratios, viscosity dominates the dynamics and the fastest growing mode can simplified as:

$$\alpha_{max} = \frac{\tau}{4a\eta} \tag{5.15}$$

Thus, capillary break-up is hindered by elasticity, surface anchoring, and viscosity. In fact, deformation of the fluid filament induced by surface instabilities increases the elastic free energy. This, in turn, hinders break-up. Even when break-up can occur, the time scale required for the evet ($\sim 1/\alpha_{max}$) is highly affected by anchoring strength, elasticity, and fluid viscosity (see Eq. 5.12, 5.14, and 5.15).

5.3 Literature Review on CNT Liquid Crystals

Given their stiffness and anisotropy, CNTs are expected to form liquid crystalline phases. The first reported CNT liquid crystalline phase dates back to 2003 [Song et al., 2003]. This and subsequent works from the same research group [Song and Windle, 2008, Li et al., 2006b, Song and Windle, 2005, Zhang et al., 2010b] reported birefringence and Schlieren texture as evidence of the liquid crystallinity of their system. However, the Schlieren texture persists as the solvent is fully evaporated, indicating that this feature can also be a characteristic of a solid sample. Also, as the sample transitions from an isotropic to a birefringent phase, the intermediate biphasic region does not show the expected tactoidal droplets typical of other systems (Fig. 5.4). Another feature that seems to be unique to CNT liquid crystals is the large topological defect density (and small birefringent domain size). Topological defects have an energy penality that is proportional to the Frank elasticity of liquid crystalline phases [Lavrentovich, 1998]. Since Frank Elasticity is a strong function of rod length (see Eq. 5.9), CNT liquid crystals should have high energy penalties associated with defect creation, hence, larger domain size.

Other groups have also reported CNT liquid crystallinity [Moulton et al., 2007, Badaire et al., 2005]. Even in these cases, liquid crystallinity is probed through birefringence. Surprisingly, when the liquid crystals are ordered through flow to yield a homogeneous nematic director, a very low order parameter (S) of about 0.1 and 0.15 was found. These values are much lower then the order parameter of rigid rods (S≈0.8) at the isotropic nematic transition, and order parameter of semiflexible chains (S≈0.46) [Zamora-Ledezma et al., 2008]. Interestingly, if longer tubes are removed from the system, a best value of S≈0.6 can be achieved [Puech et al., 2011]. The authors argue that the presence of wavy, branched CNTs is detrimental to liquid

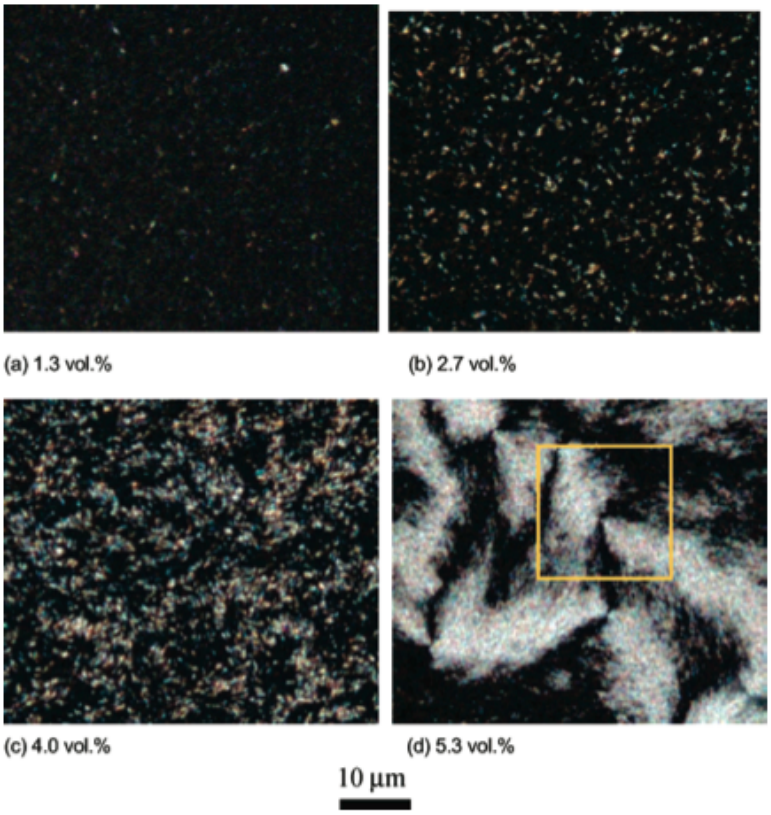

Figure 5.4 : Concentration dependent birefringence of oxidized MWNTs dispersed in water. Figure reproduced from [Song and Windle, 2005]

crystalline ordering since they act as disordering agents. Thus, extended sonication and ultracentrifugation (at least for 2 hours) are required for high order to be attained.

CNTs dissolved in superacids is another system expected to yield CNT liquid crystals [Davis et al., 2004, Ramesh et al., 2004, Rai et al., 2006, Parra-Vasquez et al., 2010, Davis et al., 2009]. Together with birefringence, the authors also use rheological signature to demonstrate liquid crystallinity of the system. In fact, similar to other lyotropic systems [Choe and Kim, 1981, Panar and Beste, 1977], a non-linear behavior of viscosity as a function of concentration is reported (Fig.5.5). However, the extent of viscosity change (ratio of the maximum to minimum) is much more pronounced on polymeric lyotropic liquid crystals. Another unique feature of CNTs in sulfuric acid is the shape of birefringent treads encountered in the biphasic region, termed "spaghetti". These are different from any nematic droplet seen in other rod–like systems (Fig. 5.6). Spaghetti-like nematic domains are observed also for silver nanowires [Murali et al., 2010]. The authors argue that the underlying physics for the spaghetti phase consists in their large persistence length and potentially attractive force.

Thus, despite the extensive work on CNT liquid crystalline phases, there is not yet a clear answer to the questions postulated at the beginning of this chapter. The large amount of topological defects [Song and Windle, 2005], low order parameter [Zamora-Ledezma et al., 2008], and unusual nematic strands in the biphasic region [Davis et al., 2004] are unexpected and justify the first postulated question:"Do carbon CNT liquid crystals show expected (as opposed to novel) structures that arise from free energy minimization?". The second question "Are CNT liquid crystals "liquid"? Can their dynamics be rationalized within existing theoretical framework" is also required since almost all the liquid crystalline evidence has been gathered by birefringence

measurements.

5.4 Experimental Details

Experimental conditions profoundly affect the formation and shape of nematic droplets. All the solution discussed in this chapter (if not noted otherwise) are made from pure chlorosulfonic acid (use as received from from the supplier). The next parameter is solution concentration. The main requirement is to attain concentrations in the biphasic region, where the isotropic phase is in equilibrium with the nematic one. There is a narrow window where isolated nematic droplets can be formed. For examples, in the case of HiPco SWNT (batch 188.3 as well as 187.5) the optimal concentration is 3500 ppm wt% (where 2000 ppm wt% yields an isotropic solution, while 4500 ppm wt% yields a concentrated solution of tactoids). When a liquid drop is confined between a glass slide and a cover slip, the reactivity of the solvent makes effective sealing difficult. Thus, samples are often compromised within an hour from sample preparation because of chemical reaction with surrounding environmental moisture. Also, the typical gap obtained ($\sim$10 microns or below) do not allow for growth of large droplets. Since most of the observed dynamics lasts for long times (from few hours to a day), (Fig. 5.7 and 5.7) an hour is not enough time for the system to equilibrate. We also noted that some of the novelties (for example the spahetti like, elongated structures observed in in chlorosulfonic acid) previously attributed to CNT liquid crystals stem from sample preparation conditions [Davis et al., 2009]. Also, despite good sample preparation, some solutions do not form tactoids. This is the case of long (L larger than 10 μm) CNT. Most probably this is due to the long time scale ($\sim$ months) required for an equilibrium shape to be attained.

The most effective way to prepare samples is by filling glass capillaries and flame

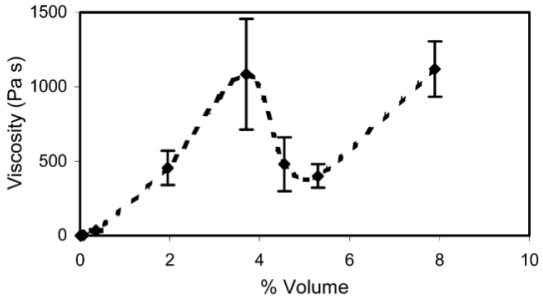

(a)

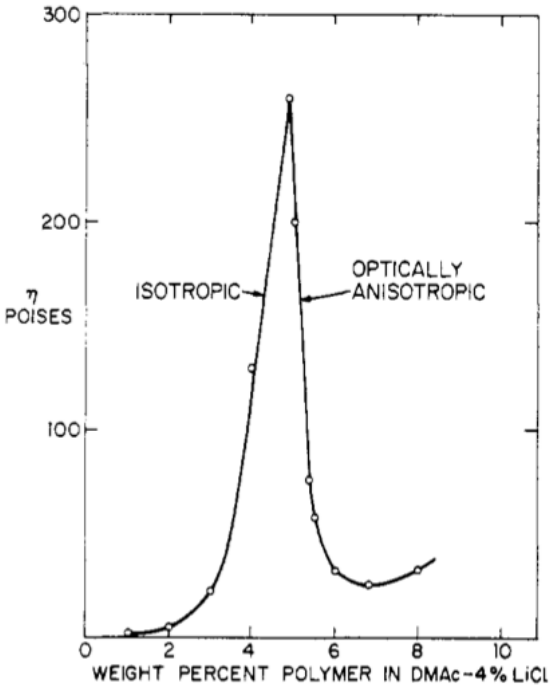

(b)

Figure 5.5 : Figure 5.5(a) shows the shear viscosity and concentration of SWNT in 102% sulfuric acid (Figure reproduced from [Davis et al., 2004]). Figure 5.5(b) shows shear viscosity data of poly(1,4-benzamide) in DMA (data reproduced from [Kwolek et al., 1977]).

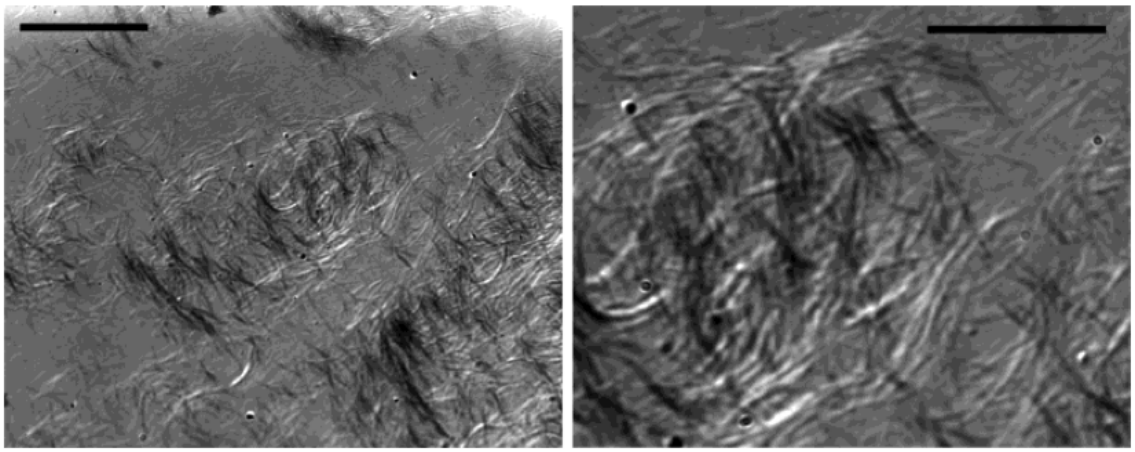

Figure 5.6 : Light micrograph of SWNT in 102% sulfuric acid under partial cross polars. The thread like structures are termed "spaghetti". Reproduced from [Davis et al., 2004]. Scale bar is 20 μm.

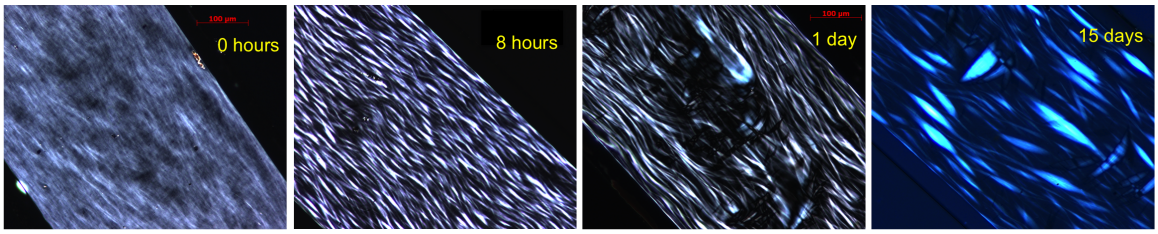

Figure 5.7 : Light micrograph under cross polars. Sample was prepared from 5000 ppm of CCNI DWNTs (batch 1001) by filling a 50 μm thick capillary.

sealing them. Good samples can last for days without being compromised. The size of the capillary limits the maximum observable droplet. When an equilibrium shape needs to be measured, the minimum requirement must be for the drop to be symmetric. Identification of droplets out of equilibrium is relatively easy when they lack symmetry (Fig. 5.8).

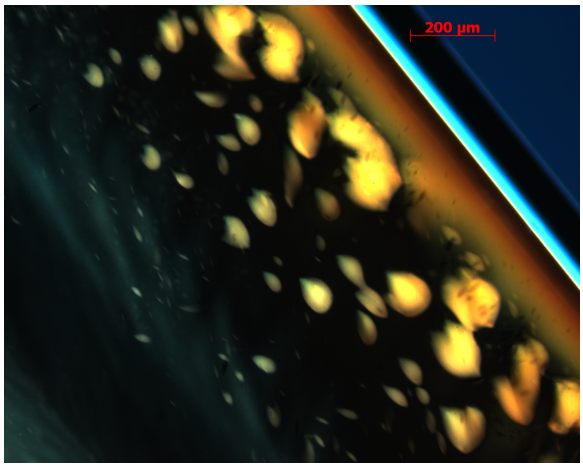

(a)

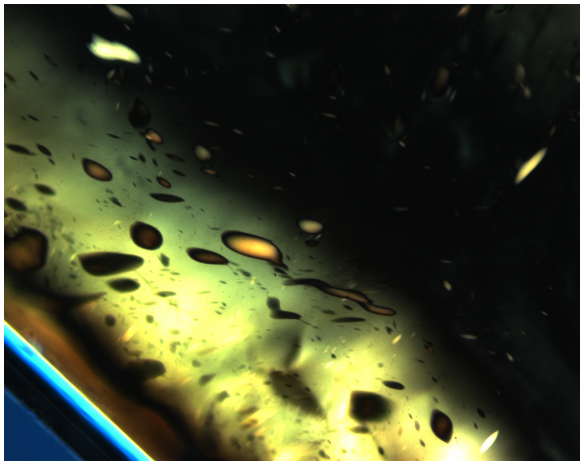

(b)

Figure 5.8 : Non-symmetric droplets.

Other times, symmetric deformation can occur. Two merging drops can look

symmetric but the equilibrium aspect ratio may not yet be attained (Fig. 5.9).

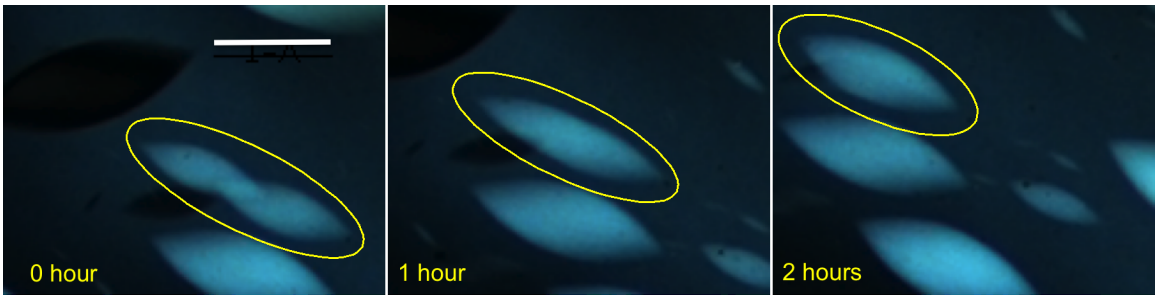

Figure 5.9 : Symmetry of merging droplets. Th merging event is circled in yellow in the three different light micrographs. Scale bar is 50 μm

Flow is also a major parameter influencing droplet shape and measured aspect ratio (Fig. 5.10). Flow can be induced within a capillary by various means. In a large capillary, gravity can induce flow while temperature and/or concentration gradients can induce flow in small capillaries. Droplets can stretch by almost an order of magnitude without breaking. Thus, flow is the parameter that affects accuracy in droplet size measurements the most.

Another source of systematic error is droplet contour measurement. In fact, when droplets are imaged at their brightest configuration (when the droplets are oriented parallel or perpendicular to the polarizer), their tips are darkened. This will induce a 10% error while measuring the long axis of the droplet (Fig 5.11). Figure 5.11 also shows how droplet size is quantified. We used the *Analyze Particle* option of ImageJ (http://rsbweb.nih.gov/ij/) to fit an ellipsoid to a given droplet. This technique has the disadvantage of overestimating the area of the droplet but it can accurately estimate the axis of the droplet. An added error source is image threshold evaluation. This could induce appreciable error particularly for low contrast images. Thus, in order to mitigate threshold related error, images for size measurement should be

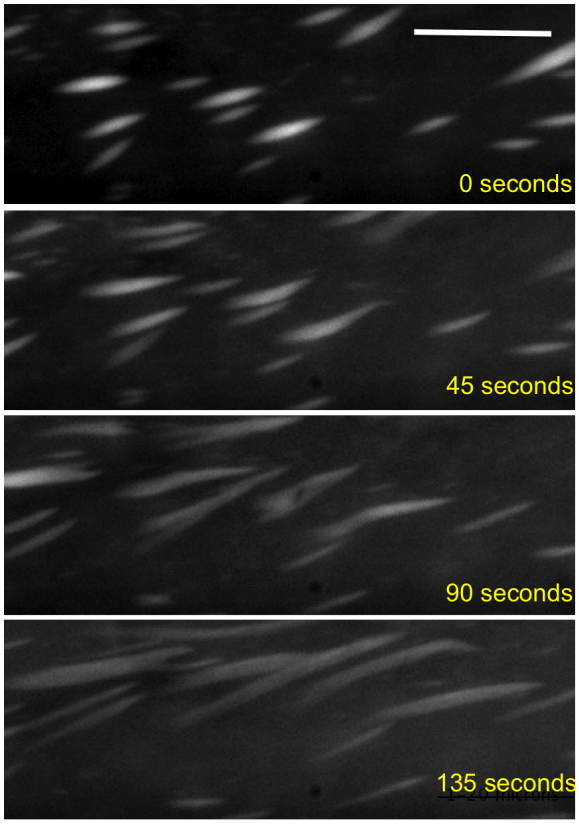

Figure 5.10 : Evolution of droplet shape as sudden flow occurs. Note the large distortion that the droplets undergo. The sample was prepared from Hipco SWNT batch 187.5 3500 ppm wt%. Scale bar is 20 μm.

overexposed to sharpen the droplet edge.

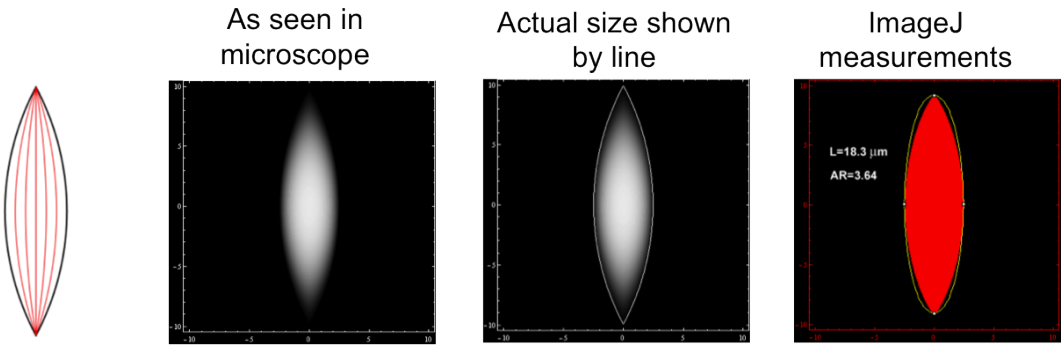

Figure 5.11 : Using Extended Jones Matrix method [Pochi and Claire, 1999], the optical texture of nematic phases can be calculated. The error induced by the darkening of the droplet tip is hereby shown. Data and simulation courtesy of Bohdan Senyuk from the Pasquali/Smalyuk group (Rice University/Colorado University)

5.5 CNT Nematic Droplets: Equilibrium Shape

We decided to explore the formation of nematic droplets with CNTs dissolved in chlorosulfonic acid. We used CCNI CNTs showing an isotropic biphasic transition between 500 and 1000 ppm wt%. This transition is 4-6 times lower than the typical transition observed with HiPco Single Walled Carbon Nanotubes (SWNTs). Since chlorosulfonic acid is an athermal solvent for CNTs [Green et al., 2009b], we can estimate the aspect ratio of the constitutive molecules to be 4 times larger that HiPco SWNTs (aspect ratio 500 [Parra-Vasquez et al., 2007]). From TEM average diameter (3 nm), the average length can be estimated to be 6 μm. If a homogeneous to a bipolar transition exists for rigid rod molecules and occur for droplet size comparable to the size of the constitutive molecules (as previously noted in section 5.2.2), the size of the molecules will allow for experimental observation of the transition.

The shape of a CNT nematic droplet in chlorosulfonic acid is elongated with

a finite aspect ratio. This behaviour is expected, but rarely encountered in CNT systems. Large droplets show the typical optical texture of a bipolar droplet where a dark cross is at the center with bright lobes close to the droplet surface (Fig. 5.12(a) and 5.12(b)). Bipolar droplets were never observed for CNT systems despite being the only type of tactoid observed for other rod–like systems. Theoretical prediction indicates that the aspect ratio of tactoids increased as the droplet size decreases (see Eq. 5.5), if the droplet is bipolar. In fact, as the size of the droplets is reduced, their aspect ratio is increased (Fig. 5.13(a)). This is the expected behavior for bipolar tactoids. More interesting is the trend of the curve at lower droplet size. Droplets with long axis as small as 30 μm still show a clear bipolar texture. However, as the aspect ratio is plotted as a function of droplets long axis, the aspect ratio becomes independent of droplet longer axis around the same value. Constant aspect ratio is indicative of a homogeneous director field. In fact, in the same size range ($\sim$ 30 μm) tactoids with homogeneous optical texture also start to appear. Such an optical texture, along with constant aspect ratio, indicates the transition of the system from bipolar to homogeneous tactoids. The measured scaling exponent for the dependence of aspect ratio from the dimensionless elasticity κ (see equation 5.5) is 0.32 $\pm$ .12, a discrepancy from the expected values of 0.6 (Fig. 5.13(c)). Thus, as expected from computer simulation [Trukhina et al., 2009], the homogeneous to bipolar transition can be observed experimentally. CNT/chlorosulfonic acid solutions are the first rigid rod system where this transition is observed. We rationalize the observation by noting that the molecules under consideration for this study are $\sim$6 μm long, which is an optimal size to observe such a transition with an optical micrograph.

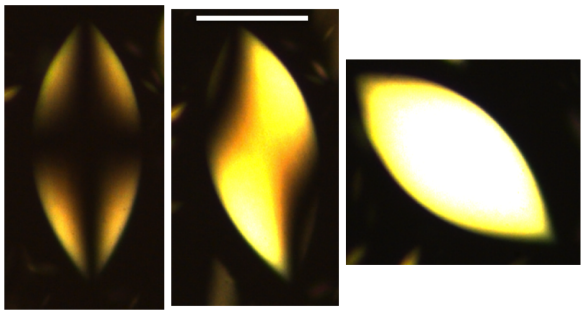

(a)

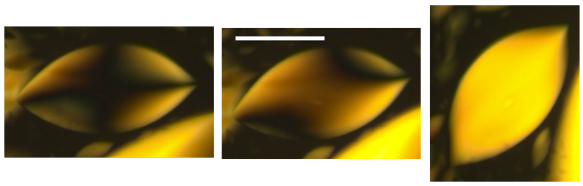

(b)

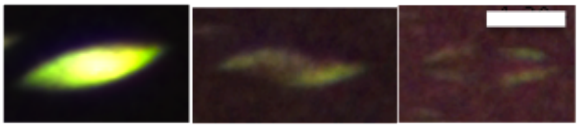

(c)

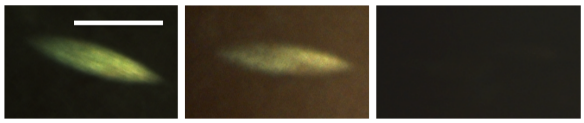

(d)

Figure 5.12 : Large and small tactoids of CNTs in chlorosulfonic acid. Figures 5.12(a), 5.12(b) and 5.12(c) show the typical optical texture of bipolar tactoids, while figure 5.12(d) shows texture of a homogeneous one. Figure scale bars are 80 μm for figure 5.12(a), 200 μm for figure 5.12(b), and 20 μm for figure 5.12(c) and 5.12(d).

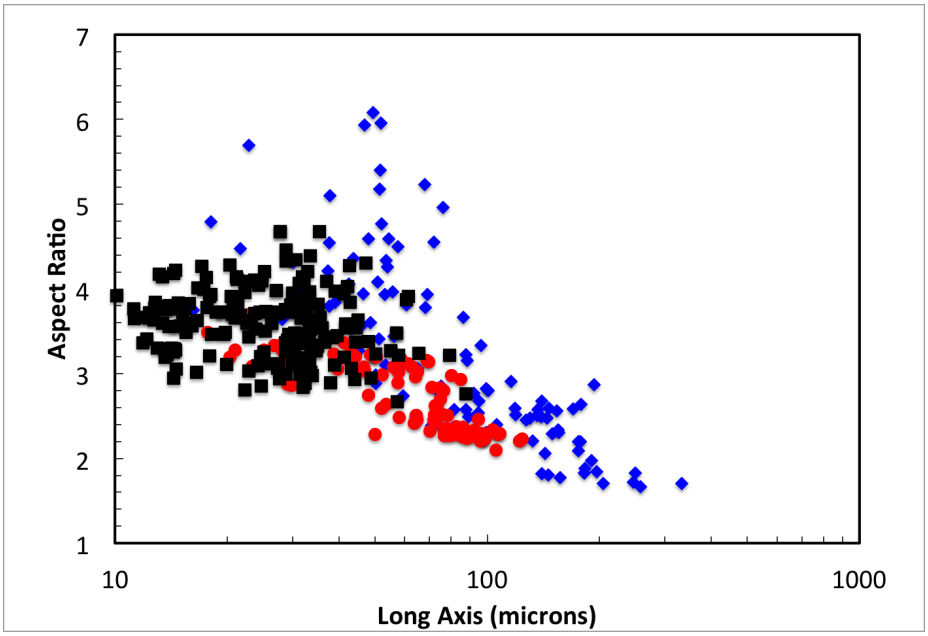

(a)

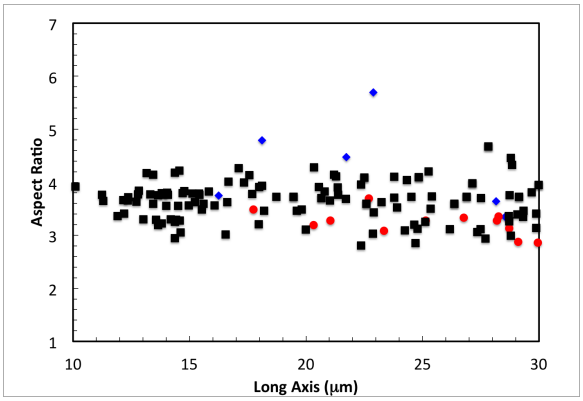

(b)

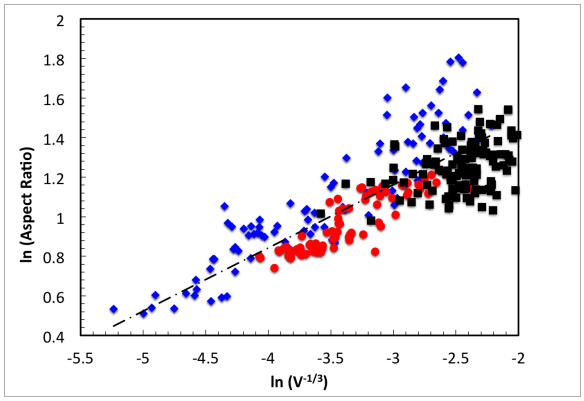

(c)

Figure 5.13 : Figure 5.13(a) shows measured tactoids equilibrium aspect ratio as a function of long axis. Three different capillaries were used to image tactoids and cover a wide range of sizes. Black squares represent data from 40 μm capillary, red circles from 100 μm capillaries and blue rhomboids refer to data acquired from 200 μm capillaries (Vitrotubes, 0.2X4 mm I.D.). The overlap of data indicate that the measured trend is not sensitive to the type of capillary used to prepare samples. However, capillary size limits the maximum attainable size. The low end of the curve (Fig. 5.13(b)), where tactoid aspect ratio becomes constant, is indicative of homogeneous tactoids. We use the portion of the curve where aspect ratio becomes a function of droplet size to quantify size scaling exponent with respect to dimensionless elasticity (Fig. 5.13(c)). We did not consider data with long axis lower than 30 μm to ensure a full dependence of aspect ratio with size. Volume is calculated as $(R\ r^2)^{1/3}$.

5.6 CNT Nematic Droplets: Dynamics

The time scale and merging dynamics of nematic droplets are essential elements to understand some of the persistent structures found at higher liquid crystalline phase concentrations. Moreover, dynamics in the liquid crystalline phase is a clear indicator of the liquid nature of liquid crystals. As the size distribution of nematic droplets is considered, the distribution shows a high frequency of droplets with long axis of ∼30-50 μm (Fig. 5.14). Droplets in this size range are persistent and are the dominating size even after several months, indicating that it is a stable feature of CNT nematic droplets. The size region with high frequency is also remarkably close to the region where the transition from homogeneous to bipolar tactoids occurs. This is expected since homogeneous droplets do not require the nucleation of a topological defect, while bipolar ones do. This energy barrier has shown to be useful to obtain homogeneous size distribution in other liquid crystalline systems [Tixier et al., 2006]; this has now been demonstrated also for CNT droplets.

Figure 5.15(a) shows two coalescence events. The first one occurs between two tactoids with long axis 25 and 70 μm, respectively. The resulting tactoid recovers the equilibrium shape within ∼10 minutes. Conversely, for the second merging event involving larger tactoids (66 and 86 μm long axis), 45 minutes are not enough for the new droplet to recover the equilibrium shape. In fact, large droplets require ∼1 hour to recover their equilibrium shape from the initial merging moment (Fig. 5.15(b)). Thus, both the probability to merge and the time scale to restore equilibrium shape are high for large droplets. Another requirement for two droplets to merge is matching their nematic director. Two tactoids can persist without merging for an extended period, despite their proximity (Fig. 5.15(c)). Merging starts when relative rotation aligns their nematic director. Visualization of more that 60 coalescence events confirms the

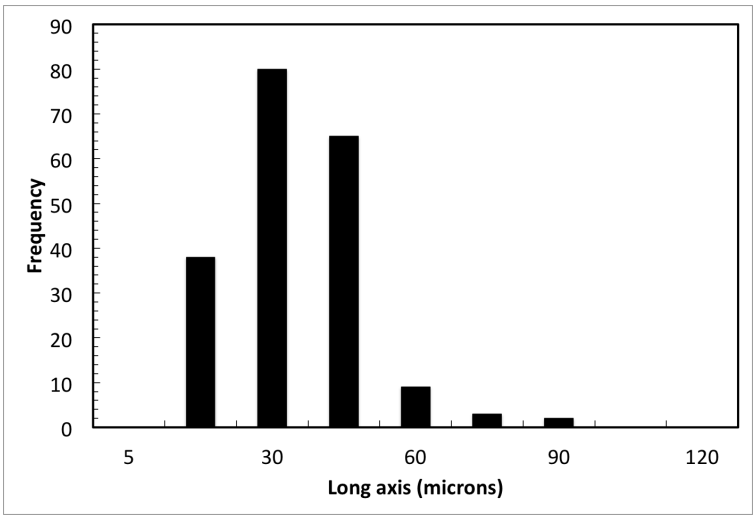

(a)

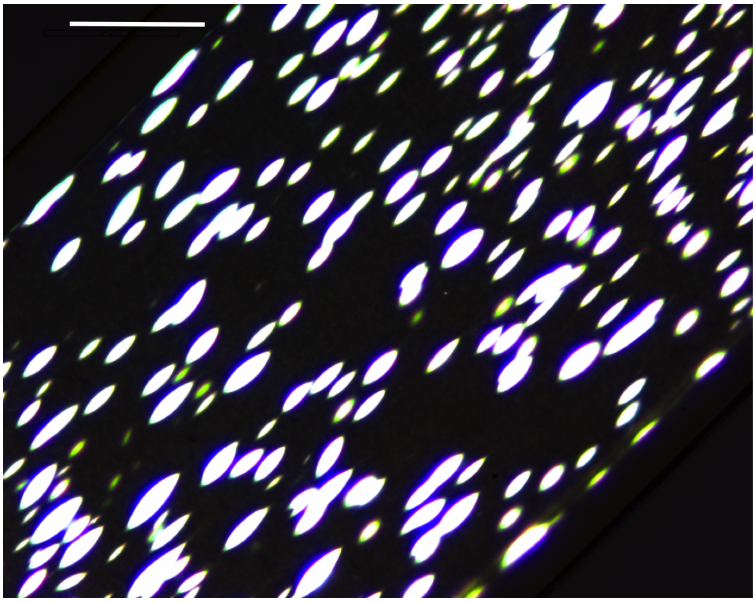

(b)

Figure 5.14 : Tactoid size distribution. Figure 5.14(b) shows a 40 μm capillary a day after preparation. A dominant droplet size within the capillary is observed. Figure scale bar is 100 μm

tangential director matching as a consistent requirement. We argue that tangential merging minimizes the elastic distortion during nucleation of negative boojums. Similar coalescence mechanisms were recently reported for microtubule droplets [Gatlin et al., 2009]. However, the coalescence dynamics we report is not mediated by active molecular motors, as reported for microtubule droplets.

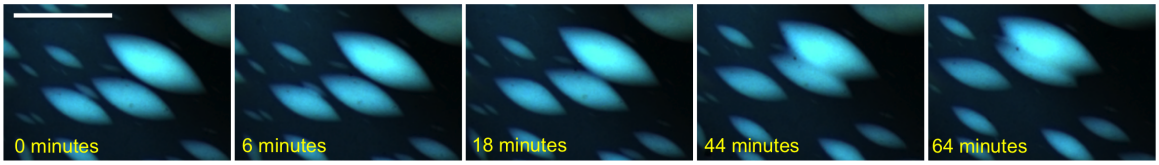

(a)

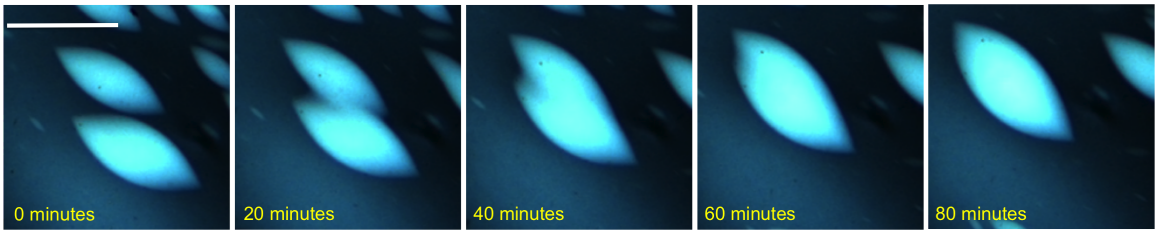

(b)

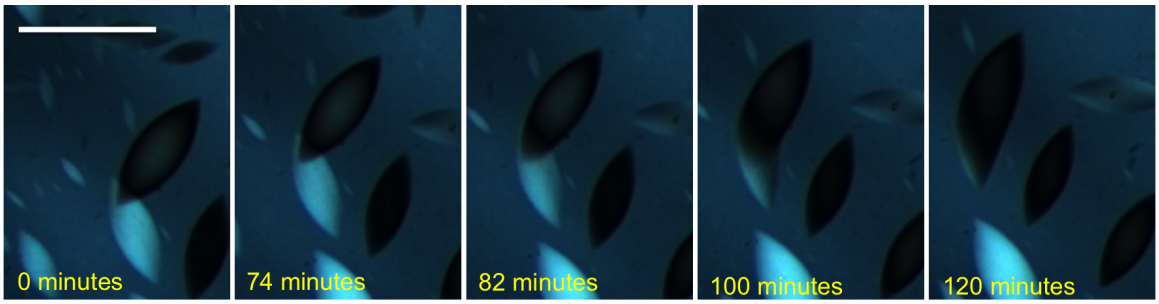

(c)

Figure 5.15 : Tactoids merging dynamics. Scale bar is 100 μm for all figures.

Nucleation, growth and coalescence are the main coarsening mechanisms [Oakes et al., 2007]. CNT droplet coarsening is dominated by coalescence of droplets with

no appreciable nucleation and growth (Fig. 5.16). We tracked the size of ten droplets over two hours. Their projected area did not change by more than 10% confirming that merging is indeed the main coarsening mechanism.

When elongated strands are observed over time, they show the typical capillary break-up of liquid filaments (Fig. 5.19). The droplets generated by the break–up event are tactoidal in shape.The long break-up time scales (10 minutes to an hour) observed in CNT nematic filaments can be rationalized through their high length and aspect ratio, which in turn yield high Frank elasticity and viscosity. Also, the time scales involved for capillary break-up of CNT fluids may be useful to rationalize the stability of elongated nematic droplets often found in CNT fluids [Davis et al., 2009] and other rigid–rod liquid crystals [Davis, 2011].

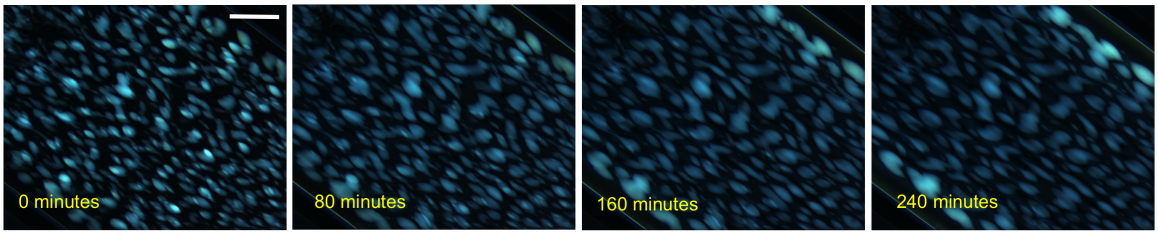

Figure 5.16 : Coalescence of multiple droplets. Scale bar is 100 μm.

In conclusion, the various dynamics observed (droplet merging and capillary break-up) for CNT droplets in chlorosulfonic acid are the clearest evidence yet to prove the liquid crystal nature of CNTs.

5.7 Negative Tactoids

The edge of the capillaries are often nucleation site for large areas homogeneous nematic phase. When an isotropic phase is included within this phase, negative tactoids

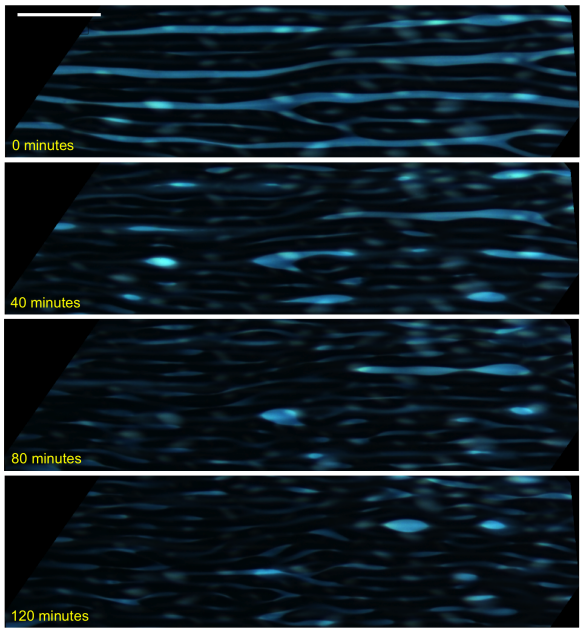

Figure 5.17 : Capillary break up. Scale bar is 200 μm.

(isotropic droplets in a nematic continuum) are created. The optical texture around the isotropic droplet suggest planar anchoring of CNTs at the isotropic nematic interface with two point defects (boojums) at the poles of the particles, aligned along the nematic direction (Fig. 5.18(a)).

The isotropic droplet induce distortion of the nematic director field (Fig. 5.18(b)). These elastic distortions create topological defects around the particles and induce anisotropic long and short range interactions between the particles [Poulin and Weitz, 1998]. We observe similar interaction for CNT negative tactoids.

Although details analysis of the interaction dynamics goes beyond the scope of the present thesis, the formation of negative tactoids and they merging dynamics are further proof of the the liquid nature of CNT liquid crystals.

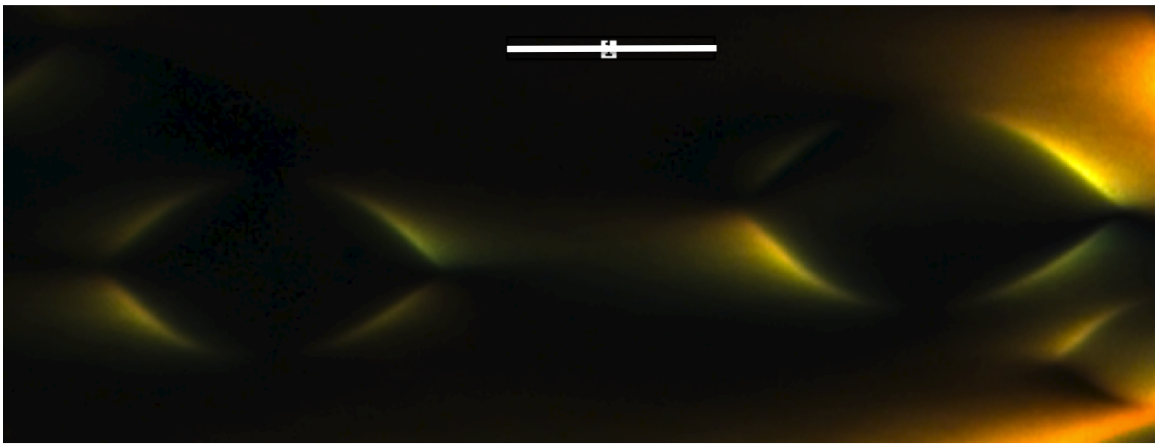

(a)

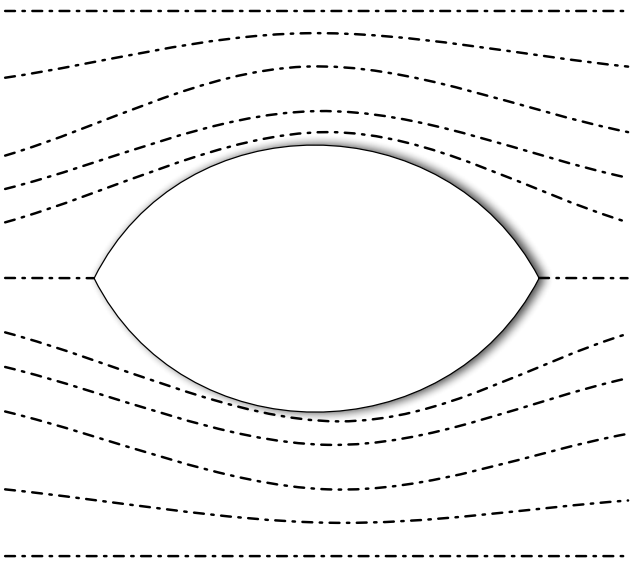

(b)

Figure 5.18 : Figure 5.18(a) shows CNT negative tactoid nucleated at the edge of the capillary tube (scale bar is 100 microns). Figure 5.18(b) a schematic of negative tactoids. The dotted lines represent show the distortion induced on the nematic director field by the present of the isotropic droplet.

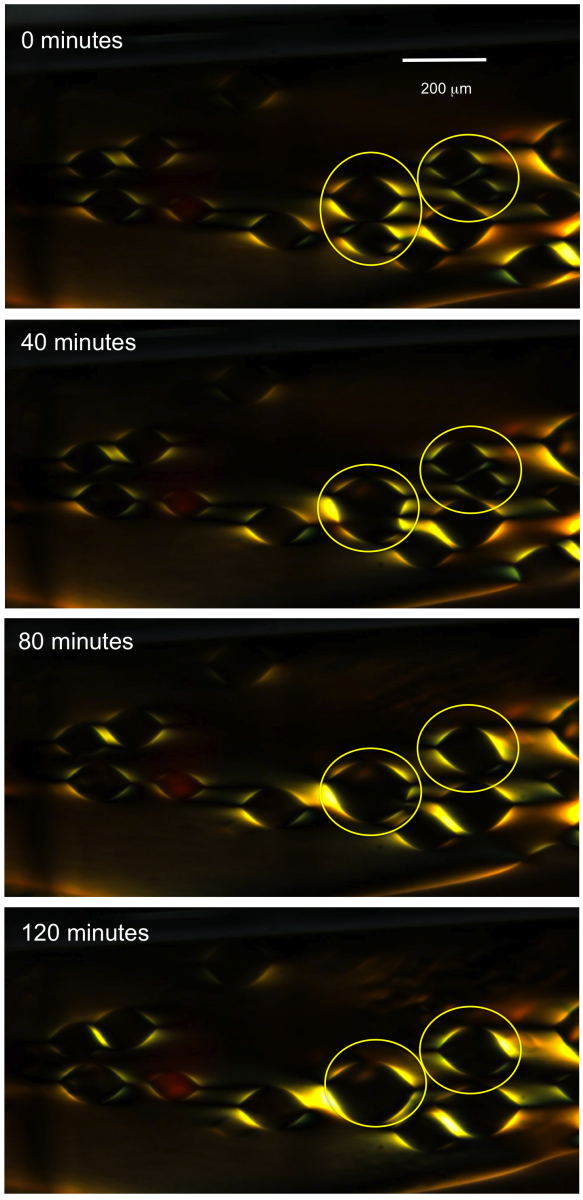

Figure 5.19 : Negative tactoids merging dynamics

5.8 Conclusions and Perspective

Formation of elongated droplets is *per se* of great relevance to the field of CNT liquid crystals. In fact, this implies that equilibrium structures dictated by free energy minimization can be achieved. From a fundamental perspective, CNT liquid crystalline droplets allow experimental observation of the transition from homogeneous to bipolar director field in rigid rod nematic droplets with tangential anchoring. Their merging dynamics stems from the interplay between surface minimization, the large energy barrier required by defect generation, and elastic deformation. Very large droplets ($\sim$300 μm) can indeed be formed to minimize surface tension, but, on average, droplet size is close to where the homogeneous to bipolar droplet transition occurs. The size distribution is a sign of the large energy barrier required for negative boojum formation during bipolar droplet merging. Droplet merging and coarsening are also complementary evidence to CNT birefringence to define CNT liquid crystallinity. Specifically, they support the notion that CNT liquid crystals are indeed "liquid".

The observation of nematic droplets and their dynamics also allows to define the underlying structure of the biphasic regime. At equilibrium nematic droplets have a short (less than 10) aspect ratio, however flow can easily deform and elongate them by an order of magnitude or more. Such elongated, metastable structures, often seen in other rigid–rod systems, may entangle and become the dominating structure at high biphasic concentration. These structures are persistent and stable because of slow dynamics (see for example Fig. 5.9), and the energy barrier created by the deformation of a liquid crystalline fluid with high Frank elasticity. High nematic concentrations, high aspect ratio molecules (see Eq. 5.9) and attractive forces between molecules are all variables that increase Frank elasticity and fluid viscosity, and will in turn affect

the observed structure (see for example the persistent elongated structure in Fig. 5.7). Systematic studies of the influence of CNT concentration, length, and solvent quality are required in the future to further elucidate how different parameters influence the underlying structure of CNT liquid crystals.

Nematic droplets represent the simplest case of CNT liquid crystals when the nematic director has a simple distortion field. High concentration (3 wt% and higher) fluids are the most interesting liquid crystalline phase for application since these are the fluid phases used for fiber spinning. Fiber spinning dopes are characterized by a more complex distortion fields and dynamics. Nevertheless, the underlying physics of their structure and dynamics is regulated by the concepts described in this chapter.

Chapter 6

Superacid/CNT solution spinning

6.1 Introduction

Material processing has a significant influence on properties. In fact, despite equal quality of starting material, small changes in the process can induce dramatic changes in the final product properties. Such process-product relationships, well known in metallurgy, applies to a greater extent to polymer processing [Walczak, 1977]. Fiber spinning complexity arises from the large number of variable that influence the process. As a consequence, identification of the most influential parameters is an essential element of fiber spinning development. This chapter is about highly explorative research, with a large number of variables and partially controlled experiments. Thus, the trends and conclusions reported in this chapter are limited to the considered parameter space. The chapter first describes the multitude of variables encountered during wet spinning. We then analyze the superacid/carbon nanotube (CNT) fiber spinning process and use the experimental evidence available to identify the most influential processing parameters with respect to fiber strength and electrical conductivity.

6.2 Overview of Spinning Parameter Space

The relevant parameters of fiber spinning process are often seriously underestimated. The various parameters can be grouped into five main sections:

- Raw material characteristics
- Spinning dope
- Dope extrusion
- Coagulation
- Post processing

Spinning variables can be further divided into independent variables and dependent variables [Walczak, 1977]. The dependent variables are usually affected by the change of more than one of the independent variables. We will now describe in detail fiber spinning parameter space and the influence of the different variables on spinning fluid and fiber final structures.

6.2.1 Raw Material Characteristics

Polymers are defined by their repeating units, molecular weight and their polydispersity. Similarly, a repeating unit and molecular weight can be defined for CNTs [Green et al., 2009a]. However the concept of molecular weight is not as useful for CNTs since the same molecular weight can be attained with various combination of number of walls, length and diameter. Thus length, external diameter, and number of walls are more widely adopted in the CNT community. Chirality and defect density (measure of SP3 carbon density within the graphitic SP2 carbon) are two other variables that have a profound influence on the electronic properties and solubility of a given raw material [O'Connell et al., 2002, Duque et al., 2010, Parra-Vasquez et al., 2010]. Another important parameter is the amount of impurities and type in the raw material. When impurities are present in the final fibers, these are weak spots that decrease

the total cross section area bearing the applied stress. Based on the type (size and chemical composition) of impurities, chemical (differential solvation, oxidation etc.) or mechanical (filtration) purification can be used. Thus, the important parameters to characterize a given CNT raw material are:

- Length (average value and polydispersity)
- External diameter (average value and polydispersity)
- Number of walls (average value and polydispersity)
- CNT Chirality
- Defect density
- Type and amount of impurities

As detailed in Chapter 2, fiber strength scales linearly with CNT aspect ratio (the ratio of CNT length to its external diameter), when a perfect crystal is attained, while specific strength scales with the length to number of walls ratio [Vilatela et al., 2011]. Aspect ratio has also a profound influence on liquid crystal phase transition as well as fluid viscosity (thus viscosity and phase transition are dependent variables) [Onsager, 1949, Flory, 1956, Straley, 1973]. Electrical properties are also expected to depend on CNT length, chirality and defect density.

Diameter and number of walls influence electronic properties [O'Connell et al., 2002] and molecular density (whith in turn affects fiber density). The relationship between number of wall and external diameter with density is as follows:

$$\rho_{molecule} = \rho_{graphite}\frac{(1-N^2)\delta_{vdW} + 2D_{ext}\cdot\delta_{vdW}(1+N)}{(D_{ext}+\delta_{vdW})^2}, \tag{6.1}$$

where $\rho_{graphite}$, D_{ext} and δ_{vdW} are graphite density (2.2 g/cm^3), tube external diameter and van der Waals distance between two CNT walls (0.34 nm, assuming that distance is equal to graphite layer spacing). This density value represents the single molecule density. Thus, when calculating the density of a macroscopic crystal, the packing efficiency of cylinders needs to be considered. Diameter polydispersity, a parameter unique to CNTs when compared to polymers, affects molecular packing. When diameter is monodisperse, a hexagonal close packing is expected for an ideal crystal, yielding a crystal density that is $0.91 \cdot \rho_{molecule}$; however, polydispersity may disrupt this order [Jalali and Li, 2007], reducing fiber density and, most importantly, the effective surface of load transfer between adjacent tubes, which in turn affects macroscopic properties. Large diameter CNTs may also loose their shape and collapse under radial buckling [Yakobson et al., 1996, Chopra et al., 1995, Benedict et al., 1998]. Collapsed CNTs are characterized by molecular density that is close to graphite density. Moreover, collapsed CNTs will have higher surface area per unit length for stress transfer, yielding stronger fibers.

Unfortunately, control of the different variables on the synthesis level is not yet available, particularly for chirality. Moreover, measurement methods most of the variable are still in their infancy. Thus, despite the importance of these variable on the final fiber properties, the state of the art does not allow controlled variation and measurements.

6.2.2 Spinning Dope

The fluid solution made by a solvent and the raw material is called the spinning dope. The independent parameters that are varied can be listed as follows:

- Solvent quality

- Dope concentration
- Dope temperature

The type of solvent has a profound influence on the induced interaction potential between the constituent molecules. This, in turn, affects the type of liquid phases attained. When rigid–rod polymers are dissolved in a good solvent they transition into a liquid crystalline phase, an ordered liquid phase beneficial to the order of the final solid fiber. Organic solvents and strong acids are the solvents of choice for rigid–rod polymers [Panar and Beste, 1977, Kwolek et al., 1977, Choe and Kim, 1981, Yang, 1989]. CNTs require even stronger solvents. In fact, superacids are the only known solvents, with chlorosulfonic acid being an athermal solvent [Ramesh et al., 2004, Davis et al., 2009, Parra-Vasquez et al., 2010, Green et al., 2009b]. Concentration is another essential parameter. In fact, as concentration is increased, a transition to a liquid crystalline phase is attained. Unlike rigid–rod polymers, the onset of isotropic to biphasic transition occurs at concentrations that are orders of magnitude smaller (0.01-0.1 wt% for CNTs, 10-15 wt% for rigid rod polymers). This is to be expected given the large aspect ratio and stiffness of CNTs [Fakhri et al., 2009, Parra-Vasquez et al., 2007]. Spinning dope concentration also affects solution viscosity [Panar and Beste, 1977, Choe and Kim, 1981, Davis et al., 2004]. High viscosity dopes are required to form a stable fluid that does not break under Plateau-Rayleigh instability or during stretching [Ide and White, 1976]. For rigid–rod molecules, the viscosity has a non-monotonous behaviour as a function of concentration, with regions where viscosity decreases as concentration is increased. This behaviour is usually observed in the biphasic region, where the nematic phase becomes the continuous phase and can be used as a sign for the onset of the transition [Davis et al., 2009, D., 2006]. High

spinning dope concentration is also attractive from an economical and coagulation stand point. In fact, high concentration dopes reduce the amount of solvent recycling or solvent disposal and increases the total solid throughput (thus higher production rate). High dope concentration is also useful to slow down coagulation rate, often beneficial to the final fiber properties. However, high concentration also poses mixing, filtration and extrusion problems due to high viscosity. Thus an optimal concentration is expected that balances the different aspects and maximizes target properties.

Temperature has also the potential to profoundly affect both fluid structure and viscosity. In fact rigid–rod polymers are often spun at high temperature (∼100 °C) because of the strong dependence of their phase behaviour on temperature [Yang, 1989]. Even when the phase diagram is not affected, temperature can still affect the overall solution viscosity, making processing and mixing easier at higher temperature. We do not expect the CNT phase to diagram to be significantly changed by temperature, but we expect the viscosity (hence processability) to be affected by temperature.

6.2.3 Dope Extrusion

Ideally, the spinning dope is extruded to yield a fluid filament that is as close as possible to an ideal crystal where the constitutive molecules are all aligned and stretched along the fiber axis. The parameters that are experimentally controlled influencing dope extrusion can be identified as follows:

- Filtration (filter size and position);
- Flow rate;
- Winding drum speed (or spin draw ratio SDR);

- Spinneret geometrical details: diameter, aspect ratio, entry shape;
- Presence of air gap during spinning.

The main purpose of filtration is to remove undispersed particles that may yield unstable flow or create weak spots during spinning. Ideally the size of the removed particles should be reduced to be a small fraction (30% or below to have particles cross section to be below 10% the total fiber cross section) of the final fiber diameter. Often fiber diameters are of the order of 10 μm, thus a filter pack should be able to remove particles as small as a few microns. Filtering packs also induce high shear rate on the spinning dope altering its structure. Often this is beneficial because high shear rate promotes mixing and homogeneity, but it may also create flow instabilities, particularly when the filtration is performed in series with fiber extrusion. When dealing with long molecules, filtration may also selectively remove the longest molecules.

Volumetric flow rate together with diameter defines the shear rate which the fluid filaments are subjected to. The shear rate at the wall for capillary flow (Eq. 6.2) and the extensional (Eq. 6.3) rate of an entrance flow can be expressed as follow [Macosko, 1994]:

$$\dot{\gamma_w} = \frac{4Q}{\pi R^3} \tag{6.2}$$

$$\dot{\epsilon} = \frac{Qsin^3(\phi)}{\pi R^3(1-cos(\phi))}, \tag{6.3}$$

where $\dot{\gamma}$, $\dot{\epsilon}$, Q, R and ϕ represent shear rate in capillary flow, elongation rate in entrance flow, flow rate, die radius and entrance angle in entrance flow, respectively. Most of the polymer fluids, including CNT fluids, are highly shear thinning. Operating fiber spinning flows at the highly thinning region of the viscosity–shear rate curve

may cause unstable flow and fibers with variable cross section along fiber axis. In fact, a small change in flow rate may induce significant variation in dope viscosity. Usually, a spinning dope undergoes a combination of shear and elongation flow and both scale linearly with flow rate and inversely with the cube of die radius. Pure capillary flow has a non-homogeneous shear field which in turn creates non–homogeneus fluid deformation and deformation rate along dope cross section. Moreover, the structure of the liquid crystalline fluids may also exhibit a complex dependence on shear rate as well as flow instabilities [Larson, 1999, Kang et al., 2006]. Conversely, elongational flow creates a more uniform extension of fluid filaments. Thus, spinning dies with short aspect ratio dies are preferred to minimize shear and enhance elongation. Short aspect ratio are also useful to minimize the spinning pressure drop. However, high molecular weight polymers display a strong die swell dependence with capillary length. When the capillary length is increased, die swell decreases rapidly and approaches a limiting value [Walczak, 1977]. Thus, spinning die aspect ratio has to be designed to avoid the region where die swell is changing rapidly with respect to aspect ratio, to minimize flow instability and cross section variation along the filament. Entrance geometry also requires optimization. Sudden contraction versus smoother entrances may change the onset of recirculation flow and/or flow instability.

Elongational flow is also obtained by collecting the filament on a drum and having the linear speed of the drum to be higher than filament linear extrusion rate. The ratio of drum linear speed to filament linear speed at the exit of extrusion die is known as Spin Draw Ratio (SDR). This value is an essential parameter to quantify the total elongation a fluid filament is undergoing. In fact, the total elongation a fluid filament undergoes during fiber spinning is the sum of die aspect ratio to SDR. The SDR is also used to quantify fiber linear density (LD). In fact, when performing

a mass balance (Eq. 6.5) on the spinning dope, the LD can be expressed in terms of spinning parameters (Eq. 6.6):

$$\rho_L = \frac{\pi D_f^2}{4}\rho_f \tag{6.4}$$

$$w\rho_d\frac{\pi D_s^2}{4}\cdot v_f = \frac{\pi D_f^2}{4}\rho_f \cdot v_d \tag{6.5}$$

$$\rho_L = \frac{\pi D_f^2}{4}\rho_f = w\frac{\pi D_s^2}{4}\cdot\frac{\rho_d}{S_R,} \tag{6.6}$$

where ρ_L,D_f, ρ_f, ρ_d, v_f, v_d w, D_s and $S_R$are fiber linear density, fiber diameter, fiber density, dope density, fiber linear speed at exit of extrusion die, winding drum linear speed, CNT weight fraction, spinneret diameter and spin draw ratio, respectively.

The dependence of die swell from flow rate is also important. In fact, positive die swells disrupt flow alignment and must be reduced by the additional elongation coming from spin draw ratio. Positive die swell is a manifestation of positive normal stress within the fluid. Liquid crystalline fluids show a complex dependence of normal stress with shear rate, which in turn changes the structure of the spinning dope [Pasquali, 2004, Davis et al., 2004].

Thus, filtration, flow rate, die diameter, and geometry need to be considered in detail when analyzing a spinning process since each variable may have significant influence on final fiber properties.

6.2.4 Coagulation

Solution spinning involves solvent removal by evaporation or using a coagulant liquid. By the end of the spinning process, solvent concentration —high in the initial mixture— must approach zero. The difference between the bulk and interface concentration is the driving force for the coagulant side mass flux:

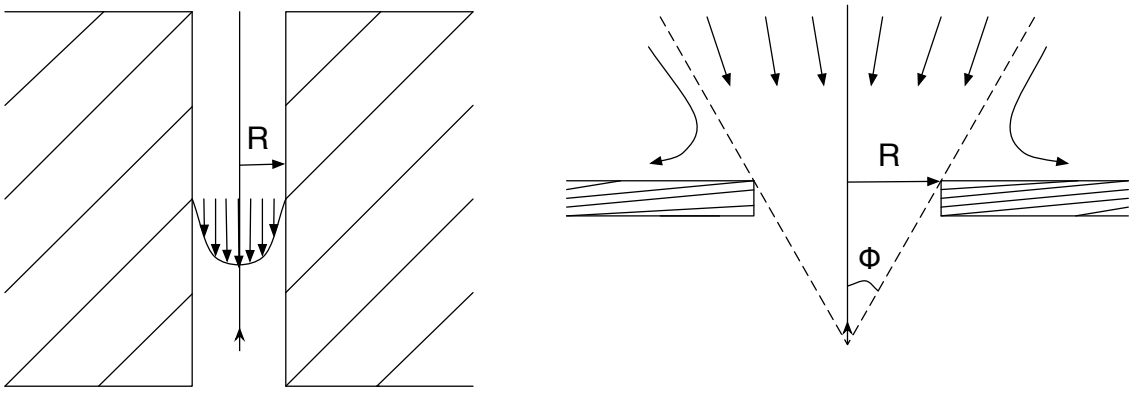

Figure 6.1 : Schematics showing the different flow field in capillary versus entrance flow. Capillary flow (on the left) is characterized mostly by shear flow, with highest shear at the wall. Entrance flow is dominated by elongational flow. Short capillary spinning dies (aspect ratio below 10) are characterized by a mixed shear and elongational flow.

$$m_{ir} = h(\omega_i^{interface} - \omega_i^{bulk}) \tag{6.7}$$

where h and m_{ir} are the convective mass transfer coefficient and the mass flux into the coagulant for the i^{th} component, while $\omega_i^{interface}$ and ω_i^{bulk} are the i^{th} component mass fraction at the interface and in the coagulant bulk phase. The solvent moves through the dope mostly through a diffusive process, whereas transport into the coagulant may be enhanced by convective flow. The mass transfer Biot number (Bi_m) is used to quantify the relative importance of each of these two processes, the ratio of the internal diffusion resistance to external convection resistance [Kojic et al., 2004] is defined as:

$$Bi_m = \frac{hD_f\alpha}{D_{in}} \tag{6.8}$$

where D_f is fiber diameter, D_{in} is the internal solvent diffusion coefficient and α is

the partition coefficient. Typically, D_{in} is orders of magnitude lower than solvent diffusion in the coagulant, making the internal resistance for mass diffusion within the fiber the limiting factor. However, as fiber size decreases, external diffusion may become relevant.

Experimentally, three parameters are controlled:

- Coagulant type;
- Coagulant temperature;
- Coagulation bath length.

Each of them, together with other parameters, control the fundamental (or dependent variables) of coagulation rate and the extent to which the fiber has been coagulated. Within the whole fiber spinning process, the coagulation region is the place where the largest number of events are taking place simultaneously. The possibility of successful design of a coagulation process offered by current theoretical solutions are inadequate by far. Thus, an empirical design with careful diagnosis and proper separation of variables is the only current way to approach the problem.

6.2.5 Post–Processing

Often, fibers are further washed to fully remove spinning solvent. This is important to avoid potential polymer degradation. Heat treatment under tension is also often used to remove residual tension from fiber processing and improve alignment and crystallinity of the final fiber, beneficial to both fiber strength and modulus. Heat treatment of rigid rod polymer can yield 100% improvement over fiber strength and modulus [Adams et al., 1989, Kwolek et al., 1977]. Superacids are also CNT doping

molecules. Thus, complete solvent removal on a post processing phase reduces electrical conductivity by an order of magnitude [Ericson et al., 2004, Zhou et al., 2004a]. As a consequence, for CNT fibers, the extent of washing and heat treatment have the adverse effect of reducing their conductivity performance. The independent variables affecting fiber post–processing can be listed as follows:

- Washing solvent;
- Washing temperature;
- Fiber tension and total elongation;
- Heat treatment temperature;
- Gas for heat treatment;
- Washing/heating/tensioning time.

6.3 Carbon Nanotube Solution Spinning

As highlighted in the previous section, fiber spinning is characterized by a wide range of experimental parameters. Thus, a complete and thorough analysis of spinning parameter space goes beyond the scope of the present thesis. Among the different superacid/CNT spinning parameters, solvent quality has been the one that has received most attention. Chlorosulfonic is the solvent of choice because of its ability to dissolve a wide range of CNTs [Ramesh et al., 2004, Parra-Vasquez et al., 2010, Davis et al., 2009, Behabtu et al., 2010]. The need for long CNTs was also recognized, although the debate is open on the length required to attain relevant fiber strength ($\sim$1 GPa and higher) [Vilatela and Windle, 2010, Behabtu et al., 2008]. In the following sections we will analyze the following parameters:

- Type of CNTs;
- Dope making and influence of dope concentration on fiber strength;
- Spinneret diameter, spin draw ratio and die swell;
- Coagulation.

6.3.1 Influence of CNT Type on Fiber Strength and Electrical Conductivity

Different approaches can be taken to compare the influence of single variables (i.e. CNT type) on final fiber properties. One approach is to change only the variable under consideration (CNT type in this case), by keeping all other spinning parameters constant. Although this approach seems the most plausible, the different CNT types will induce different viscoelastic properties, maximum attainable spin draw ratios and coagulation dynamics. A different approach is to compare the best properties attained by different batches, irrespective of spinning condition. This approach also has its drawbacks because of the implicit assumption that the "best" properties can be identified. In fact this requires a complete mapping of all the fiber spinning parameters space. We used both methods keeping in mind their drawbacks.

We first compared two different batches, CCNI XBC 1001 and CCNI XBC 1101, by spinning them under the same spinning conditions (see table 6.1). We chose the specific spinning condition based on the parameters that gave optimal properties for XBC 1101.

There is a noticeable qualitative difference between the two dopes. XBC 1001 flows slowly under gravity while XBC 1101 does not. This indicates the different viscoelasticity of the spinning dopes induced by aspect ratio of the constitutive molecules.

dope concentration (wt%)	3
Spinneret diameter (μm)	65
Spinneret aspect ratio (μm)	3
Linear extrusion rate (m/min)	2
Spin draw ratio	2
Coagulant	acetone
Spinneret drum distance (cm)	20

Table 6.1 : Spinning condition XBC 1001 vs 1101.

Both dopes were filtered using kt-15 (∼15 micron mesh size). Filtration was also indicative of the different flow behaviour of the two dopes. In fact XBC 1001 flowed through the filter at significantly lower pressure (∼ 10 times lower using the same apparatus and flow rates) compared to XBC 1101.

The morphology of the spun fibers was also noticeably different (Fig. 6.2). In fact, fibers spun from CCNI 1101 yield regular, almost round cross section, unlike fibers spun from batch 1001, despite the two dopes being spun under the same exact conditions.

These fibers differ also in their mechanical strength (Fig. 6.3). Because of the irregular cross section, direct comparison of breaking stress would be inaccurate, thus we directly compare breaking forces*.

Despite the variability on breaking force within a giving spinning condition†, on

*Breaking force is equivalent to specific strength (Force/Linear Density) since the fibers were spun under the same spinning condition. This is because linear density (LD= $\text{mass}_{fiber}/\text{length}_{fiber}$) is expected to be the same (see Eq. 6.6).

†Although fiber uniformity has not been given adequate attention in most published works, it

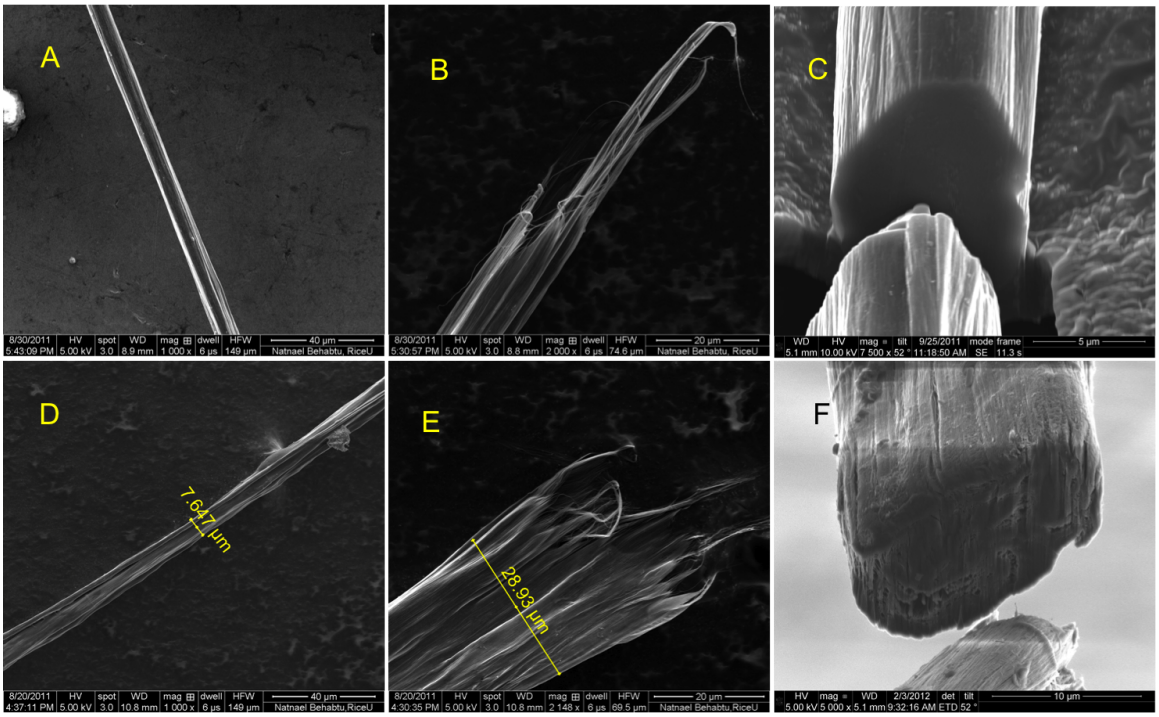

Figure 6.2 : Figures A, B and C are SEM micrographs of fibers spun from CCNI XBC 1101 while figures D,E and F are micrographs of fibers spun from batch 1001. The fiber were spun under the same spinning conditions. FIB images are courtesy of Talmon/Cohen group, Technion, Israel Institute of Technology, Haifa and John B. Ferguson, Materials and Manufacturing Directorate, Air Force Research Laboratory, Wright-Patterson Air Force Base, Dayton, OH.

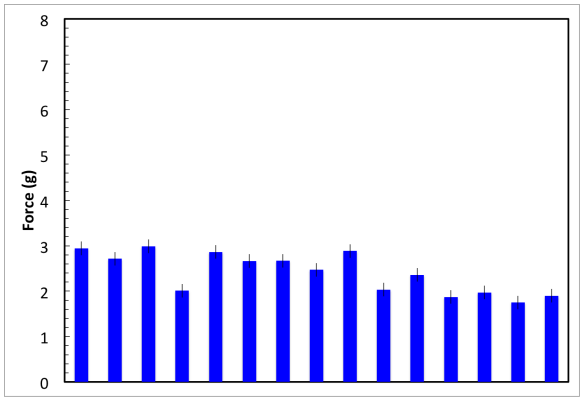

(a)

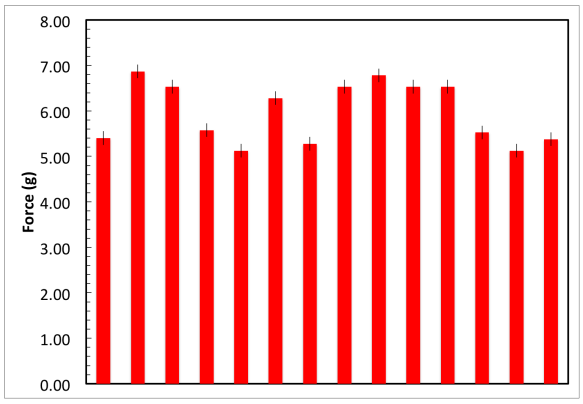

(b)

Figure 6.3 : Breaking force of fibers spun from XBC 1001 (Fig. 6.3(a)) and XBC 1101 (6.3(b). Each bar represent the breaking force of single filament. The error bar (0.3 grams) represent the noise of the measuring instrument. Fiber gauge length is 20 mm.

average the breaking force for fibers spun from XBC 1101 are more than double compared to fibers spun from XBC 1001.

Some spinning conditions can yield round cross sections for XBC 1001. Specifically, higher concentration dopes and low temperature coagulation yield rounder filaments (Fig. 6.4).

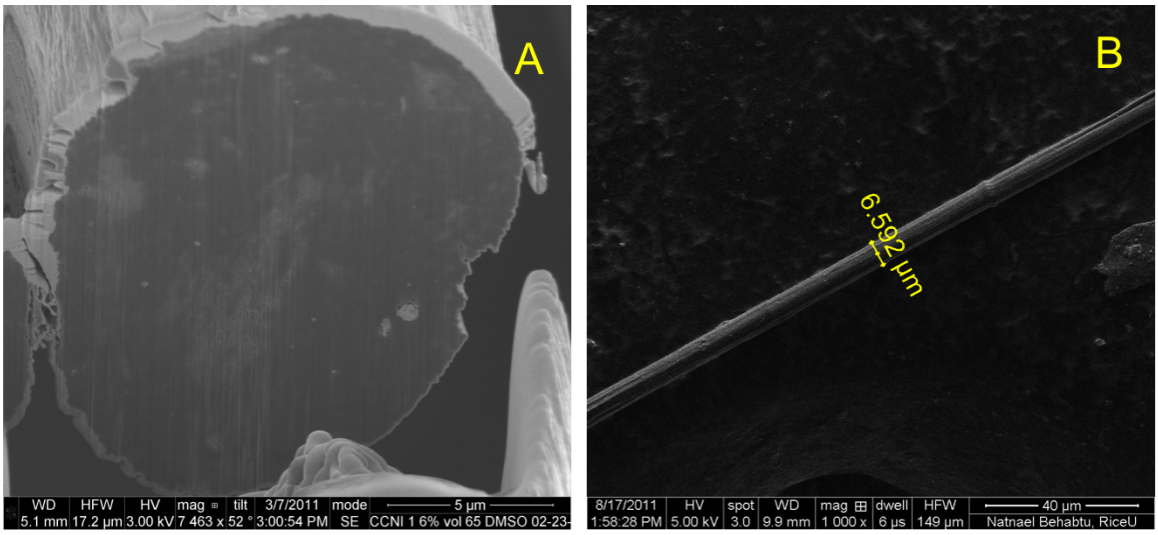

Figure 6.4 : Regular cross section of fibers produced from XBC 1001. Figure A is a cross section of a fiber spun from a 6wt% dope in a room temperature DMSO. Linear extrusion rate and drum speed were both at 10 m/min. The coating is platinum coating used during FIB cutting. Fiber in figure B was spun from the same spinning dope used for the fiber in figure 6.2 D-F except the coagulant (acetone) temperature (-70 C, achieved by directly sublimating dry ice into acetone). FIB images courtesy of Talmon/Cohen group, Technion, Israel Institute of Technology, Haifa.

Turning to the second approach, we compared the best specific strength obtained for the two batches (The best out of 13 different spinning trials for XBC 1001, and the

represents a subject of constant concern in fiber manufacturing [Walczak, 1977]. Non–uniformity may originate from many sources. Some reasons for fiber non uniformity are: polymer inhomogeneity, impurities, dead spots in flow pattern, flow instabilities,variation in spin draw ratio, viscous friction and/or turbulent flow in coagulating bath, vibrations.

best out of 11 spinning trials from XBC1101). Each spinning trials is characterized by the same dope and filtration, but multiple flow (flow rate and spinning die) and coagulation conditions. We have also verified the consistency, repeatability, and reproducibility of the process by spinning Batch XBC 1101 three times under the same spinning conditions and different operators. The morphology, breaking strength and electrical conductivity of the fibers were indeed repeatable and reproducible.

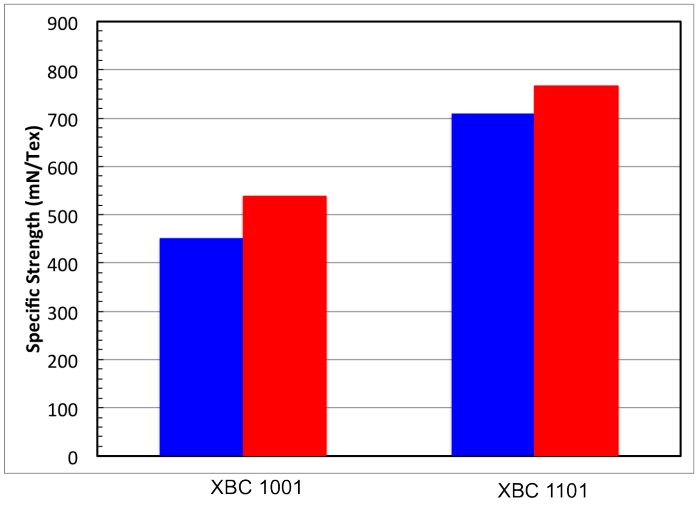

Figure 6.5 : Specific strength for the spinning conditions that gave best fiber strength. Blue bar refers to average (over 8 tensile strength measurements) value and red to best specific strength. The spinning condition that gave best properties for 1001 are as follows: 6wt% dope, 10 m/min linear extrusion rate from 65 μm spinneret with aspect ratio of 2 and winding drum speed of 13.3 m/min. The coagulant was room temperature water.

Even when the best values are compared, XBC 1101 yields better specific and absolute strength. A morphology comparison of the fibers (Fig. 6.6) does not show major differences. In fact, both fibers are characterized by a fibrillar structure with the fibrils aligned along fiber axis. Thus, assuming that the difference is not arising from fiber morphology and alignment, we can infer that the main difference in strength comes from the actual difference in the constitutive molecules.

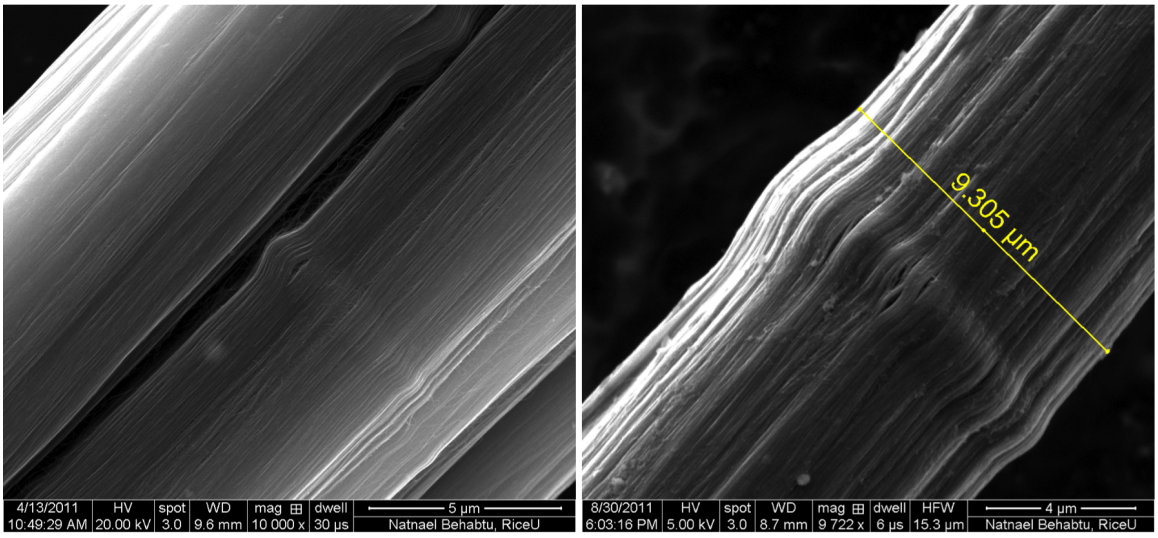

Figure 6.6 : Morphology comparison between the best fibers spun under the spinning condition that gave best fiber strength. On the left is XBC 1001 on the right XBC 1101

The main parameter that differs among different batches is CNT length. In fact, when fiber strength and specific strength are plotted as a function of constitutive aspect ratio (Fig. 6.7) and L/N (Fig. 6.8), fiber strength and specific strength scale linearly with aspect ratio and L/D. Some of the deviation from the expected linear behaviour can be interpreted as lack of optimal processing that maximizes the properties achievable for a given CNT type. Unlike fiber strength, electrical resistivity has almost no influence from CNT type (Fig. 6.9). This may indicate that the limiting factor for electrical conduction is not anymore CNT length.

The amount of impurities is also a critical parameter that characterized the raw material. CNTs synthesis is characterized by a number of impurities that depends often on the synthesis route. Common impurities are nanometer–sized catalyst (ion oxide, copper oxide etc.), fullerenes, and amorphous carbon. Purification procedures that remove catalyst and amorphous carbon are well established [Xu et al., 2005].

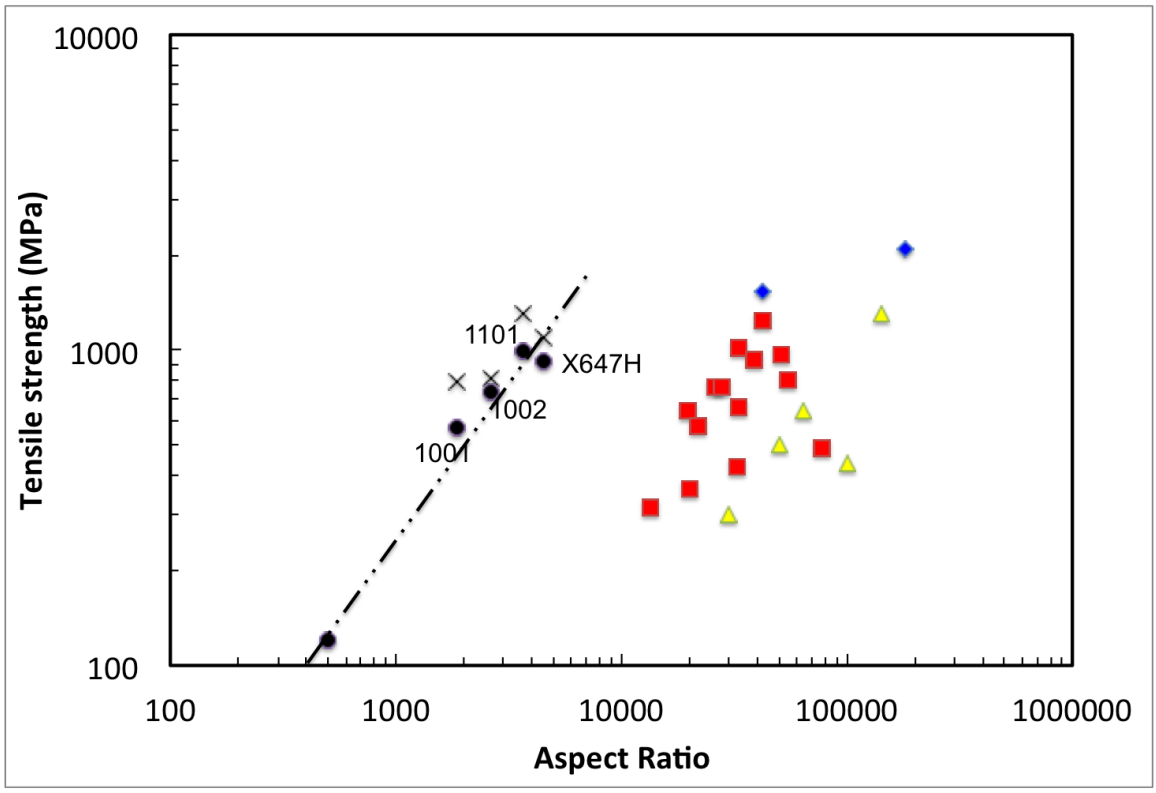

Figure 6.7 : This figure is the same as figure 2.6 in Chapter 2 where fiber strength is plotted as a function of constitutive CNTs aspect ratio. Four points were added from CCNI/superacid spinning (the specific batch number is added next to each point). The Points indicated by X refers to the best single values, while the spherical points represents best average values. The dotted black line has a slope of 1, indicating the expected scaling of strength with aspect ratio.

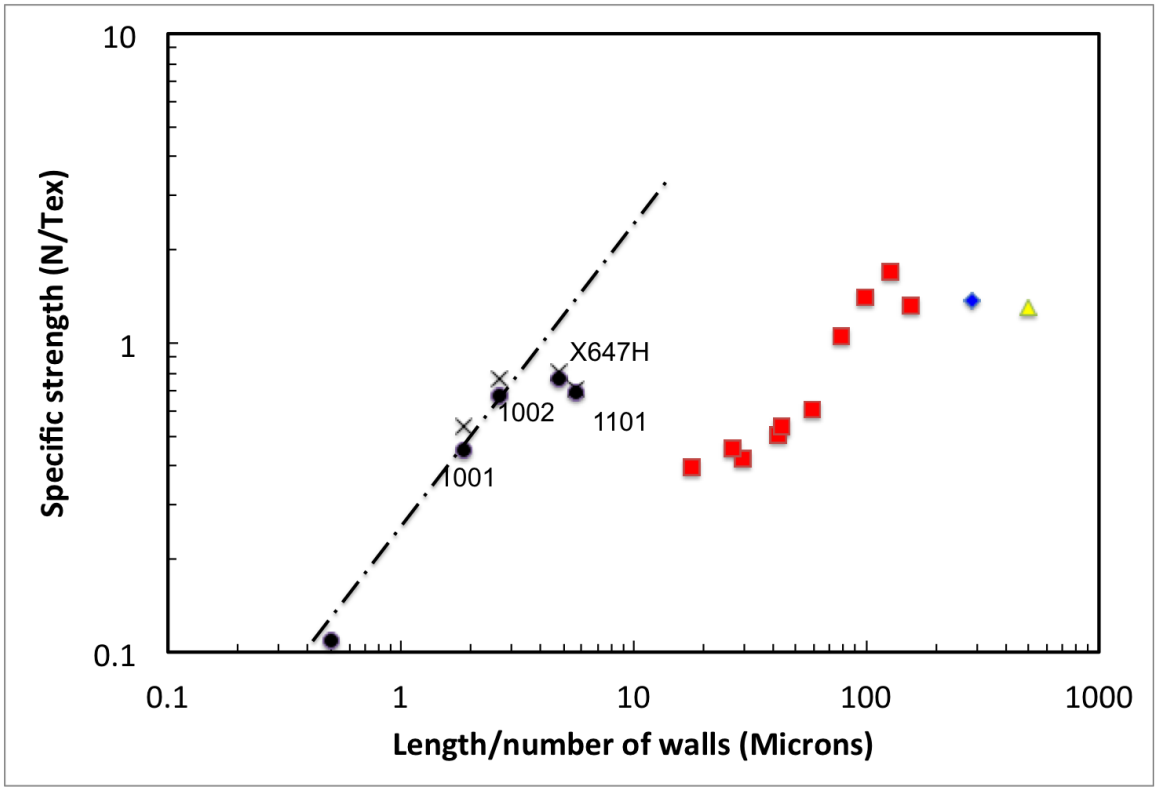

Figure 6.8 : This figure is the same as figure 2.7(b) in Chapter 2 where specific strength of different fibers are plotted as a fuction of the constitutive CNTs length divided by their wall numbers. Four points were added from CCNI/superacid spinning (the specific batch number is added next to each point, see Tab. 6.2 for the different batch characteristics). The points indicated by X refer to the best single values, while the spherical points represent best average values. The dotted black line has a slope of 1, indicating the expected scaling of specific strength with L/N.

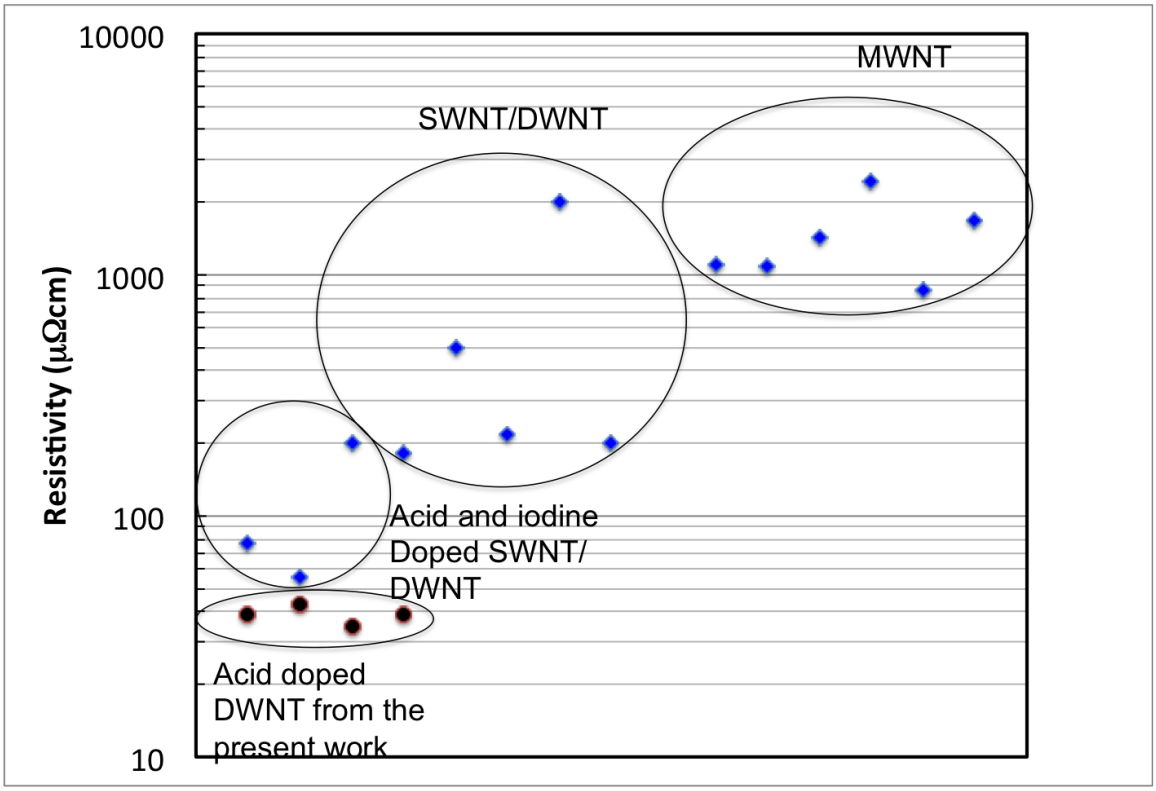

Figure 6.9 : This figure is the same as figure 2.9(b) in chapter 2 where fiber electrical conductivities are grouped by the constitutive CNTs type. The electrical conductivity measure for the different batches does not show strong dependence with CNT batch and all the measured values are the lowest average values ever reported for neat CNT fibers.

These processes take advantage of metal oxide solubility in weak acids such as HCl and the lower oxidation stability of fullerenes and amorphous carbon. More problematic are graphitic residual particles, very common in laser ablation SWNTs [Arepalli, 2004]. In fact, despite the good characteristics of laser ablation tubes (single walled, high quality, high aspect ratio when compared to HiPco SWNT), the amount and size of undispersed particles make fiber spinning problematic (small spinneret clogging and presence of un–dispersed particles in the final fiber). Even when spinning is performed from a larger spinneret (> 250 μm), the final fibers are still weakened by the presence of undispersed particles (Fig. 6.10). Despite the weak fibers, it is still remarkable how low concentration (less than 1 wt%) dopes with more than 50% impurities can still be continuously spun into fibers. In fact, this indicates the high quality of the SWNT and shows a potential approach to use CNT fibers as scaffolds to support functional nano or micron particles.

In conclusion, we have shown that spinning conditions need to be optimized for each single batch, with longer CNTs requiring lower concentration for optimal spinning (see Section 6.3.2 for further discussion about influence of spinning dope concentration on fiber properties). When the highest strength values are compared, the dependence on CNT type still holds, with longer CNT yielding the highest strength. The linear scaling is not perfect, particularly for long CNTs. This may indicate that spinning from long CNTs needs to be further optimized.

6.3.2 Influence of Spinning Dope Concentration on Fiber Properties

Rod–like polymers spinning dopes are usually characterized by high polymer concentrations (15-20% [Adams et al., 1989]). High concentrations are usually beneficial to fiber properties up to a limit where the dope becomes unprocessable.

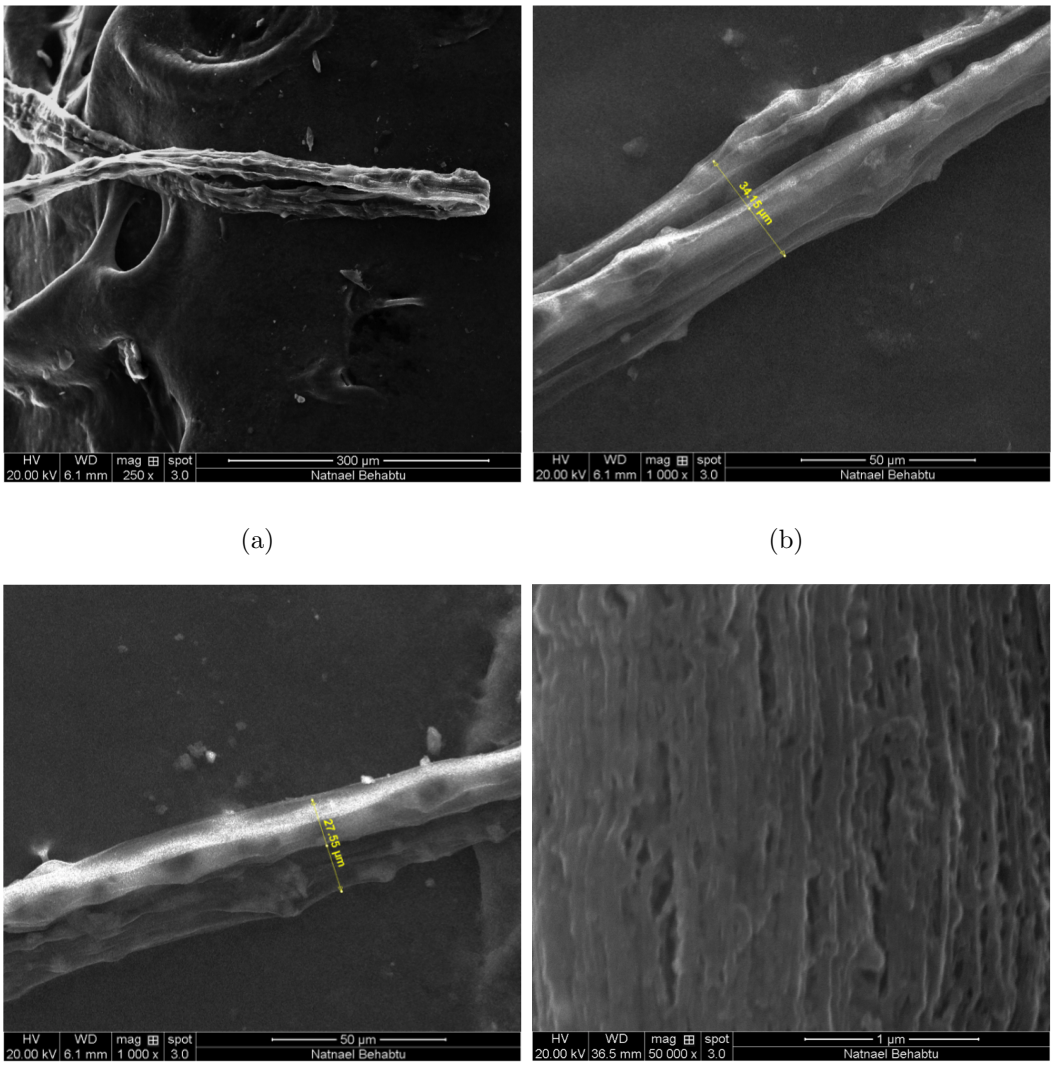

(a) (b)

(c) (d)

Figure 6.10 : Morphology of fibers spun from bio-laser oven SWNTs. Note the large amount of undispersed particles within the final fiber. Filtration of these undipspersed particles is very challenging due to the amount of undispersed particles (60 wt%) as well as their size (5-30 microns) comparable to the smallest filter available. Note how the morphology at higher magnification (Fig. 6.10(d)) is characterized by aligned bundles. These fibers were spun from 0.8 wt% SWNT/chlorosulfonic acid into DMSO coagulant from $\sim$ 300 μm tapered glass needle. The spun bio-laser SWNT were received from Dr. Benoit Simard's team at National Research Council, Canada

Superacid/CNT dopes can also be mixed to high concentrations with 20 wt% being the limiting values for the mixing procedure we have used so far (see section 6.5.2). The different concentrations show different fluid structure. The microscopy slides to visualize fluid structure are prepared by confining a small volume between a glass slide and a cover slip as detailed in [Davis et al., 2009]. Usually the sample is thinned to create an area where the sample can be visualized in transmission mode. High concentration dopes fracture while dope with at 6wt% or below can be thinned without major fractures (Fig. 6.11).

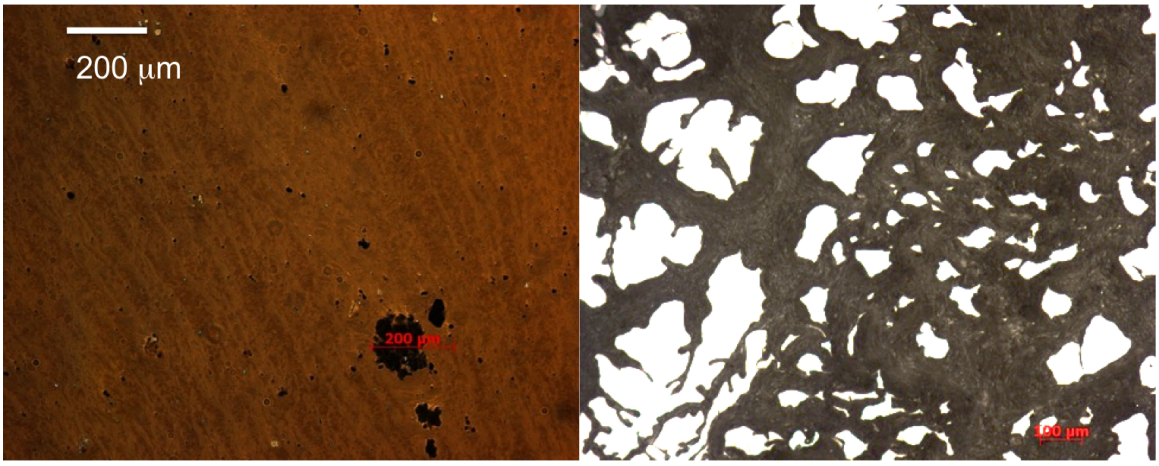

Figure 6.11 : Low magnification light micrographs of 6wt% dope (left) and 15 wt% dope. The images are acquired in transmission more. Note how lower concentration dopes are easily thinned while high concetration dopes tend to fracture.

Further differences are found at high magnification (Fig. 6.12 and 6.13). In fact, high concentration dopes are characterized by distinct birefringent nematic domains while 6wt% dope remains more homogeneous. As noticed in Chapter 5, sample preparation may dominate the observed structure, and the higher the concentration the longer is the characteristic time to attain equilibrium phases, thus we cannot interpret the observed structure through phases of equilibrium thermodynamics. A

possible explanation for the observed structures is the swelling of bundles found in the starting CNT powder. This idea is supported by the similarity of the dry material with and dope′s light micrograph (Fig. 6.15).

Inhomogeneous fluid structures persist even at low concentration. In fact, at concentration as low as 3 wt% darker (with higher optical absorption, thus denser) areas are clearly visible. Most probably, these are residual swelled domains in a lower concentration liquid crystal. Interestingly, their shape is reminiscent of liquid crystalline droplets in isotropic phase (see chapter 5).

Concentration differences translate directly into flowing behaviour. As expected, lower concentrations are easily filtered and filtration becomes increasingly difficult (higher filtration pressure and the requirement of multiple filtration units) at higher concentrations. Higher concentrations are also beneficial to coagulation. In fact, when fibers are spun with no tension into water, there is a visible increase in their diameter due to formation of HCl gas. Such an increase is less noticeable at higher concentration (Fig. 6.16). High dope concentration are also characterized by lower attainable spin draw ratio. This can be rationalized by the high elasticity of the spinning dope as a function of concentration. Thus, the same amount of deformation will induce higher stress on the fluid. The lower spin draw ratio values attained by high concentration spinning dope limits the fiber strength. In fact when fiber strength is plotted as a function of dope concentration, an optimal value can be found (Fig. 6.17).

Rigid–rod polymer spinning is characterized by an air–gap [Kwolek et al., 1977] (∼few centimetres) between the spinning die and coagulation bath. This gap is critical in achieving high strength fibers and has the main goal of separating two fundamental spinning processes: dope elongation and coagulation. We attempted

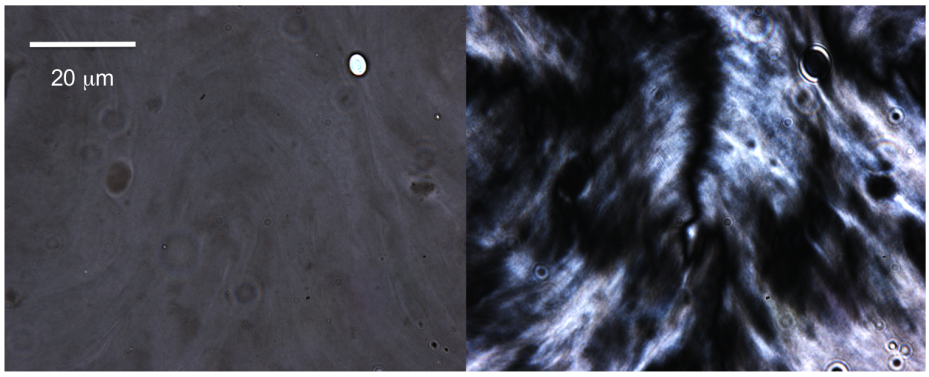

(a)

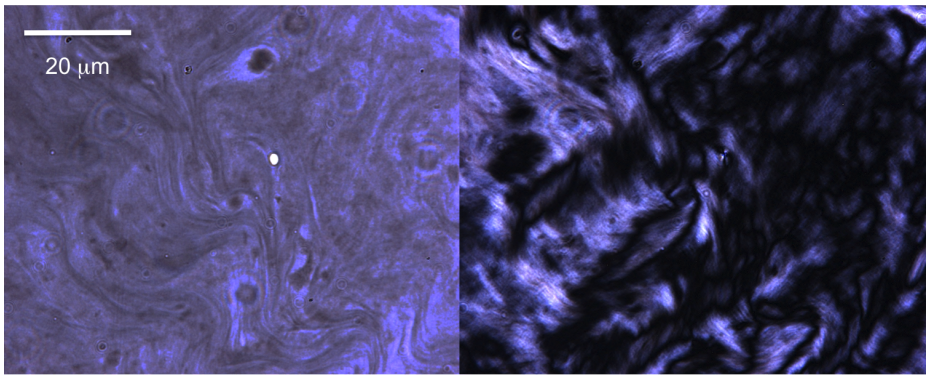

(b)

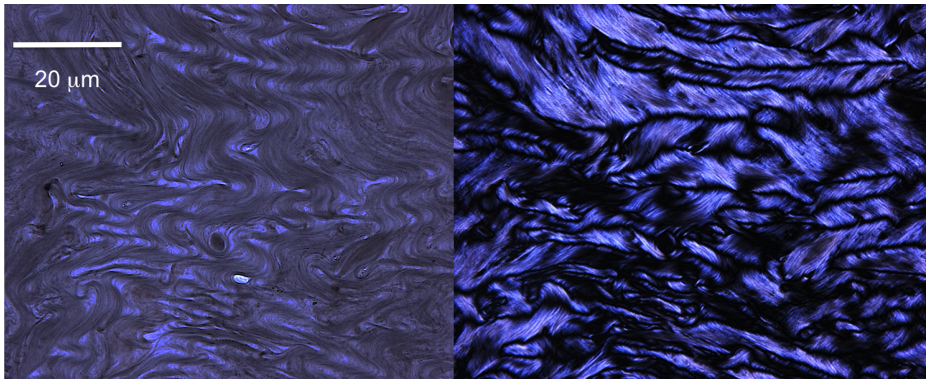

(c)

Figure 6.12 : Spinning dope at different concetration for XBC 1002 in chlorosulfonic acid. Figure 6.12(a),6.12(b) and 6.12(c) represent 5, 10 and 15 wt% respectively. Images on the left are in transmission mode. Images on the right are taken under cross polars.

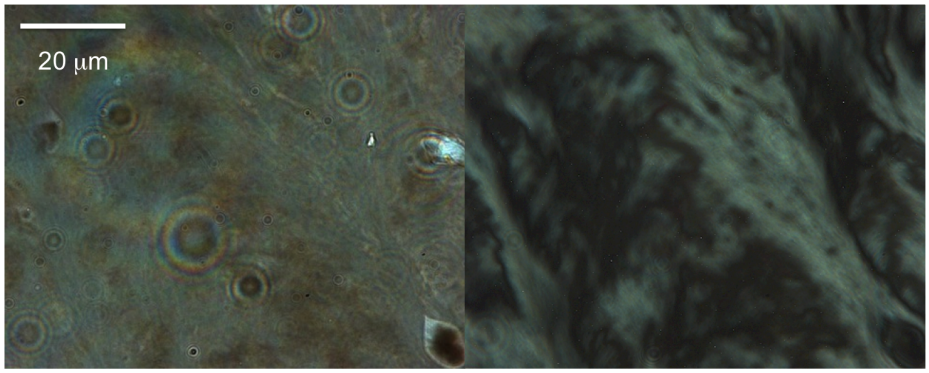

(a)

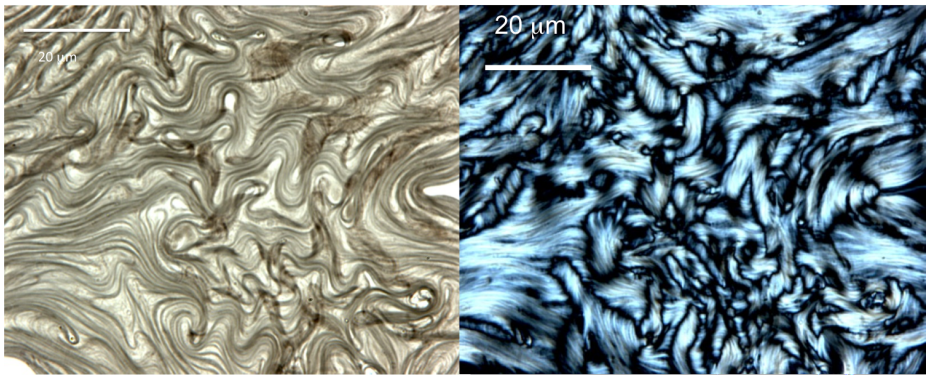

(b)

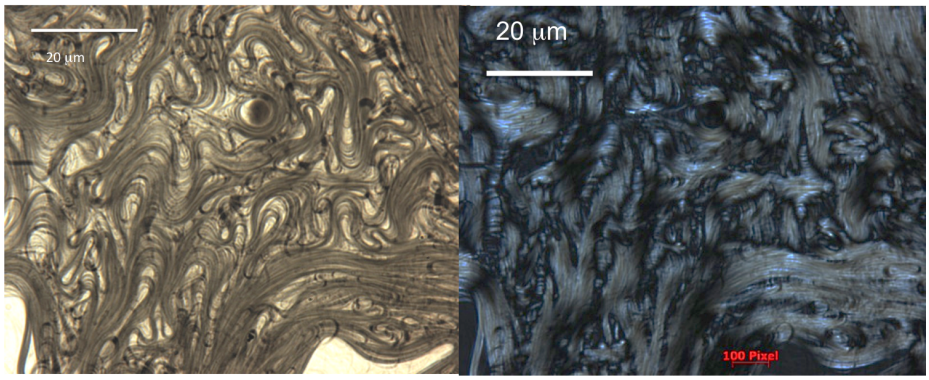

(c)

Figure 6.13 : Spinning dope at different concetration for XBC 1001 in chlorosulfonic acid. Figure 6.13(a),6.13(b) and 6.13(c) represent 6, 9 and 15 wt% respectively. Images on the left are in transmission mode. Images on the right are taken under cross polars.

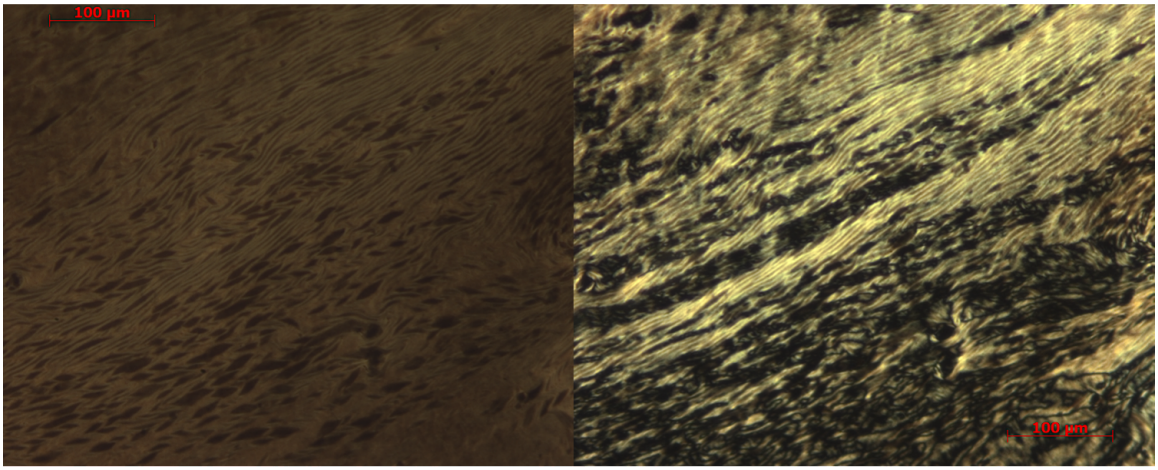

Figure 6.14 : Light microscopy of 3 wt% dope XBC 1001. Right image is aquired in transmission mode, the left image is the same spot under cross polarized light.

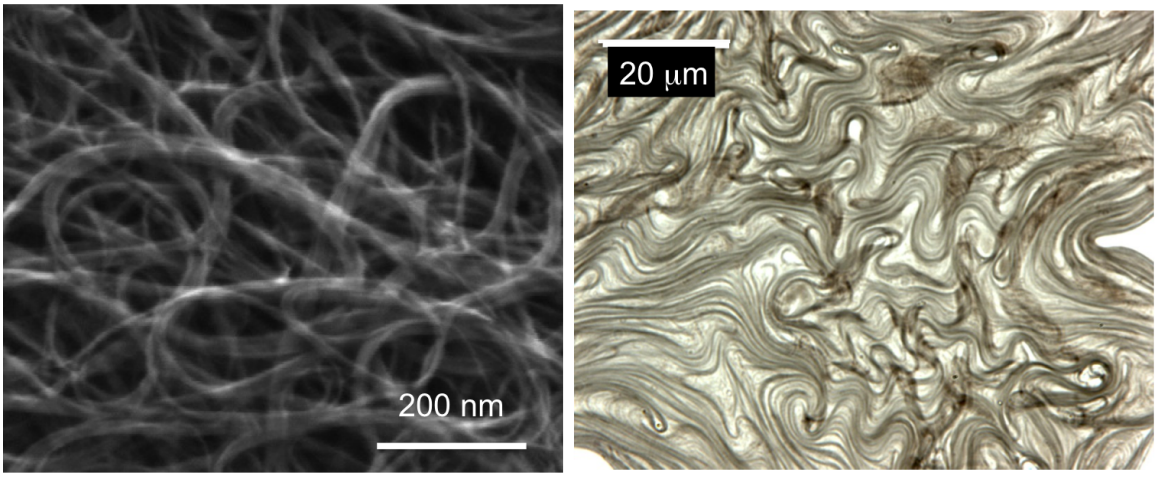

Figure 6.15 : On the left, an SEM micrograph of raw (as received before any acid processing) CCNI. On the right a 9wt% dope light micrograph. Note how the structure is similar, despite the difference in length scale.

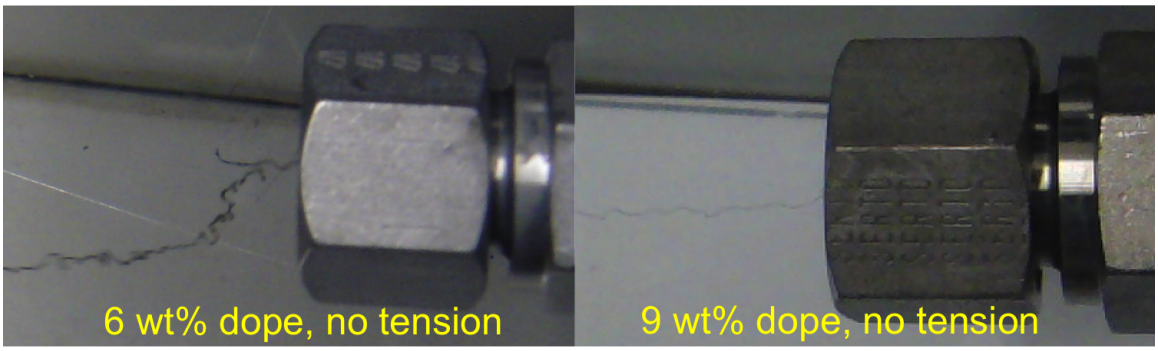

Figure 6.16 : Micro graph showing Die swell for 6 and 9 wt% dopes. The dopes are prepared from CCNI XBC 1001 and spun from 65 μm spinneret in water.

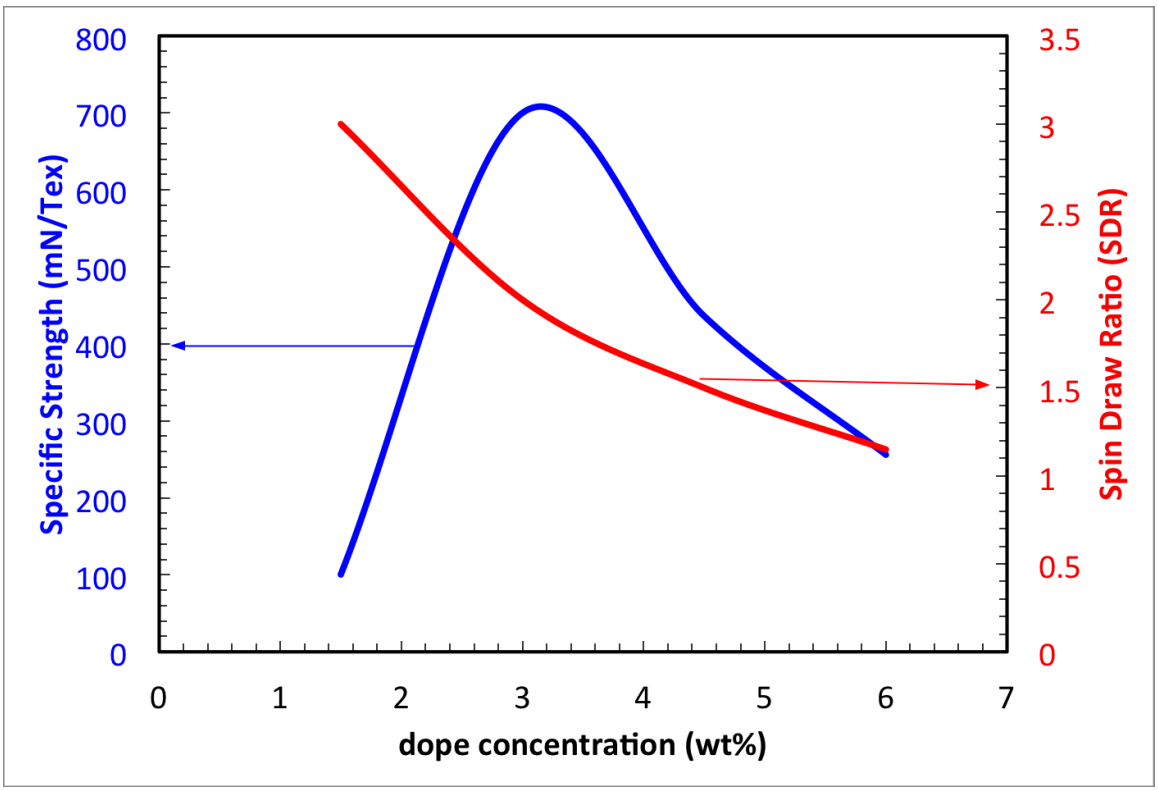

Figure 6.17 : Fiber strength as a function of dope concentration. The data refer to XBC 1101 spun at 1.5, 3, 4.5 and 6 wt%. The fiber spun at 1.5 wt% was too weak to be tested (also because it had too small of a cross section to be handled). They were all spun in acetone with a linear extrusion rate of 2 m/min and 65 micron spinneret.

to achieve air–gap spinning with multiple dopes and dies. However, a stable jet could not be obtained and it was often breaking and/or wetting the spinning die. Stable extruding jets were achieved with air gaps as large as 50 cm for dopes with concentration of 9 wt% and higher (Fig. 6.18); however, no tension could be applied on the spinning dope, indicating a relatively weak dope. This behaviour is in striking contrast with rigid–rod polymer spinning. This difference can be rationalized by the difference in dope strength, where rigid–rod polymer dope require higher stress before filament break–up while CNT dope breaks at relatively low stress. In fact, rigid–rod solutions may have hydrogen bonding even when in solution or they could become stronger as the solution cools down in the air–gap, preventing filament break-up during fiber thinning. Conversely, CNTs do not have any hydrogen bond interaction and they do not show strong phase transition (from liquid crystals to crystal solvates) as a function of temperature. Thus, the dope is weak. We expect longer CNTs to allow air–gap spinning since they increase the interaction per unit length, hence, the breaking stress of the fluid filament. In section 6.3.4 we will further discuss the influence of coagulation on the amount of tension (thus spin draw ratio) the fiber can handle during spinning.

In conclusion, CNTs can be mixed at high concentration (up to 20 wt%). At high concentration (higher than 6wt%) the structure of the spinning dope is characterized by elongated nematic structure which resembles the bundles found in the starting powder. We argue that at higher concentration the liquid phase may be simply characterized by swollen bundles. Even at concentration as low as 3wt% the spinning dope is non homogeneous. The spinning concentration influences coagulation, with higher dopes showing less reactivity that lower concentration dopes. We also argue that the elasticity of high concentration dopes limits the amount of spin draw ratio

Figure 6.18 : Air gap spinning from 15wt% CCNI XBC 1002 dope. Spinning die is 65 micron, aspect ratio of 2.

attained by a given spinning dope. This, in turn, limits the ultimate fiber strength. Moreover, tensioning during air gap spinning, a key spinning detail in rigid–rod fiber spinning, has not be attained with CNT/superacid spinning yet.

6.3.3 CNT/Superacid Flow Behavior and its Influence on Fiber Properties

Deformation rate and total deformation are two fundamental variables for fiber spinning since they promote or destroy alignment along the fiber axis. Deformation and deformation rate are influenced by flow rate, die geometry, drum speed and dope viscoelasticity (which in turn depends on CNT aspect ratio, concentration, and temperature). SWNTs in sulfuric acid show a typical shear thinning behaviour, found also in other rigid–rod nematic phases [Davis et al., 2004]. Similarly, chlorosulfonic acid solutions show a shear thinning behaviour at shear rates relevant for the fiber spinning process 6.19.

At low shear rate, liquid crystalline fluids show a highly nonlinear dependence of normal stress with respect to shear rate where a transition from positive to negative normal stress can occur. These transition often corresponsd to profound structural transformation within the fluid. From a fiber spinning point of view, positive normal forces correspond to fiber die swell and disruption of the order coming from elongation flow. Negative normal force correspond to die contraction, which may induce further order. SWNT/sulfuric acid show negative normal stress al low shear rate ($\dot{\gamma} \sim$ 10-100 s^{-1}) [Davis et al., 2004] similar to other nematic fluids. Extreme die swell can be encountered during CNT/chlorosulfonic dope spinning (Fig. 6.20). Thus it is important to quantify the extent of die swell under flow regimes relevant to the fiber spinning condition.

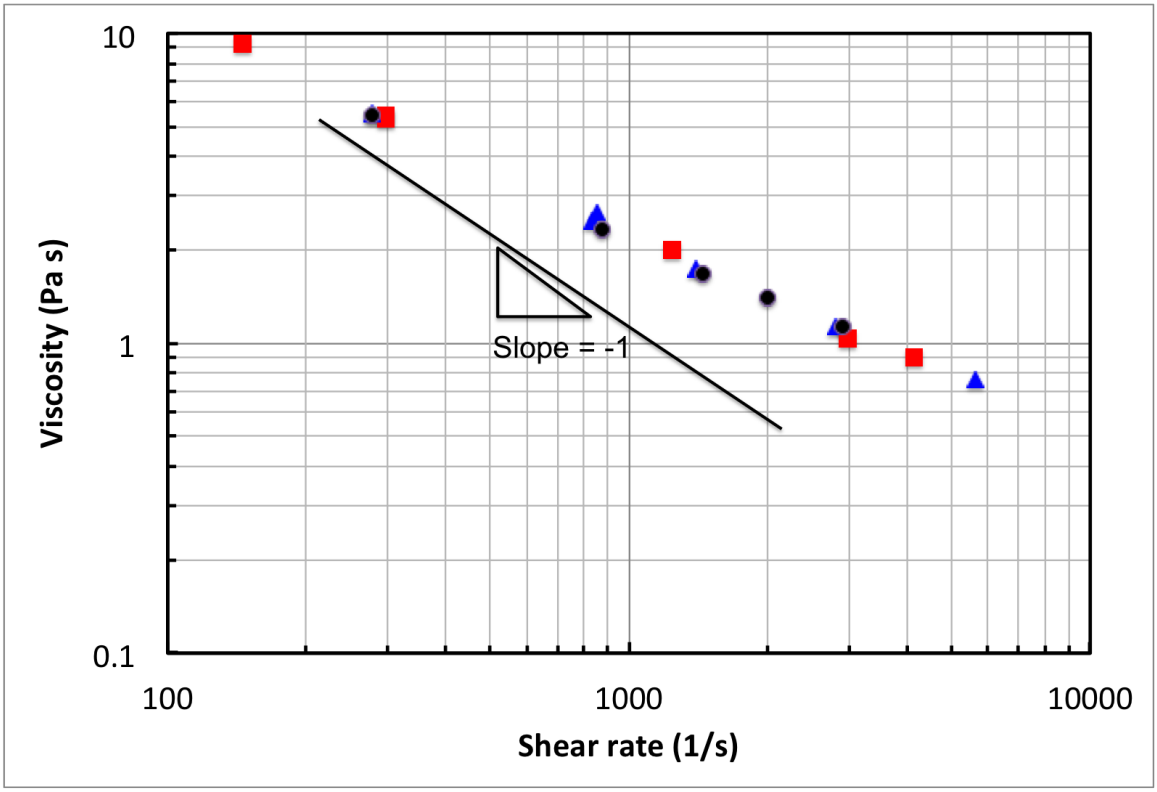

Figure 6.19 : Viscosity vs. shear rate for 6wt% dope CCNI XBC 1001. The data was acquired by measuring the pressure drop across a capillary 2.5 cm long and 175 μm internal diameter. The pressure and flow rate data was converted into viscosity and shear rate data by using the Weissenberg-Rabinowitsch equation [Macosko, 1994]. The data have a slope that is less steep than -1 (indicated by the black line in the plot) indicating that there was not wall slippage during data acquisition. The different labels (blue, red and black) represent data acquired at different times with the same dope, thus the data points differ in the pre–shear history. The overlap between different experimental points (at the same shear rate) indicate that the experiment is not altered by shear history of the dope.

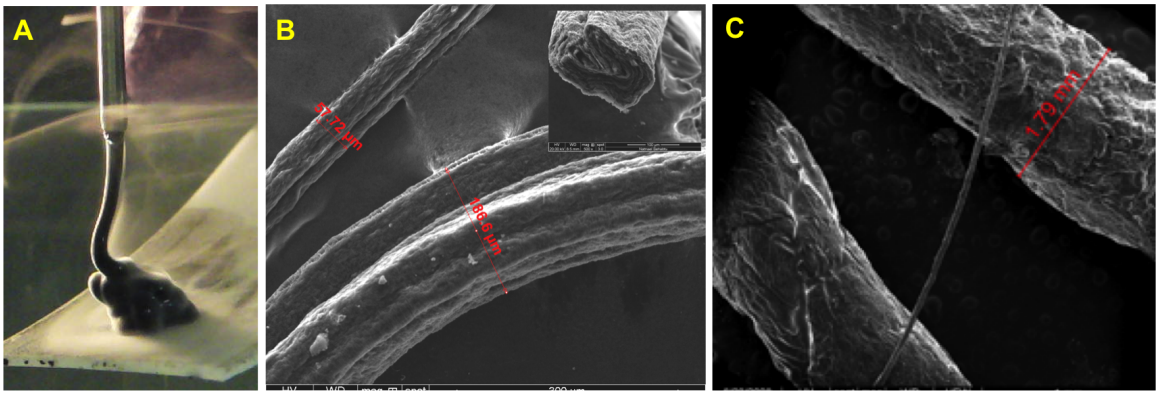

Figure 6.20 : Various examples showing significant die swell. A) 4 wt% HiPco Batch 195.3 in chlorosulfonic acid spun from 175 micron needle, 2.5 cm length. The dope is spun at 2.5 m/min. Note how the dope has a diameter comparable to external needle diameter (∼2 mm), thus a die swell of 10. B) fiber spun from 8wt% HiPco/chlorosulfonic acid dope from a 175 micron needle. Note how the dry fiber has a diameter that is larger than the spinning needle diameter. C) When long carpet are added in HiPco dope, dry fibers with diameter 10 times the spinning die (175 μm) can be obtained. Thus, die swell becomes even more significant when the length of the spun molecules become comparable or larger that the spinning die.

We quantified die swell by comparing the imposed linear extrusion speed to the actual linear extrusion speed measured at die exit. At the shear rate explored we did not encounter die shrinkage (or negative normal forces) and die swell increases with shear rate (Fig 6.21). Thus, high flow rates are expected to harm fiber strength since they are characterized by larger die swell, which disrupts order. The lack of air gap enhances the problem because there is not a coagulant free region where the fluid filament can thin down under the elongation imposed from the winding drum.

High flow rate influences also the maximum achievable spin draw ratio. (Fig. 6.22).

This can be rationalized by considering the stress contribution to a viscoelastic fluid. In fact both shear rate (which increases with flow) and total strain (whith increases with SDR) contribute to the total stress of the fluid. In fact, the fluid breaks at a critical stress, and a high stress contribution from shear rate imposes

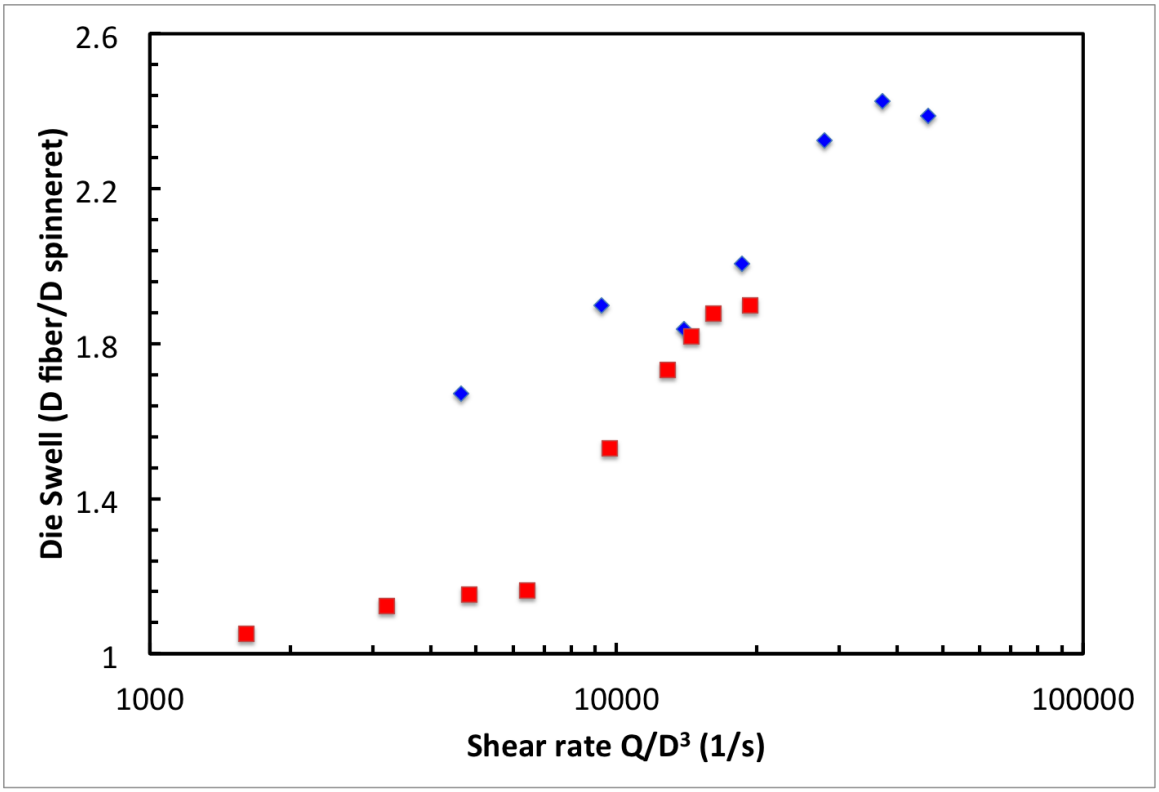

Figure 6.21 : Die swell as a function of shear rate. The dope is 6wt% XBC 1001 and the coagulation bath is water. The blue points are from 45 micron spinneret while the red points refer to 65 micron spinneret. The die swell was calculated as follows: after imposing a flow rate, the linear speed of the exiting fiber was calculated by measuring the fiber length per unit time. The square root of the ratio of the imposed linear extrusion rate and measured fiber linear speed is the die swell. Although the data may be influenced by the coagulant, the trend is representative of the typical behaviour of CNT/chlorosulfonic acid dopes as a function of shear rate.

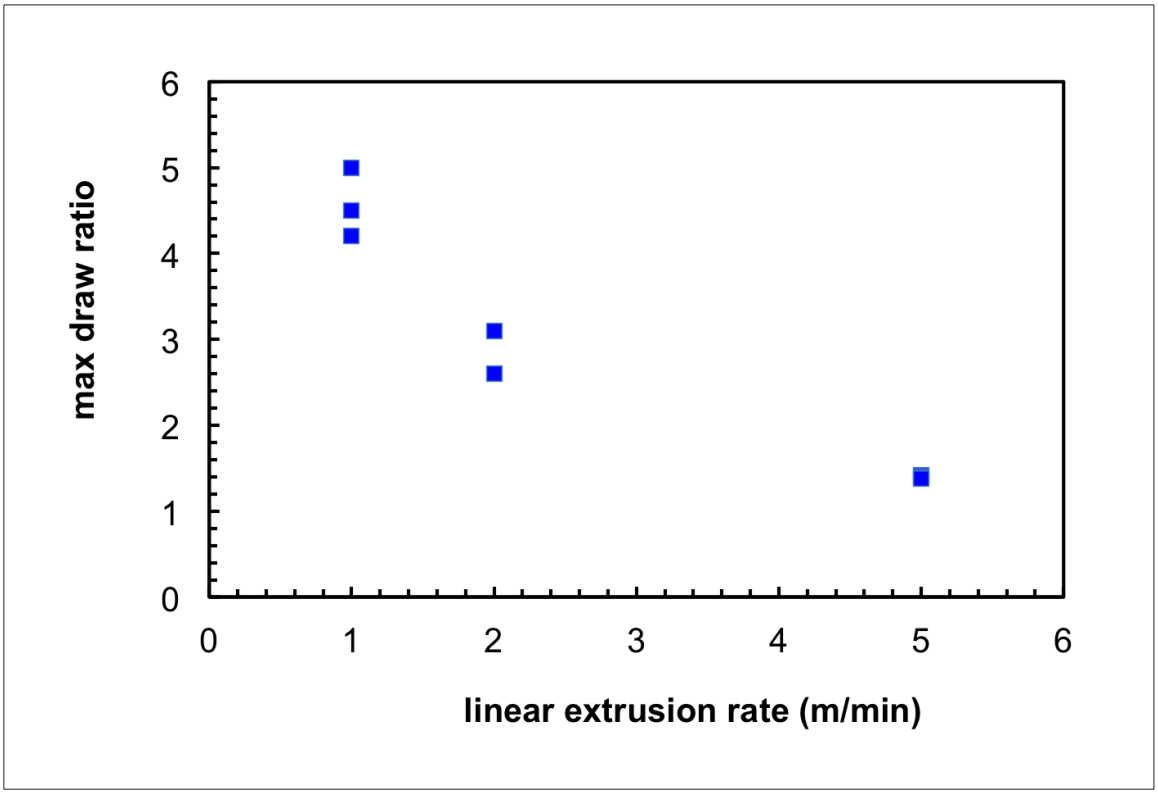

Figure 6.22 : Maximum spin draw ratio versus linear extrusion rate. For each flow rate the value was measured at least twice. The Maximum spin draw ratio is thus a decreasing function of linear extrusion rate.

lower stress from fluid strain, thus a lower SDR. This will thus give the observed behaviour of lower spin draw ratio for higher flow rate. The expected influence on fiber strength will thus be that higher flow rates (thus higher misalignment from die swell, and less alignment coming from SDR) yield worse fibers. Figure 6.23 shows fiber strength dependence as a function of flow rate. Specifically, fibers spun at high flow rate (hence lower spin draw ratio) yield significantly lower strength (both absolute and specific).

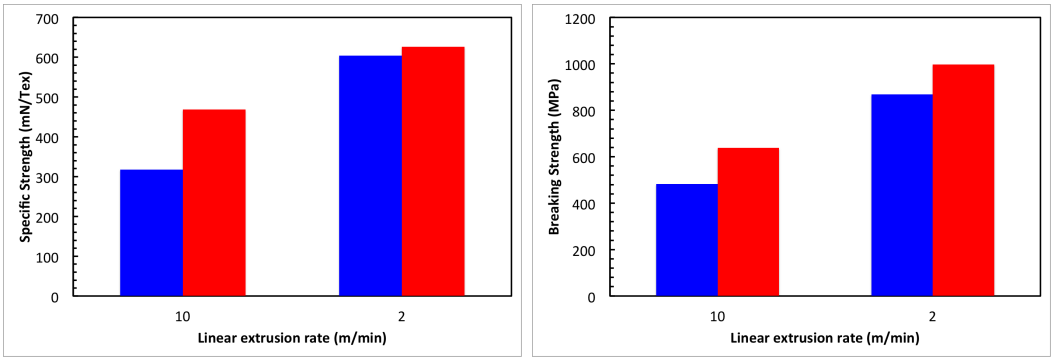

(a) (b)

Figure 6.23 : Influence of flow rate on fiber strength. Figure 6.23(a) and 6.23(b) are specific and absolute breaking strength for fibers spun from CCNI XBC 1101, 6wt% in acetone from 65 micron spinneret. Data in blue are average (over six breaking force measurements) values while in red are highest values. Fibers spun at lower flow rate (2 m/min vs. 10 m/min) yield stronger fibers. This is because the spin draw ratio (chosen to be close to the maximum draw ratio) is substantially different (1.5 for 2 m/min and 0.7 for 10 m/min).

A recurring theme is to maximize spinning conditions that lead to high spin draw ratio. We have observed this trend with concentration (Fig. 6.17) and now with flow rate (Fig. 6.23). In fact, when fiber strength and electrical conductivity are plotted as a function of spin draw ratio, irrespective of the specific spinning condition, a clear trend is found, where both fiber strength and electrical conductivity increase with

spin draw ratio.

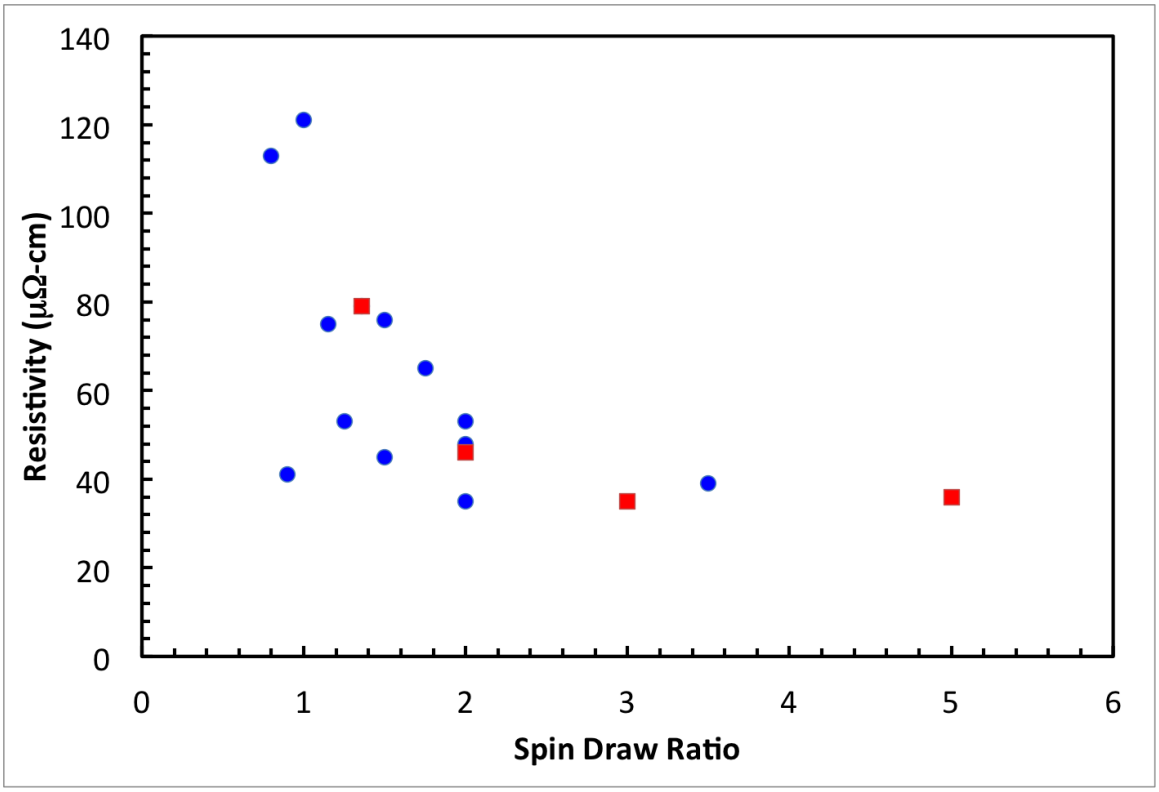

Figure 6.24 : The blue data points are for fibers spun from CCNI XBC 1101 while red points refer to CCNI X647H. The data refer to various coagulation bath, spinneret size, flow rate and dope concentration.

Extreme draw ratio can be achieved by using large diameter and low shear rate. We measured spin draw ratio as high as 96 when spinning from 250 micron spinneret. However, the fiber properties plateau around SDR=2, while spin draw ratio that are very large yield flat, ribbon-like fibers (Fig. 6.26).

We also compared the influence of spinning die on fiber strength when the fibers are spun under the same shear rate. Different spinning diameters are expected to give different coagulation dynamics. Moreover, small fibers are expected to yield higher strength than larger one [Wagner, 1989]. By spinning the same dope with the same

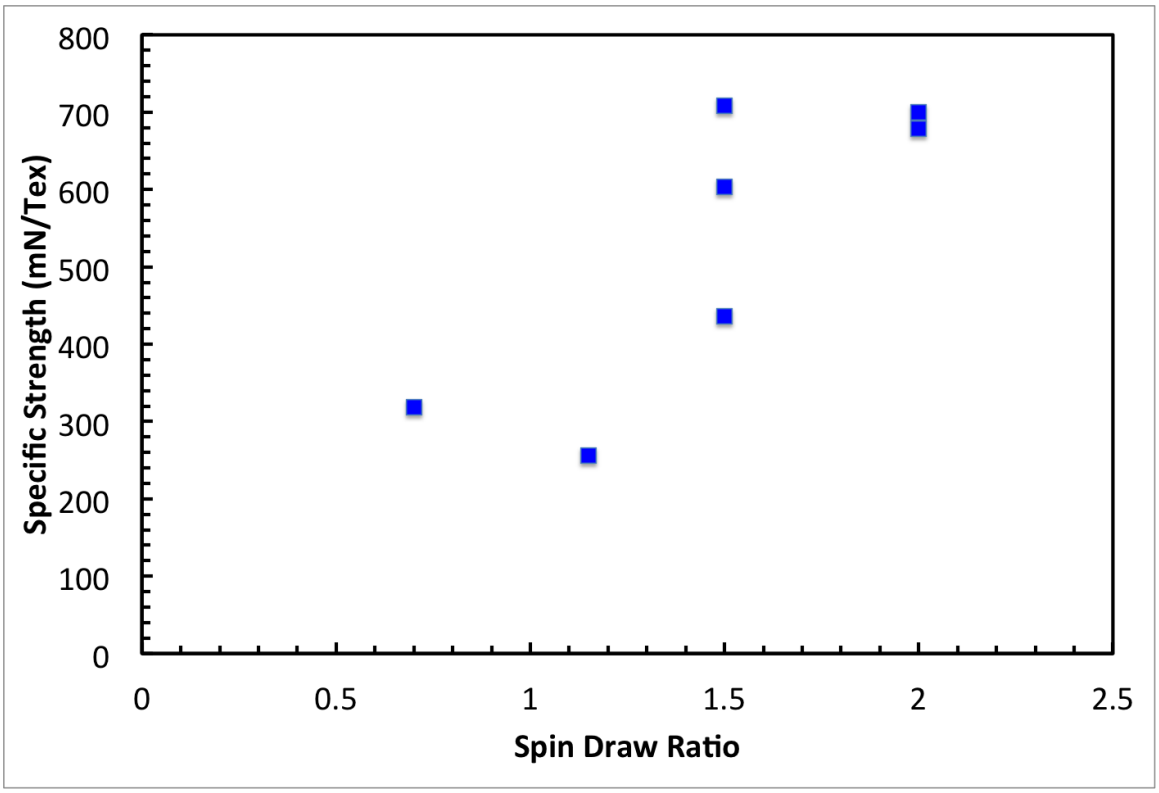

Figure 6.25 : The blue data points are for fibers spun from CCNI XBC 1101. The data refer to various coagulation bath, spinneret size, flow rate and dope concentration.

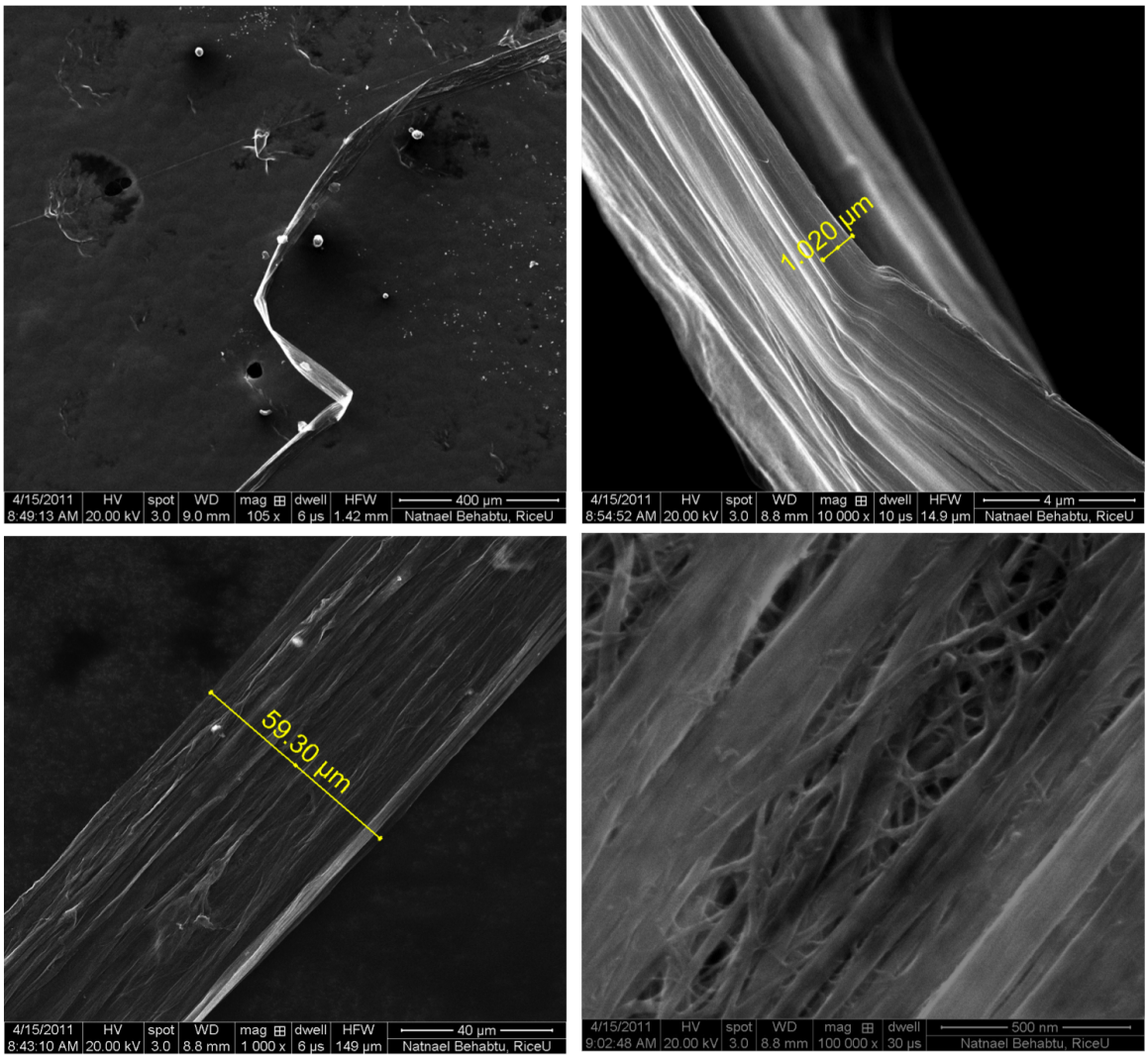

Figure 6.26 : Fibers spun from CCNI XBC 1001 6wt%, 125 μm spinneret, 10 mm long, spun at 0.5 m/min, SDR=24.

coagulant and flowing condition but different die diameters, surprisingly the fibers' specific strength is the same. But for tensile strength, smaller filaments (65 μm spinneret) were 50% stronger than fibers spun from a 130 μm spinneret. The same difference is also found in fiber resistivity (45 $\mu\Omega$ cm vs 35 $\mu\Omega$). These differences can be interpreted as differences arising from fiber density, with larger fibers being more porous that smaller one. This hypothesis needs to be further confirmed by analysing fiber cross section by FIB cutting.

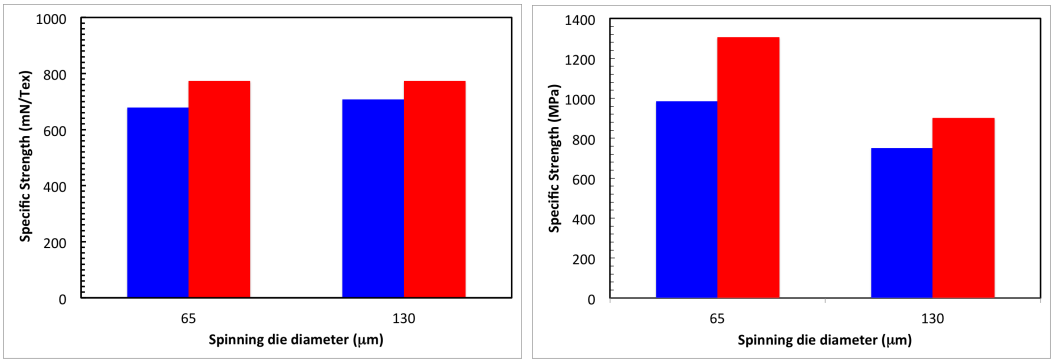

(a) (b)

Figure 6.27 : Figure 6.27(a) and 6.27(b) are the specific strength and tensile strength of fibers spun from two different spinneret size (65 and 130 μm). The dope was a 3wt% CCNI 1101 and the coagulant is acetone. The two fibers were spun keeping the same shear rate (2 m/min from 65 micron spinneret, 4 m/min for 130 micron spinneret). The spin draw ratio was 2 and 1.5 for 65 and 130 μm respectively. The SDR for fibers spun from 130μm could not be increased to 2 because of fiber breakage. Blue bars are average value, while red bars represent the highest single filament properties

In conclusion, we find that flow has a significant effect on fiber strength. This is because high flow rate induces large die swell and limits the total spin draw ratio the filament can undergo. In fact, both fiber strength and conductivity are strongly correlated with spin draw ratio with major changes occurring between SRD=1 and SRD=2. Very high spin draw ratio can be achieved from large spinnerets or low shear

rates; however, there is no corresponding improvement in fiber properties while the fiber morphology is strongly affected. We also compare fiber produced by different spinneret size and found that specific strength and conductivity are not affected.

6.3.4 Coagulation

The reactivity of chlorosulfonic acid imposes a strong limitation on the type of coagulant that can be used. Few solvents are not reactive. Chloroform and dichloromethane are among the few solvents that are miscible with chlorosulfonic acid without reacting. However, if we expand the coagulation list to slowly reacting fluids, diethyl ether, dimethyl sulfoxide (DMSO) and acetone can also be used as coagulants. However, they all complicate the fiber spinning process due to their flammability (diethyl ether, acetone) or for being carcinogenic (chloroform, dichloromethane), or because of the smell of the volatile reaction bi-product (DMSO). Water is an ideal coagulant because of low cost and its benign bi-product (acidic water with Cl^- and SO_4^{--} ions). However, the reaction of water with chorosulfonic acid is highly exothermic, leading to HCl gas formation, which in turn compromises fiber structure (Fig. 6.28).

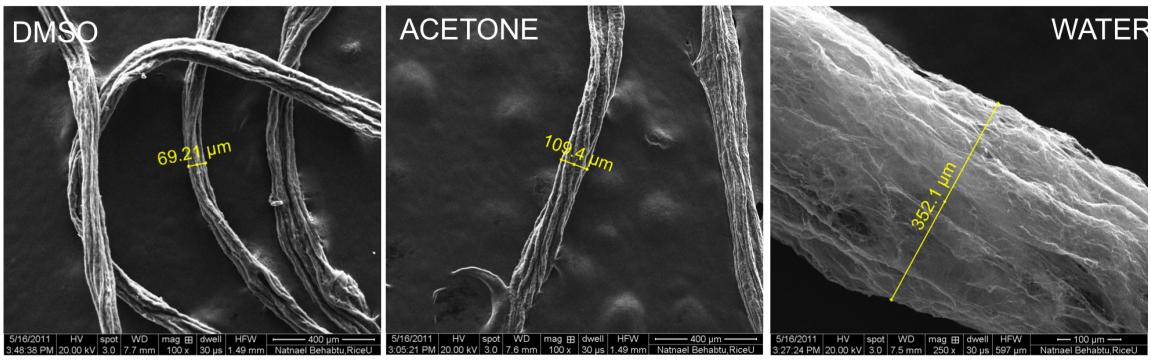

Figure 6.28 : Hand spun fiber from 0.5 wt% 500 micron long carpets (Received from Dr. Hata group, AIST, Japan). Note how the water coagulated fibers have high porosity with diameter three to five times the size of acetone and DMSO coagulated fiber.

In order to decrease the amount of reacting water, 98% sulfuric acid can be used. However, the low solubility of HCl in sulfuric acid induces major release of HCl gas from the forming fiber during coagulation, which disrupts fiber morphology (Fig. 6.29). Interestingly, HCl solubility in water is higher than in concentrated sulfuric acid [Luo et al., 1994]. In fact, when the fiber is tension with SDR larger than one, a more regular fiber is formed (Fig. 6.29(c)). Thus, small fibers (that do not saturate the coagulation bath with HCl) allow for a successful (without HCl release from the coagulating fiber) spinning. We have empirically found that 3wt% is a lower bound for CNT concentration when dope is spun from 65 μm spinneret. Coagulant and dope temperature as well as coagulant composition can strongly affect solubility, thus this bound can be easily modified by designing experimental conditions that increase HCl solubility in the coagulation bath.

Even more interesting is the dependence of maximum attained draw ratio with various coagulant. Despite the specific values of maximum spin draw ratio varies based on spinning conditions (dope concentration and flow rate and CNT type) we found the following order (ordered from the fluid that allow for the highest draw ratio to the fluids that allow for the smalles maximum draw ratio):

1. Water;
2. Acetone;
3. DMSO;
4. Concentrated sulfuric acid (98%), chloroform and dichloromethane.

This list also corresponds to the coagulation rate of the different coagulants with water being the fastest coagulant while chloroform and dichloromethane being the

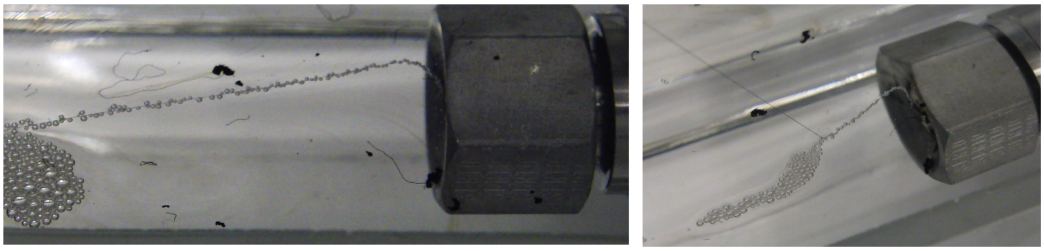

(a)

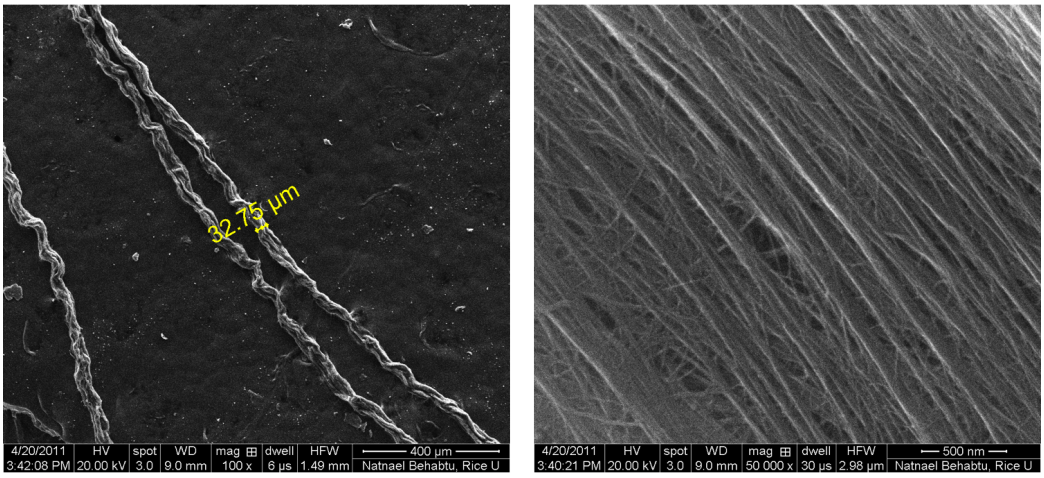

(b)

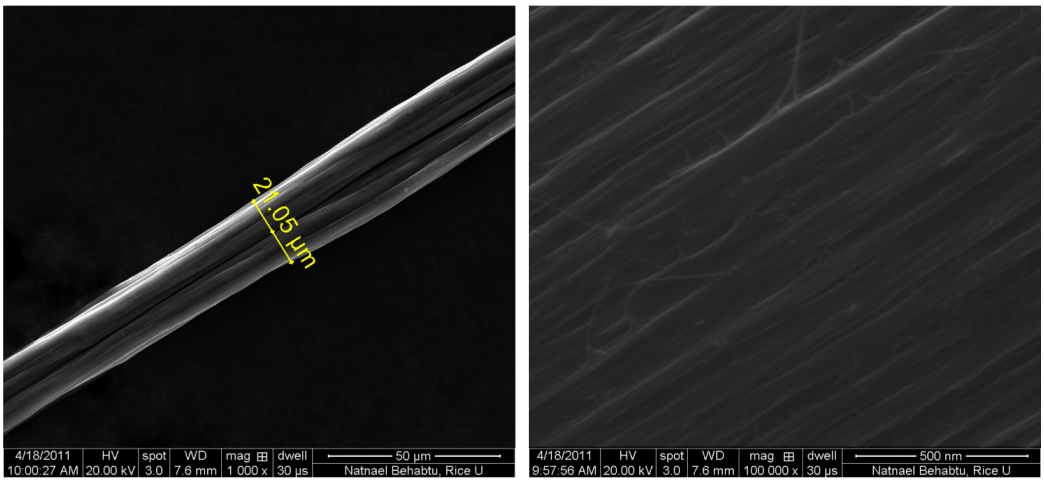

(c)

Figure 6.29 : Fiber formation in 98% sulfuric acid. Figure 6.29(a) shows a 9wt% dope (CCNI XBC 1001) spun from 65 micron spinneret being coagulated in 98% sulfuric acid. Note the amount of bubbles formed around the filament. Figure 6.29(b) shows the morphology of the fibers thus formed. The fiber looks irregular, although order is locally maintained. Figure 6.29(c) shows a fiber made from the same dope coagulated in water with a SDR of 1.1. HCl gas does not saturate water, avoiding bubble formation.

slowest coagulants of the list. Often fast coagulation corresponds to collapsed irregular cross section. This is true also for CNT/super acid spinning (Fig. 6.30). However, this difference in coagulation rate does not seem to translate as difference in fiber strength. In fact when 3wt% CCNI is spun in acetone and water, the fiber yields optimal electrical resistivity (39 and 35 $\mu\Omega$ for water and acetone respectively) and strength (average strength of 1GPa for both).

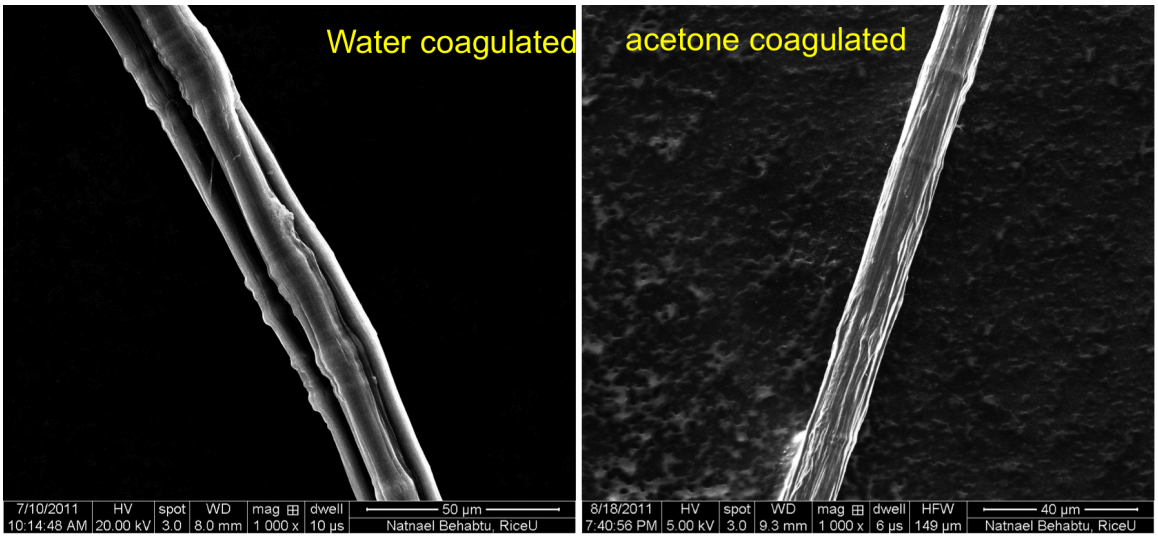

Figure 6.30 : Water vs. acetone coagulated fibers. Both fibers were spun from 6wt% CCNI XBC 1101 under similar flow conditions. The main difference is the coagulant.

In conclusion, we find that water can be successfully used as a coagulant. This is surprising since water and chlorosulfonic acid are highly reactive. Successful coagulation requires small filaments (achieved by small spinneret die and/or high spin draw ratio) to limit the amount of released HCl from chlorosulfonic/water reaction. We also find that the maximum attainable spin draw ratio is affected by the type of coagulant, with water being again the fluid that allows for the highest attainable draw rate. As expected, fiber morphology is affected by such a fast coagulant. However, irregularities in fiber morphology seem not to translate into different fiber properties.

6.4 Preliminary Studies on Spinning Scale-up

High performance is only one of the two requisites for technology adaptation. Manufacturability is key for cost control through process scale–up. In fact, difficult scale-up has been a key roadblock to the commercialization of nanotechnology products. The cost C of building and operating chemical and manufacturing equipment follows the power law $C \sim V^n$, where V is the material throughput (hence, the unit cost c drops as $c \sim V^{n-1}$). Replicating equipment (n=1) is one way to scale-up. Historically, the scale–up of fiber production by wet–spinning has followed $n = 0.7$, which is typical of large–scale production of chemicals [Perry and Green, 1997]. As an example, scaling–up from single filament (10 μm diameter, 1 g/cm^3 density, 10 m/min, typical of both wet and direct CNT spinning) to the Defense Advanced Research Projects Agency (DARPA) requirements[‡] for high-performance CNT fibers (600 kg/yr) requires a scale–up factor of ∼1500, which translates to a ten fold reduction of unit costs by wet spinning compared to replication of single–filament spinning lines. We demonstrated scalability of solution spinning by using multi–hole spinneret under the same condition as the single hole spinning (same linear extrusion rate per hole and spinneret diameter) (Fig. 6.31(a) and 6.31(b)). The only required change was a simple switch of the spinning plate, with no alteration of any other hardware. The produced 7–filament fibers showed the same average breaking strength as the monofilament ones. Scaling–up to 1000 hole (which is typical for commercial spinning of aramids and carbon fibers) would readily meet DARPA throughput requirements.

[‡]https://www.fbo.gov/index?s=opportunitymode=formid=4da93a9815f8c24420353b6f43f1824dtab=core_cview=0

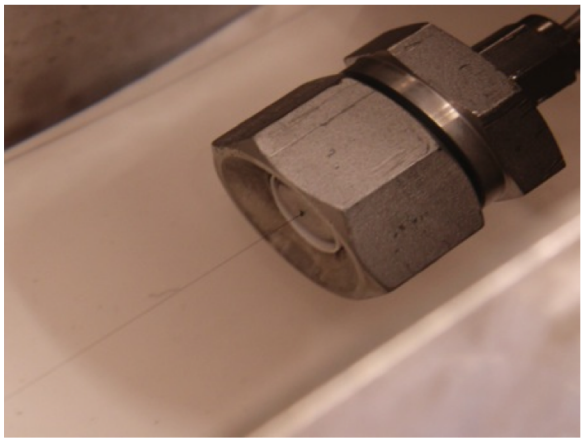

(a)

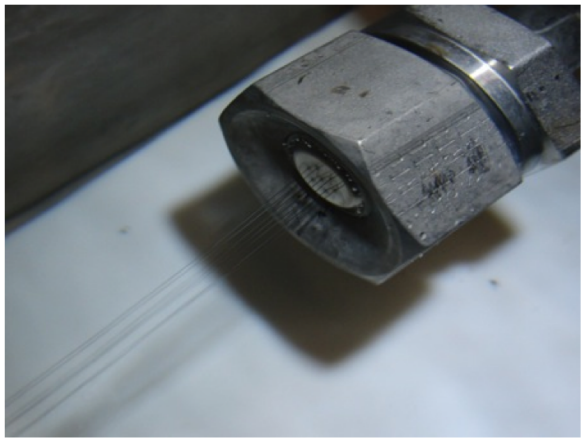

(b)

Figure 6.31 : Figure 6.31(a) shows a single filament wet spinning. Figure 6.31(b) shows spinning from seven hole spinneret.

6.5 Experimental Details

6.5.1 Spinning and Filtration Apparatus

In a typical spinning experiment, the dope is loaded by hand in one spinning chamber in an inert environment (dry air glove box). The chamber is then attached to another spinning chamber through a filtration unit (Fig. 6.32). If the filtration cannot be performed by hand, one side of the spinning chamber is connected to a hydraulic piston driven by a syringe pump (Harvard Apparatus PHD Ultra Hpsi Programmable Syringe Pumps) capable of applying pressure up to 2000 psi. If one filter unit is not sufficient to fully filter the dope, the filter unit is changed and the filtration continued. We have noticed that this operation can introduce air bubbles within the dope making the dope compressible and spinning problematic[§] (Fig. 6.33).

Once the dope is filtered, the two chambers are decoupled and the spinneret is attached to the dope–containing chamber through a bendable pipe (SS 2 mm I.D.). Although we conducted a few successful spinnings while having a guide roll, we have conducted most of the spinning experiments in a horizontal configuration with no guide roll. We did so to avoid introducing an extra experimental variable. A winding drum was also immersed in the coagulant fluid. Thus, we effectively have a coagulation time as long as the experiment (∼few hours). We performed some experiments with the winding drum outside the coagulation bath while using DMSO as a coagulant. With very short residence time (half a seconds) the fiber emerging from the coagulant would fume and release HCl gas. The HCl gas is formed by the reaction of residual chlorosulfonic acid with moisture indicating lack of coagulation. Moreover,

[§]When air is present in the dope this will expand near the spinneret as the pressure drops making dope flow rate variable and unstable.

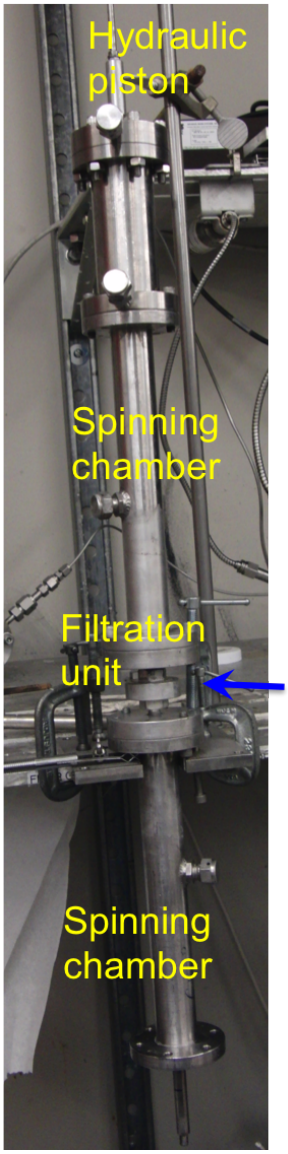

Figure 6.32 : Filtration unit.

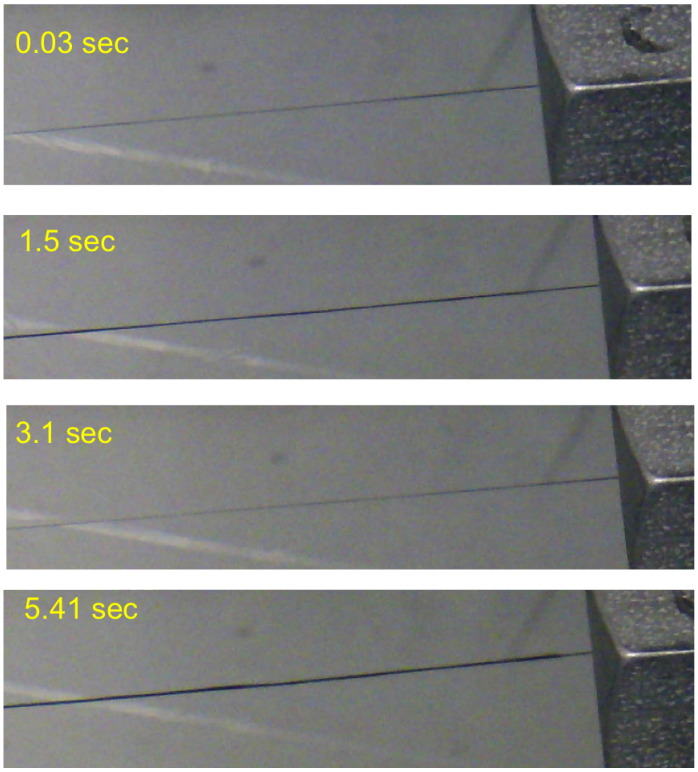

Figure 6.33 : Irregular flow behavior while spinning 6wt% CCNI XBC 1001 6wt% in water from 65 μm spinneret.

when stainless steel drums are used, a clear sign of corrosion can be seen.

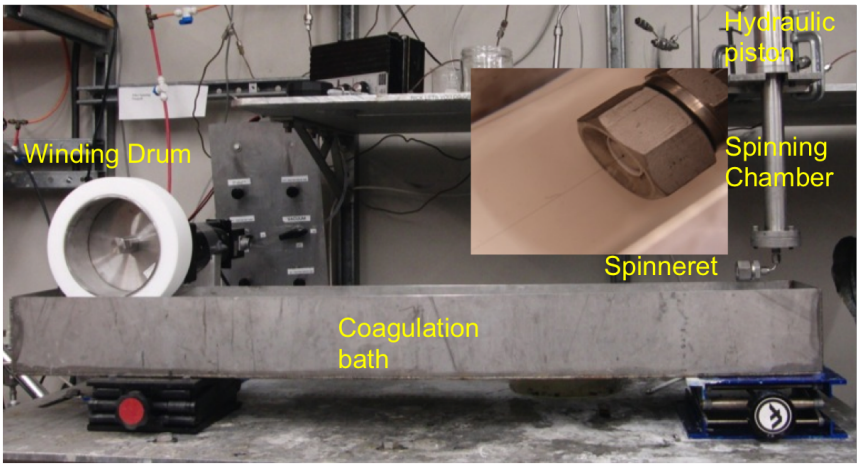

Figure 6.34 : Fiber spinning apparatus with winding roll not immersed in the coagulant.

6.5.2 Dope Mixing

We used the speedmixer (DAC 150.1 FV-K, FlackTek Inc), a dual asymmetric centrifugal mixer that allows mixing without having moving apparatus in contact with the solvent [Massing et al., 2008]. Mixing is usually carried out for a total of 40 minutes at 3500 rpm. The surface of the solution with the mixing gives a first indication about mixing quality (Fig. 6.35).

Rough free surface on the mixing vials were obtained mixing at 25 and 20 wt% of XBC 1002; thus, for the type of mixing adopted, 20 wt% can be considered as an upper processing bound. Since mixing was performed at room temperature, high temperature mixing may further push this limit. High concentration dopes (up to 15wt% for both XBC 1002 and XBC 1001) have been mixed, filtered and spun into fibers.

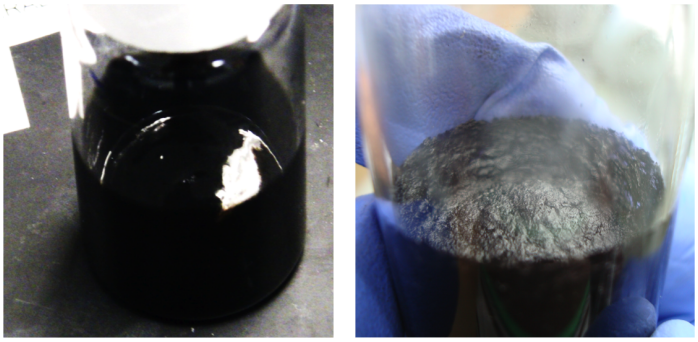

Figure 6.35 : Two vials showing CNT chlorosulfonic acid solution. The left vial shows a typical well-mixed solution with smooth top surface. The right vial shows a rough top surface after mixing, typical of incomplete mixing.

6.5.3 Capillary Rheometry

A capillary rheometer was built by modifying the spinning apparatus. In fact, two spinning chambers were connected by a SS capillary tube (Fig. 6.36).

The raw experimental data are pressure drop and and flow rate. This data can be fitted to calculate dope viscosity of a power law fluid following the Weissenberg-Rabinowitsch equation [Macosko, 1994]:

$$\dot{\gamma}_w = \frac{Q}{\pi R^3}\left[3 + \frac{dlnQ}{dln\tau_w}\right] \tag{6.9}$$

$$\tau_w = \frac{Rp_c}{2L}, \tag{6.10}$$

where Q, $\dot{\gamma}_w$, τ_w, L, R and p_c are flow rate, shear rate at wall, shear stress at wall, capillary length, capillary radius, and pressure drop across capillary. The experimental data can be used to evaluate the slope of ln(Q) as a function of ln(τ_w) as well as the shear stress at the wall. Once these values are known, the viscosity can be calculated as follows:

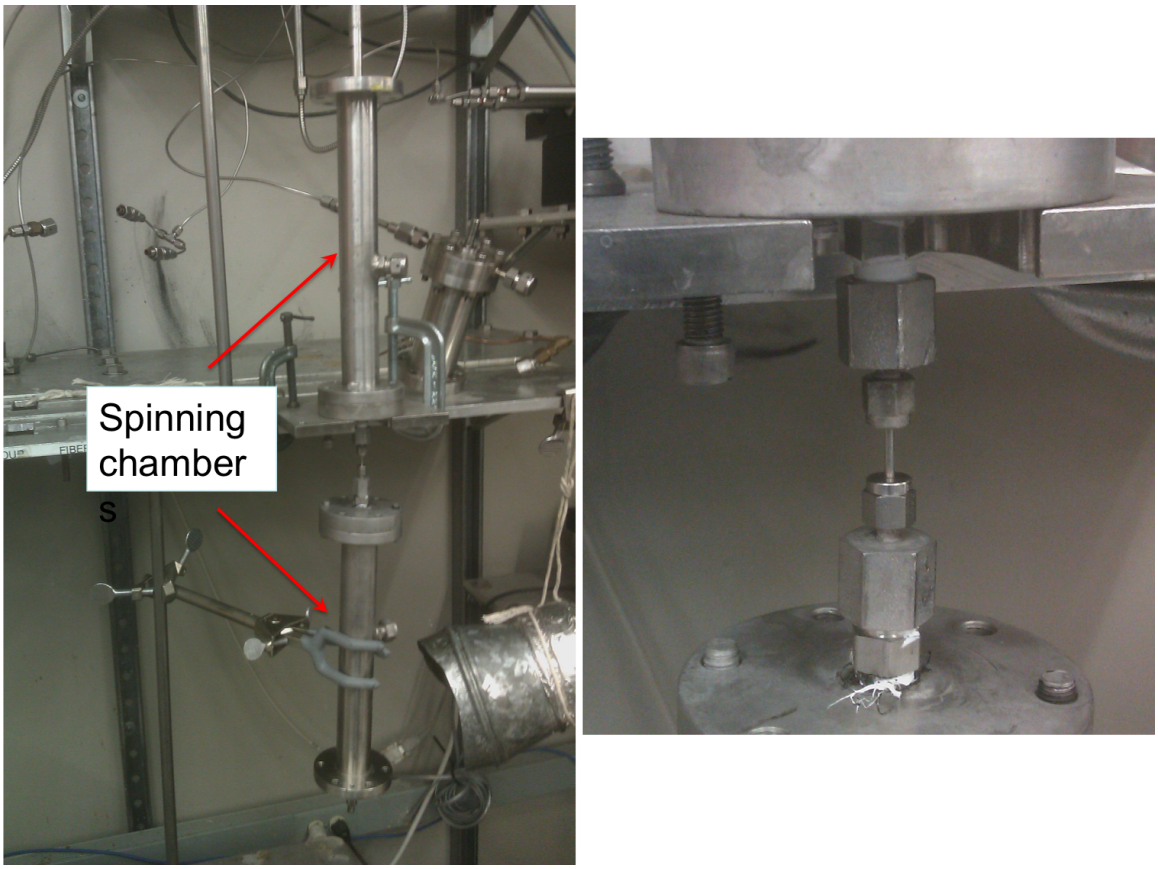

Figure 6.36 : Capillary rheometer. The two chambers are connected by a capillary tube 9175 μm I.D., 1 in. long. A typical experiment has as raw data the flow rate and the pressure drop across the capillary.

$$\eta(\dot{\gamma}) = \frac{\tau}{\dot{\gamma}} \tag{6.11}$$

The experiment can be further refined by using capillaries with different length and extrapolate the extra pressure drop created by the system.

6.5.4 Assessing Spinning Flow Stability Though Measurement of Maximum Spin Draw Ratio

Spinning pressure drop is often small (∼10 Psi). Thus, small pressure variation may change flow output. Thus, a stable pressure profile may not always correspond to stable flow rate. A better indication of stable flow rate is the maximum achievable spin draw ratio (Fig. 6.37). For the typical spinning condition, tens of minutes are usually required for a stable spin draw ratio, hence flow rate, to be achieved.

6.5.5 Nanotube Batch Characterization

Table 6.2 reports some of the variables that are experimentally measured to characterize a given batch. The average aspect ratio is quantified by capillary rheology[¶]. These measurements are further supported by the isotropic to biphasic transition concentration. In fact, this transition is another bulk measurement that can be correlated to aspect ratio by assuming that chlorosulfonic is an athermal solvent (assumption validated by modelling results [Green et al., 2009b]) and that rod polydispersity is not too large.

[¶] This methodology is still under development by Dmitri Tsentalovitch, Pasquali Lab Rice University

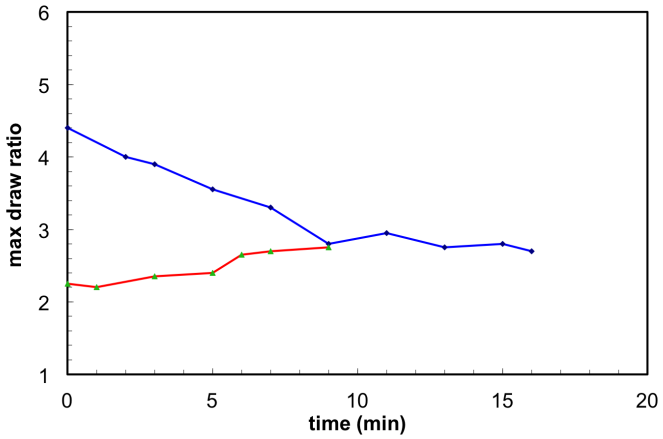

Figure 6.37 : Maximum spin draw ratio versus time. The blue curve shows the maximum spin draw ratio as a function of time as flow rate is changed from 5 m/min to 2 m/min. The red curve refers to a change in flow rate from 1 m/min to 2 m/min. Both curves was obtained from 3 wt% CCNI XBC 1101 spun from 65 micron spinneret, aspect ratio of 2. The coagulant is room temperature acetone. Note that roughly 10 minutes are required for stable spinning to be attained. As SDR is changing spinning pressure is stable at 10 PSI with no noticeable trend

Photoluminiscence is a viable technique to quickly measure the diameter distribution of semiconducting SWNTs in a bulk phase [O'Connell et al., 2002]. There is an ongoing debate about photoluminuscence of DWNT (the most promising CNT for fiber processing up to date). Specifically, it is unclear if the detected photoluminiscence is due to SWNT by–products. Even when emission is clearly coming from the inner wall of DWNTs, this has significantly lower intensity with some double walled carbon nanotubes (DWNTs) emitting light but most DWNTs having zero emission [Yang et al., 2011]. Thus, DWNT diameter measurements are usually performed by high resolution TEM. Albeit direct, such a technique is time consuming and impractical for statistically significant measurements.

	XBC 1001	XBC 1002	XBC 1101	X647H	HiPco 183.6
$wt\%_{iso}$(ppm)	325	225	162	-	
$(L/D)_{\eta}$	1860	2460	3660	4510	1600
Number of walls	2	2	2.55	2.25	1
$\langle D \rangle_{ex}$ (nm)	2	2	3.2	2.4	1
ρ	1.7	1.7	1.5	1.73	1.7

Table 6.2 : Carbon nanotube characterization. XBC 1001, XBC 1002, XBC 1101 and X647H are all carbon nanotube from CCNI while HiPco 183.6 comes from HiPco reactor at Rice University. The different materials are characterized through the isotropic/biphasic transition concentration (expressed at weight fraction – $wt\%_{iso}$) isotropic to biphasic transition, aspect ratio as measured through solution extensional viscosity at 500 ppm wt% (except for HiPco 183.6), number of walls and average external diameter $\langle D \rangle_{ex}$. Number of walls and external diameter are quantified through high resolution TEM by measuring at least 50 different nanotubes. Extensional viscosity and isotropic to biphasic transition data were acquired and processed by Dmitri Tsentalovich, Pasquali Group, Rice University, Houston, TX.

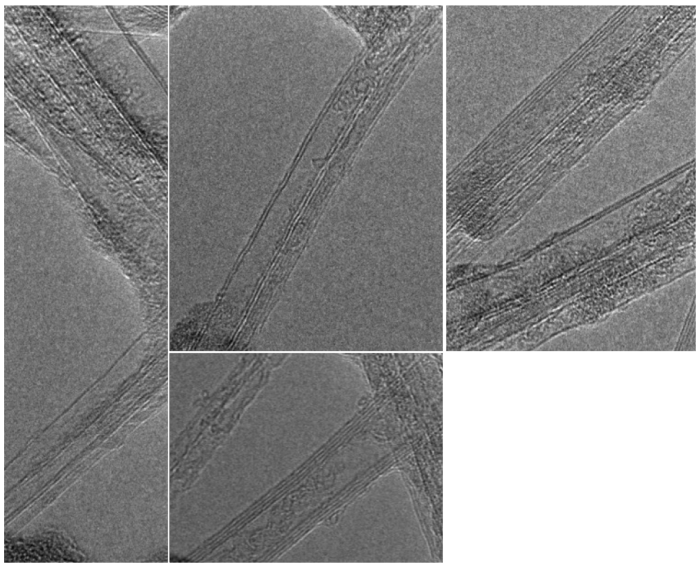

Figure 6.38 : High resolution TEM of CCNI XBC 1101. These type of images are used to quantify the external diameter and number of walls of a given batch. The wall spacing is assumed constant and equal to 0.34 nm and used as an internal scale bar to measure CNT diameter.

6.5.6 Electrical Conductivity and Mechanical Properties Measurements

Room temperature electrical resistivity measurements were performed on pieces of fiber that were approximately 25 mm long by measuring the fiber resistance with a Fluka multimeter and the fiber diameters with SEM. Fibers were attached to a glass slide with silver paste. Three silver paste contacts were made so that the space between the first two contacts was approximately 4 mm and the space between the second and third contact was about 16 mm. This spacing was chosen in order to make it possible to calculate the contact resistance of the silver paste. The glass slide was placed on a hot plate ($\sim$100 °C) for 20 minutes and then allowed to cool down for 1 hour. Then, the resistance, length, and average diameter of the fiber between each contact was measured. We used the following equation to calculate electrical resistivity:

$$\rho_{el} = R_{el} \cdot \frac{\pi}{4L} D_f^2 \tag{6.12}$$

where ρ_{el}, R_{el}, D_f and L are electrical resistivity, electrical resistance, fiber diameter (average over multiple SEM projection measurements) and fiber length. The contact resistance for each piece of fiber was calculated by performing a linear fit of the resistance as a function of length and calculating the resistance when length equals zero. Then, the contact resistance was subtracted from the measured resistance and the resistivity of the fiber was calculated by equation 6.12.

Stress–strain curves were obtained on an Instron machine with 5 gram load cell. The samples were prepared by fixing single filaments on a hollow card mount with a gauge length of 20 mm. The card was cut prior to application of strain. Tensile strength and modulus are calculated based on SEM diameter measurements (at least 5 measurements per filament). Specific properties are calculated by calculating linear density based on mass balance (see Eq. 6.5). We have verified experimentally (by measuring the mass of a known length) that this assumption is accurate within 10% of the experimental values.

Measurements of fiber cross section as well as assumption of an average linear density present inaccuracies. When specific properties are measured by dividing the breaking force by the linear density, we assume the linear density to be constant. However, the scattered breaking force (we find 30% scattering within a given spinning conditions) may be caused by variation in cross section along the filament, which makes the assumption of constant linear density invalid. When absolute stresses are calculated, the measured raw force values are divided by fiber cross section. However, even the most regular fibers are still slightly ellipsoidal. In order to account for the

ellisoidal cross section, fiber projection are measured in multiple point along the fiber by SEM or light microscopy (at least 5 measurements are taken). However, the larger scattering on measured breaking stress when compared to specific stress may be induced by inaccurate cross section measurements. The advantage of this method is that it can account for local variation along the fiber.

Note that specific strength can also be calculated by fiber strength (calculated by dividing the maximum force by fiber cross section) by the average calculated density. This method assumes the density (and not linear density) to be constant. Thus, it leads to specific strength values that are higher than values calculated by assuming linear density. This last method was not used in the present chapter.

6.6 Conclusions and Perspective

Superacid/CNT solution spinning is characterized by a large number of parameters that influence the outcome of a given spinning experiment. Among the various parameters CNT length and spin draw ratio are found to be the most critical ones. Fiber tensile strength is linearly proportional to CNT aspect ratio. This trend emerges when the best fiber properties are plotted for each batch as a function of aspect ratio. Unlike fiber strength, electrical conductivity does not show a strong dependence on CNT type. Dope concentration, flow rate, coagulation are also considered. The emerging trend among these parameters is that the spinning conditions that allow for high spin draw ratio are the ones to also yield the best properties. Both fiber strength and electrical conductivity scale with spin draw ratio up to SDR of 2. Extreme draw ratio (as high as 96) can be achieved; however, fiber properties do not improve significantly.

Superacid/CNT solution spinning differs from rigid–rod solution spinning in a

number of points. First of all, air gap spinning, the hallmark of rigid–rod spinning could not be attained at dope concentration at high as 15wt%. Moreover, optimal properties are attained at relatively low dope concentrations (3 to 6 wt%).

This chapter is about highly explorative research, with many unknowns and partially controlled experiments. Thus, the trends and conclusions reported in this chapter are valid within the considered parameter space. For example, two important parameters have not been considered in this chapter: the effect of temperature (and its effect on mixing and spinning) and post–processing. High spinning temperature may allow higher drawability of high concentration dopes. Swelling in a weak solvent such as concentrated sulfuric acid under tension may have the same effect as heat treatment of rigid–rod polymer fibers by reducing internal stresses and increasing alignment. A more radical approach could be to fuse (or sinter) CNT by heat treatment of electron radiation. Both techniques have been proven to be a valid approach on a nanometer scale, but there has been no attempt to reproduce it on a macroscopic scale.

Chapter 7

Superacid/CNT fibers: structure and properties

7.1 Introduction

Evolution* of civilization is tied to humans' ability to process and use materials. Stone, wood, and metals have dominated our past and are still essential at present. Superior properties (tied to functionality) or easy, scalable processing (tied to cost) are the essential requirements for the introduction of new materials and for the displacement of established ones. Synthetic polymers displaced traditional products (wood, natural fibers) because of ease of processing; they later evolved into highly engineered mechanical materials [Wang et al., 2011]. In neat or composite form, these materials are the basis for bulletproof vests, racecars, golf clubs, and airplanes. Yet, millennia-old metals still move electrons from power plants to our homes, wire our electronic devices, and dissipate the heat generated during electron transport. Although some engineered materials have higher specific conductivity than copper, e.g., doped graphite [Vogel, 1977] and superconductors, their chemical reactivity, difficult manufacturing, or need for low–temperature environment makes them impractical for widespread use. On a molecular level, carbon nanotubes (CNTs) have an outstanding combination of mechanical strength and stiffness, electrical and thermal conductivity, and low density, making them an ideal material that combines the best properties of polymers and metals [Baughman, 2000]. However, such outstanding properties

*This chapter will be submitted as a research article

have remained elusive on a macroscopic scale. In fact, CNT high molecular weight, stiffness, and chemical inertness create major challenges in material processing.

Fibers are a key building block for engineering materials. Two distinct routes have been developed for manufacturing neat CNT fibers [Behabtu et al., 2008]. One route employs a solid–state process where CNTs are grown in a reactor and directly spun into a fiber [Koziol et al., 2007, Zhang et al., 2004, Lashmore et al., 2006]. This approach does not lend itself to the typical easy scale-up of chemical process, as it combines multiple steps into a single one, limiting the options for process and material optimization. In fact, solid–state fibers have low packing, poor orientation, and include impurities within their structure [Davies et al., 2009]. Despite these shortcomings, so far solid–state CNT fibers have delivered the best properties [Koziol et al., 2007, Lashmore et al., 2006, Boncel et al., 2011]. The reason for this relative success is the length of the CNTs that comprise the fiberone millimeter or more [Behabtu et al., 2008]. Wet spinning is the alternate route, and was the first method for producing CNT fibers [Vigolo et al., 2000]. In this process, pre–made CNTs are dissolved or dispersed in a fluid, extruded out of a spinneret, and coagulated into a solid fiber by extraction of the dispersant. Wet spinning is scaled easily by enlarging equipment size and is the route by which high–performance fibers are manufactured (including ballistic fibers such as Kevlar® and Twaron® and structural fibers such as Toho Tenax®, Thornel® carbon fibers) [Yang, 1989]. Decoupling the manufacturing of CNTs from the spinning of the fibers allows the independent optimization of the two steps (including material purification). So far, wet spinning has yielded ordered, dense CNT fibers [Ericson et al., 2004]. Yet, their properties have been disappointing. Inadequate CNT length has been the presumed culprit [Behabtu et al., 2008], and the literature concurs that wet spinning is inappropriate for handling long CNTs and

therefore reaching exciting properties.

Here we report wet spun lightweight multifunctional fibers that outclass earlier macroscopic CNT fibers and define a new area of material properties by combining the high specific strength of polymeric and carbon fibers with the high specific electrical and thermal conductivity of metals. Such fibers are uniquely positioned for high–value applications such as electronics for aerospace use and field emission, and provide the bridgehead for a more widespread research and development effort that promises long-term impact in consumer electronics as well as long–range power transmission.

7.2 Fiber Properties

In this chapter we discuss the structure and properties of CNT spun from chlorosulfonic acid. The CNTs were mixed at 3 wt% in 100% chlorosulfonic acid and spun from a 65 μm spinneret in acetone (see Table 6.1 and section 6.5 of Chapter 6 for mixing and spinning details). Linear extrusion rate was 2 m/min and a spin draw ratio of 2 was applied (close to the maximum attainable spin draw ratio under these spinning conditions). We chose batch XBC 1101 (see Tab. 6.2 for further details about this specific batch) because this batch and spinning conditions are the ones that gave the best tensile strength and electrical conductivity (See section 6.3.1 of Chapter 6 and figure 6.7).

Fibers were tested for mechanical, electrical, and thermal properties and density. Tensile strength, modulus and elongation to break were measured from stress–strain curves (Fig. 7.1) on macroscopic (20 mm long) individual filaments cut from large spools (100 to 500 m). Stress was calculated by dividing the applied force by the fiber cross–sectional area (determined by Scanning Electron Microscopy (SEM)). The

modulus was calculated by a linear fit of the stress strain from 0 to 0.4% strain (see section 6.5.6 in Chapter 6 for further details).

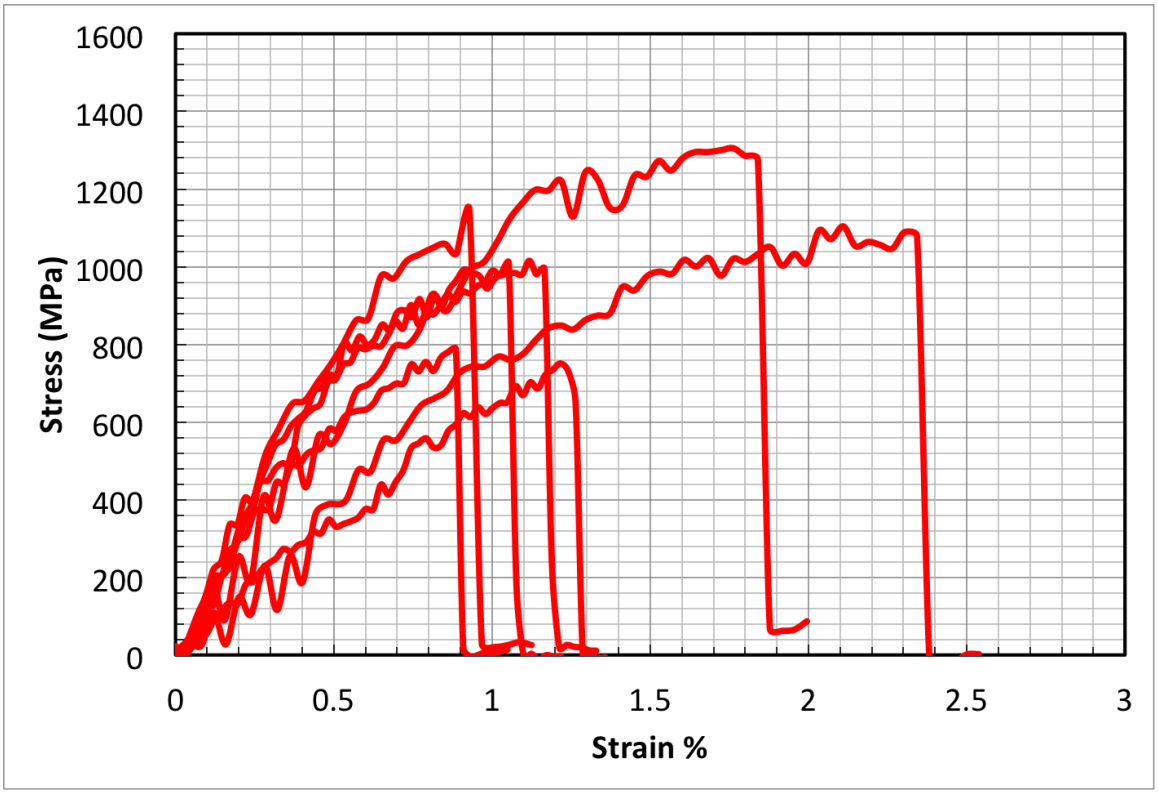

Figure 7.1 : Stress strain curves for fibers spun from CCNI XBC 1101 under spinning conditions, as detailed in Table 6.1.

The average tensile strength was 1 GPa (best value 1.3 GPa) and average modulus was 130 GPa (best value 200 GPa). These same fibers displayed low electrical resistivity (measured by 2 and 4-point probe on 25 mm single filaments). The average electrical conductivity was 2.9 ± 0.3 MS/m (resistivity of 35 ± 3 $\mu\Omega$ cm) at room temperature; doping by iodine — a known, stable CNT dopant [Grigorian et al., 1998] — increased conductivity to 5 ± 0.5 MS/m (resistivity 22 ± 4 $\mu\Omega$ cm, best value of 17.5 $\mu\Omega$ cm) (Fig. 7.2). We also measured an average thermal conductivity of 380 ± 15 W/m K on 1.5 mm long samples using the 3-omega method [Lu et al.,

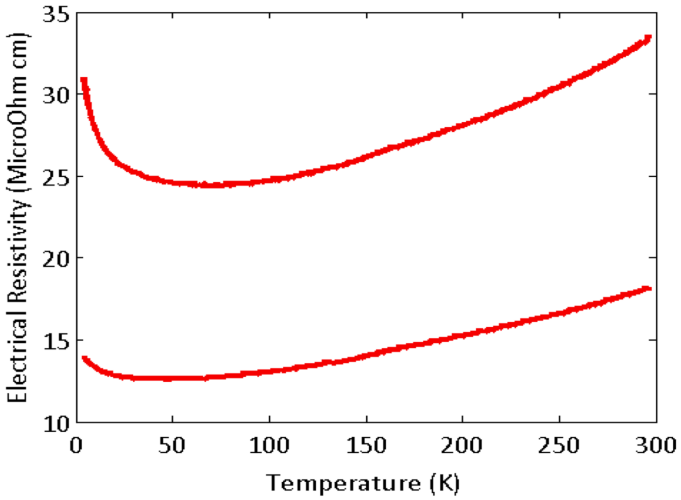

Figure 7.2 : Electrical resistivity as a function of temperature, for fibers spun from CCNI XBC 1101 under spinning conditions detailed in Table 6.1. The top curve refers to the electrical resistivity of as spun fibers. The bottom curve refers to iodine doped filaments. The electrical conductivity data as a function of temperature are courtesy of Xuan Wang, Dr. Junichiro Kono Group, Rice University, Houston, TX.

2001]. Iodine doping doubled thermal conductivity (635 W/m K). Such high thermal conductivity remains unchanged after annealing at 600 C, while the electrical conductivity drops by an order of magnitude to 0.4 MS/m (resistivity of 240 $\mu\Omega$ cm). Density (measured by weighing a 60 m filament with 9.0 $\pm$ 0.6 μm diameter) was 1.3 $\pm$ 0.1 g/cm^3; iodine doping increased density to 1.4 g/cm^3, as measured by TGA (see experimental section for further details).

These combined properties are remarkable when compared to other CNT fibers (Fig. 7.3) and high–performance materials (Fig. 7.4 and 7.5). Tensile strength shows a tenfold improvement over previous wet–spun fibers ($\sim$0.11 GPa, [Ericson et al., 2004]) and is comparable to the best macroscopic samples of neat, solid–state spun fibers of mm long CNTs (best values of $\sim$1.8 GPa assuming a density of 1 g/cm^3 [Boncel et al., 2011]). The modulus is improved over earlier wet spun fibers (120

GPa [Ericson et al., 2004]), and higher than the best solid–state CNT fibers (∼120 GPa assuming a density of 1 g/cm^3 [Boncel et al., 2011]). Electrical conductivity is tenfold higher than previous wet–spun fibers and the best continuous, undoped solid–state fibers (0.5 MS/m [Zhong et al., 2010]), 3 to 5 times better than the best doped CNT fibers (∼1.3 MS/m [Alvarenga et al., 2010]) and isolated ropes (∼1 MS/m [Fischer et al., 1997, Thess et al., 1996]), and comparable to the best solid–state, acid-densified, iodine doped individual CNT fibrils (5.8 MS/m [Zhao et al., 2011]). The fiber electrical conductivity did not degrade when kinks were progressively introduced, indicating that these fibers, unlike copper [Jarosz et al., 2011], resist bending fatigue. Thermal conductivity is ∼30x higher than previous wet–spun fibers (21 W/m K [Ericson et al., 2004]), ∼10x higher than the best solid–state CNT fibers (60 W/m K [Jakubinek et al., 2012]) and ∼3x higher than the best magnetically aligned discrete CNT films (200 W/m K [Hone et al., 2000]).

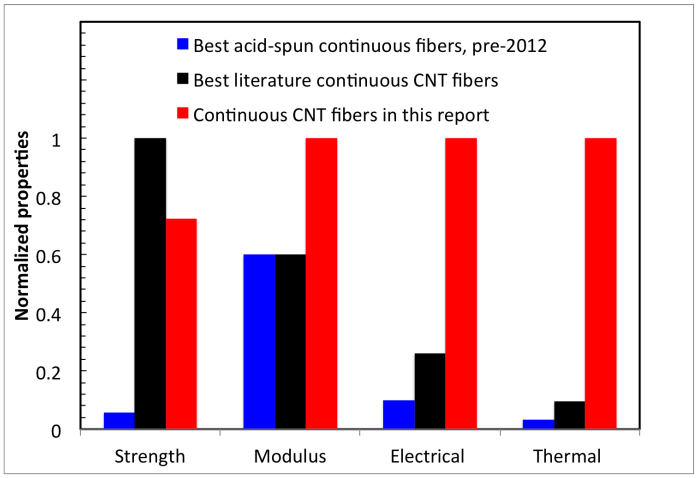

Figure 7.3 : Comparison of continuous, neat, CNT fibers properties. The blue bars represent wet–spun fiber while the black bars are the best properties reported so far for continuous, neat CNT fibers (see the main text for references). The red bars are the properties for the fibers from this report. The properties are normalized with respect to the highest value.

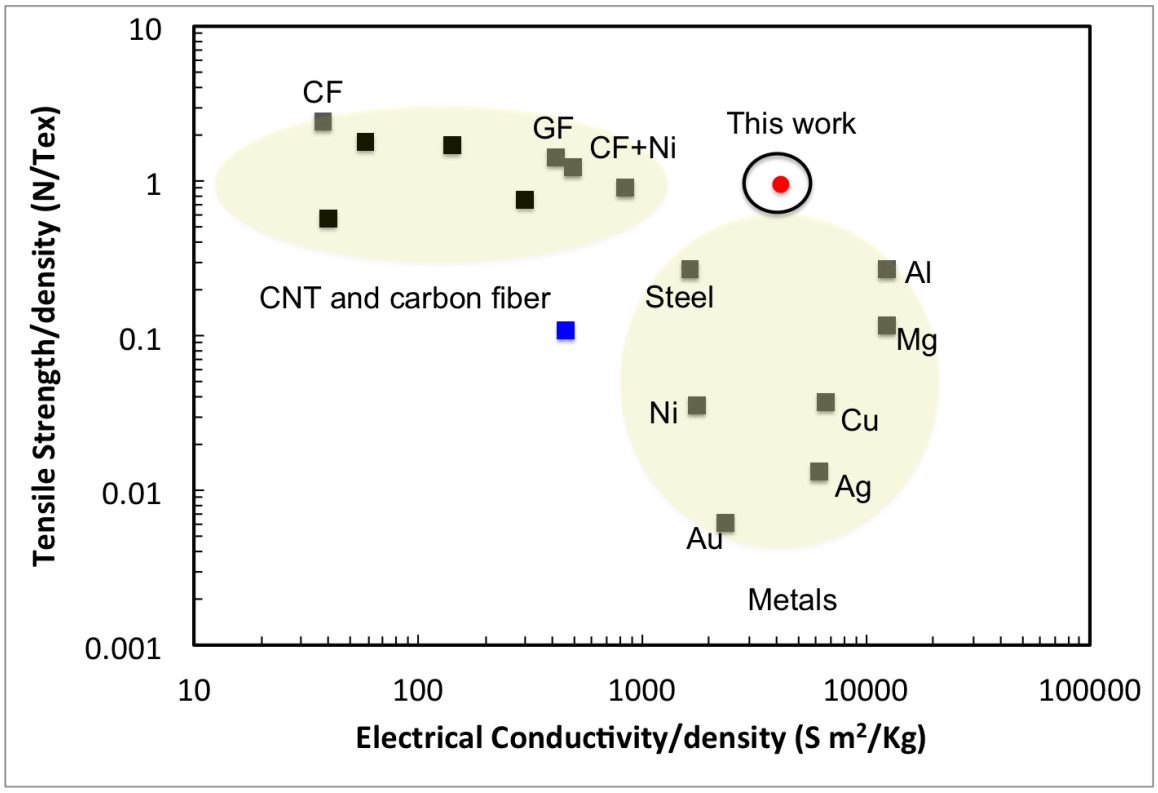

Figure 7.4 : Ashby plots showing specific tensile strength as a function of specific electrical conductivity for different materials. Two distinct areas (circled in yellow) can be identifies: a high strength, low conductivity characteristic of neat CNT fibers, PAN–based carbon fiber (CF) and pitch based graphitic fiber (GF) and high conductivity and low strength typical of metals. As in figure 7.3 the blue color represent wet–spun fiber while the black color refers to the best properties reported so far for continuous, neat CNT fibers and the red color represents the data for the fibers from this report. The gray square represent data from engineered materials.

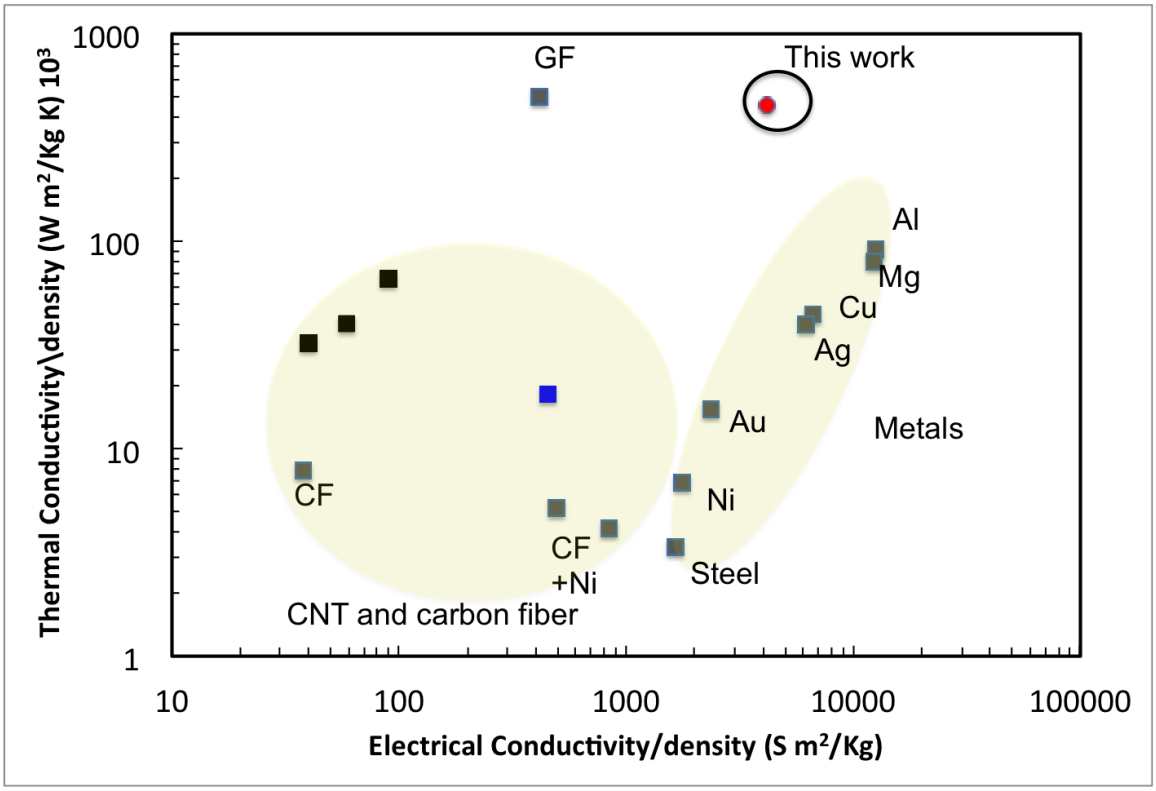

Figure 7.5 : Ashby plot showing specific electrical conductivity vs. specific thermal conductivity plot for different materials. Two distinct regions for metals and carbon fiber can be seen as in figure 7.4. As in figure 7.3 the blue color represent wet–spun fiber while the black color refers to the best properties reported so far for continuous, neat CNT fibers and the red color represents the data for the fibers from this report. The gray square represent data from engineered materials. The thermal conductivity data are courtesy of John B. Ferguson, Materials and Manufacturing Directorate, Air Force Research Laboratory, Wright-Patterson Air Force Base, Dayton, OH.

Specific (rather than volumetric) properties are important for weight-sensitive applications, e.g., aerospace materials. Figures 7.4 and 7.5 compare CNT fibers (from this article and from literature) to the current materials with the best mechanical, electrical, and thermal properties. Clearly, our CNT fibers combine the typical specific electrical conductivity of metal wires (copper, silver, and aluminum) with the typical specific strength of high performance carbon fibers. The combination of specific thermal and electrical conductivities is outside the present parameter space. Thus, our CNT fibers are unique multifunctional materials that expand the existing design space.

7.3 Fiber Structure

For a perfect CNT crystal, specific strength scales linearly with the constitutive molecular length up to a critical length (L_{cr}) (Fig. 7.6, see also Fig. 2.5 in chapter 2), after which the intrinsic molecular limit is achieved. This is because the molecular mechanism to increase fiber strength —friction between adjacent molecules— increases linearly with length.

Similar underlying physics governs electron and phonon transport on CNT assemblies. Both thermal [Zhong and Lukes, 2006] and electrical interfacial resistance are expected to decrease with CNT length. After a critical length, single CNT properties will be the dominant factor to resistance. Estimates of critical length for different properties vary widely [Yakobson et al., 2000, Vilatela et al., 2011]. Yakobson *et al.* [2000] estimate 10 μm for fiber strength critical length while Vilatela *et al* [2011] estimates 1000 μm, two orders of magnitude larger. Nevertheless the underlying scaling holds. However, the single crystal properties are a limiting value, while mesoscale structures dominate real CNTs macroscopic properties. In fact, a self–similar argu-

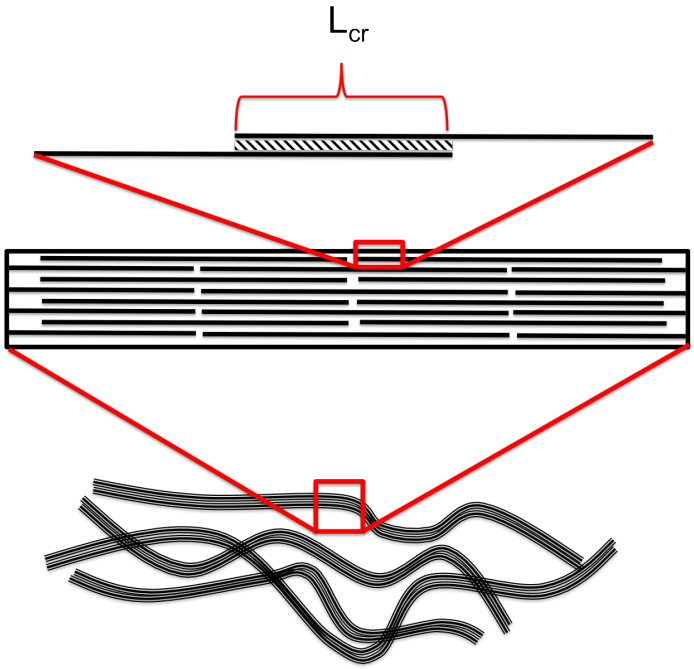

Figure 7.6 : Schematics of CNT fiber hierarchical structure. The fundamental units are single CNTs. Their length is a crucial parameter that fixes the amount of overlap, $L_c r$. Single CNTs are then bundled in fibrils, the mesoscopic structures forming macroscopic fibers and films.

ment can be re-iterated by changing single CNTs with fibrils. Thus, optimal fibers will have long and aligned fibrils and the limiting fiber value will be single-fibril properties.

The alignment between CNTs is a critical criterion for the perfect crystal model. In fact, misalignment of the constitutive molecules may decrease overlap length and worsen the ideal limit of a perfect crystal. We decided to probe misalignment within thin films. We did so because the film making process (see Chapter 4 for further details) —filtration from an isotropic solution— does not promote any alignment. This process is quite different when compared to fiber processing where a pre–ordered liquid crystalline fluid is further aligned through shear and extensional flow.

Figure 7.7(a) shows the typical microstructure of thin films fabricated by acid filtration. These films are characterized by a random network of fibrils. However, despite the isotropic nature of the starting fluid and a flow behaviour that does not induce alignment, the fibrils are still characterized by highly ordered CNTs (see Fig. 7.7(b)). Thus, for solution processed CNTs, fibrils can be considered a close approximation to an ideal crystal.

We now turn to study fiber morphology (by SEM), alignment (by single filament Wide Angle X–ray Diffraction, WAXD, (Fig. 7.8(a)), see section 7.5.1 for details of the experimental set up and fitting procedure), and packing fraction (by high–resolution TEM) to understand the fiber structure-properties relationship. SEM revealed that the fiber comprises well–aligned, thin CNT fibrils (Fig. 7.8(b)) (typical diameter of 10-100 nm and length $> 50\ \mu$m), similar to earlier wet–spun fibers [Ericson et al., 2004] as well as high–strength polymeric fibers [Cohen and Thomas, 1985]. WAXD showed sharp reflections at $2\theta = 25.3°$ (Fig. 7.8(a)), corresponding to the (002) reflection of inter–layer spacing of a few walled CNT [Amelinckx et al., 1999]. The azimuthal scan

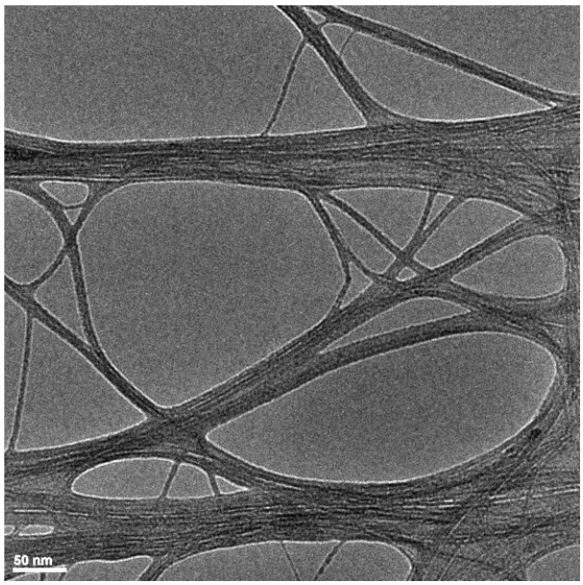

(a)

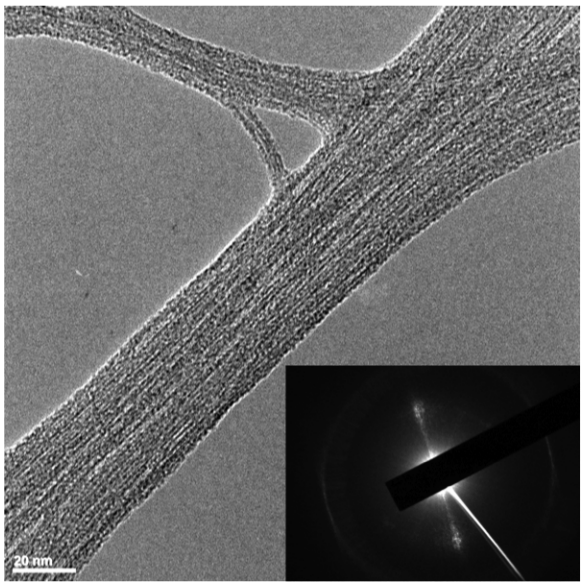

(b)

Figure 7.7 : TEM micrograph showing the structure of thin films. Figure 7.7(a) is a low magnification TEM showing a random network of CNT fibrils. Figure 7.7(b) shows a higher magnification TEM of a single fibril. Electron diffraction of single fibrils (see insert of Figure 7.7(b)) reveal the highly aligned nature of CNT fibrils. The thin film was prepared by filtering 4 ml isotropic solution (5 ppm), on a 35 mm filter area (see Chapter 4 for further details of sample preparation). We used the same CNTs used for the fibers discussed in this chapter (CCNI XVC 1101). Thus, even in the absence of an ordered phase and an aligning flow, CNTs have a very strong tendency to bundle into aligned ropes.

of the (002) peak gave Full Width Half Maximum (FWHM) of 9.4° (which corresponds to a Herman orientation factor of 0.986), averaged over four different points along a single fiber (lowest and highest values were 7.3 and 11.2°). Electron diffraction on isolated single fibrils (peeled off the fibers) displayed better order (FWHM 5°), indicating slight misalignment of fibrils within the fiber (Fig. 7.8(c)). Fiber FWHM is the lowest measured for CNT fibers so far (FWHM=31° for wet–spun fibers [Ericson et al., 2004] and FWHM between 10° and 14° for solid state spun fibers [Vilatela et al., 2011]).

Fibers and thin films differ mostly by the macroscopic order of the constitutive fibrils. This difference gives rise to a remarkable difference also in specific conductivity. In fact, thin film specific conductivity (242 S m^2/kg for 100 Ω/sq and 80.4% transparency) is an order of magnitude lower than for as spun fiber specific conductivity (2232 S m^2/kg). This example shows how overall fibril alignment is as critical as the length of the constitutive molecules.

We also quantified packing fraction by calculating a maximum theoretical packing density of 1.5 g/cm^3 from high resolution TEM on the starting CNT material. Hence, the fiber density (1.3 g/cm^3) is ∼90% of the theoretical close-packed density. We verified the high packing fraction by visualizing fiber cross–section. The images showed occasional ∼100 nm voids, but no micro scale voids (Fig. 7.9(a) and 7.9(b)). Such high packing represents the highest measured for neat carbon nanotube fibers so far (78% for wet–spun fibers [Ericson et al., 2004], ∼50% for solid–state fibers [Koziol et al., 2007]). High alignment and packing density are likely responsible for the remarkable properties attained with "short" CNTs, because they improve interfacial transfer of stress, current, and heat between adjacent CNTs. Thus, the achieved fiber strength (comparable to solid–state spun fibers from millimeter long CNTs) is

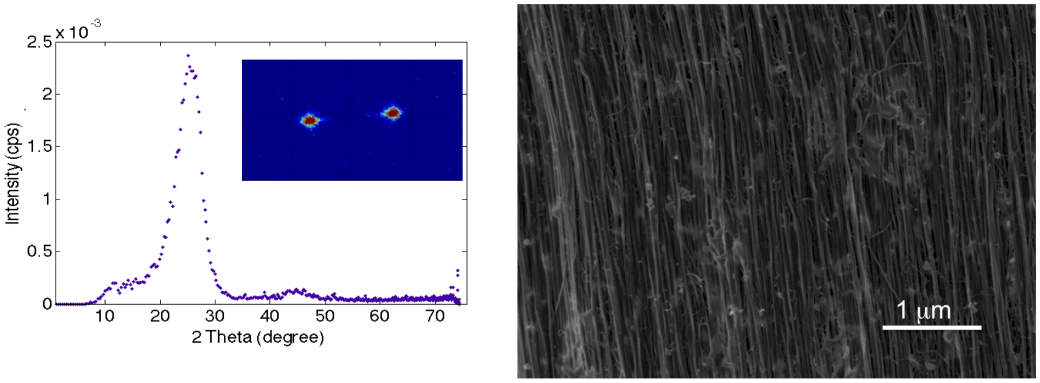

(a) (b)

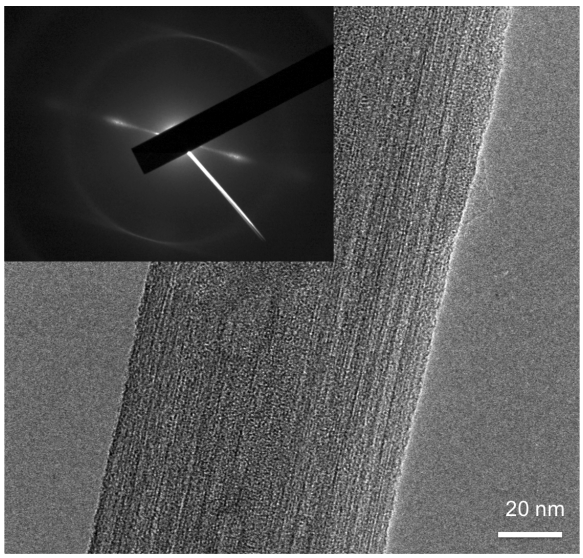

(c)

Figure 7.8 : Fiber morphology and alignment. Figure 7.8(a) is a single fiber X-ray diffraction pattern showing sharp (002) reflection (2θ=25.2°) from MWNTs wall. Figure 7.8(b) shows a high resolution SEM of fiber surface revealing the typical morphology of CNT fibers composed of 100 nanometer wide fibrils aligned along fiber axis. Figure 7.8(c) shows single-fibril electron TEM and electron diffraction. SEM and X-ray diffraction are courtesy of Talmon/Cohen group, Technion, Israel Institute of Technology.

a consequence of the optimal structure of solution-spun fibers. Conversely, improvement over previously solution-spun fibers, is mainly due to the increased length of the constitutive molecules.

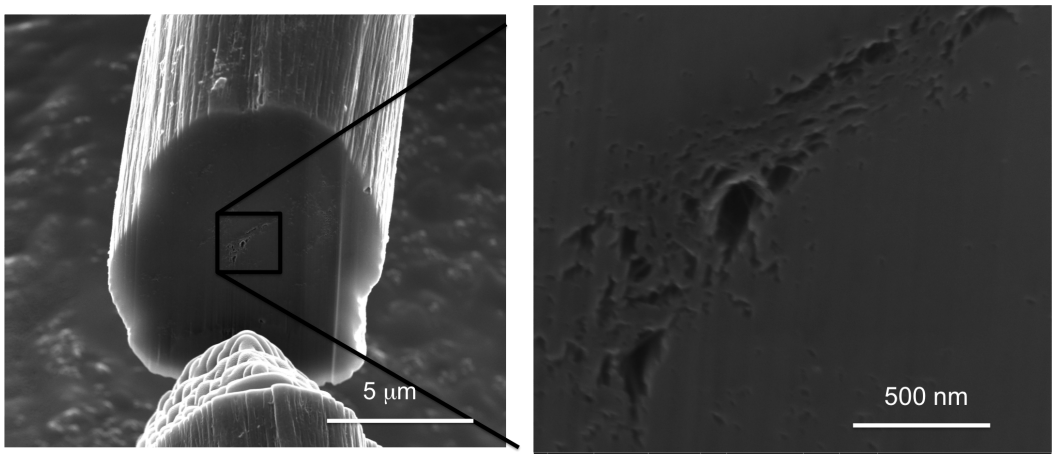

(a) (b)

Figure 7.9 : Figure 7.9(a) shows a fiber cross section SEM after FIB cutting. The cross section does not reveal micron-sized voids. At higher magnification (Fig. 7.9(b)) a few hundred nano-meter sized voids can be identified. FIB and micrographs courtesy of Talmon/Cohen Group, Technion, Israel Institute of Technology.

7.4 Applications

We demonstrate the multifunctional properties of our fibers by supporting and wiring a Light Emitting Diode (LED, 50 g) and fabricating cold electron emitting cathodes. The LED was supported by four CNT fibers (20 μm diameter, two fibers per contact) (Fig. 7.10). The stress in each fiber was 400 MPa, well above the breaking strength of copper wires. Yet, the filament resistance was low enough to run 30 mA current ($4.8{\cdot}10^7$ A/m^2 current density) and light the device. This example shows how the combination of electrical conductivity and mechanical strength can unlock engineering

solution that are otherwise unfeasible with common electrical wires.

Figure 7.10 : This image shows an LED light supported and wired to an electrical circuit by a CNT fiber, showcasing the multifunctional nature of our fibers.

A field–emitting device was fabricated in a cathode (fiber)–anode configuration (Fig. 7.11). The emitted current density was $5.7{\cdot}10^7$ A/m^2 (3.6 mA from a 9 μm diameter fiber) at 0.86 kV and 1 mm anode–cathode distance. This current density is over two orders of magnitude higher than fibers of short ($\sim$0.5 μm) SWNTs [Fairchild et al., 2010], solid–state spun DWNTs fibers [Ci et al., 2007], and MWNTs yarns [Yang et al., 2012, Jang et al., 2010]. This value is also higher than the highest emission reported for solid–state spun CNT fibers, $1.5{\cdot}10^7$ A/m^2 (1.2 mA from 10 μm diameter fiber, which is somewhat surprising because the relatively low electrical ($6{\cdot}10^4$ S/m) and thermal (below 100 W/m K) conductivity of these solid state fibers) [Zakhidov et al., 2007]. We directly compare CNT fiber emission to graphite fiber

emitter — a common material used for large area cathodes. Our fibers emit two orders of magnitude higher (50 μA, 1 kV and 250 μm cathode–anode distance from 10 μm diameter fiber) current (Fig. 7.11). The high current density of our fibers can be explained by the combination of electrical and thermal conductivity, which both reduce the fiber temperature by generating less Joule heating and dissipating it efficiently, thereby preventing tip failure [Zakhidov et al., 2007].

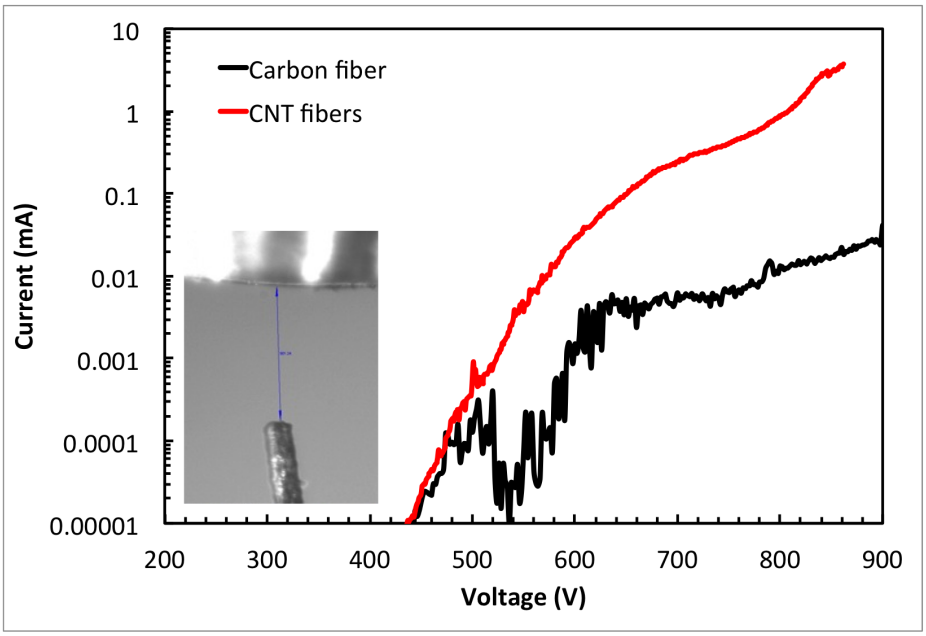

Figure 7.11 : Field emission measurement set-up. Below is single filament fiber facing the anode (top). Measurements were taken with a Keithley 6517a Sourcemeter, controlled by LabView program. FE system is load locked, main chamber has 400 L/s ion pump, chamber pressure typically $< 2 \cdot 10^{-8}$ Torr during measurements. C) Current-voltage plot showing field emission properties of pitch based carbon fibers (black) and CNT fiber (red).

7.5 Experimental Details

7.5.1 WAXS Experimental Details

The sample was studied using X-ray diffraction (XRD). Experiments were performed using a small/wide–angle diffractometer (Molecular Metrology SAXS system) equipped with a sealed microfocus tube (MicroMax-002+S) emitting Cu Kα radiation (wavelength - 0.1542 nm), two Gobel mirrors, and three pinhole slits. The generator was powered at 45 kV and 0.9 mA. The scattering patterns were recorded by a 15 x 15 cm image plate (BAS-IP-MS, FUJIFILM), positioned about 2.8 cm behind the sample. The scattering intensity was recorded in the interval $3^\circ < 2\theta < 68^\circ$, where 2θ is the scattering angle. Exposure time was 120 min. The thin fiber samples were glued on a two-dimensional holder perpendicular to the beam, and measured under vacuum at ambient temperature. The imaging plate was scanned by a Fluorescent Image Analyzing System (FLA-7000) and analyzed by FLA-7000 Image Reader software (version 10) with 100 μm resolution.

7.5.2 RT–HRSEM and FIB Experimental Details

CNT fibers were attached to the aluminum stub, using conductive carbon tape. The stub was inserted into a Zeiss Ultra Plus HRSEM, equipped with a Schottky field emission electron gun. Specimens were examined at very low electron acceleration voltage (1 to 2kV) and short working distance (2.9-3.3 mm) for high–resolution imaging of surface nanostructures. We used both the InLens and the Everhart-Thornley secondary electron imaging detectors.

The fiber was mounted on SEM stab with carbon tape. The sample was tilted by 52° and cuts were made orthogonal to fiber by using the Strata 400 STEM Dual

Beam system, which is equipped with Focused Ion Beam (FIB) technology. Ion beam source is the Sidewinder® field emission focused ion beam with liquid Gallium ion emitter, with ion beam voltage of 30kV and beam current of 21 nA. The deposited Ga was partially removed from the cross section by the ion beam using a lower beam current (2.8 nA). After cutting and cleaning procedure, images of each cross section were taking by using the fully digital Field Emission Scanning Electron Microscope (FE-SEM) mode of the instrument with the following parameters:

- Electron source = Schottky field emission gun.
- Detector = in-lens SE detector.
- Work distance = 5.1 mm.
- Electron beam voltage = 5 - 10 kV.

No Pt or other coating was deposited on the cross section.

7.5.3 Three Omega Method for Thermal Conductivity Measurements

Four copper epoxy contacts were placed in a row on a sapphire substrate. 1 cm long fiber was laid across the four contacts and evacuated to $\sim 1 \cdot 10^{-5}$ Torr in a MMR Technology Variable Temperature Micro Probe System (VTMP). Lead wires were connected to the contacts and ac current was applied at several temperatures. AC current is applied to sample at frequency of ω (sample is self–heated). Joule heating leads to resistance fluctuation at frequency of 2ω which corresponds to a voltage ($V_{3\omega}$) at 3ω. The 3ω voltage is related to thermal conductivity, κ, for a long, slender wire:

$$V_{3\omega} \approx \frac{4I^3 LRR'}{\pi^4 \kappa S \sqrt{1 + (2\omega\gamma)^2}} \tag{7.1}$$

where I, L, R, R' and S are electric current, sample length, electrical resistance, electrical resistance derivative with temperature, and fiber cross section respectively. γ is defined as follow:

$$\gamma \equiv \frac{L^2 \rho C_p}{\kappa \pi^2} \tag{7.2}$$

where C_p is the heat capacity of the fiber. Equation assumes that heating power inhomogeneity $\ll$ total heat power and negligible radiation heat loss. We have tested the 3ω method for pitch based carbon (Cytec® P-100) fiber and found the value to be accurate to within 5 % of the literature value. Also, we have used the same fiber for the field emission experiment comparison.

7.5.4 Iodine Doping

Iodine doping details

As–spun fibers were doped in a sealed vacuum oven (0.2 Atm) with solid iodine. The sample was kept in the oven at 200 C for 24 hours. Doping was performed under tension by attaching weights (10% of breaking force) to each end of a fiber filament using Graphi-Bond (551-RN Aremco) (a graphite adhesive suitable for high temperature applications). After 24 hours the fibers were removed from the oven, allowed to cool, and then washed with ethanol to remove any excess iodine from their surfaces.

Mass gain after iodine doping was measured by thermo gravimetric analysis (TGA). As–spun and iodine–doped samples were considered. The iodine–doped sample was washed briefly with ethanol to remove excess Iodine bound on the surface of the fibers. TGA analysis was performed in an inert Argon atmosphere. The temperature was initially held at 260 degrees for each sample (overnight), and then raised

to 800 degrees C for half an hour (this TGA protocol had the dual purpose of determining whether heating in an oven at 260 degrees could effectively remove the added Iodine). The total mass loss for the as–spun fiber was 7%, with only 2% of this mass loss occurring before the increase to 800 degrees C. The mass loss of the doped fiber was 17%, with 10% of this loss coming before the increase to 800 degrees C. This indicates an increase of roughly 10% of the original mass after Iodine doping.

7.6 Conclusions

The combined achievement of CNT fiber multifunctionality and scalable manufacturing process is a major step toward macroscopic CNT based materials. Our work dispels the deep–rooted notion that very long (∼mm long or more) CNTs are required to obtain relevant macroscopic properties. Like in high performance polymeric fibers, optimal morphology (alignment, packing density, lack of impurities, and high–quality molecular constituents) is crucial for the final CNT fiber properties. The unique combination of properties of these CNT fibers will generate new engineering solutions in various applications, including data and light power transmission and field emission. Yet, the fiber properties are still a fraction (∼2% to 15%) of the ultimate intrinsic properties of CNTs. Increasing fiber strength will require longer, thin, defect–free CNTs (length above 50 μm, diameter below 3 nm), and preferably SWNTs. Reaching ultimate conductivity may require the synthesis of all–armchair SWNTs. The synthesis of large quantities (gram–level or higher), defect–free CNTs with such control on length, diameter, and chirality, is now, more than ever, a key technological barrier that must be overcome to enlarge greatly the design space of CNT fibers and make and make macroscopic materials of CNTs "be all they can be".

Material type	**Spec. Electrical cond. (S m^2/Kg)**	**Specific strength (N/Tex)**	**Spec. Thermal Cond. (W m^2/Kg K)·10^3**	**Reference**
Twisted MWNTs	40	0.58	32.5	[Aliev et al., 2007, Fang et al., 2010]
Twisted MWNTs	89	–	66.67	[Jakubinek et al., 2012]
Twisted MWNTs	141	1.71		[Liu et al., 2010b]
Collapsed DWNTs	301	0.758		[Zhong et al., 2010]
Collapsed DWNTs	59	1.8	40.00	[Boncel et al., 2011, Vilatela et al., 2012]
Acid Spun SWNTs	455	0.11	18.18	[Ericson et al., 2004]
DWNT fibers	367	1.37		[Cheng et al., 2009]
PVA infiltrated MWNTs	94	2.00		[Liu et al., 2010a]
Twisted MWNTs	141	1.71		[Liu et al., 2010b]
This Work (iodine doped)	4596	1.3	156.25	

CNT fibers specific properties. Data used for figure 7.4 and 7.5

Material type	**Spec. Electrical cond. (S m^2/Kg)**	**Specific strength (N/Tex)**	**Spec. Thermal Cond. (W m^2/Kg K)·10^3**	**Reference**
TohoTenax Besfight MC Type I	494	1.23	5.19	http://www.matweb.com/
TohoTenax Besfight MC Type II	840	0.91	4.12	”
Cytec Thornel pitch	413	1.41	500	”
Pan based carbon fiber	38	2.42	7.91	”
Copper	6587	0.04	44.57	”
Steel	1639	0.27	3.33	”
Silver	6150	0.01	39.94	”
Gold	2353	0.01	15.58	”
Nikel	1760	0.04	6.84	”
Alluminum alloy	12315	0.27	79.29	”
Magnesium	12494	0.118	91.38	”

Engineered materials specific properties. Data used for figure 7.4 and 7.5

Chapter 8

Conclusions and Outlook

Spontaneous dissolution of carbon nanotube (CNTs) and graphite, once considered unattainable, is now an accepted scientific fact. Chlorosulfonic acid dissolves a wide variety of CNTs and graphite and allows fluid phases processing of both graphite and CNTs. Solution processing allows manufacturing of macroscopic objects such as fibers and films. For example, thin films one atom–thick can be manufactured by filtration and used as support for TEM specimen imaging or as transparent and conducting films, while liquid crystalline fluid phases are used for wet spinning of continuous fibers. Table 8.1 shows property progression of wet–spun CNT fibers from the beginning of the project, up to now.

Changes in fiber properties are a consequence of profound changes in fiber processing (Tab. 8.2). The most important changes are related to solvent quality (Chlorosulfonic acid instead of sulfuric acid) which has in turn allowed processing of long CNTs (∼tens of micron long instead of submicron long CNTs). Dopes consisting of long CNTs have allowed tensioning during fiber spinning, improving fiber alignment.

CNT liquid crystalline phase is the liquid phase utilized for fiber spinning. We addressed some open question related to CNT liquid crystals by studying CNT/chlorosulfonic acid nematic droplets. CNT nematic droplets form elongated structures as a result of free energy minimization. Such a structure is rarely encountered in other CNT liquid crystals, despite being the result of free energy minimization. For the first time we observe the transition from homogeneous nematic droplets

	Summer 2001	Spring 2006	Summer 2011
Tensile Strength (MPa)	Too small to measure	120	1300
Young's Modulus	Too small to measure	100	200
Electrical conductivity (MS/m)	Too small to measure	0.5	5
Thermal conductivity(W/K·m)	Too small to measure	20	635

Table 8.1 : Overview of the evolution of acid spun CNT fibers' properties in the past 10 years at Rice University (Summer 2001).

	Summer 2001	Spring 2006	Summer 2011
Length	Centimeters	Continuous	Continuous
Minimum diameter	80μm	30μm	5 μm
Void fraction	>50%	<20%	<10%
Alignment(FWHM, degree)	poor	31	9
solvent	sulfuric acid	sulfuric acid	chlorosulfonic acid
nanotube type	sub micron long SWNT	sub micron long SWNT	tens of micron long DWNTs
tension during spinning	no	no	Yes

Table 8.2 : Overview on how fiber processing and morphology has evolvedfrom the beginning of the wet–spinning effort at Rice University (Summer 2001).

(where the constitutive molecules have no distortion) to bipolar droplets (where the constitutive rods are tangential to the isotropic–nematic interface), as expected from scaling arguments. The droplet merging dynamics also show the true liquid nature of CNT liquid crystals, complementing birefringence measurements, while the narrow size distribution of CNT droplets reveals the kinetic barrier for droplet merging, with a dominant size occurring at the transition from homogeneous to bipolar tactoids. CNT liquid crystals require further understanding. In particular, it is unclear whether the elongated structures observed in the fiber spinning dopes derive are sample preparation artefacts or if they represent equilibrium phases. Ideally, one single liquid crytstalline mono domain would be the ideal starting point for the fiber spinning process.

Fiber and thin film properties (strength, modulus, and conductivity) can be further improved if longer high quality CNTs are used. However, longer tubes will pose additional processing difficulties. Specific properties could be doubled by simply using SWNTs instead of DWNTs. In fact, inner walls of DWNT and MWNTs do not participate in stress transfer [Yu et al., 2000c] to the same extent the external wall does, making SWNTs a better choice. From a processing point of view, the influence of dope temperature on mixing and spinning has not been explored yet. High temperature can lower fluid viscoelasticity allowing easier mixing and spinning from higher dope concentrations. Post processing (doping, heat treatment under tension, swelling and tensioning in weaker acids) all have the potential to further improve both fiber and thin film properties.

The ability to dissolve CNTs, graphite, and fullerenes in a common solvent (chlorosulfonic acid) gives a unique perspective toward hybrid CNT/graphite structures. Such structures are under consideration for a number of applications, including su-

perconductivity, lithium ion batteries, hydrogen storage, transparent and conducting films, and super lubricity [Tung et al., 2009, Kuc et al., 2007, Gupta et al., 2005, Dimitrakakis et al., 2008]. Although a number of numerical models have been proposed, highlighting the advantage of hybrid structure for a number of applications, scalable and effective processing of such structures is still lacking [Fan et al., 2010, Kuc et al., 2007, Dimitrakakis et al., 2008].

In conclusion, we have demonstrated that chlorosulfonic processing of graphite and CNTs unlock the true potential of these exceptional molecules. The variety of applications showcases the versatility of these molecules and their multifunctional properties. Most importantly, increasing fractions of single molecule properties (the properties that have fuelled much of the research on CNTs and graphene) can be attained on macroscopic object if the right molecular weight (or CNT length) and processing is used.

Bibliography

W. W. Adams, R. K. Eby, and D. E. McLemore. *The materials science and engineering of rigid-rod polymers*, volume 134. Materials Research Society, 1989.

A. E. Aliev, C. Guthy, M. Zhang, S. Fang, A. A. Zakhidov, J. E. Fisher, and R. H. Baughman. Thermal transport in MWCNT sheets and yarns. *Carbon*, 45:2880–2888, 2007.

J. Alvarenga, R. P. Jarosz, M. C. Schauerman, T. B. Moses, J. B. Landi, D. C. Cress, and P.R. Raffaelle. High conductivity carbon nanotube wires from radial densification and ionic doping. *Applied Physics Letters*, 97(18), 2010.

Placidus B. Amama, Cary L. Pint, Laura McJilton, Seung Min Kim, Eric A. Stach, P. Terry Murray, Robert H. Hauge, and Benji Maruyama. Role of water in super growth of single-walled carbon nanotube carpets. *Nano Letters*, 9(1):44–49, 2009.

S. Amelinckx, A. Lucas, and P. Lambin. Electron diffraction and microscopy of nanotubes. *Reports on Progress in Physics*, 62(11):1471–1524, 1999.

S. Arepalli. Laser ablation process for single-walled carbon nanotube production. *Journal of Nanoscience and Nanotechnology*, 4(4):317–325, 2004.

S. Badaire, V. Pichot, C. Zakri, P. Poulin, P. Launois, J. Vavro, C. Guthy, M. Chen, and J. E. Fischer. Correlation of properties with preferred orientation in coagulated

and stretch-aligned single-wall carbon nanotubes. *Journal of Applied Physics*, 96 (12):7509–7513, 2004.

S. Badaire, C. Zakri, M. Maugey, A. Derre, J. N. Barisci, G. Wallace, and P. Poulin. Liquid crystals of dna-stabilized carbon nanotubes. *Advanced Materials*, 17(13): 1673–1679, 2005.

A. A. Balandin, S. Ghosh, W. Z. Bao, I. Calizo, D. Teweldebrhan, F. Miao, and C. N. Lau. Superior thermal conductivity of single-layer graphene. *Nano Letters*, 8(3): 902–907, 2008.

J. N. Barisci, M. Tahhan, G. G. Wallace, S. Badaire, T. Vaugien, M. Maugey, and P. Poulin. Properties of carbon nanotube fibers spun from dna-stabilized dispersions. *Advanced Functional Materials*, 14(2):133–138, 2004.

M. A. Bates and D. Frenkel. Nematic-isotropic transition in polydisperse systems of infinitely thin hard platelets. *Journal of Chemical Physics*, 110(13):6553–6559, 1999.

R. H. Baughman. Materials science - putting a new spin on carbon nanotubes. *Science*, 290(5495):1310–1311, 2000.

A. H. Becerril, J. Mao, Z. Liu, M. R. Stoltenberg, Z. Bao, and Y. Chen. Evaluation of solution-processed reduced graphene oxide films as transparent conductors. *ACS Nano*, 2(3):463–470, 2008.

N. Behabtu, M. J. Green, and M. Pasquali. Carbon nanotube-based neat fibers. *Nano Today*, 3(5-6):24–34, 2008.

N. Behabtu, J. R. Lomeda, M. J. Green, A. L. Higginbotham, A. Sinitskii, D. V. Kosynkin, D. Tsentalovich, A. N. G. Parra-Vasquez, J. Schmidt, E. Kesselman, Y. Cohen, Y. Talmon, J. M. Tour, and M. Pasquali. Spontaneous high-concentration dispersions and liquid crystals of graphene. *Nature Nanotechnology*, 5(6):406–411, 2010.

L. X. Benedict, N. G. Chopra, M. L. Cohen, A. Zettl, S. G. Louie, and V. H. Crespi. Microscopic determination of the interlayer binding energy in graphite. *Chemical Physics Letters*, 286(5-6):490–496, 1998.

J. D. Bernal and I. Fankuchen. X-ray and crystallographic studies of plant virus preparations i. introduction and preparation of specimens i. modes of aggregation of the virus particles. *Journal of General Physiology*, 25(1):111–146, 1941a.

J. D. Bernal and I. Fankuchen. X-ray and crystallographic studies of plant virus preparations. iii. *Journal of General Physiology*, 25(1):147–165, 1941b.

D. S. Bethune, C. H. Kiang, M. S. Devries, G. Gorman, R. Savoy, J. Vazquez, and R. Beyers. Cobalt-catalyzed growth of carbon nanotubes with single-atomic-layerwalls. *Nature*, 363(6430):605–607, 1993.

V.K. Bets and I.B. Yakobson. Spontaneous twist and intrinsic instabilities of pristine graphene nanoribbons. *Nano Research*, 2(2):161–166, 2009.

M. J. Biercuk, S. Ilani, C. M. Marcus, and P. L. McEuen. Electrical transport in single-wall carbon nanotubes. *Carbon Nanotubes*, 111:455–493, 2008.

S. Boncel, M.R. Sundaram, A.H. Windle, and K.K.K Koziol. Enhancement of the mechanical properties of directly spun cnt fibers by chemical treatment. *ACS nano*, 5(12):9339–9344, 2011.

Anders Borjesson and Kim Bolton. First principles studies of the effect of ostwald ripening on carbon nanotube chirality distributions. *ACS Nano*, 5(2):771–779, 2011.

David Brandon and D. Wayne Kaplan. *Microstructural characterization of materials*. Wiley, second edition edition, 2008.

E. Brown, L. Hao, J. C. Gallop, and J. C. Macfarlane. Ballistic thermal and electrical conductance measurements on individual multiwall carbon nanotubes. *Applied Physics Letters*, 87(2), 2005.

J. Campos-Delgado, J. M. Romo-Herrera, X. T. Jia, D. A. Cullen, H. Muramatsu, Y. A. Kim, T. Hayashi, Z. F. Ren, D. J. Smith, Y. Okuno, T. Ohba, H. Kanoh, K. Kaneko, M. Endo, H. Terrones, M. S. Dresselhaus, and M. Terrones. Bulk production of a new form of sp(2) carbon: Crystalline graphene nanoribbons. *Nano Letters*, 8(9):2773–2778, 2008.

L. G. Cancado, K. Takai, T. Enoki, M. Endo, Y. A. Kim, H. Mizusaki, N. L. Speziali, A. Jorio, and M. A. Pimenta. Measuring the degree of stacking order in graphite by raman spectroscopy. *Carbon*, 46(2):272–275, 2008.

A. Y. Cao, B. Q. Wei, Y. Jung, R. Vajtai, P. M. Ajayan, and G. Ramanath. Growth of aligned carbon nanotubes on self-similar macroscopic templates. *Applied Physics Letters*, 81(7):1297–1299, 2002.

R. L. Carver, H. Peng, A. K. Sadana, P. Nikolaev, S. Arepalli, C. D. Scott, W. E. Billups, R. H. Hauge, and R. E. Smalley. A model for nucleation and growth of single wall carbon nanotubes via the hipco process: A catalyst concentration study. *Journal of Nanoscience and Nanotechnology*, 5(7):1035–1040, 2005.

H. G. Chae and S. Kumar. Rigid-rod polymeric fibers. *Journal of Applied Polymer Science*, 100(1):791–802, 2006.

S. Chandrasekhar. *Liquid crystals*. Cambridge University Press, 1992.

Q. Cheng, J. Bao, G.J. Park, Z. Liang, C. Zhang, and B. Wang. High mechanical performance composite conductor: Multi-walled carbon nanotube sheet/bismaleimide nanocomposites. *Advanced Functional Materials*, 19(20):3219–3225, 2009.

A. G. Cheong and A. D. Rey. Texture dependence of capillary instabilities in nematic liquid crystalline fibres. *Liquid Crystals*, 31(9):1271–1284, 2004.

E. W. Choe and S. N. Kim. Synthesis, spinning, and fiber mechanical properties of poly(pphenylenebenzobisoxazo1e). *Macromolecules*, 14:920–924, 1981.

H. J. Choi, J. Ihm, S. G. Louie, and M. L. Cohen. Defects, quasibound states, and quantum conductance in metallic carbon nanotubes. *Physical Review Letters*, 84 (13):2917–2920, 2000.

T. Y. Choi, D. Poulikakos, J. Tharian, and U. Sennhauser. Measurement of thermal conductivity of individual multiwalled carbon nanotubes by the 3-omega method. *Applied Physics Letters*, 87(1), 2005.

Tae-Youl Choi, Dimos Poulikakos, Joy Tharian, and Urs Sennhauser. Measurement of the thermal conductivity of individual carbon nanotubes by the four-point three-omega method. *Nano Letters*, 6(8):1589–1593, 2006.

N. G. Chopra, L. X. Benedict, V. H. Crespi, M. L. Cohen, S. G. Louie, and A. Zettl. Fully collapsed carbon nanotubes. *Nature*, 377(6545):135–138, 1995.

L. Ci, N. Punbusayakul, J. Q. Wei, R. Vajtai, S. Talapatra, and P. M. Ajayan. Multifunctional macroarchitectures of double-walled carbon nanotube fibers. *Advanced Materials*, 19(13):1719 – 1723, 2007.

Y. Cohen and E. L. Thomas. Structure formation during spinning of poly (paraphenylenebenzobisthiazole) fiber. *Polymer Engineering and Science*, 25(17):1093–1096, 1985.

J. Cremlyn, R. *Chlorosulfonic acid: A versatile reagent*. The Royal Society of Chemistry, 2002.

C. A. Crouse and A. R. Barron. Reagent control over the size, uniformity, and composition of co-fe-o nanoparticles. *Journal of Materials Chemistry*, 18(35):4146–4153, 2008.

Christopher A. Crouse, Benji Maruyama, Jr. Colorado, Ramon, Tyson Back, and Andrew R. Barron. Growth, new growth, and amplification of carbon nanotubes as a function of catalyst composition. *Journal of the American Chemical Society*, 130(25):7946–7954, 2008.

Virginia. A. D. *Phase behavior and rheology of single-walled carbon nanotubes (SWNTs) in superacids with application to fibers spinning*. PhD thesis, Rice University, 2006.

H. J. Dai, J. Kong, C. W. Zhou, N. Franklin, T. Tombler, A. Cassell, S. S. Fan, and M. Chapline. Controlled chemical routes to nanotube architectures, physics, and devices. *Journal of Physical Chemistry B*, 103(51):11246–11255, 1999.

A. B. Dalton, S. Collins, E. Munoz, J. M. Razal, V. H. Ebron, J. P. Ferraris, J. N. Coleman, B. G. Kim, and R. H. Baughman. Super-tough carbon-nanotube fibres -

these extraordinary composite fibres can be woven into electronic textiles. *Nature*, 423(6941):703–703, 2003.

B. Dan, G. C. Irvin, and M. Pasquali. Continuous and scalable fabrication of transparent conducting carbon nanotube films. *ACS nano*, 3(4):835–843, 2009.

B. Dan, N. Behabtu, A. Martinez, S. J. Evans, V. D. Kosynkin, M. J. Tour, M. Pasquali, and I. I. Smalyukh. Liquid crystals of aqueous, giant graphene oxide flakes. *Soft Matter*, 7:11154–11159, 2011.

Richard J. Davies, Christian Riekel, Krzysztof K. Koziol, Juan J. Vilatela, and Alan H. Windle. Structural studies on carbon nanotube fibres by synchrotron radiation microdiffraction and microfluorescence. *Journal of Applied Crystallography*, 42:1122–1128, 2009.

V. A. Davis, L. M. Ericson, A. N. G. Parra-Vasquez, H. Fan, Y. H. Wang, V. Prieto, J. A. Longoria, S. Ramesh, R. K. Saini, C. Kittrell, W. E. Billups, W. W. Adams, R. H. Hauge, R. E. Smalley, and M. Pasquali. Phase behavior and rheology of SWNTs in superacids. *Macromolecules*, 37(1):154–160, 2004.

V. A. Davis, A. N. G. Parra-Vasquez, M. J. Green, P. K. Rai, N. Behabtu, V. Prieto, R. D. Booker, J. Schmidt, E. Kesselman, W. Zhou, H. Fan, W. W. Adams, R. H. Hauge, J. E. Fischer, Y. Cohen, Y. Talmon, R. E. Smalley, and M. Pasquali. True solutions of single-walled carbon nanotubes for assembly into macroscopic materials. *Nature Nanotechnology*, 4(12):830–834, 2009.

Virginia A. Davis. Liquid crystalline assembly of nanocylinders. *Journal of Materials Research*, 26(2):140–153, 2011.

P. G de Gennes. *The physics of liquid crystals*. Oxford University Press: New York, 1974.

G. K. Dimitrakakis, E. Tylianakis, and G. E. Froudakis. Pillared graphene: A new 3-d network nanostructure for enhanced hydrogen storage. *Nano Letters*, 8(10): 3166–3170, 2008.

F. Ding, R.A. Harutyunyan, and I.B. Yakobson. Dislocation theory of chirality-controlled nanotube growth. *Proceedings of the National Academy of Sciences of the United States of America*, 106(8):2506–2509, 2009.

Z. Dogic. Surface freezing and a two-step pathway of the isotropic-smectic phase transition in colloidal rods. *Physical Review Letters*, 91(16), 2003.

Z. Dogic and S. Fraden. Ordered phases of filamentous viruses. *Current Opinion in Colloid & Interface Science*, 11(1):47–55, 2006.

R. Duggal and M. Pasquali. Dynamics of individual single-walled carbon nanotubes in water by real-time visualization. *Physical Review Letters*, 96:246104, 2006.

J. G. Duque, A. N. G. Parra-Vasquez, N. Behabtu, M. J. Green, A. L. Higginbotham, B. K. Price, A. D. Leonard, H. K. Schmidt, B. Lounis, J. M. Tour, S. K. Doorn, L. Cognet, and M. Pasquali. Diameter-dependent solubility of single-walled carbon nanotubes. *ACS Nano*, 4(6):3063–3072, 2010.

T. Durkop, S. A. Getty, E. Cobas, and M. S. Fuhrer. Extraordinary mobility in semiconducting carbon nanotubes. *Nano Letters*, 4(1):35–39, 2004.

T. W. Ebbesen and P. M. Ajayan. Large-scale synthesis of carbon nanotubes. *Nature*, 358(6383):220–222, 1992.

W. F. Egelhoff and G. G. Tibbetts. Growth of copper, nickel, and palladium films on graphite and amourphous carbon. *Physical Review B*, 19(10):5028–5035, 1979.

C. Engtrakul, M. F. Davis, T. Gennett, A. C. Dillon, K. M. Jones, , and M. J. Heben. Protonation of carbon single-walled nanotubes studied using 13c and 1h-13c cross polarization nuclear magnetic resonance and raman spectroscopies. *Journal American Chemical Society*, 127:17548–17555, 2005.

L. M. Ericson, H. Fan, H. Q. Peng, V. A. Davis, W. Zhou, J. Sulpizio, Y. H. Wang, R. Booker, J. Vavro, C. Guthy, A. N. G. Parra-Vasquez, M. J. Kim, S. Ramesh, R. K. Saini, C. Kittrell, G. Lavin, H. Schmidt, W. W. Adams, W. E. Billups, M. Pasquali, W. F. Hwang, R. H. Hauge, J. E. Fischer, and R. E. Smalley. Macroscopic, neat, single-walled carbon nanotube fibers. *Science*, 305(5689):1447–1450, 2004.

Lars Martin Ericson. *Macroscopic neat single-wall carbon nanotube fibers*. PhD thesis, Rice University, 2003. Figure 3.25, pag. 101.

B.S. Fairchild, B. Maruyama, J.J. Boecki, A.D. Shiffer, O.N. Lockwood, C. Young, and M. Pasquali. SWNT fiber field emission cathodes, 2010.

N. Fakhri, A.D. Tsyboulski, L. Cognet, R. B. Weisman, and M. Pasquali. Diameter-dependent bending dynamics of single-walled carbon nanotubes in liquids. *Proceedings of the National Academy of Sciences*, 106(34):14219–14223, 2009.

N. Fakhri, C.F. MacKintosh, B. Lounis, L. Cognet, and M. Pasquali. Brownian motion of stiff filaments in a crowded environment. *Science*, 330(6012):1804–1807, 2010.

S. S. Fan, M. G. Chapline, N. R. Franklin, T. W. Tombler, A. M. Cassell, and H. J. Dai. Self-oriented regular arrays of carbon nanotubes and their field emission properties. *Science*, 283(5401):512–514, 1999.

Z. J. Fan, J. Yan, L. J. Zhi, Q. A. Zhang, T. Wei, J. Feng, M. L. Zhang, W. Z. Qian, and F. Wei. A three-dimensional carbon nanotube/graphene sandwich and its application as electrode in supercapacitors. *Advanced Materials*, 22(33):3723–3729, 2010.

M. Fang, S.and Zhang, A.A. Zakhidov, and H.R. Baughman. Structure and process-dependent properties of solid-state spun carbon nanotube yarns. *Journal of Physics*, 22(33), 2010.

C. Fantini, E. Cruz, A. Jorio, M. Terrones, H. Terrones, G. Van Lier, J. C. Charlier, M. S. Dresselhaus, R. Saito, Y. A. Kim, T. Hayashi, H. Muramatsu, M. Endo, and M. A. Pimenta. Resonance raman study of linear carbon chains formed by the heat treatment of double-wall carbon nanotubes. *Physical Review B*, 73(19), 2006.

A. C. Ferrari, J. C. Meyer, V. Scardaci, C. Casiraghi, M. Lazzeri, F. Mauri, S. Piscanec, D. Jiang, K. S. Novoselov, S. Roth, and A. K. Geim. Raman spectrum of graphene and graphene layers. *Physical Review Letters*, 97(18), 2006.

J. E. Fischer, H. Dai, A. Thess, R. Lee, N. M. Hanjani, D. L. Dehaas, and R. E. Smalley. Metallic resistivity in crystalline ropes of single-wall carbon nanotubes. *Physical Review B*, 55(8):R4921–R4924, 1997.

P. J. Flory. Phase equilibria in solutions of rod-like particles. *Proceedings of the Royal Society of London Series A*, 234(1196):73–89, 1956.

P. J. Flory and R. S. Frost. Statistical thermodynamics of mixtures of rodlike particles .3. most probable distribution. *Macromolecules*, 11(6):1126–1133, 1978.

F. C. Frank. On the theory of liquid crystals. *Discussions of the Faraday Society*, (25):19–28, 1958.

C. J. Gatlin, A. Matov, C.A. Groen, J.D. Needleman, J.T. Maresca, G. Danuser, J.T. Mitchison, and E. D. Salmon. Spindle fusion requires dynein-mediated sliding of oppositely oriented microtubules. *Current Biology*, 19(4):287–296, 2009.

M. J. Green, N. Behabtu, M. Pasquali, and W. W. Adams. Nanotubes as polymers. *Polymer*, 50(21):4979–4997, 2009a.

M. J. Green, A. N. G. Parra-Vasquez, N. Behabtu, and M. Pasquali. Modeling the phase behavior of polydisperse rigid rods with attractive interactions with applications to single-walled carbon nanotubes in superacids. *Journal of Chemical Physics*, 131(8), 2009b.

L. Grigorian, K. A. Williams, S. Fang, G. U. Sumanasekera, A. L. Loper, E. C. Dickey, S. J. Pennycook, and P. C. Eklund. Reversible intercalation of charged iodine chains into carbon nanotube ropes. *Physical Review Letters*, 80(25):5560–5563, 1998.

T. Guo, P. Nikolaev, A. Thess, D. T. Colbert, and R. E. Smalley. Catalytic growth of single-walled nanotubes by laser vaporization. *Chemical Physics Letters*, 243(1-2): 49–54, 1995.

K.A. Gupta, J.T. Russin, R.H. Gutierrez, and C.P. Eklund. Probing graphene edges via raman scattering. *ACS Nano*, 3(1):45–52, 2009.

V. Gupta, P. Scharff, L. C. Abelmann, and L. Spiess. C-60 intercalated graphite: A new form of carbon. *Fullerenes Nanotubes and Carbon Nanostructures*, 13:427–430, 2005.

Y. Hernandez, V. Nicolosi, M. Lotya, F. M. Blighe, Z. Y. Sun, S. De, I. T. McGovern, B. Holland, M. Byrne, Y. K. Gun'ko, J. J. Boland, P. Niraj, G. Duesberg, S. Krishnamurthy, R. Goodhue, J. Hutchison, V. Scardaci, A. C. Ferrari, and J. N. Coleman. High-yield production of graphene by liquid-phase exfoliation of graphite. *Nature Nanotechnology*, 3(9):563–568, 2008.

J. Hone. Phonons and thermal properties of carbon nanotubes. *Carbon Nanotubes*, 80:273–286, 2001.

J. Hone, M. Whitney, C. Piskoti, and A. Zettl. Thermal conductivity of single-walled carbon nanotubes. *Physical Review B*, 59(4):R2514–R2516, 1999a.

J. Hone, M. Whitney, C. Piskoti, and A. Zettl. Thermal conductivity of single-walled carbon nanotubes. *Physical Review B*, 59(4):R2514–R2516, 1999b.

J. Hone, M. C. Llaguno, N. M. Nemes, A. T. Johnson, J. E. Fischer, D. A. Walters, M. J. Casavant, J. Schmidt, and R. E. Smalley. Electrical and thermal transport properties of magnetically aligned single wall carbon nanotube films. *Applied Physics Letters*, 77(5):666–668, 2000.

F. Hua. *Wet-spinning of neat single-walled carbon nanotube fiber from 100+% H_2SO_4*. PhD thesis, Rice University, 2007.

W. S. Hummers and R. E. Offeman. Preparation of graphitic oxide. *Journal of the American Chemical Society*, 80(6):1339–1339, 1958.

Y. Ide and J. L. White. Spinnability of polymer fluid filaments. *Journal of Applied Polymer Science*, 20(9):2511–2531, 1976.

S. Iijima. Helical microtubules of graphitic carbon. *Nature*, 354(6348):56–58, 1991.

Bronikowski M. J., P. A. Willis, D. T. Colbert, K. A. Smith, and R. E. Smalley. Gas-phase production of carbon single-walled nanotubes from carbon monoxide via the hipco process: A parametric study. *Journal of Vacuum Science & Technology A*, 19:1800– 1805, 2001.

M. B. Jakubinek, M. B. Johnson, M. A. White, C. Jayasinghe, G. Li, W. Cho, M. J. Schulz, and V. Shanov. Thermal and electrical conductivity of array-spun multi-walled carbon nanotube yarns. *Carbon*, 50(1):244–248, 2012.

P. Jalali and M. Li. Model for estimation of critical packing density in polydisperse hard-disk packings. *Physica a-Statistical Mechanics and Its Applications*, 381:230–238, 2007.

Hoon-Sik Jang, Sang Koo Jeon, and Seung Hoon Nahm. Field emission properties from the tip and side of multi-walled carbon nanotube yarns. *Carbon*, 48(14): 4019–4023, 2010.

Paul Jarosz, Christopher Schauerman, Jack Alvarenga, Brian Moses, Thomas Mastrangelo, Ryne Raffaelle, Richard Ridgley, and Brian Landi. Carbon nanotube wires and cables: Near-term applications and future perspectives. *Nanoscale*, 3 (11):4542–4553, 2011.

Ji.and Xu G.and Di J. Jia, J.and Zhao, Z. Yong, Y. Tao, C. Fang, Z. Zhang, X. Zhang, L. Zheng, and Q. Li. A comparison of the mechanical properties of fibers spun from different carbon nanotubes. *Carbon*, 49(4):1333–1339, 2011.

E. Joselevich, H. J. Dai, J. Liu, K. Hata, and A. H. Windle. *Carbon nanotubes*, chapter Carbon nanotube synthesis and organization, pages 101–164. Springer-Verlag, 2008.

Kyongok Kang, M. P. Lettinga, Z. Dogic, and Jan K. G. Dhont. Vorticity banding in rodlike virus suspensions. *Physical Review E*, 74(2), 2006.

A. V. Kaznacheev, M. M. Bogdanov, and S. A. Taraskin. The nature of prolate shape of tactoids in lyotropic inorganic liquid crystals. *Journal of Experimental and Theoretical Physics*, 95(1):57–63, 2002.

P. Kim, L. Shi, A. Majumdar, and P. L. McEuen. Thermal transport measurements of individual multiwalled nanotubes. *Physical Review Letters*, 87(21), 2001.

Y. A. Kim, H. Muramatsu, T. Hayashi, M. Endo, M. Terrones, and M. S. Dresselhaus. Thermal stability and structural changes of double-walled carbon nanotubes by heat treatment. *Chemical Physics Letters*, 398(1-3):87–92, 2004.

D. L. Koch and O. G. Harlen. Interfacial tension at the boundary between nematic and isotropic phases of a hard rod solution. *Macromolecules*, 32(1):219–226, 1999.

N. Kojic, M. Kojic, S. Gudlavalleti, and M. McKinley. Solvent removal during synthetic and nephila fiber spinning. *Biomacromolecules*, 5:1698–1707, 2004.

D. V. Kosynkin, A. L. Higginbotham, A. Sinitskii, J. R. Lomeda, A. Dimiev, B. K. Price, and J. M. Tour. Longitudinal unzipping of carbon nanotubes to form graphene nanoribbons. *Nature*, 458(7240):872–U5, 2009.

K. Koziol, J. Vilatela, A. Moisala, M. Motta, P. Cunniff, M. Sennett, and A. H. Windle. High-performance carbon nanotube fiber. *Science*, 318:1892–1895, 2007.

M. E. Kozlov, R. C. Capps, W. M. Sampson, V. H. Ebron, J. P. Ferraris, and R. H. Baughman. Spinning solid and hollow polymer-free carbon nanotube fibers. *Advanced Materials*, 17(5):614–617, 2005.

W. Kratschmer, L. D. Lamb, K. Fostiropoulos, and D. R. Huffman. Solid c-60 - a new form of carbon. *Nature*, 347(6291):354–358, 1990.

A. Krishnan, E. Dujardin, T. W. Ebbesen, P. N. Yianilos, and M. M. J. Treacy. Young's modulus of single-walled nanotubes. *Physical Review B*, 58(20):14013–14019, 1998.

H. W. Kroto, J. R. Heath, S. C. Obrien, R. F. Curl, and R. E. Smalley. C-60 - buckminsterfullerene. *Nature*, 318(6042):162–163, 1985.

A. Kuc, L. Zhechkov, S. Patchkovskii, G. Seifert, and T. Heine. Hydrogen sieving and storage in fullerene intercalated graphite. *Nano Letters*, 7(1):1–5, 2007.

Alexander A. Kuznetsov, Alexandre F. Fonseca, Ray H. Baughman, and Anvar A. Zakhidov. Structural model for dry-drawing of sheets and yarns from carbon nanotube forests. *ACS Nano*, 5(2):985–993, 2011.

S. L. Kwolek, P. W. Morgan, J. R. Schaefgen, and L. W. Gulrich. Synthesis, anisotropic solutions, and fibers of poly (,4-benzamide). *Macromolecules*, 10(6): 1390–1396, 1977.

B. J. Landi and R. P. Raffaelle. Effects of carrier gas dynamics on single wall carbon nanotube chiral distributions during laser vaporization synthesis. *Journal of Nanoscience and Nanotechnology*, 7(3):883–890, 2007.

G. R. Larson. *The structure and rheology of complex fluids*. Oxford University Press, 1999.

S.D. Lashmore, J.J. Brown, K.J. Chaffee, B. Resnicoff, and P. Antoinette. Systems and methods for formation and harvesting of nanofibrous materials. United States Patent 7,993,620, July 17 2006.

J. G. Lavin, D. R. Boyington, L. Lahijani, B. Nysten, and J. P. Issi. The correlation of thermal conductivity with electrical resistivity in mesophase pitch-based carbon fiber. *Carbon*, 31(6):1001–1002, 1993.

O. D. Lavrentovich. Topological defects in dispersed liquid crystals, or words and worlds around liquid crystal drops. *Liquid Crystals*, 24(1):117–125, 1998.

C. Lee, X. D. Wei, J. W. Kysar, and J. Hone. Measurement of the elastic properties and intrinsic strength of monolayer graphene. *Science*, 321(5887):385–388, 2008.

R. S. Lee, H. J. Kim, J. E. Fischer, A. Thess, and R. E. Smalley. Conductivity enhancement in single-walled carbon nanotube bundles doped with k and br. *Nature*, 388(6639):255–257, 1997.

S. D. Lee and R. B. Meyer. Computations of the phase equilibrium, elastic constants, and viscosities of a hard-rod nematic liquid crystal. *Journal of Chemical Physics*, 84(6):3443–3448, 1986.

Q. W. Li, X. F. Zhang, R. F. DePaula, L. X. Zheng, Y. H. Zhao, L. Stan, T. G. Holesinger, P. N. Arendt, D. E. Peterson, and Y. T. Zhu. Sustained growth of ultralong carbon nanotube arrays for fiber spinning. *Advanced Materials*, 18(23): 3160 – 3163, 2006a.

Q. W. Li, Y. Li, X. F. Zhang, S. B. Chikkannanavar, Y. H. Zhao, A. M. Dangelewicz, L. X. Zheng, S. K. Doorn, Q. X. Jia, D. E. Peterson, P. N. Arendt, and Y. T. Zhu. Structure-dependent electrical properties of carbon nanotube fibers. *Advanced Materials*, 19:2567 – 2570, 2007.

Qingwen Li, Yuntian T. Zhu, Ian A. Kinloch, and Alan H. Windle. Self-organization of carbon nanotubes in evaporating droplets. *Journal of Physical Chemistry B*, 110 (28):13926–13930, 2006b.

Y. L. Li, I. A. Kinloch, and A. H. Windle. Direct spinning of carbon nanotube fibers from chemical vapor deposition synthesis. *Science*, 304(5668):276–278, 2004.

F. Liang, A. K. Sadana, A. Peera, J. Chattopadhyay, Z. N. Gu, R. H. Hauge, and W. E. Billups. A convenient route to functionalized carbon nanotubes. *Nano Letters*, 4(7):1257–1260, 2004.

K. Liu, Y. Sun, X. Lin, R. Zhou, J. Wang, S. Fan, and K. Jiang. Scratch-resistant, highly conductive, and high-strength carbon nanotube-based composite yarns. *ACS Nano*, 4(10):5827–5834, 2010a.

K. Liu, Y. Sun, R. Zhou, H. Zhu, J. Wang, L. Liu, S. Fan, and K. Jiang. Carbon nanotube yarns with high tensile strength made by a twisting and shrinking method. *Nanotechnology*, 21(4), 2010b.

M. Lotya, Y. Hernandez, P. J. King, R. J. Smith, V. Nicolosi, L. S. Karlsson, F. M. Blighe, S. De, Z. M. Wang, I. T. McGovern, G. S. Duesberg, and J. N. Coleman. Liquid phase production of graphene by exfoliation of graphite in surfactant/water solutions. *Journal of the American Chemical Society*, 131(10):3611–3620, 2009.

L. Lu, W. Yi, and D. L. Zhang. 3 omega method for specific heat and thermal conductivity measurements. *Review of Scientific Instruments*, 72(7):2996–3003, 2001.

T. C. Lubensky, D. Pettey, N. Currier, and H. Stark. Topological defects and interactions in nematic emulsions. *Physical Review E*, 57(1):610–625, 1998.

A. Lucas, C. Zakri, M. Maugey, M. Pasquali, P. van der Schoot, and P. Poulin. Kinetics of nanotube and microfiber scission under sonication. *Journal of Physical Chemistry C*, 113(48):20599–20605, 2009.

S. J. Ludtke, D. H. Chen, J. L. Song, D. T. Chuang, and W. Chiu. Seeing groel at 6 angstrom resolution by single particle electron cryo microscopy. *Structure*, 12(7): 1129–1136, 2004.

B. P. Luo, S. L. Clegg, Peter Th., R. Muller, and J. P. Crutzen. Hcl solubility and liquid diffusion in aqueous sulfuric acid under stratospheric conditions. *Geophysical Research Letters*, 21(1):49–52, 1994.

W. Ma, L. Liu, Z. Zhang, R. Yang, G. Liu, T. Zhang, X. An, X. Yi, Y. Ren, Z. Niu, J. Li, H. Dong, W. Zhou, M.P. Ajayan, and S. Xie. High-strength composite fibers: realizing true potential of carbon nanotubes in polymer matrix through continuous reticulate architecture and molecular level couplings. *Nano Letters*, 9(8):2855–2861, 2009.

W. Christopher Macosko. *Rheology principles, measurements, and applications*. VCH Publishers, 1994.

U. Massing, S. Cicko, and V. Ziroli. Dual asymmetric centrifugation (dac) - a new

technique for liposome preparation. *Journal of Controlled Release*, 125(1):16–24, 2008.

R. A. Matula. Electrical resistivity of copper, gold, palladium, and silver. *Journal of Physical and Chemical Reference Data*, 8(4):1147–1298, 1979.

M. J. McAllister, J. L. Li, D. H. Adamson, H. C. Schniepp, A. A. Abdala, J. Liu, M. Herrera-Alonso, D. L. Milius, R. Car, R. K. Prud'homme, and I. A. Aksay. Single sheet functionalized graphene by oxidation and thermal expansion of graphite. *Chemistry of Materials*, 19(18):4396–4404, 2007.

J. Melin, G. Furdin, H. Fuzellier, R. Vasse, and A. Herold. Reaction of chloride solutions with graphite in chlorosulfonic acid. *Materials Science and Engineering*, 31:61–65, 1977.

C. Mercader, A. Lucas, A. Derre, C. Zakri, S. Moisan, M. Maugey, and P. Poulin. Kinetics of fiber solidification. *Proceedings of the National Academy of Sciences*, 107(43):18331–18335, 2010.

J. C. Meyer, A. K. Geim, M. I. Katsnelson, K. S. Novoselov, D. Obergfell, S. Roth, C. Girit, and A. Zettl. On the roughness of single- and bi-layer graphene membranes. *Solid State Communications*, 143(1-2):101–109, 2007.

P. Miaudet, S. Badaire, M. Maugey, A. Derre, V. Pichot, P. Launois, P. Poulin, and C. Zakri. Hot-drawing of single and multiwall carbon nanotube fibers for high toughness and alignment. *Nano Letters*, 5(11):2212–2215, 2005.

M. L. Minus and S. Kumar. The processing, properties, and structure of carbon fibers. *Journal of the Minerals, Metals and Materials Society*, 57(2):52–58, 2005.

S. M. Mominuzzaman, K. M. Krishna, T. Soga, T. Jimbo, and M. Umeno. Optical absorption and electrical conductivity of amorphous carbon thin films from camphor: A natural source. *Japanese Journal of Applied Physics*, 38(2A):658–663, 1999.

M. Monthioux and V. L. Kuznetsov. Who should be given the credit for the discovery of carbon nanotubes? *Carbon*, 44(9):1621–1623, 2006.

W. E. Morton and W. S. Hearle. *Physical properties of textile fibres*. Butterworth & Co., 1962.

M. Motta, Y. L. Li, I. Kinloch, and A. Windle. Mechanical properties of continuously spun fibers of carbon nanotubes. *Nano Letters*, 5(8):1529–1533, 2005.

M. Motta, A. Moisala, I. A. Kinloch, and A. H. Windle. High performance fibres from 'dog bone' carbon nanotubes. *Advanced Material*, 19:3721 – 3726, 2007.

J. A. Moulijn, A. E. van Diepen, and F. Kapteijn. Catalyst deactivation: is it predictable? what to do? *Applied Catalysis A*, 212(1-2):3–16, 2001.

Simon E. Moulton, Maryse Maugey, Philippe Poulin, and Gordon G. Wallace. Liquid crystal behavior of single-walled carbon nanotubes dispersed in biological hyaluronic acid solutions. *Journal of the American Chemical Society*, 129(30): 9452–9457, 2007.

D. A. Muller, L. F. Kourkoutis, M. Murfitt, J. H. Song, H. Y. Hwang, J. Silcox, N. Dellby, and O. L. Krivanek. Atomic-scale chemical imaging of composition and bonding by aberration-corrected microscopy. *Science*, 319(5866):1073–1076, 2008.

E. Munoz, A. B. Dalton, S. Collins, M. Kozlov, J. Razal, J. N. Coleman, B. G. Kim, V. H. Ebron, M. Selvidge, J. P. Ferraris, and R. H. Baughman. Multifunctional

carbon nanotube composite fibers. *Advanced Engineering Materials*, 6(10):801–804, 2004.

S. Murali, T. Xu, D.B. Marshall, J.M. Kayatin, K. Pizarro, K.V. Radhakrishnan, D. Nepal, and A.V. Davis. Lyotropic liquid crystalline self-assembly in dispersions of silver nanowires and nanoparticles. *Langmuir*, 26(13):11176–11183, 2010.

R. R. Nair, P. Blake, A. N. Grigorenko, K. S. Novoselov, T. J. Booth, T. Stauber, N. M. R. Peres, and A. K. Geim. Fine structure constant defines visual transparency of graphene. *Science*, 320(5881):1308–1308, 2008.

T. Naraghi, M.and Filleter, A. Moravsky, M. Locascio, O.R. Loutfy, and D.H. Espinosa. A multiscale study of high performance double-walled nanotube-polymer fibers. *ACS Nano*, 4(11):6463–6476, 2010.

J. Nehring and A. Saupe. Elastic theory of uniaxial liquid crystals. *Journal of Chemical Physics*, 54(1):337–343, 1971.

W. Neri, M. Maugey, P. Miaudet, A. Derre, C. Zakri, and P. Poulin. Surfactant-free spinning of composite carbon nanotube fibers. *Macromolecular Rapid Communications*, 27(13):1035–1038, 2006.

P. Nikolaev. Gas-phase production of single-walled carbon nanotubes from carbon monoxide: A review of the hipco process. *Journal of Nanoscience and Nanotechnology*, 4:307–316, 2004.

P. Nikolaev, M. J. Bronikowski, R. K. Bradley, F. Rohmund, D. T. Colbert, K. A. Smith, and R. E. Smalley. Gas-phase catalytic growth of single-walled carbon nanotubes from carbon monoxide. *Chemical Physics Letters*, 313(1-2):91–97, 1999.

H. Nishino, S. Yasuda, T. Namai, D. N. Futaba, T. Yamada, M. Yumura, S. Iijima, and K. Hata. Water-assisted highly efficient synthesis of single-walled carbon nanotubes forests from colloidal nanoparticle catalysts. *Journal of Physical Chemistry C*, 111:17961–17965, 2007.

C. T. Nottbohm, A. Beyer, A. S. Sologubenko, I. Ennen, A. Hutten, H. Rosner, W. Eck, J. Mayer, and A. Golzhauser. Novel carbon nanosheets as support for ultrahigh-resolution structural analysis of nanoparticles. *Ultramicroscopy*, 108(9): 885–892, 2008.

K. S. Novoselov, A. K. Geim, S. V. Morozov, D. Jiang, Y. Zhang, S. V. Dubonos, I. V. Grigorieva, and A. A. Firsov. Electric field effect in atomically thin carbon films. *Science*, 306(5296):666–669, 2004.

K. S. Novoselov, D. Jiang, F. Schedin, T. J. Booth, V. V. Khotkevich, S. V. Morozov, and A. K. Geim. Two-dimensional atomic crystals. *Proceedings of the National Academy of Sciences of the United States of America*, 102(30):10451–10453, 2005.

Patrick W. Oakes, Jorge Viamontes, and Jay X. Tang. Growth of tactoidal droplets during the first-order isotropic to nematic phase transition of f-actin. *Physical Review E*, 75(6), 2007.

M. J. O'Connell, S. M. Bachilo, C. B. Huffman, V. C. Moore, M. S. Strano, E. H. Haroz, K. L. Rialon, P. J. Boul, W. H. Noon, C. Kittrell, J. P. Ma, R. H. Hauge, R. B. Weisman, and R. E. Smalley. Band gap fluorescence from individual single-walled carbon nanotubes. *Science*, 297(5581):593–596, 2002.

T. Odijk and H. N. W. Lekkerkerker. Theory of the isotropic liquid-crystal phase-

separation for a solution of bidisperse rodlike macromolecules. *Journal of Physical Chemistry*, 89(10):2090–2096, 1985.

L. Onsager. The effects of shape on the interaction of colloidal particles. *Annals of the New York Academy of Sciences*, 51(4):627–659, 1949.

Alvin W. Orbaek, Andrew C. Owens, and Andrew R. Barron. Increasing the efficiency of single walled carbon nanotube amplification by fe-co catalysts through the optimization of CH4/H2 partial pressures. *Nano Letters*, 11(7):2871–2874, 2011.

M. Panar and L. F. Beste. Structure of poly(1,4-benzamide) solutions. *Macromolecules*, 10(6):1401–1406, 1977.

J. I. Paredes, S. Villar-Rodil, A. Martinez-Alonso, and J. M. D. Tascon. Graphene oxide dispersions in organic solvents. *Langmuir*, 24(19):10560–10564, 2008.

A.N.G. Parra-Vasquez, I. Stepanek, V.A. Davis, V.C. Moore, Haroz E.H., J. Shaver, R.H. Hauge, R.E. Smalley, and M. Pasquali. Simple length determination of single-walled carbon nanotubes by viscosity measurements in diluite suspension. *Macromolecules*, 40:4043–4047, 2007.

A.N.G. Parra-Vasquez, N. Behabtu, M.J. Green, L.C. Pint, C.C. Young, J. Schmidt, E. Kesselman, A. Goyal, M.P. Ajayan, Y. Cohen, Y. Talmon, H.R. Hauge, and M. Pasquali. Spontaneous dissolution of ultralong single- and multiwalled carbon nanotubes. *ACS Nano*, 4(7):3969–3978, 2010.

M. Pasquali. Swell properties and swift processing. *Nature Materials*, 3(8):509–510, 2004.

Bei Peng, Mark Locascio, Peter Zapol, Shuyou Li, Steven L. Mielke, George C. Schatz, and Horacio D. Espinosa. Measurements of near-ultimate strength for multiwalled carbon nanotubes and irradiation-induced crosslinking improvements. *Nature Nanotechnology*, 3(10):626–631, 2008.

Robert H. Perry and Don W. Green. *Perry's Chemical Engineers' Handbook*. McGraw-Hill, seventh edition, 1997. Section 9, page 40.

L.C. Pint, T.S. Pheasant, A.N.G. Parra-Vasquez, C. Horton, Y. Xu, and H.R. Hauge. Investigation of optimal parameters for oxide-assisted growth of vertically aligned single-walled carbon nanotubes. *Journal of Physical Chemistry C*, 113(10):4125–4133, 2009.

Yeh Pochi and Gu Claire. *Optics of liquid crystal displays*. John Wiley and Sons, Inc., 1999.

E. Pop, D. Mann, J. Cao, Q. Wang, K. Goodson, and H. J. Dai. Negative differential conductance and hot phonons in suspended nanotube molecular wires. *Physical Review Letters*, 95(15), 2005.

E. Pop, D. Mann, Q. Wang, K. Goodson, and H. J. Dai. Thermal conductance of an individual single-wall carbon nanotube above room temperature. *Nano Letters*, 6 (1):96–100, 2006.

P. Poulin and D. A. Weitz. Inverted and multiple nematic emulsions. *Physical Review E*, 57(1):626–637, 1998.

P. Poulin, B. Vigolo, and P. Launois. Films and fibers of oriented single wall nanotubes. *Carbon*, 40(10):1741–1749, 2002.

P. Prinsen and P. van der Schoot. Shape and director-field transformation of tactoids. *Physical Review E*, 68(2), 2003.

P. Prinsen and P. van der Schoot. Continuous director-field transformation of nematic tactoids. *European Physical Journal E*, 13(1):35–41, 2004a.

P. Prinsen and P. van der Schoot. Parity breaking in nematic tactoids. *Journal of Physics*, 16(49):8835–8850, 2004b.

N. Puech, E. Grelet, P. Poulin, C. Blanc, and P. van der Schoot. Nematic droplets in aqueous dispersions of carbon nanotubes. *Physical Review E*, 82(2 Pt 1):020702, 2010.

Nicolas Puech, Christophe Blanc, Eric Grelet, Camilo Zamora-Ledezma, Maryse Maugey, Cecile Zakri, Eric Anglaret, and Philippe Poulin. Highly ordered carbon nanotube nematic liquid crystals. *Journal of Physical Chemistry C*, 115(8): 3272–3278, 2011.

P. K. Rai, R. A. Pinnick, A. N. G. Parra-Vasquez, V. A. Davis, H. K. Schmidt, R. H. Hauge, R. E. Smalley, and M. Pasquali. Isotropic-nematic phase transition of single-walled carbon nanotubes in strong acids. *Journal of the American Chemical Society*, 128(2):591–595, 2006.

P. K. Rai, A. N. G. Parra-Vasquez, H. Peng, R. H. Hauge, and M. Pasquali. Solubility and size separation of large fullerenes in concentrated sulfuric acids. *Journal of Physical Chemistry C*, 111(48):17966–17969, 2007.

S. Ramesh, L. M. Ericson, V. A. Davis, R. K. Saini, C. Kittrell, M. Pasquali, W. E. Billups, W. W. Adams, R. H. Hauge, and R. E. Smalley. Dissolution of pristine

single walled carbon nanotubes in superacids by direct protonation. *Journal of Physical Chemistry B*, 108(26):8794–8798, 2004.

A. Rapini and M. Papoular. Distortion d'une lamelle nematique sous champ magnetique conditions d'ancrage aux parois. *Le Journal de Physique Colloques*, 30(C4): 54–57, 1969.

J. M. Razal, J. N. Coleman, E. Munoz, B. Lund, Y. Gogotsi, H. Ye, S. Collins, A. B. Dalton, and R. H. Baughman. Arbitrarily shaped fiber assemblies from spun carbon nanotube gel fibers. *Advanced Functional Materials*, 17:2918–2924, 2007.

Arava Leela Mohana Reddy, Anchal Srivastava, Sanketh R. Gowda, Hemtej Gullapalli, Madan Dubey, and Pulickel M. Ajayan. Synthesis of nitrogen-doped graphene films for lithium battery application. *ACS Nano*, 4(11):6337–6342, 2010.

D. E. Resasco, W. E. Alvarez, F. Pompeo, L. Balzano, J. E. Herrera, B. Kitiyanan, and A. Borgna. A scalable process for production of single-walled carbon nanotubes (SWNTs) by catalytic disproportionation of co on a solid catalyst. *Journal of Nanoparticle Research*, 4(1-2):131–136, 2002.

A. D. Rey. Linear stability theory of break-up dynamics of nematic liquid crystalline fibers. *Journal De Physique Ii*, 7(7):1001–1011, 1997.

D.A. Rey. Capillary models for liquid crystal fibers, membranes, films, and drops. *Soft Matter*, 3(11):1349–1368, 2007.

Rod Ruoff. Calling all chemists. *Nature Nanotechnology*, 3(1):10–11, 2008.

S. Ryu, Y. Lee, J.W. Hwang, C. Hong, S.and Kim, T.G. Park, H. Lee, and S.H. Hong. High-strength carbon nanotube fibers fabricated by infiltration and curing

of mussel-inspired catecholamine polymer. *Advanced Materials*, 23(17):1971–1975, 2011.

D. Sanchez-Portal, E. Artacho, J. M. Soler, A. Rubio, and P. Ordejon. Ab initio structural, elastic, and vibrational properties of carbon nanotubes. *Physical Review B*, 59(19):12678–12688, 1999.

A. V. Savin, B. Hu, and Y. S. Kivshar. Thermal conductivity of single-walled carbon nanotubes. *Physical Review B*, 80(19), 2009.

V. Scardaci, R. Coull, and J. N. Coleman. Very thin transparent, conductive carbon nanotube films on flexible substrates. *Applied Physics Letters*, 97(2), 2010.

T. Schwamb, R.B. Burg, C.N. Schirmer, and D. Poulikakos. An electrical method for the measurement of the thermal and electrical conductivity of reduced graphene oxide nanostructures. *Nanotechnology*, 20(40), 2009.

C. H. See and A. T. Harris. A review of carbon nanotube synthesis via fluidized-bed chemical vapor deposition. *Industrial & Engineering Chemistry Research*, 46(4): 997–1012, 2007.

P. K. Seelam, M. Huuhtanen, A. Sapi, M. Szabo, K. Kordas, E. Turpeinen, G. Toth, and R. L. Keiski. Cnt-based catalysts for h(2) production by ethanol reforming. *International Journal of Hydrogen Energy*, 35(22):12588–12595, 2010.

M. Segal. Selling graphene by the ton. *Nature Nanotechnology*, 4(10):611–613, 2009.

R. E. Smalley. Discovering the fullerenes. *Reviews of Modern Physics*, 69(3):723–730, 1997.

Richard E. Smalley, Yubao Li, Valerie C. Moore, B. Katherine Price, Jr. Colorado, Ramon, Howard K. Schmidt, Robert H. Hauge, Andrew R. Barron, and James M. Tour. Single wall carbon nanotube amplification: En route to a type-specific growth mechanism. *Journal of the American Chemical Society*, 128(49):15824–15829, 2006.

B. W. Smith and D. E. Luzzi. Electron irradiation effects in single wall carbon nanotubes. *Journal of Applied Physics*, 90(7):3509–3515, 2001.

J.M. Solomon and T.P. Spicer. Microstructural regimes of colloidal rod suspensions, gels, and glasses. *Soft Matter*, 6(7):1391–1400, 2010.

W. H. Song and A. H. Windle. Isotropic-nematic phase transition of dispersions of multiwall carbon nanotubes. *Macromolecules*, 38(14):6181–6188, 2005.

W. H. Song, I. A. Kinloch, and A. H. Windle. Nematic liquid crystallinity of multiwall carbon nanotubes. *Science*, 302(5649):1363–1363, 2003.

Wenhui Song and Alan H. Windle. Size-dependence and elasticity of liquid-crystalline multiwalled carbon nanotubes. *Advanced Materials*, 20(16):3149–3154, 2008.

M. S. Spector, E. Naranjo, S. Chiruvolu, and J. A. Zasadzinski. Conformation of a tethered membrane - crumpling in graphite oxide. *Physical Review Letters*, 73(21): 2867–2870, 1994.

S. Stankovich, D. A. Dikin, G. H. B. Dommett, K. M. Kohlhaas, E. J. Zimney, E. A. Stach, R. D. Piner, S. T. Nguyen, and R. S. Ruoff. Graphene-based composite materials. *Nature*, 442(7100):282–286, 2006.

S. Stankovich, D. A. Dikin, R. D. Piner, K. A. Kohlhaas, A. Kleinhammes, Y. Jia,

Y. Wu, S. T. Nguyen, and R. S. Ruoff. Synthesis of graphene-based nanosheets via chemical reduction of exfoliated graphite oxide. *Carbon*, 45(7):1558–1565, 2007.

H. Staudinger. *Die Hochmolekularen Organischen Verbindungen.* Berlin:Pringer, 1932.

J. Steinmetz, M. Glerup, M. Paillet, P. Bernier, and M. Holzinger. Production of pure nanotube fibers using a modified wet-spinning method. *Carbon*, 43(11):2397–2400, 2005.

J. P. Straley. Frank elastic constants of hard-rod liquid crystal. *Physical Review A*, 8(4):2181–2183, 1973.

G. U. Sumanasekera, J. L. Allen, S. L. Fang, A. L. Loper, A. M. Rao, and P. C. Eklund. Electrochemical oxidation of single wall carbon nanotube bundles in sulfuric acid. *Journal of Physical Chemistry B*, 103(21):4292–4297, 1999.

Y. Talmon. Transmission electron microscopy of complex fluids: The state of the art. *Berichte Der Bunsen-Gesellschaft-Physical Chemistry Chemical Physics*, 100 (3):364–372, 1996.

Y. Talmon. *Seeing Giant Micelles by Cryogenic-Temperature Transmission Electron Microscopy (Cryo-TEM), In Giant Micelles*, pages 163–178. 2007.

S. J. Tans, M. H. Devoret, H. J. Dai, A. Thess, R. E. Smalley, L. J. Geerligs, and C. Dekker. Individual single-wall carbon nanotubes as quantum wires. *Nature*, 386 (6624):474–477, 1997.

E. M. Terentjev. Stability of liquid-crystalline macroemulsions. *Europhysics Letters*, 32(7):607–612, 1995.

A. Thess, R. Lee, P. Nikolaev, H. J. Dai, P. Petit, J. Robert, C. H. Xu, Y. H. Lee, S. G. Kim, A. G. Rinzler, D. T. Colbert, G. E. Scuseria, D. Tomanek, J. E. Fischer, and R. E. Smalley. Crystalline ropes of metallic carbon nanotubes. *Science*, 273 (5274):483–487, 1996.

J. M. Thomas and P. L. Walker. Mobility of metal particles on graphite substrate. *Journal of Chemical Physics*, 41(2):587–588, 1964.

T. Tixier, M. Heppenstall-Butler, and E. M. Terentjev. Spontaneous size selection in cholesteric and nematic emulsions. *Langmuir*, 22(5):2365–2370, 2006.

M. M. J. Treacy, T. W. Ebbesen, and J. M. Gibson. Exceptionally high young's modulus observed for individual carbon nanotubes. *Nature*, 381(6584):678–680, 1996.

Yu Trukhina, S. Jungblut, P. van der Schoot, and T. Schilling. Osmotic compression of droplets of hard rods: A computer simulation study. *Journal of Chemical Physics*, 130(16), 2009.

V. C. Tung, L. M. Chen, M. J. Allen, J. K. Wassei, K. Nelson, R. B. Kaner, and Y. Yang. Low-temperature solution processing of graphene-carbon nanotube hybrid materials for high-performance transparent conductors. *Nano Letters*, 9(5):1949–1955, 2009.

C. Valles, C. Drummond, H. Saadaoui, C. A. Furtado, M. He, O. Roubeau, L. Ortolani, M. Monthioux, and A. Penicaud. Solutions of negatively charged graphene sheets and ribbons. *Journal of the American Chemical Society*, 130(47):15802–15804, 2008.

D. van der Beek and H. N. W. Lekkerkerker. Liquid crystal phases of charged colloidal platelets. *Langmuir*, 20(20):8582–8586, 2004.

F. M. van der Kooij and H. N. W. Lekkerkerker. Liquid-crystalline phase behavior of a colloidal rod-plate mixture. *Physical Review Letters*, 84(4):781–784, 2000.

F. M. van der Kooij, K. Kassapidou, and H. N. W. Lekkerkerker. Liquid crystal phase transitions in suspensions of polydisperse plate-like particles. *Nature*, 406(6798): 868–871, 2000.

P. van der Schoot. Remarks on the interfacial tension in colloidal systems. *Journal of Physical Chemistry B*, 103(42):8804–8808, 1999.

A. A. Verhoeff, I. A. Bakelaar, R. H. J. Otten, P. van der Schoot, and H. N. W. Lekkerkerker. Tactoids of plate-like particles: size, shape, and director field. *Langmuir*, 27(1):116–125, 2011.

B. Vigolo, A. Penicaud, C. Coulon, C. Sauder, R. Pailler, C. Journet, P. Bernier, and P. Poulin. Macroscopic fibers and ribbons of oriented carbon nanotubes. *Science*, 290(5495):1331–1334, 2000.

B. Vigolo, P. Poulin, M. Lucas, P. Launois, and P. Bernier. Improved structure and properties of single-wall carbon nanotube spun fibers. *Applied Physics Letters*, 81 (7):1210–1212, 2002.

B. Vigolo, C. Coulon, M. Maugey, C. Zakri, and P. Poulin. An experimental approach to the percolation of sticky nanotubes. *Science*, 309(5736):920–923, 2005.

Juan J. Vilatela and Alan H. Windle. Yarn-like carbon nanotube fibers. *Advanced Materials*, 22(44):4959–+, 2010.

Juan J. Vilatela, James A. Elliott, and Alan H. Windle. A model for the strength of yarn-like carbon nanotube fibers. *ACS Nano*, 5(3):1921–1927, 2011.

Juan J. Vilatela, Rupesh Khare, and Alan H. Windle. The hierarchical structure and properties of multifunctional carbon nanotube fibre composites. *Carbon*, 50 (3):1227–1234, 2012.

F. L. Vogel. Electrical conductivity of graphite intercalated with superacid fluorides - experiments with antimony pentafluoride. *Journal of Materials Science*, 12(5): 982–986, 1977.

H. D. Wagner. Stochastic concepts in the study of size effects in the mechanical strength of highly oriented polymeric materials. *Journal of Polymer Science Part B*, 27(1):115–149, 1989.

Zbigniew K. Walczak. *Formation of synthetic fibers*. Gordon and Breach Science Publishers, 1977.

David H. Wang, Hao Jiang, and W. Wade Adams. Rigid-rod polymers, 2011.

Z. L. Wang, D. W. Tang, X. B. Li, X. H. Zheng, W. G. Zhang, L. X. Zheng, Y. T. Zhu, A.Z. Jin, H. F. Y., and C. Z. Gu. Length-dependent thermal conductivity of an individual single-wall carbon nanotube. *Applied Physics Letters*, 91(12), 2007.

H. H. Wensink and G. J. Vroege. Isotropic-nematic phase behavior of length-polydisperse hard rods. *Journal of Chemical Physics*, 119(13):6868–6882, 2003.

A. Williamson. Note on the decomposition of sulphuric acid by pentachloride of phosphorus. *Proceedings of the Royal Society of London*, 7:11–15, 1854.

N. R. Wilson, P. A. Pandey, R. Beanland, R. J. Young, I. A. Kinloch, L. Gong, Z. Liu, K. Suenaga, J. P. Rourke, S. J. York, and J. Sloan. Graphene oxide: Structural analysis and application as a highly transparent support for electron microscopy. *ACS Nano*, 3(9):2547–2556, 2009.

Y. Q. Xu, H. Q. Peng, R. H. Hauge, and R. E. Smalley. Controlled multistep purification of single-walled carbon nanotubes. *Nano Letters*, 5(1):163–168, 2005.

B. I. Yakobson, C. J. Brabec, and J. Bernholc. Nanomechanics of carbon tubes: Instabilities beyond linear response. *Physical Review Letters*, 76(14):2511–2514, 1996.

B. I. Yakobson, G. Samsonidze, and G. G. Samsonidze. Atomistic theory of mechanical relaxation in fullerene nanotubes. *Carbon*, 38(11-12):1675–1680, 2000.

T. Yamamoto, K. Watanabe, and E. R. Hernandez. Mechanical properties, thermal stability and heat transport in carbon nanotubes. *Carbon Nanotubes*, 111:165–194, 2008.

H.H. Yang. *Aromatic high strength fibers*. Wiley, 1989.

S. Yang, N.A. Parks, A.S. Saba, P. L. Ferguson, and J. Liu. Photoluminescence from inner walls in double-walled carbon nanotubes: some do, some do not. *Nano Letters*, 11(10):4405–4410, 2011.

YuanChao Yang, Liang Liu, and ShouShan Fan. A vacuum sensor using field emitters made by multiwall carbon nanotube yarn. *Vacuum*, 86:885–888, 2012.

C. H. Yu, L. Shi, Z. Yao, D. Y. Li, and A. Majumdar. Thermal conductance and

thermopower of an individual single-wall carbon nanotube. *Nano Letters*, 5(9): 1842–1846, 2005.

M. F. Yu, B. S. Files, S. Arepalli, and R. S. Ruoff. Tensile loading of ropes of single wall carbon nanotubes and their mechanical properties. *Physical Review Letters*, 84(24):5552–5555, 2000a.

M. F. Yu, O. Lourie, M. J. Dyer, K. Moloni, T. F. Kelly, and R. S. Ruoff. Strength and breaking mechanism of multiwalled carbon nanotubes under tensile load. *Science*, 287(5453):637–640, 2000b.

M. F. Yu, B. I. Yakobson, and R. S. Ruoff. Controlled sliding and pullout of nested shells in individual multiwalled carbon nanotubes. *Journal of Physical Chemistry B*, 104(37):8764–8767, 2000c.

A. A. Zakhidov, R. Nanjundaswamy, A. N. Obraztsov, M. Zhang, S. Fang, V. I. Klesch, and R. H. Baughman. Field emission of electrons by carbon nanotube twist-yarns. *Applied Physics A*, 88(4):593–600, 2007.

Camilo Zamora-Ledezma, Christophe Blanc, Maryse Maugey, Cecile Zakri, Philippe Poulin, and Eric Anglaret. Anisotropic thin films of single-wall carbon nanotubes from aligned lyotropic nematic suspensions. *Nano Letters*, 8(12):4103–4107, 2008.

L. Zhang, C. Feng, Z. Chen, L. Liu, K. L. Jiang, Q. Q. Li, and S. S. Fan. Super-aligned carbon nanotube grid for high resolution transmission electron microscopy of nanomaterials. *Nano Letters*, 8(8):2564–2569, 2008a.

M. Zhang, K. R. Atkinson, and R. H. Baughman. Multifunctional carbon nanotube yarns by downsizing an ancient technology. *Science*, 306(5700):1358–1361, 2004.

Q. Zhang, D.G. Wang, J.Q. Huang, W.P. Zhou, G.H. Luo, W.Z. Qian, and F. Wei. Dry spinning yarns from vertically aligned carbon nanotube arrays produced by an improved floating catalyst chemical vapor deposition method. *Carbon*, 48(10): 2855–2861, 2010a.

S. Zhang, L. Zhu, M. L. Minus, H. G. Chae, S. Jagannathan, C. P. Wong, J. Kowalik, L. B. Roberson, and S. Kumar. Solid-state spun fibers and yarns from 1-mm long carbon nanotube forests synthesized by water-assisted chemical vapor deposition. *Journal of Materials Science*, 43(13):4356–4362, 2008b.

Shanju Zhang, Krzysztof K. K. Koziol, Ian A. Kinloch, and Alan H. Windle. Macroscopic fibers of well-aligned carbon nanotubes by wet spinning. *Small*, 4(8):1217–1222, 2008c.

Shanju Zhang, Qingwen Li, Ian A. Kinloch, and Alan H. Windle. Ordering in a droplet of an aqueous suspension of single-wall carbon nanotubes on a solid substrate. *Langmuir*, 26(3):2107–2112, 2010b.

X. B. Zhang, K. L. Jiang, C. Teng, P. Liu, L. Zhang, J. Kong, T. H. Zhang, Q. Q. Li, and S. S. Fan. Spinning and processing continuous yarns from 4-inch wafer scale super-aligned carbon nanotube arrays. *Advanced Materials*, 18(12):1505 – 1510, 2006.

X. F. Zhang, Q. W. Li, T. G. Holesinger, P. N. Arendt, J. Y. Huang, P. D. Kirven, T. G. Clapp, R. F. DePaula, X. Z. Liao, Y. H. Zhao, L. X. Zheng, D. E. Peterson, and Y. T. Zhu. Ultrastrong, stiff, and lightweight carbon-nanotube fibers. *Advanced Materials*, 19:4198 – 4201, 2007a.

X. F. Zhang, Q. W. Li, Y. Tu, Y. A. Li, J. Y. Coulter, L. X. Zheng, Y. H. Zhao, Q. X.

Jia, D. E. Peterson, and Y. T. Zhu. Strong carbon-nanotube fibers spun from long carbon-nanotube arrays. *Small*, 3(2):244–248, 2007b.

Yao Zhao, Jinquan Wei, Robert Vajtai, Pulickel M. Ajayan, and Enrique V. Barrera. Iodine doped carbon nanotube cables exceeding specific electrical conductivity of metals. *Scientific Reports*, 1, 2011.

L. X. Zheng, X. F. Zhang, Q. W. Li, S. B. Chikkannanavar, Y. Li, Y. H. Zhao, X. Z. Liao, Q. X. Jia, S. K. Doorn, D. E. Peterson, and Y. T. Zhu. Carbon-nanotube cotton for large-scale fibers. *Advanced Materials*, 19:2567 – 2570, 2007.

H. Zhong and R.J. Lukes. Interfacial thermal resistance between carbon nanotubes: Molecular dynamics simulations and analytical thermal modeling. *Physical Review B*, 74(12), 2006.

X.H. Zhong, Y.L. Li, Y.K. Liu, X.H. Qiao, Y. Feng, J. Liang, J. Jin, L. Zhu, F. Hou, and J.Y. Li. Continuous multilayered carbon nanotube yarns. *Advanced Materials*, 22(6):692–696, 2010.

W. Zhou, J. Vavro, C. Guthy, K. I. Winey, J. E. Fischer, L. M. Ericson, S. Ramesh, R. Saini, V. A. Davis, C. Kittrell, M. Pasquali, R. H. Hauge, and R. E. Smalley. Single wall carbon nanotube fibers extruded from super-acid suspensions: Preferred orientation, electrical, and thermal transport. *Journal of Applied Physics*, 95(2): 649–655, 2004a.

W. Zhou, J. Vavro, C. Guthy, K. I. Winey, J. E. Fischer, L. M. Ericson, S. Ramesh, R. Saini, V. A. Davis, C. Kittrell, M. Pasquali, R. H. Hauge, and R. E. Smalley. Single wall carbon nanotube fibers extruded from super-acid suspensions: Preferred

orientation, electrical, and thermal transport. *Journal of Applied Physics*, 95(2): 649–655, 2004b.

H. Zocher. On independent structure formation in brine. *Zeitschrift Fur Anorganische Und Allgemeine Chemie*, 147(1/3):91–U15, 1925.